



UNIVERSITAT DE  
BARCELONA

## Multisensitive polyurethane/polyurea nanocapsules for smart drug delivery

Cristina Cuscó Marigó

**ADVERTIMENT.** La consulta d'aquesta tesi queda condicionada a l'acceptació de les següents condicions d'ús: La difusió d'aquesta tesi per mitjà del servei TDX ([www.tdx.cat](http://www.tdx.cat)) i a través del Dipòsit Digital de la UB ([diposit.ub.edu](http://diposit.ub.edu)) ha estat autoritzada pels titulars dels drets de propietat intel·lectual únicament per a usos privats emmarcats en activitats d'investigació i docència. No s'autoritza la seva reproducció amb finalitats de lucre ni la seva difusió i posada a disposició des d'un lloc aliè al servei TDX ni al Dipòsit Digital de la UB. No s'autoritza la presentació del seu contingut en una finestra o marc aliè a TDX o al Dipòsit Digital de la UB (framing). Aquesta reserva de drets afecta tant al resum de presentació de la tesi com als seus continguts. En la utilització o cita de parts de la tesi és obligat indicar el nom de la persona autora.

**ADVERTENCIA.** La consulta de esta tesis queda condicionada a la aceptación de las siguientes condiciones de uso: La difusión de esta tesis por medio del servicio TDR ([www.tdx.cat](http://www.tdx.cat)) y a través del Repositorio Digital de la UB ([diposit.ub.edu](http://diposit.ub.edu)) ha sido autorizada por los titulares de los derechos de propiedad intelectual únicamente para usos privados enmarcados en actividades de investigación y docencia. No se autoriza su reproducción con finalidades de lucro ni su difusión y puesta a disposición desde un sitio ajeno al servicio TDR o al Repositorio Digital de la UB. No se autoriza la presentación de su contenido en una ventana o marco ajeno a TDR o al Repositorio Digital de la UB (framing). Esta reserva de derechos afecta tanto al resumen de presentación de la tesis como a sus contenidos. En la utilización o cita de partes de la tesis es obligado indicar el nombre de la persona autora.

**WARNING.** On having consulted this thesis you're accepting the following use conditions: Spreading this thesis by the TDX ([www.tdx.cat](http://www.tdx.cat)) service and by the UB Digital Repository ([diposit.ub.edu](http://diposit.ub.edu)) has been authorized by the titular of the intellectual property rights only for private uses placed in investigation and teaching activities. Reproduction with lucrative aims is not authorized nor its spreading and availability from a site foreign to the TDX service or to the UB Digital Repository. Introducing its content in a window or frame foreign to the TDX service or to the UB Digital Repository is not authorized (framing). Those rights affect to the presentation summary of the thesis as well as to its contents. In the using or citation of parts of the thesis it's obliged to indicate the name of the author.



UNIVERSITAT<sub>DE</sub>  
BARCELONA

**Multisensitive polyurethane/polyurea  
nanocapsules for smart drug delivery**

Cristina Cuscó Marigó

Barcelona, February 2018



Programa de Doctorat en Química Orgànica

**Multisensitive polyurethane/polyurea  
nanocapsules for smart drug delivery**

Doctoral Thesis submitted by:

**Cristina Cuscó Marigó**

Supervised by:

Dr. Ernesto Nicolás Galindo  
Departament de Química  
Inorgànica i Orgànica  
Secció de Química Orgànica  
Universitat de Barcelona

Dr. José Rocas Sorolla  
Ecopol Tech, S. L.

Barcelona, February 2018



# Agraïments

Primer de tot m'agradaria agrair-li al Josep l'oportunitat que em va brindar per fer una tesi industrial a Ecopol Tech sobre un tema tant apassionant com són els sistemes d'alliberació controlats aplicats a càncer. Ha estat una etapa intensa en la qual he viscut un procés maduratiu brutal, com a persona i com a professional. M'agradaria agrair especialment l'oportunitat que vaig tenir per conèixer l'ecosistema científic i d'empreses de Boston, així com també tota la llibertat que sempre m'has donat per innovar a l'investigar, per tots els reptes que m'has plantejat i totes les hores que hem passat al teu despatx discutint sobre resultats. He après molt de tu i del teu entusiasme.

En segon lloc, m'agradaria agrair-li a l'Ernesto haver-me tutoritzat la tesi i haver-me acompanyat en aquest camí, així com també al Jordi, qui va guiar-me en les primeres etapes de la tesi.

Voldria continuar agraït a la meva mare i al meu pare el suport incondicional amb que sempre he comptat i per haver-me ensenyat a guanyar-me les coses; també a la Laura i al Patit per haver estat a costat meu sempre, tant en les èpoques més complicades com en aquelles en què tot anava sobre rodes. Gràcies a vosaltres sóc qui sóc avui. I també m'agradaria seguir dedicant aquests agraïments a tots aquells que formen part de la família que es tria, és a dir, als amics. No els puc escriure tots, però voldria destacar la meva Marina, els Ramallets, les Divas, els amics d'Ecopol, companys de la uni i les titis, la meva parella preferida (la Lídia i el Roc) i els meus satèl·lits que formen part de mi, la Rosinha i la Beltzane. Vull fer una especial menció a l'Arnald, que com ja sap, ha esdevingut un pilar fonamental a la meva vida i no m'ha deixat sola ni un segon des d'aquell juliol del 2012. No podré mai tornar-te tot el que has fet per mi, ets un sol. I al Joan també li vull agrair que hagi cregut en mi sempre, des del primer dia que ens vam conèixer. I que hagi estat a costat meu en tots els moments, per ajudar-me a aixecar i per celebrar les victòries. Ja saps que aquesta tesi va, en part, dedicada a tu.

Per últim, vull acabar aquests agraïments dedicant-li unes paraules a la Mar, la meva celestina, qui va portar-me aquell 9 de juliol a una de les persones més importants de la meva vida. Carles, ja saps què penso de tu. Sobren les paraules.



*A la meva família i amics,  
és un plaer créixer amb vosaltres*



*El més important en ciència no és obtenir nous resultats,  
sinó descobrir noves formes de pensar en ells*

*William Lawrence Bragg*



# Abbreviations and acronyms

## **A**

AABA	$\gamma$ -Aminobutyric acid
AFM	Atomic force microscopy
AQC	6-Aminoquinolyl- <i>N</i> -hydroxysuccinimidyl carbamate

## **B**

BAPMA	<i>N,N</i> -bis(3-aminopropyl)- <i>N</i> -methylamine
BC	Breast cancer
BSA	Bovine serum albumin

## **C**

CSC	Cancer stem cell
CU	Curcumin

## **D**

DDS	Drug delivery system
DEDS	2,2'-Dihydroxyethyl disulfide
DETA	Diethylenetriamine
DiI	1,1'-Dioctadecyl-3,3,3',3'-tetramethylindocarbocyanine perchlorate
DiO	3,3'-Dioctadecyloxacarbocyanine perchlorate
DiR	1,1-Dioctadecyl-3,3,3,3-tetramethylindotricarbocyanine iodide
DL	Drug loading
DLS	Dynamic light scattering
DMEM	Dulbecco's modified eagle medium
DMPA	2,2-Dihydroxymethylpropanoic acid
DMSO	Dimethyl sulfoxide
DOX	Doxorubicin
DPPC	Dipalmitoylphosphatidylcholine
DSPC	Distearoylphosphatidylcholine

## **E**

ECM	Extracellular matrix
EDC	<i>N</i> -(3-dimethylaminopropyl)- <i>N'</i> -ethylcarbodiimide
EE	Encapsulation efficiency
EMA	European medicines agency
EPR	Enhanced permeation and retention
ER	Estrogen receptor

## **F**

FBS	Fetal bovine serum
FDA	Food and drug administration
FLI	Fluorescence imaging
FRET	Förster resonance energy transfer

## **G**

Genamin TAP 100D	1,3-Diamino- <i>N</i> -octadecylpropane
GSH	Glutathione
GTCC	Capric/caprylic triglyceride

## **H**

HEPES	4-(2-Hydroxyethyl)-1-piperazineethanesulfonic acid
HER2	Human epidermal growth factor receptor type 2
HLB	Hydrophilic lipophilic balance
HPLC	High performance liquid chromatography
HPLC-MS	High performance liquid chromatography-mass spectrometry
HSA	Human serum albumin

## **I**

IPDI	Isophorone diisocyanate
IR	Infrared spectroscopy
IS	Internal standard

## **J**

Jeffamine ED2003 Water-soluble aliphatic diamine derived from a propylene oxide capped polyethylene glycol

Jeffcat DPA *N*-(3-Dimethylaminopropyl)-*N,N*-diisopropanolamine

## **K**

KDa Kilodalton

## **L**

LC Lung cancer

## **M**

MAb Monoclonal antibody

Mal Maleimide

MALDI-TOF Matrix-assisted laser desorption/ionization time of flight

MDI Methylene diphenyl diisocyanate

MFI Mean fluorescence intensity

Mowiol 4-88 Poly(vinyl)alcohol with a 4 mPa·s viscosity (4% wt aqueous solution at 20 °C) and 88% degree of hydrolysis.

MTT 3-(4,5-Dimethylthiazol-2-yl)-2,5-diphenyltetrazolium bromide

MWCO Molecular weight cutoff

## **N**

NALA Sodium laurate

NAST Sodium stearate

NB Neuroblastoma

NC Nanocapsule

NEAA Non-essential aminoacids

NHS *N*-hydroxysuccinimide

NLE Norleucine

NMR Nuclear magnetic resonance

NP Nanoparticle

NSCLC Non-small cell lung cancer

## **O**

O/W Oil in water

## **P**

PBS Phosphate buffered saline

PCL Poly(caprolactone)

PECA Poly(ethyl cyanoacrylate)

PEG Poly(ethylene glycol)

PPG Poly(propylene glycol)

PFA Paraformaldehyde

PGA Poly(glycolic acid)

pH<sub>e</sub> Extracellular pH

pH<sub>i</sub> Intracellular pH

PLA Poly(lactic acid)

PLGA Poly(lactic-*co*-glycolic acid)

PMMA Poly(methyl methacrylate)

PNIPAAM Poly(N-isopropyl acrylamide)

PR Progesterone receptor

PS Polystyrene

PTX Paclitaxel

PVA Poly(vinyl alcohol)

PVP Poly(vinyl pyrrolidone)

## **R**

RES Rethiculoendothelial system

RPMI Roswell park memorial institute

RP-HPLC Reverse-phase HPLC

rt Room temperature

## **S**

SCLC Small cell lung cancer

## **T**

T17	Tambjamine 17
T18	Tambjamine 18
TDI	Toluene diisocyanate
TEA	Triethylamine
TEM	Transmission electron microscopy
TFA	Trifluoroacetic acid
THF	Tetrahydrofuran
TMXDI	Tetramethyl-1,3-xylylene diisocyanate
TNBC	Triple-negative breast cancer

## **U**

UV/Vis	Ultraviolet/Visible
--------	---------------------

## **V**

VEGF	Vascular endothelial growth factor
VEGFR	Vascular endothelial growth factor receptor
$V_m$	Membrane potential

## **W**

W/O/W	Water-in-oil-in-water
Wt	Weight

## **Y**

YMER N-120	Non-ionic hydrophilic polymer with two primary hydroxyl groups and a long capped ethoxyxylated side chain
------------	---

## **Z**

$\zeta$ -pot	Zeta potential
--------------	----------------



# Table of Contents

## CHAPTER 1

<b>1. Drug delivery systems for biomedical applications .....</b>	<b>1</b>
<b>2. Preparation of polymer nanoparticles .....</b>	<b>6</b>
2.1. NPs obtained from dispersion of preformed polymers .....	7
<b>2.1.1. Emulsification/solvent evaporation.....</b>	<b>7</b>
<b>2.1.2. Salting-out.....</b>	<b>8</b>
<b>2.1.3. Dialysis.....</b>	<b>10</b>
<b>2.1.4. Supercritical fluid technology .....</b>	<b>10</b>
2.2. NPs obtained from polymerization of monomers.....	11
<b>2.2.1. Emulsion polymerization.....</b>	<b>12</b>
<b>2.2.2. Interfacial polymerization.....</b>	<b>13</b>
<b>2.2.3. Controlled/living radical polymerization.....</b>	<b>13</b>
<b>3. Most relevant polyurethane and polyurea DDS .....</b>	<b>14</b>
3.1. Polyurethane NPs .....	14
3.2. Polyurethane nanomicelles.....	15
3.3. Polyurethane hydrogel NPs .....	15
3.4. Polyurethane-polysaccharide hybrid NPs.....	16
<b>4. Biological considerations.....</b>	<b>16</b>
4.1. Tumor targeting .....	17
<b>4.1.1. Tumor microenvironment.....</b>	<b>17</b>
<b>4.1.2. Passive targeting by the EPR effect.....</b>	<b>19</b>
<b>4.1.3. Active targeting.....</b>	<b>19</b>
4.2. Intracellular delivery .....	20
<b>4.2.1. Endocytosis .....</b>	<b>21</b>
<b>4.2.2. Intracellular trafficking, endosomal escape and degradation.....</b>	<b>22</b>
4.3. Drug release .....	23
<b>4.3.1. Exogenous.....</b>	<b>24</b>
<b>4.3.1.1. Thermoresponsive systems .....</b>	<b>24</b>
<b>4.3.1.2. Magnetically responsive systems .....</b>	<b>25</b>
<b>4.3.1.3. Photoresponsive systems .....</b>	<b>26</b>
<b>4.3.1.4. Ultrasound and electric responsive systems.....</b>	<b>27</b>

4.3.2. Endogenous.....	29
4.3.2.1. pH-responsive systems.....	29
4.3.2.2. Glutathione-responsive systems.....	30
4.3.2.3. Enzymatically responsive systems.....	31
<b>5. Clinically approved NP therapies and diagnostics .....</b>	<b>32</b>
<b>6. Bibliography .....</b>	<b>35</b>

<b>General Objectives.....</b>	<b>47</b>
--------------------------------	-----------

## **CHAPTER 2**

<b>1. Introduction.....</b>	<b>51</b>
1.1. Polyurethane and polyurea DDS.....	51
1.2. Chemistry of polyurethanes and polyureas.....	51
1.2.1. Chemistry of isocyanates .....	51
1.2.2. Main reactions derived from isocyanates .....	54
1.2.3. Side-reactions derived from isocyanates .....	56
1.2.4. Polymer functionality.....	58
1.3. Important considerations in DDS design.....	59
1.3.1. Biocompatibility .....	60
1.3.2. Shell tunability .....	60
1.3.3. Stratified nanostructured shell.....	62
1.3.3.1. The hydrophobic effect and micelle formation .....	62
1.3.3.2. Self-ordered and compact structures.....	64
1.3.4. Interactions with the biological medium.....	65
1.3.5. Encapsulation efficiency and stability .....	66
1.3.5.1. Preformed amphiphilic shell .....	66
1.3.5.2. Tailor-made polymer shell .....	67
1.3.6. Particle size .....	68
1.3.7. Smart targeting .....	69
1.3.8. Biodegradability .....	71
<b>2. Objectives.....</b>	<b>72</b>

<b>3. Results and discussion .....</b>	<b>73</b>
3.1. General experimental design.....	73
3.2. Preparation of the polymers.....	75
<b>3.2.1. Monomers considered .....</b>	<b>75</b>
<b>3.2.2. Polymers syntheses and characterization.....</b>	<b>80</b>
3.3. Nanoencapsulation.....	89
<b>3.3.1. Preparation of the NCs.....</b>	<b>89</b>
<b>3.3.2. Characterization of the NCs .....</b>	<b>95</b>
<b>3.3.2.1. Morphology and size.....</b>	<b>96</b>
<b>3.3.2.2. Surface properties .....</b>	<b>98</b>
<b>3.3.2.3. Encapsulation efficiency and drug loading .....</b>	<b>103</b>
<b>3.3.2.4. NC degradation and release.....</b>	<b>105</b>
<b>4. Conclusions .....</b>	<b>113</b>
<b>5. Bibliography .....</b>	<b>115</b>

## CHAPTER 3

<b>1. Introduction.....</b>	<b>127</b>
1.1. Lung cancer .....	127
<b>1.1.1. Epidemiology and risk factors .....</b>	<b>127</b>
<b>1.1.2. Histology.....</b>	<b>128</b>
<b>1.1.2.1. Small cell lung cancer (SCLC) .....</b>	<b>129</b>
<b>1.1.2.2. Non-small cell lung cancer (NSCLC) .....</b>	<b>129</b>
<b>1.1.3. Treatments .....</b>	<b>129</b>
<b>1.1.3.1. Conventional treatments.....</b>	<b>130</b>
<b>1.1.3.2. Experimental treatments: ionophores.....</b>	<b>133</b>
<b>1.1.3.3. Tambjamines .....</b>	<b>137</b>
<b>1.1.3.4. FDA-approved nanosystems applied to LC.....</b>	<b>140</b>

1.2.	Neuroblastoma .....	141
1.2.1.	Origin .....	141
1.2.2.	Epidemiology and prognostics .....	142
1.2.3.	Treatments .....	143
1.2.3.1.	Conventional therapies.....	143
1.2.3.2.	Targeted treatments .....	144
2.	<b>Objectives.....</b>	<b>145</b>
3.	<b>Results and discussion .....</b>	<b>145</b>
3.1.	Application of Chapter 2 methodology.....	147
3.1.1.	Preparation of the NCs.....	147
3.1.2.	Characterization of the NCs .....	149
3.2.	Optimization .....	155
3.2.1.	Preparation of the NCs.....	155
3.2.2.	Characterization of the NCs .....	157
3.3.	<i>In vitro</i> studies in LC and NB cell lines.....	163
3.3.1.	Cell viability.....	163
3.3.1.1.	LC cell lines .....	163
3.3.1.2.	NB cell lines .....	167
3.3.2.	Cell uptake .....	168
3.3.2.1.	Physiological conditions.....	169
3.3.2.2.	Slightly acidic conditions .....	170
3.3.3.	Cell internalization .....	172
3.4.	<i>In vivo</i> biodistribution in a NB mouse model.....	175
3.4.1.	Preparation of the NCs.....	176
3.4.2.	Characterization .....	180
3.4.2.1.	Morphology and size.....	180
3.4.2.2.	Surface properties .....	182
3.4.2.3.	Antibody conjugation efficiency.....	183
3.5.	<i>In vivo</i> and <i>ex vivo</i> data.....	185
3.5.1.	Incidences .....	186
3.5.2.	Body weight change during treatment.....	187
3.5.3.	<i>In vivo</i> whole-body biodistribution kinetics.....	188
3.5.4.	<i>Ex vivo</i> tumor and whole-body tissue-accumulation kinetics .....	189

3.5.5. Percentage of <i>ex vivo</i> tissue-accumulation per tissue weight.....	201
<b>4. Conclusions .....</b>	<b>202</b>
<b>5. Bibliography .....</b>	<b>204</b>

## CHAPTER 4

<b>1. Introduction.....</b>	<b>211</b>
1.1. Breast cancer .....	211
1.1.1. Epidemiology and risk factors .....	211
1.1.2. Subtypes .....	212
1.1.3. Treatments .....	214
1.1.3.1. Conventional treatments.....	214
1.1.3.2. Targeted therapies .....	217
1.1.3.3. FDA-approved nanosystems applied to BC.....	219
<b>2. Objectives.....</b>	<b>220</b>
<b>3. Results and discussion .....</b>	<b>221</b>
3.1. Amphoteric NCs.....	221
3.1.1. Preparation of the NCs.....	221
3.1.2. Characterization of the NCs .....	223
3.1.3. Cell viability.....	226
3.2. Use of peptides to target BC cells.....	227
3.3. Functionalization considerations .....	228
3.4. Functionalization with A5 .....	231
3.4.1. Preparation of hydrophilic linkers and conjugates .....	231
3.4.2. Preparation of A5-functionalized NCs .....	236
3.4.3. Characterization of the NCs .....	238
3.4.3.1. Morphology and size.....	239
3.4.3.2. Surface properties .....	242
3.4.3.3. A5 conjugation efficiency.....	243
3.4.4. Cell uptake .....	245
3.5. Functionalization with IPEP .....	247
3.5.1. Preparation of the hydrophilic linker and the conjugate .....	247
3.5.2. Preparation of IPEP-functionalized NCs.....	251

3.5.3. Characterization of the NCs .....	253
3.5.3.1. Morphology and size.....	253
3.5.3.2. Surface properties .....	255
3.5.3.3. Peptide conjugation efficiency.....	256
3.5.4. Cell uptake .....	256
<b>4. Conclusions .....</b>	<b>258</b>
<b>5. Bibliography .....</b>	<b>259</b>

## CHAPTER 5

<b>1. Materials .....</b>	<b>265</b>
1.1. Building blocks and crosslinkers.....	265
1.2. Targeting molecules.....	265
1.3. Encapsulated molecules.....	265
1.4. Solvents and auxiliary solutions .....	266
1.5. Materials for biological studies .....	266
1.5.1. <i>In vitro</i> studies.....	266
1.5.2. <i>In vivo</i> studies.....	266
<b>2. Analytical techniques .....</b>	<b>267</b>
2.1. Infrared spectroscopy (IR).....	267
2.2. pH measurements.....	267
2.3. Automatic isocyanate titration .....	268
2.4. Nuclear magnetic resonance (NMR).....	268
2.5. High Pressure Liquid Chromatography (HPLC) .....	268
2.6. Amino acid analysis.....	269
2.7. Dynamic light scattering (DLS).....	271
2.8. Zeta potential ( $\zeta$ -pot) .....	271
2.9. Transmission electron microscopy (TEM).....	271
2.10. Atomic force microscopy (AFM) .....	271
2.11. Ultraviolet/visible spectroscopy (UV/Vis) .....	272
2.12. Fluorescence spectroscopy .....	272
2.13. Lyophilization and reconstitution.....	274
2.14. Solids concentration .....	274
2.15. Centrifugal separation .....	274

2.16.	Dialysis purification.....	275
<b>3.</b>	<b><i>In vitro</i> assays .....</b>	<b>275</b>
3.1.	Lung cancer .....	275
3.2.	Neuroblastoma .....	280
3.3.	Breast cancer .....	280
<b>4.</b>	<b><i>In vivo</i> biodistribution .....</b>	<b>282</b>
<b>5.</b>	<b>Synthetic procedures of Chapter 2.....</b>	<b>286</b>
<b>6.</b>	<b>Synthetic procedures of Chapter 3.....</b>	<b>294</b>
<b>7.</b>	<b>Synthetic procedures of Chapter 4.....</b>	<b>305</b>

**General Conclusions..... 321**

<b>1.</b>	<b>Methodology .....</b>	<b>321</b>
<b>2.</b>	<b>Properties of the NCs .....</b>	<b>321</b>
<b>3.</b>	<b>Biological studies .....</b>	<b>322</b>

**Future Prospects..... 323**

**ANNEXES**

<b>1.</b>	<b>Reactive molecules .....</b>	<b>327</b>
1.1.	Building blocks and crosslinkers.....	327
1.2.	Targeting molecules .....	328
<b>2.</b>	<b>Encapsulated molecules.....</b>	<b>329</b>
2.1.	Drugs .....	329
2.2.	Superhydrophobic agents.....	331
2.3.	Fluorophores.....	332
<b>3.</b>	<b>NMR spectra of the monomers.....</b>	<b>333</b>
<b>4.</b>	<b>Z-potential measurements.....</b>	<b>339</b>
<b>5.</b>	<b>Cytometry raw data .....</b>	<b>340</b>
<b>6.</b>	<b>Chromatograms .....</b>	<b>341</b>
<b>7.</b>	<b><i>In vivo</i> data (organs weight) .....</b>	<b>352</b>



# **CHAPTER 1**

*General Introduction*



## 1. Drug delivery systems for biomedical applications

One of the most important long-term goals of pharmaceutical industry is to develop therapeutic agents that can specifically reach a target site and be delivered at the right time, leaving the rest of the body unaffected. The therapeutic system should be concentrated at the tissue or organ of interest, providing sufficient drug concentration to effectively perform its cytotoxic effect at the desired site. This would lead to a maximization of the therapeutic index of the drug and a decrease of potential side-effects, along with an improvement of the quality of life of the patient.<sup>1-4</sup>

Drugs are the perfect candidates to destroy cancer cells, but their inherent toxicity also damages normal tissues, causing undesired life-threatening consequences.<sup>5,6</sup> To overcome these hurdles, different disciplines have been combining forces to design alternative therapies, but unfortunately most of the times these efforts do not translate into tangible clinical applications.<sup>2,7</sup> This is due to low solubility at physiological pH,<sup>8</sup> poor oral absorption,<sup>9,10</sup> reduced bioavailability, low biodistribution profiles,<sup>11,12</sup> limited cellular uptake,<sup>6,13-15</sup> premature inactivation or rapid elimination.<sup>16</sup>

Given these limitations, a wide range of DDS with improved efficacy and negligible toxicity has emerged, especially in the field of nanotechnology.<sup>4,6,17-19</sup> Nanoparticle-based drugs have unique properties due to their small size, large surface-to-volume ratios and the possibility to functionalize their surface, resulting in better pharmacokinetic and pharmacodynamic profiles compared to the corresponding free drugs.<sup>11,12,20</sup> The first generation of DDS was developed to address single challenges, such as the *in vivo* drug stability, the half-life in bloodstream, the delivery of the drug across the membrane or its targeted delivery to the desired site.<sup>19,21</sup> From then, the systems have evolved to multifunctional and multisensitive entities able to carry out different roles simultaneously, improving their *in vivo* residence times and enhancing the delivery of the drug at the target site. However, despite of the current progress made in this field, most of the advances have not been materialized into commercial products<sup>22</sup> due to different reasons. Firstly, the developed nanosystems are not sufficiently robust and compact,

therefore, they can eventually leak the encapsulated cargo before reaching the target tissue,<sup>23</sup> causing local toxicities and a decrease of drug concentration. Secondly, the encapsulation efficiency and drug entrapment are low,<sup>24,25</sup> forcing the use of higher amounts of encapsulating material, which increases the toxicity and makes the whole process less efficient. Thirdly, common diblock and triblock copolymers present invariable surface properties,<sup>5,25-28</sup> with the consequent lack of reactive sites for modification or functionalization, and the inability to respond to changing external conditions. Finally, the complexity of scaling-up multistep processes requiring several synthetic steps and purification cycles also limits the industrial development of multifunctional systems.<sup>7,15</sup> Overall, these disadvantages make the manufacturing process unfeasible and non-affordable for the consumer.

In this scenario, the intensive research activity has focused on resolving some of the drawbacks presented above and have prioritized the development of scalable DDS. These goals have been considered from different nanotechnological approaches that have led to a wide range of novel DDS. The most important ones are reviewed in the following paragraphs.

**Quantum dots** constitute the first example and are nanometric semiconductor crystals acting as inorganic fluorophores that have become emerging materials due to their photophysical properties<sup>29,30</sup> (**Figure 1**).

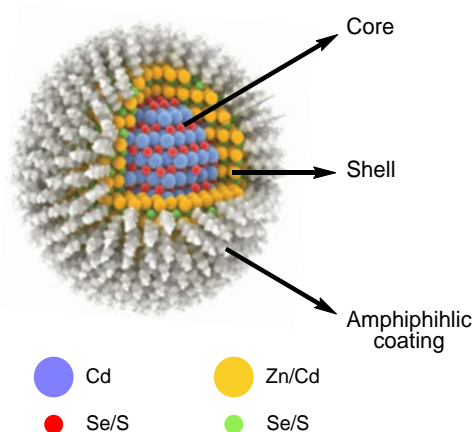


**Figure 1.** Example of the structure of a quantum dot. Adapted from reference 31

Depending on the specific functionalization of quantum dots, they can be used in the monitoring of protein interactions or conformational changes, given the possibility to use them in Förster Resonance Energy Transfer (FRET) technologies.

Other applications involve the fluorescent labelling of cellular proteins, the determination of toxins and pathogens and the *in vivo* imaging or tumor biology investigation.<sup>30,32-34</sup>

Secondly, dendritic structures have also played an important role in the biomedical area, and particularly, **dendrimers**, which are tree-like macromolecules with layered architectures that start from the central core and grow to the terminal sites (**Figure 2**).

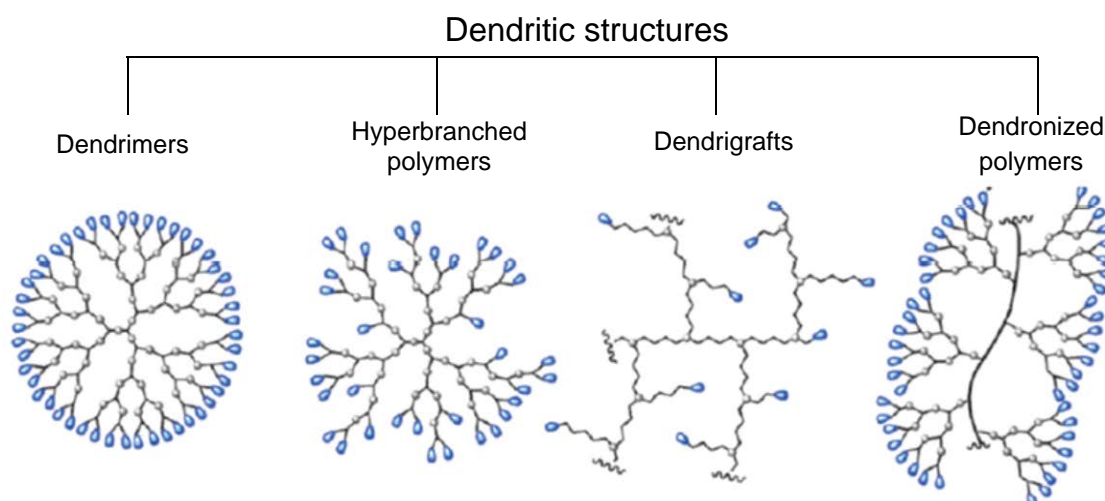


**Figure 2.** Schematic presentation of dendritic structures. Reproduced from reference 35

Dendrimers are synthesized in a step-by-step fashion starting either from the core (divergent process) or from the outer shell (convergent sequence).<sup>36-38</sup> The control over branching achieved by a step-by-step synthesis makes dendrimers unique compared to other randomly crosslinked polymers and have been applied to drug and gene delivery, imaging, tissue repair<sup>39</sup> and photodynamic therapy.<sup>37</sup> Nevertheless, dendrimers generally show low entrapment efficiencies and rapid renal excretion rates due to their small sizes.<sup>35</sup>

Thirdly, **hydrogels** are three-dimensional networks composed of hydrophilic polymer chains that can absorb a high amount of water (**Figure 3**).

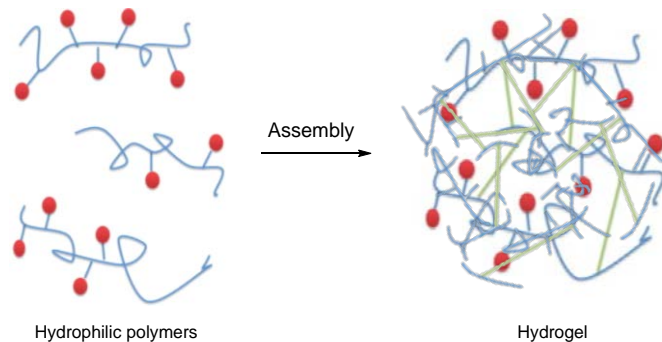


**Figure 3.** Schematic presentation of the formation of a hydrogel. Adapted from reference 40

In medicine, dozens of hydrogel products are being currently used, such as contact lenses, biological adhesives or wound dressings.<sup>40</sup> Since they are highly biocompatible due to their similarities to biological systems, they have been extended to other biomedical purposes. Some of them involve stem cell and cancer research, cell therapy, tissue engineering, immunomodulation and *in vitro* diagnostics.<sup>37,41,42</sup>

In fourth place, **liposomes** are nanovesicles made of phospholipids disposed in a unilamellar or multilamellar construction.<sup>43,44</sup> Bilayer structures are called liposomes, whereas monolayer structures are named micelles (**Figure 4**).

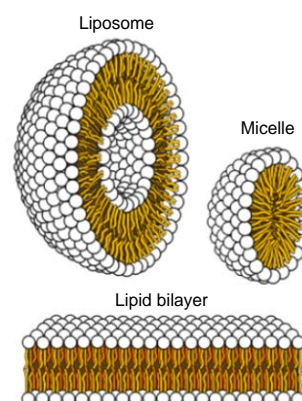


**Figure 4.** Schematic structure of liposomes and micelles from lipid bilayers. Adapted from reference 45

Liposomes are advantageous to other DDS, since they can load both hydrophilic and hydrophobic drugs, which are entrapped in the aqueous core and in the lipid phase, respectively. In fact, these benefits, along with their enhanced biocompatibility, have situated both liposomes and micelles in a number of clinical trials and clinically-approved nanomedicines.<sup>46,47</sup> Despite their clear advantages in terms of biocompatibility and wide applicability,<sup>48</sup> the manufacturing cost is high, they frequently suffer cargo leakage, are rapidly cleared from blood and they can undergo phospholipid oxidation *in vivo*.<sup>23,49,50</sup>

Other well-known DDS are **metal nanoparticles (NPs)** and, as their name suggests, they are NPs made of materials like iron, iron oxides, zinc oxides, gold and silver.<sup>51</sup> Owing to the inherent properties of metal NPs, they have been explored for diagnostic, imaging and therapeutic purposes. For instance, the superparamagnetic properties are useful for imaging, whereas their ability to produce reactive oxygen species can be used to kill cancer cells, which is especially attractive to avoid their conjugation to drugs<sup>52</sup> (**Figure 5**).

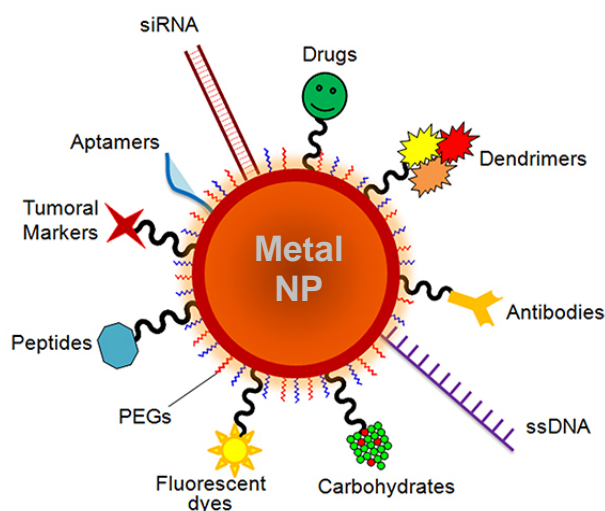


**Figure 5.** Example of a multifunctionalized metal NP. Adapted from reference 53

Metal NPs offer the possibility to link drugs, polymer coatings, targeting ligands, fluorescent dyes, radioisotopes, gene sequences and imaging agents and have become multipurpose tools for diagnosis, therapy and monitoring all within one formulation.<sup>53,54</sup> However, despite these advantages, some toxicological issues have been reported frequently, due to excessive oxidative stress that can trigger

irreversible damage to proteins, lipids, and DNA, and can eventually lead to necrosis and/or apoptosis.

Finally, **polymer NPs** are defined as solid and colloidal particles composed of polymer materials that can be classified into nanocapsules (NCs) and nanospheres<sup>2,3,55-57</sup> (**Figure 6**).

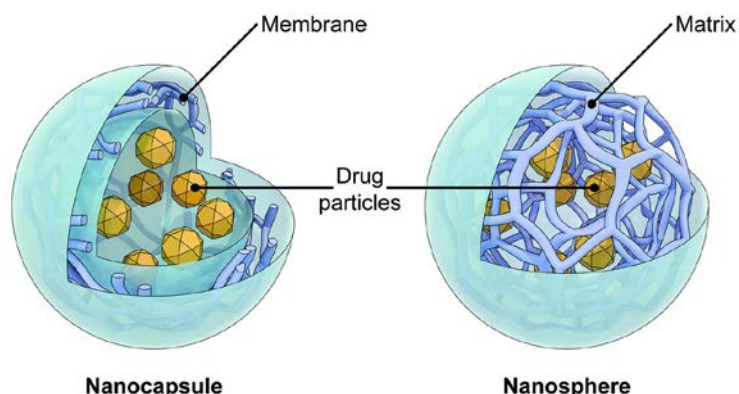


**Figure 6.** The structure of nanocapsules and nanospheres. Reproduced from reference 57

NCs are composed of vesicles that offer a physical cavity (core) where the molecules are entrapped, surrounded by a polymer shell; nanospheres are composed of a solid matrix where the molecules are adsorbed at the surface or encapsulated in the particle.<sup>26,55,56,58-60</sup>

Polymer NPs can be synthesized easily, they present more biocompatibility compared to existing metal NPs and can be tuned for the desired applications. Among the most common ones, polymer NPs stand out as DDS to encapsulate both hydrophilic and hydrophobic molecules and as bioimaging and biosensing tools.<sup>56,60</sup>

## 2. Preparation of polymer nanoparticles

A wide range of methods have been developed to prepare polymer NPs depending on different parameters, such as the type and area of application, desired size, physicochemical properties of the core, desired surface properties, stability requirements, method feasibility and the scaling-up associated cost, among others.<sup>55,61,62</sup> In this regard, the polymer NPs can be divided into two main categories regarding the preparation techniques: NPs obtained from preformed polymers and NPs synthesized from direct polymerization of monomers.<sup>56,63-66</sup>

## 2.1. NPs obtained from dispersion of preformed polymers

The nanoparticulate systems obtained from the dispersion of preformed polymers can be synthesized by using different methods, which are listed below.

### 2.1.1. Emulsification/solvent evaporation

Solvent evaporation was the first method developed to prepare polymer NPs from preformed polymers and it is still the most widely used technique in this category.<sup>56,59,65,67</sup> The NPs are formed from a two-step synthesis that involves the emulsification of an organic polymer solution containing the drug into an aqueous phase, followed by the evaporation of the solvent, which induces polymer precipitation into nanospheres<sup>56,59,66</sup> (**Figure 7**).

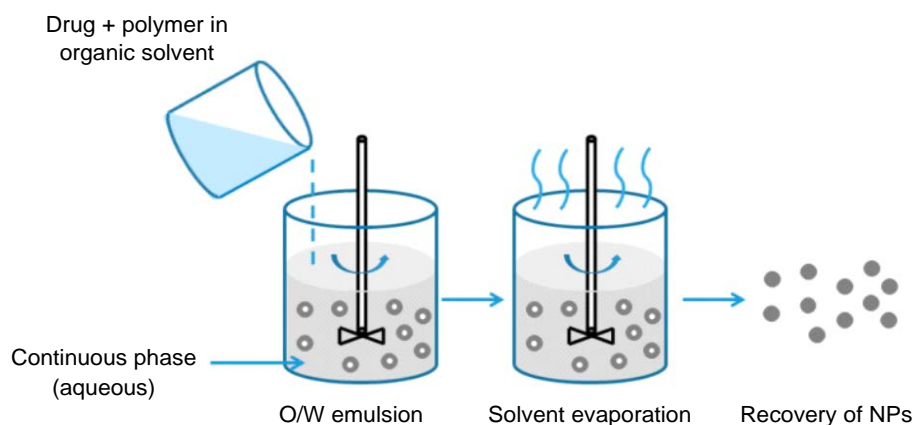


**Figure 7.** Schematic process of emulsification/evaporation method. Adapted from reference 66

In this process, the drug, which is mixed with a polymer in an organic solvent, is introduced into the aqueous phase using surfactants and high-energy homogenization/ultrasonication, which contribute to the micelle stabilization. The word surfactant is a contraction of the descriptive words surface-active agent. These molecules present amphiphilic structures and tend to concentrate at interfacial regions, such as air-water, oil-water and solid-liquid.<sup>68</sup> Once the polymer precipitates, the solvents are removed by increasing the temperature, under reduced pressure or by continuous stirring. Afterwards, the solidified NPs are usually collected by ultracentrifugation and washed several times to remove the dispersing agents.<sup>65,67</sup>

This method allows the preparation of both single and double emulsions, depending on the physicochemical properties of the encapsulated drug. In the first case, the molecules in the core are hydrophobic and yield oil in water (o/w) emulsions. In the second group, the hydrophilic bioactive molecules are dispersed in an oily phase, which is subsequently emulsified into an aqueous medium, leading to (water-in-oil)-in-water (w/o/w) emulsions.<sup>56,65,67</sup>

The limitations of this method are imposed by the scale-up of the high energy homogenization processes that are necessary to adjust the desired size. The most frequently used polymers to prepare these NPs are poly(lactic acid) (PLA), poly(lactic-co-glycolic acid) (PLGA), ethylcellulose, poly(caprolactone) (PCL) and poly(vinyl alcohol) (PVA)<sup>56,59,65,67</sup> (**Figure 8**).

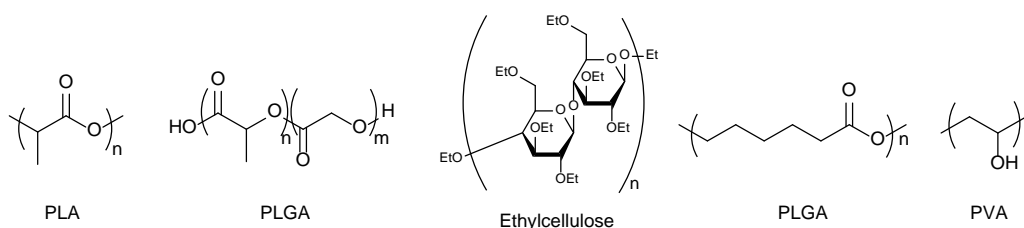


**Figure 8.** Chemical structures of the polymers used in emulsification/evaporation method

The polymers used in the preparation of NPs through this method are usually hydrophilic, since they help with the dispersion and stabilization of the oily droplets in the aqueous phase.

### 2.1.2. Salting-out

Bindschaedler *et al.*<sup>69</sup> reported a modified version of the previous technique in order to avoid the use of hazardous solvents and surfactants. In the salting-out process, the polymer and the drug are initially dissolved in a solvent, such as acetone, which is emulsified into an aqueous gel containing a salting-out agent (electrolytes and non-electrolytic molecules as sucrose) and a colloidal stabilizer, like poly(vinyl pyrrolidone) (PVP) or hydroxyethylcellulose<sup>66</sup> (**Figure 9**).

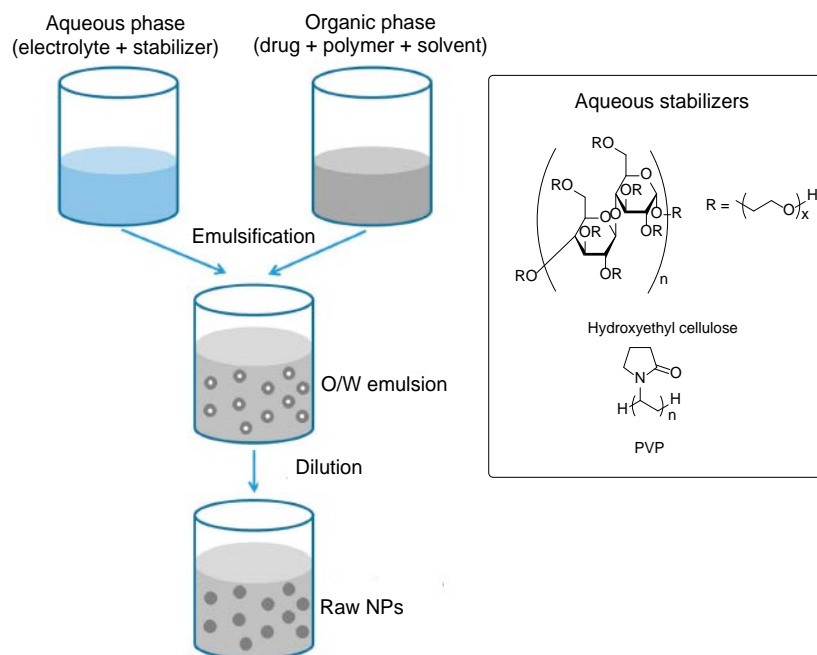


**Figure 9.** Schematic process of the salting-out method. Adapted from reference 66

The o/w emulsion is diluted with a sufficient volume of aqueous solution to enhance the diffusion of acetone into the aqueous phase, inducing the formation of nanospheres. The selection of the salting-out agent is important to guarantee the encapsulation efficiency of the drug. Both the solvent and the salting-out molecules are removed at the end of the process by cross-flow filtration.<sup>65</sup>

The main advantage of this technique is that proteins can be encapsulated, since harsh conditions such as high temperature, high-intensity stirring or shearing are avoided. However, the greatest drawbacks are the exclusive application of hydrophobic molecules and the extensive NP washing steps.<sup>56</sup>

### 2.1.3. Dialysis

Dialysis is a simple and effective method to prepare small and narrow-distributed NPs<sup>56,65</sup> (**Figure 10**).

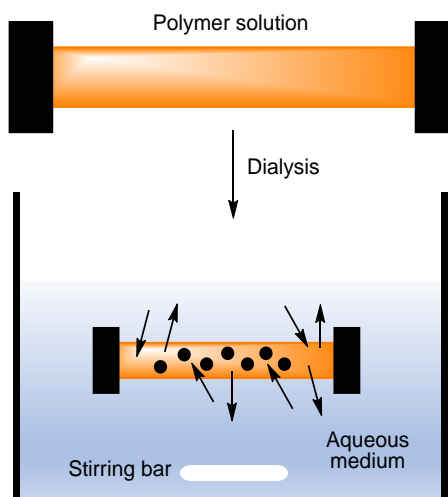


**Figure 10.** Schematic process of the dialysis method. Adapted from reference 56

The polymer is dissolved in an organic solvent and placed inside a dialysis tube with the desired molecular weight cutoff (MWCO). The dialysis is performed against an aqueous medium that is not miscible with the solvent containing the polymer. Then, the displacement of the solvent from the interior of the membrane results in a progressive aggregation of polymer due to a loss of solubility.<sup>56,63</sup>

The mechanism of formation of NPs through this method is not fully understood, but it is thought that it may be based on a sort of nanoprecipitation of the polymer on the organic phase.<sup>70</sup> A wide range of NPs have been developed by using solvents such as DMF, DMA and DMSO, and dialysis periods between 12 and 96 h.<sup>56,65</sup>

### 2.1.4. Supercritical fluid technology

Some of the techniques described above are complex and the products derived thereof are usually characterized by a high content of residual solvents, low drug loading, drug denaturation or undesired physicochemical properties.<sup>59</sup> In this scenario, the techniques based on compressed or supercritical fluids, such as

supercritical CO<sub>2</sub>, can be an interesting alternative to prepare nanoparticulate products (**Figure 11**).

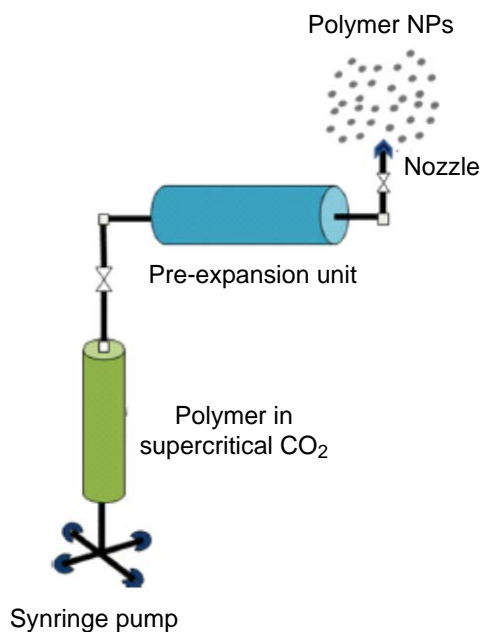


**Figure 11.** Schematic process to prepare NPs through supercritical fluid technology. Adapted from reference 56

This process consists of dissolving the polymer and the drug into a supercritical fluid, which passes through an expansion unit to finally reach a nozzle. Then, the fluid is evaporated in the spraying process where solute particles precipitate.<sup>56,71,72</sup>

The main advantages of this technique are the elimination of solvents and the possibility to prepare the products in high quality, including protein DDS. Nevertheless, the equipment requires a considerable capital investment and elevated pressures that are associated with high energy costs.<sup>65</sup>

## **2.2. NPs obtained from polymerization of monomers**

This section describes the process that allows the preparation of polymer NPs from the polymerization of monomers followed by the emulsion of the polymers. In this category, the polymerization techniques can be further divided into: emulsion polymerization, interfacial polymerization and controlled/living radical polymerization.<sup>56,65</sup>

### 2.2.1. Emulsion polymerization

Emulsion polymerization is the most common technique to manufacture a wide variety of specialty polymers, since water is used as the dispersion medium, providing environmentally friendly properties and excellent heat dissipation during polymerization. This technique is further classified as conventional and surfactant-free emulsion polymerization, depending on the presence of surfactants in the process.<sup>56</sup>

On one hand, the conventional emulsion polymerization involves emulsification of a relatively hydrophobic monomer in water with an emulsifier, followed by the initiation reaction. The polymerization process can be initiated either when the monomer, dissolved in the continuous phase, collides with the initiator or when it is converted into an initiating radical by applying high-energy radiation. Then, the chain growth occurs when the initiated monomer collides with other monomers, extending the length of the polymer in water. An extremely large oil–water interfacial area is generated as the particle nuclei form and grow in size with the progress of the polymerization. Thus, an effective stabilizer is incorporated onto the particle surface, preventing coagulation.

Typical monomers used in emulsion polymerization include polystyrene (PS), poly(methyl methacrylate) (PMMA) or poly(ethyl cyanoacrylate) (PECA)<sup>56,63,65</sup> (**Figure 12**).

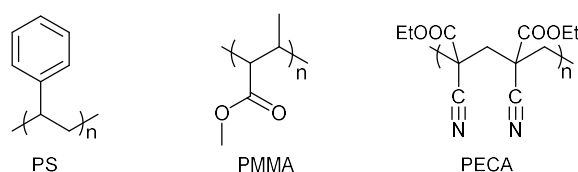


**Figure 12.** Some of the polymers that are used in emulsion polymerization

On the other hand, surfactant-free emulsion polymerization avoids the addition and subsequent removal of surfactants once the products are synthesized. Therefore, the main components of this technique are water, an aqueous-soluble initiator and a monomer, such as vinyl or acryl derivatives. In this particular case, the stabilization of the NPs occurs through the use of ionizable initiators or ionic co-

monomers and their formation is done via micellar or homogeneous nucleation.<sup>56,63,65</sup>

Although surfactant-free emulsion polymerization emerged as a simple and green process for the preparation of NPs without stabilizers, several challenges are still unresolved and hinder their manufacturing. Among them, the preparation of monodisperse emulsions and the controlled particle size systems.<sup>56</sup>

### **2.2.2. Interfacial polymerization**

Interfacial polymerization involves two reactive monomers dissolved in two different phases (continuous and disperse phase), which polymerize at the interface of the two liquids to form the shell of the NPs.<sup>56,73-76</sup> This technique has been widely used in many fields, ranging from the encapsulation of pharmaceutical products to the preparation of conducting polymers.

Oil-containing NPs can be obtained by the polymerization of the monomers at the o/w interface of very fine emulsions. In this case, a water-soluble solvent is used as a vehicle and the polymerization takes place at the surface of the oil droplets formed during emulsification. Alternatively, water-containing NPs can be obtained from w/o emulsions and the polymer formed at the interface precipitates to form the NP shell.

Interfacial polymerization combined with spontaneous emulsification in a single stage is a new technique used for the preparation of NPs. More specifically, polyurethane NPs with different physicochemical properties have been prepared using polyols and isocyanates, as reported by different groups.<sup>76-81</sup> In this case, a fast dispersion of the droplets is produced by spontaneous emulsification and subsequent polycondensation reactions take place at the oil surface to yield the polyurethane shell.

### **2.2.3. Controlled/living radical polymerization**

Radical polymerization is a method by which a polymer is formed by successive addition of free-radical building blocks<sup>82-84</sup> but, despite of its frequent presence in different applications, it presents important limitations. The primary drawbacks include the lack of control over the molar mass, molar mass distribution, end-functionalities and the macromolecular architecture due to the unavoidable fast

radical-radical termination reactions.<sup>65,85</sup> In this scenario, by using controlled/living radical polymerization, most of these issues are addressed, besides the improvement of the processes from the environmental point of view.

There are three main approaches for controlled/living radical polymerization: nitroxide-mediated polymerization, atom transfer radical polymerization and reversible addition and fragmentation transfer chain polymerization. Despite of the progress achieved in this particular type of polymerization, there are still some issues to be solved. For instance, the process complexity or the presence of residual control agents in the final product that lead to color, odor and stability problems.<sup>56,65</sup>

### **3. Most relevant polyurethane and polyurea DDS**

First conceived in 1950s, polymer NPs have evolved from very simple nanostructures to clinically accepted smart nanosystems for multiple purposes.<sup>2,3,55,56</sup> Although there is still modest research activity to develop nanocarriers based on polyurethane and polyurea chemistry, some of them have either entered the market or are in different phases of clinical trials.<sup>86</sup> Given the chemical versatility of this chemistry, nanomedicines based on these materials are currently one of the most promising systems for drug delivery. In this section some of the most common types of polyurethane and polyurea all-in-one nanosystems are reviewed.

#### **3.1. Polyurethane NPs**

Polyurethane NPs can be prepared from environmentally friendly processes by different techniques, being emulsification the most common one.<sup>76,87</sup> They can present different functionalities due to their chemical versatility and they can load both hydrophobic and hydrophilic molecules.<sup>88</sup> Hydrophobic drugs can be incorporated inside the NP by means of an amphiphilic polymer, while hydrophilic drugs can be loaded by w/o/w double emulsions or incorporated onto the NP surface after manufacturing.<sup>56,65</sup>

Given that polyurethane NPs are still novel DDS, deeper studies have to be performed to determine their biodegradation rates to allow the prediction of their release profiles. In this regard, Uscátegui *et al.*<sup>89</sup> studied the effects of the type of

polyol and concentration of PCL in polyurethanes on microbial degradability, cytotoxicity, biological properties and antibacterial activity. Another example is based on the work of Ou *et al.*,<sup>90</sup> who demonstrated that one type of biodegradable polyurethane NPs was a smart tool to deliver drugs close to body temperature. This effect was achieved by the modulation of hard and soft segments of the polymer, which led to different degree of crystallinity around 37 °C.

### **3.2. Polyurethane nanomicelles**

Polyurethane nanomicelles aim to combine the advantages of shell flexibility of liposomes and the chemical tunability of polymers. To prepare this kind of nanosystems, the polymers forming the shell self-assemble only by physical interactions and lead most of the times to non-controlled molecular weight, polydispersed polymers and *in vivo* unpredicted release profiles.<sup>23</sup>

However, some groups have reported benefits upon the use of polyurethane nanomicelles, in terms of controlled intracellular drug release and cell internalization.<sup>91,92</sup> For instance, Jabbarzadegan *et al.*<sup>93</sup> prepared arteether-loaded polyurethane nanomicelles with a rapid delivery at acidic pH, along with an inhibitory effect of the growth of a specific breast cancer cell line. In another study, Ajorlou *et al.*<sup>94</sup> demonstrated that polyurethane nanomicelles loaded with paclitaxel (PTX) caused a significant tumor shrinking in an *in vivo* mouse model, compared to the free drug.

### **3.3. Polyurethane hydrogel NPs**

Hydrogel NPs are three-dimensional highly crosslinked networks of hydrophilic polymers with high capacity for water and physiological fluids, promoting ordered gelification into nanometric systems.<sup>95</sup> In the last decade, polyurethane hydrogels have gained importance, since they exhibit high chemical tunability and outstanding biocompatibility.<sup>96-98</sup> In addition, polyurethane hydrogels can easily incorporate specific moieties to make them responsive to temperature or enzymatic environments or the drug loading can be tuned by controlling the porosity of the material. In this line, thermoresponsive polyurethane

dispersions were prepared by Hsieh *et al.*<sup>99,100</sup> and showed outstanding performance in restoring the brain function of injured adult zebrafish.

### 3.4. Polyurethane-polysaccharide hybrid NPs

A common issue encountered when nanosystems are tested *in vivo* is the formation of a physisorbed protein corona on their surfaces. This causes the modification of the size, targeting abilities and surface properties of the NPs, which jeopardizes their biodistribution, circulation rates and clearance.

In this scenario, polysaccharides, conjugated to the NP surface, have been reported to reduce protein-particle interactions and lower sequestration by the reticuloendothelial system (RES) when conjugated to the NP surface. For instance, several groups<sup>101,102</sup> developed hybrid hydroxyethyl starch-polyurethane NPs and succeeded in minimizing plasma protein interactions and achieving an efficient and stealth targeting. Likewise, Xu *et al.*<sup>103</sup> reported a series of core-shell NPs containing anionic polyurethane moieties and functionalized with chitosan. They were tested in cell culture experiments and exhibited very low protein absorption, along with very low cytotoxicity.

## 4. Biological considerations

A DDS should be designed considering not only the desired physicochemical properties but also the biological interactions it will face from its administration to its degradation in the target tissue. This process entails four important phases, which are depicted in **Figure 13**.

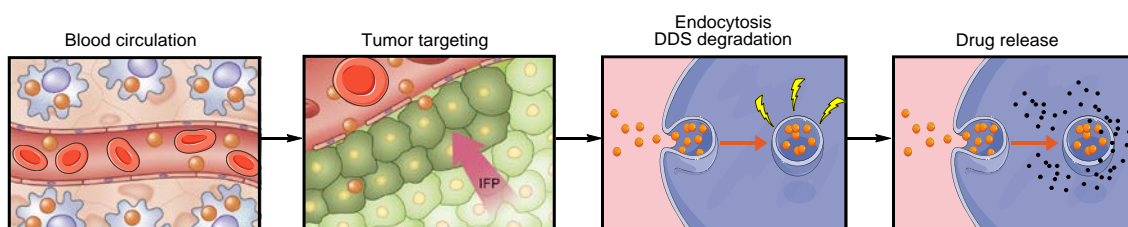


**Figure 13.** Different stages that a DDS faces. Adapted from reference 104

In line with the figure, there are some requirements that the DDS should fulfill in order to ensure its expected performance. Firstly, it is crucial that the DDS does not release the drug prematurely upon contact with macromolecules, when it is in circulation. Secondly, it should be able to target the tumor site as efficiently as possible to avoid its accumulation in undesired tissues and organs. Once in the target site, it should be able to penetrate the cancer cells in a controlled manner to prevent cell saturation, and finally, it should degrade under a specific stimulus occurring in the target tissue. Once the DDS is disassembled, it should release the drug that will lead to the therapeutic effect. Each one of these aspects will be explained in more detail in the following sections.

#### **4.1. Tumor targeting**

Tumor targeting is the ability of a given nanosystem to specifically reach the diseased site, the tumor environment in the case of cancer, leaving the rest of the organism unaffected. Tumor targeting is key to ensure that the administered drug is sufficiently concentrated at the desired site and thus can lead to a therapeutic effect. In addition, an appropriate tumor targeting also avoids the use of higher and unnecessary drug doses that are harmful to healthy tissues and organs and promote the appearance of side-effects. In this regard, there are two main mechanisms to achieve tumor targeting, the so-called passive and active targeting. However, before going in depth with these two pathways, the biological features of the target site, the tumor microenvironment, will be firstly discussed.

##### **4.1.1. Tumor microenvironment**

In cancer therapy, the tumor microenvironment is the physical scaffold composed of proliferating tumor cells, tumor stroma, blood vessels, fibroblasts, immune cells, non-cancerous cells and the extracellular matrix (ECM).<sup>105,106</sup> This network is altered due to cancer progression and thus presents numerous differences compared to normal tissues, including vascular abnormalities, acidity, oxygenation, perfusion and abnormal metabolic state. Among them, the first two will be particularly described as they influence the tumor-targeted DDS.<sup>105</sup>

On one hand, angiogenesis is the formation of new blood vessels from existing ones. For small tumors having 1–2 mm<sup>3</sup>, the oxygen and nutrients can be supplied by simple diffusion from the microenvironment, but once tumors grow to larger sizes, a state of cellular hypoxia starts and angiogenic processes are activated. Different complex steps take place in the construction of new vessels, but the result is an immature vasculature with a heterogeneous dilated shape. This process is crucial for cancer progression and dissemination and is directly related to the enhanced permeability and retention (EPR) effect,<sup>107-109</sup> which will be discussed later.

On the other hand, pH is also deregulated in the tumor microenvironment due to an increased glucose metabolism that has to respond to highly proliferating cells.<sup>110,111</sup> (**Figure 14**).

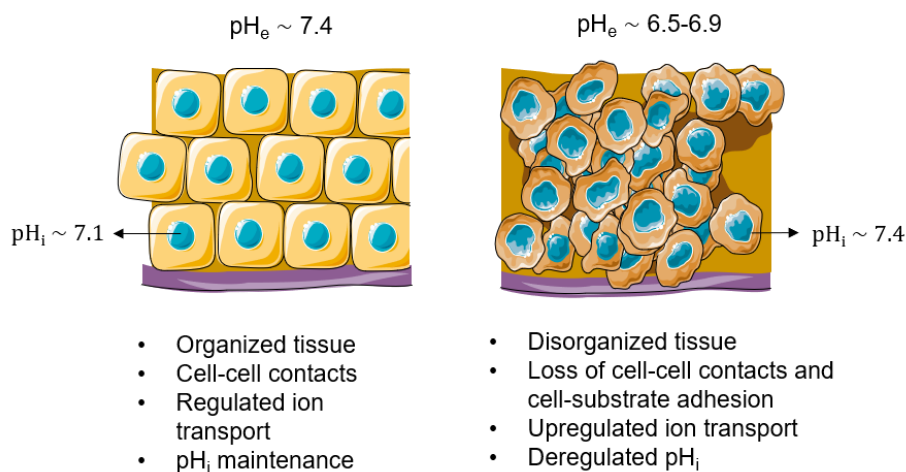


**Figure 14.** Differential features between normal and cancer tissues

This effect is combined with a poor perfusion and results into a more acidic extracellular pH ( $pH_e$ ) in malignant tumors ( $pH_e = 6.5-6.9$ ), compared to a normal tissue under physiologic conditions ( $pH_e = 7.2-7.4$ ). This reversed pH gradient ( $pH_e < pH_i$ ) is responsible for the proton migration from the tumor into adjacent normal tissues and the alteration of healthy cells at the tumor-stroma interface.

### 4.1.2. Passive targeting by the EPR effect

Passive targeting consists on the transport of nanocarriers through leaky tumor capillaries into the tumor interstitium by convection and diffusion.<sup>112</sup> Such spontaneous accumulation works specially well in these conditions, since the high permeability of the tumor vasculature allows NPs to enter the tumor interstitial space, while the compromised lymphatic filtration avoids their excretion. This combination of events is called the EPR effect and is the basis of tumor accumulation for all nanocarriers around 10–100 nm (**Figure 15**). Indeed, the EPR effect is observed in most of the human cancers, but there is variability regarding the tumor types and the anatomical sites.<sup>105</sup>

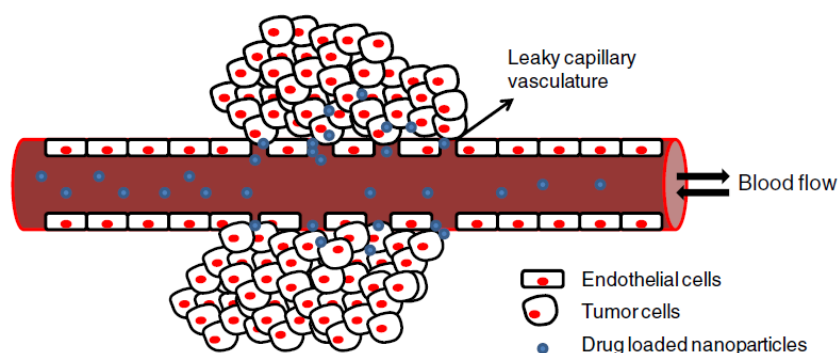


**Figure 15.** Passive tumor targeting. Adapted from reference 113

The EPR effect is optimal if nanocarriers can evade immune sequestration and are long-circulating, since they will have a greater chance to reach the tumor tissues.<sup>114,115</sup> Therefore, stealth nanocarriers will predominantly accumulate in tumors than in healthy cells and will release their cargo and generate an anticancer effect.<sup>107</sup> However, there are two key parameters that the nanomedicines should fulfill. The ideal size should be larger than 10 nm to avoid renal accumulation and smaller than 100 nm to prevent liver sequestration. Moreover, the charge should be neutral to anionic to evade renal elimination and capture by the RES.<sup>105</sup>

### 4.1.3. Active targeting

In this approach, targeting ligands are attached on the surface of the nanocarrier to interact with the receptors specifically overexpressed at the tumor cell membrane or at the tumor vasculature. Targeting entities can be monoclonal

antibodies (mAb), antibody fragments, peptides, carbohydrates or nucleic acid sequences<sup>105,112,116,117</sup> (**Figure 16**).

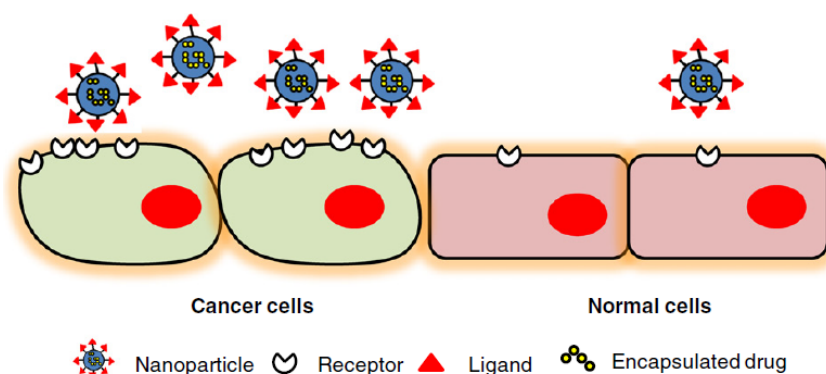


**Figure 16.** Active tumor targeting. Adapted from reference 113

MAbs target specific receptors and interfere to different signal-transduction pathways, regulating certain oncogenes involved in cancer proliferation and thus they can function as targeting ligands or as drugs (i.e. trastuzumab, bevacizumab). For the rest of the cases, the targeting ligand only addresses the nanocarrier to the tumor without displaying any anticancer effect.<sup>105,118</sup>

Regardless the type of functionalization, targeted nanomedicines should also avoid clearance by RES, show prolonged blood circulation, specific interaction with the cell receptor and degrade at the target site. Likewise, other parameters such as the size, density and type of ligand should also be considered to ensure an enhanced therapeutic effect.

## 4.2. *Intracellular delivery*

After a given nanosystem has reached the tumor site, either by passive or active targeting mechanisms, it is internalized by endocytosis and transferred to different organelles, such as endosomes, lysosomes, mitochondria, endoplasmic reticulum or the nucleus.<sup>119,120</sup> In this section, the most important endosomal mechanisms and intracellular delivery are presented.

### 4.2.1. Endocytosis

Endocytosis is a common mechanism found in all cells in the body in which macromolecules are internalized and retained in transport vesicles which traffic along the endolysosomal scaffold.<sup>121</sup> This process can be achieved selectively, whereby a cell-interacting moiety is presented on the nanocarrier surface, or non-selectively, which occurs by hydrophobic and electrostatic interactions.<sup>122-124</sup>

Different internalization pathways have been described depending mainly on the nature and size of the nanosystems.<sup>120,125-127</sup> (**Figure 17**).

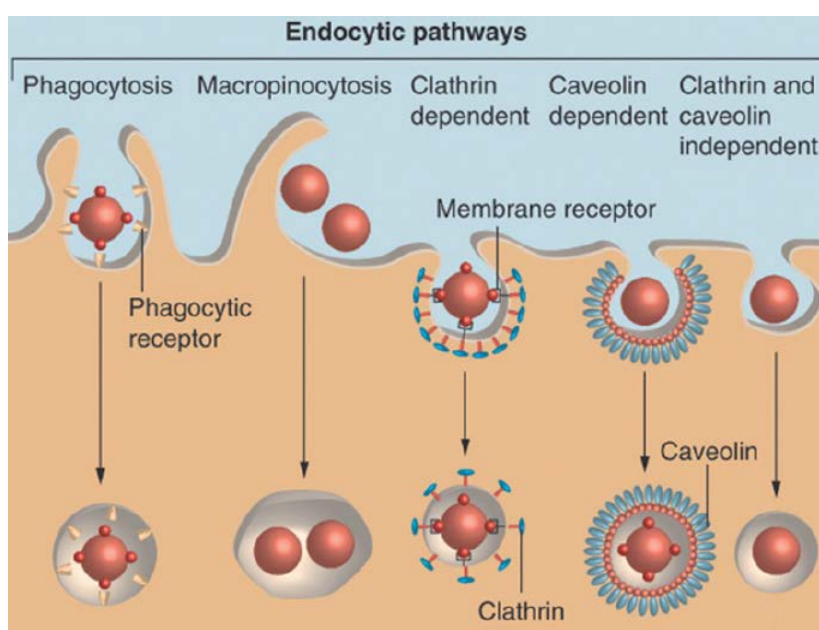


**Figure 17.** Different endocytic pathways. Adapted from reference 127

Phagocytosis has been frequently associated to large particles ( $> 1 \mu\text{m}$ ), although some examples of nanosized medicines have been reported to internalize through this mechanism.<sup>121,128</sup> Similarly, macropinocytosis is exploited for the uptake of large particles having up to 1 mm of diameter and it operates in synchrony with other entry mechanisms because a wide range of cargo sizes can be accommodated. Moreover, eukaryotic cells can use clathrin-mediated entry to internalize particles ranging from 10 to 300 nm and calveolin-mediated endocytosis for 50 to 80 nm.<sup>120</sup> In addition, pinocytosis, also known as cell drinking, is a process that starts with the formation of a pocket through the erosion of the cell membrane

and then the pocket is subsequently englobed into the cell, generating a vesicle containing the particles and extracellular fluid.<sup>129</sup>

Both pinocytosis and phagocytosis involve the uptake of much larger areas of cell compared to clathrin- and caveolin-mediated pathways. In addition, while pinocytosis can occur in all types of cells, phagocytosis only can be performed by a specialized set of mammalian cells, such as macrophages, monocytes and neutrophils.

#### 4.2.2. Intracellular trafficking, endosomal escape and degradation

Endocytosis transports NPs into cells within vesicles and, depending on the mechanism of internalization, they can be either recycled, driven out of the cell or trafficked to organelles.<sup>123</sup> (**Figure 18**).

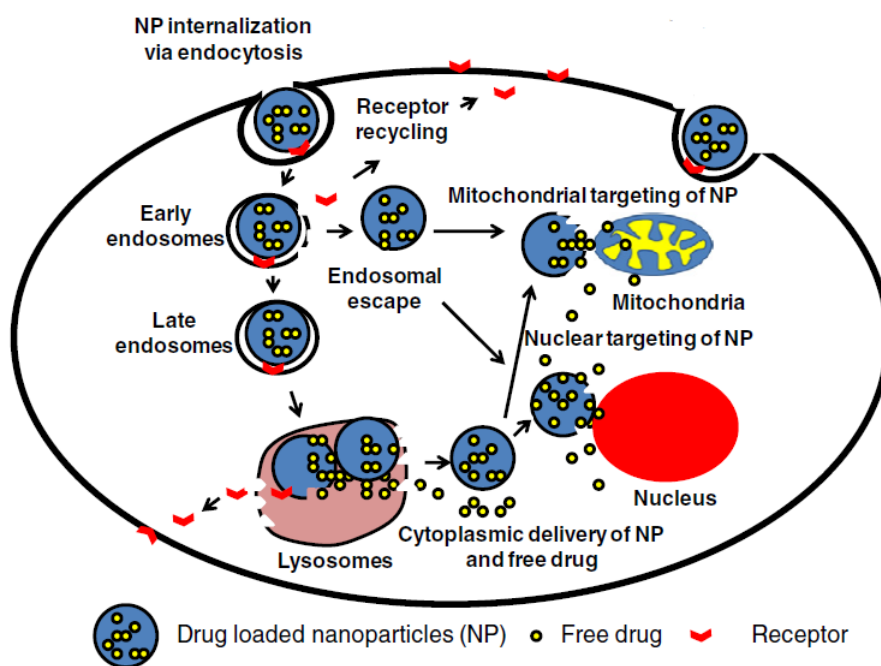


**Figure 18.** Intracellular trafficking, endosomal escape and degradation. From reference 113

During endosomal trafficking, vesicles are sorted, fused or dissociated, as well as matured into endosomes and lysosomes. For those nanosystems intended to target the endolysosomal network, the endocytic uptake is the best option, since it allows accessibility to their targets. Nevertheless, for the rest of the nanosystems, this fate is undesired, since the maturation of the vesicles into late endosomes and lysosomes implies a pH decrease from 6 to 4 and their digestion by

enzymes.<sup>122,123,129</sup> Several strategies have been developed to overcome the endosomal barrier. For instance, coating with virus-like envelopes or pH-sensitive peptides that can disrupt the vesicle membrane. Another strategy is the functionalization the nanosystems with polymers showing buffer capacities that mediate their escape through the “proton-sponge effect”.<sup>113,122,130</sup>

Once the nanosystems are released from endosomal vesicles, they have to move across the cytoplasm to bind their targets. During this process, they bind to intracellular components that modify their mobility. For instance, there are motor proteins that typically transport vesicular cargoes or propel the particle in and out of the cell.<sup>113,122,130</sup> Exocytosis mechanisms have been superficially explored and thus have led to important unanswered questions regarding toxicity issues and accumulation of NPs in filtration organs. Overall, more investigation in these aspects should be performed in order to achieve more reliable results and to move more confidently from *in vitro* preclinical phases to clinical trials.<sup>131,132</sup>

### **4.3. Drug release**

Recent chronopharmacology studies indicate that some diseases, such as tumor stages and progression of cancer, present a strong circadian influence.<sup>133</sup> Therefore, the treatment of these diseases requires an accurate and predictable control of the release of drugs in response to a single or multiple stimuli.<sup>134</sup> This effect can be achieved by inserting specific chemical moieties along the polymer shell that can be activated or cleaved under certain conditions. In this regard, two different types of drug release can be differentiated depending on the source of the stimulus: exogeneous and endogenous release.<sup>135,136</sup> The former is related to those DDS that take advantage of externally applied stimuli, while the latter is based on those nanosystems that respond to internal stimuli.<sup>130,135,136</sup>

### 4.3.1. Exogenous

#### 4.3.1.1. Thermoresponsive systems

A thermoresponsive system is based on conformational and structural changes that experience the components of the nanocarrier when local heat is applied and results in some variations on the shell permeability. Ideally, thermoresponsive carriers should retain their cargo at body temperature and rapidly deliver the drug within a locally heated tumor ( $\sim 40\text{--}42\text{ }^{\circ}\text{C}$ )<sup>137</sup> (**Figure 19**).

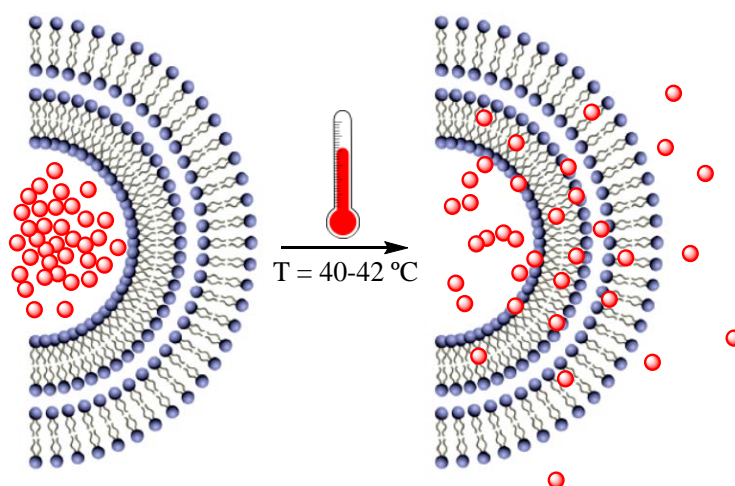


**Figure 19.** Example of thermoresponsive DDS. Adapted from reference 137

The prime thermoresponsive polymer is poly(*N*-isopropyl acrylamide) (PNIPAAm) (**Figure 20**), which becomes water soluble or insoluble when temperature is above or below a certain value, respectively. This value, though, can be raised by copolymerization or conjugation with other hydrophilic polymers and vice versa.<sup>135</sup>

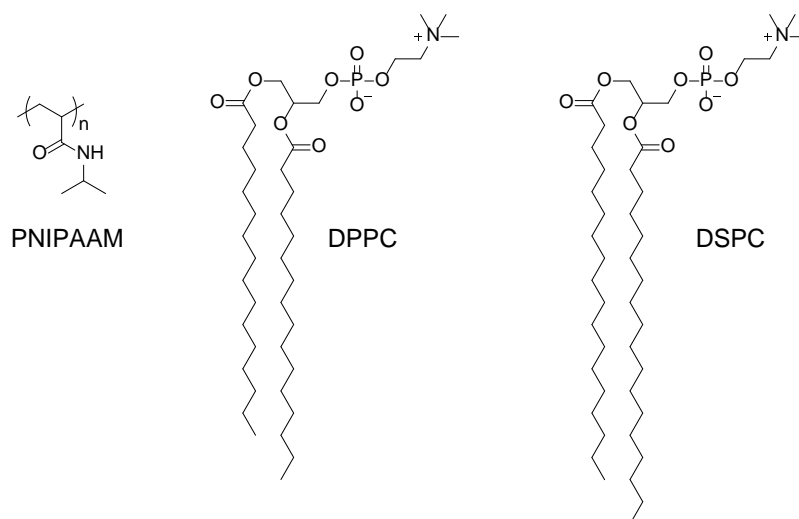


**Figure 20.** Examples of thermoresponsive polymers

Another well-known example of thermoresponsiveness is found in liposomes. In this case, temperature causes the phase transition of the constituent lipids that induce conformational variations in the lipid bilayers. For instance, dipalmitoylphosphatidylcholine (DPPC) and distearoylphosphatidylcholine (DSPC) (**Figure 20**), evolve from gel to a liquid crystalline state and result in passive permeability when heat is applied. When the ratio of DPPC and DSPC is modulated, the phase transition temperature can be varied. For instance, a higher content of DPPC results in a lower transition temperature and more diffuse liposomes.

Thermoresponsiveness can also occur on a brief temperature decrease, also known as cold shock or cryotherapy. In this case, a thermally reversible swelling or de-swelling of the nanocarrier leads to free diffusion of the encapsulated drugs as a consequence of increased porosity.<sup>130,134-136</sup>

#### 4.3.1.2. Magnetically responsive systems

Although a temperature change is normally achieved by applying heat at the diseased site, it is also possible to trigger the drug release by providing a magnetic field.<sup>135</sup> The main advantage of that is the possibility to generate different responses that can be used for magnetic guidance, a temperature increase that could result into drug release, or both. Therefore, magnetic responsive systems are very potent tools, since they can act both as diagnosis and therapeutic agents (theranostics)<sup>135-137</sup> (**Figure 21**).

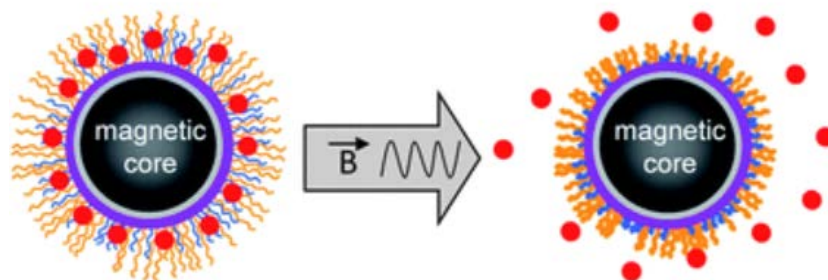


**Figure 21.** Example of a magnetically responsive DDS. Adapted from reference 138

Magnetic guidance is typically achieved by focusing an external magnetic field on the biological target during the infection of a magnetically responsive nanocarrier. Commonly known candidates are core-shell NPs, where the core is made of magnetite ( $\text{Fe}_3\text{O}_4$ ) coated with silica; magnetoliposomes, which are liposomes that contain magnetite or maghemite ( $\text{Fe}_2\text{O}_3$ ) and porous metal NPs.

The use of magnetically responsive NPs, either for magnetic guidance or local hyperthermia, is generally applicable to accessible tumors and not to metastasis. They are especially suitable in those cases that tumors are not removable by surgery or when they are very hemorrhagic. Moreover, magnetic guidance is nowadays hampered by the complexity of the set-up of the magnetic fields, which need adequate focusing and deep penetration into the tissues.<sup>137</sup>

#### 4.3.1.3. Photoresponsive systems

The use of light as a stimulus to trigger drug release has been actively explored owing to its non-invasiveness and the possibility of remote spatiotemporal control. In this regard, a large variety of photosensitive systems has been engineered to achieve an on-demand drug delivery in response to illumination in the UV, Vis or Near IR regions<sup>18,137,139</sup> (**Figure 22**).

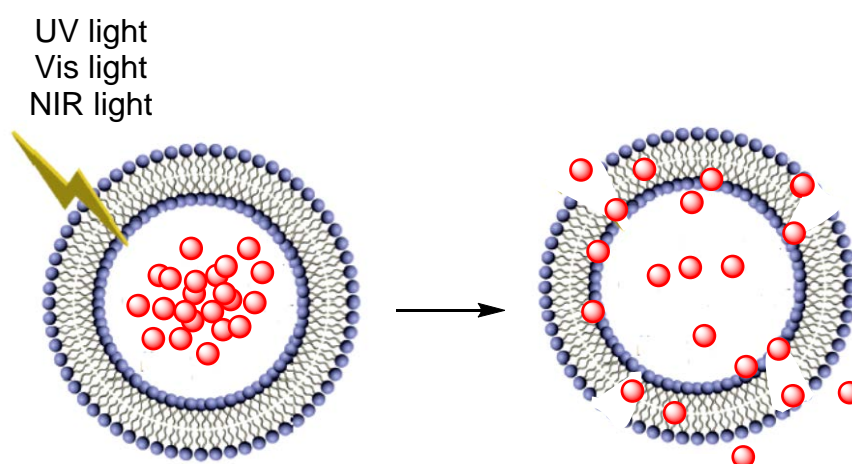


**Figure 22.** Example of photoresponsive DDS. Adapted from reference 137

Photosensitiveness is achieved by introducing certain functional groups that can change their conformations or other properties upon irradiation at a certain wavelength. For instance, the UV/Vis reversible photoisomerization of azobenzene derivatives from *trans* to *cis* on irradiation at 300–380 nm, and from *cis* to *trans* by shining light in the Vis region, enables a photoregulated control of drug release.<sup>137</sup> Other groups, such as *o*-nitrobenzyl and its derivatives, have been used for the same purpose, by attaching these moieties to Au NPs or as crosslinkers incorporated to the backbone of polymers.<sup>137</sup>

Regarding polyurethane-based DDS, Rosenbauer *et al.*<sup>140</sup> prepared multivalent polyurethane NPs from a diisocyanate and an azo-containing diol that triggered the release of sulforhodamine via UV light. In another study, Lv *et al.*<sup>141</sup> developed 2-nitrophenylethylene glycol-containing micelles and observed selective cell death as a consequence of UV light irradiation.

#### 4.3.1.4. *Ultrasound and electric responsive systems*

Ultrasounds represent an effective method to regulate drug release with a spatiotemporal control. Moreover, they provide non-invasiveness, the absence of ionizing radiations and the selection of the degree of penetration depth by tuning frequency, number of cycles and time of exposure. Ultrasound waves can trigger the release of drugs through thermal and/or mechanical effects generated by cavitation or radiation forces. In fact, these forces have been proved to induce nanocarrier destabilization and an increase in vessel permeability<sup>137</sup> (**Figure 23**).

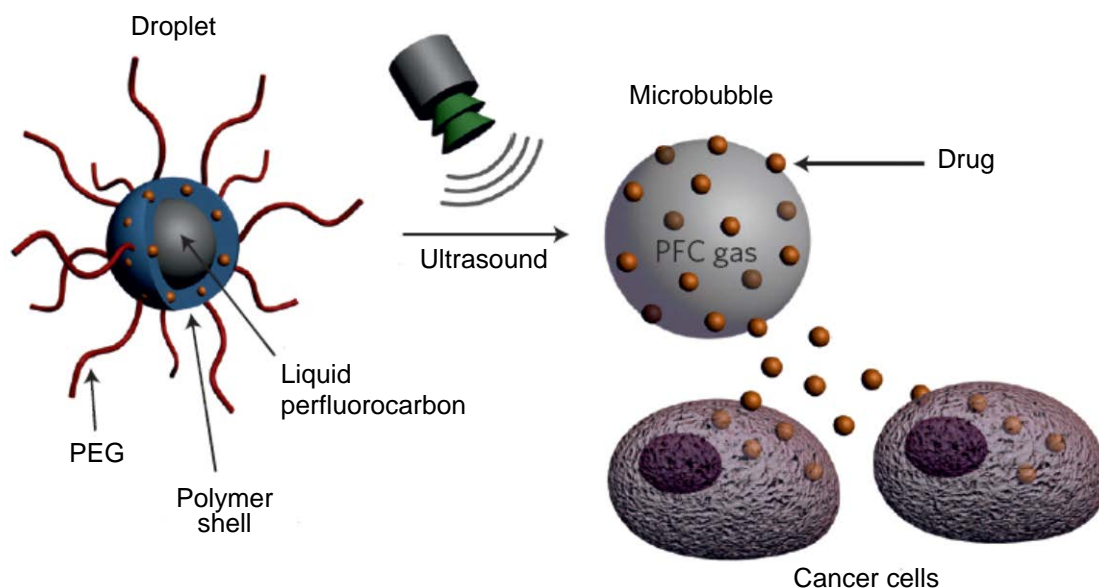


**Figure 23.** Example of an ultrasound-sensitive DDS. Adapted from reference 137

It is believed that the mechanism of delivery involves a droplet-to-bubble transition under the action of ultrasound. The microbubbles generated promote cellular uptake and the release of the drugs in the tumor site.

Another approach for stimuli responsiveness is based on weak electric fields to achieve a pulsed or sustained drug release. For instance, polypyrrole-based NPs, a conductive polymer, exhibited a tailored-drug release, and multiwalled carbon nanotubes have been sometimes added as a conductive additive to increase electrical sensitivity of certain DDS. Similarly, supramolecular polymersomes formed through host-guest complexation between  $\beta$ -cyclodextrin, ferrocene and a pair of homopolymers underwent vesicle splitting after a specific voltage was provided.

Despite the promising properties of electroresponsive systems, low tissue penetration and the need to avoid undesired tissue damage restrict their application in therapy.<sup>137</sup>

### 4.3.2. Endogenous

#### 4.3.2.1. pH-responsive systems

pH variations have been widely explored to control delivery of drugs in specific organs, such as the gastrointestinal tract or the vagina, the intracellular compartments (endosomes and lysosomes) and pathological sites, such as cancer or inflammation. In this regard, pH sensitiveness can be achieved with polymers that experience conformational or solubility changes upon pH variations or with polymers containing acid-cleavable bonds.

Countless nanosystems have been developed to respond to the difference existing between the ECM of tumor ( $\text{pH}_e = 6.5\text{--}6.9$ ) and healthy cells ( $\text{pH}_e = 7.2\text{--}7.4$ ), as a consequence of the tumor microenvironment. Some of the most common nanocarriers that benefit from this differential feature are imine-, hydrazone-, hydrazide-, oxime-, ketal- and acetal-based polymers<sup>142-144</sup> (**Figure 24**).

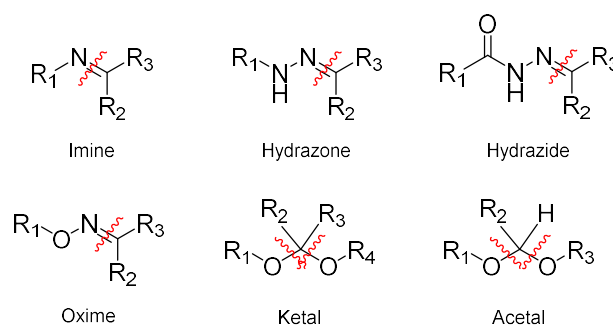


**Figure 24.** Some of the acid cleavable bonds commonly used in polymers

For instance, Wu *et al.*<sup>145</sup> prepared micelles based on hydrophobic segments that were conjugated to doxorubicin through hydrazone bonds. A selective release of the drug at endosomal pH was able to suppress tumor growth in mice, with a better therapeutic effect compared to free doxorubicin. In another study, Huang *et al.*<sup>146</sup> introduced acetal moieties into the urethane backbone and proved a pH-dependent release of PTX, as well as an enhanced performance *in vivo*.

Another strategy to achieve pH responsiveness is by conjugating “titrable” groups in the copolymers, such as amines or carboxylic acids. Some examples of these polymers are shown in **Figure 25**.<sup>147</sup>

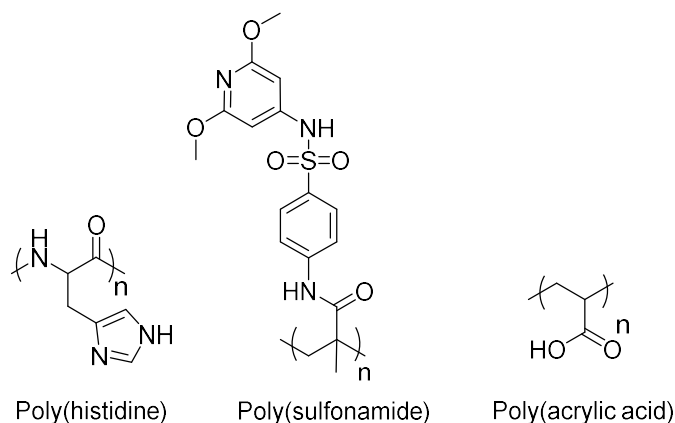


**Figure 25.** Chemical structure of pH-sensitive polymers

In this case, the pH-sensitive polymers forming the hydrophobic core are protonated under acidic conditions and undergo conformational changes that result in the drug release.

#### 4.3.2.2. Glutathione-responsive systems

Glutathione (GSH) is a tripeptide composed of L- $\gamma$ -glutamyl-L-cysteinyl-glycine and is found in high concentration in intracellular compartments of cells, along with its oxidized form (GSSG),<sup>148</sup> configuring one of the most representative redox couple.<sup>149</sup>

GSH plays a critical role in many different functions, such as cellular, gene expression, immune responses, cell cycle regulation and activation of cell death, among others. In fact, the GSH level is related to some human diseases and in the case of cancer, an abnormal GSH concentration protects the cells against the anticancer drugs and free radicals generated during radiotherapy, which leads to resistance to drugs and radiation.<sup>135</sup>

GSH is found at millimolar concentrations (2–10 mM) in intracellular compartments, while its concentration is much smaller in extracellular milieu (<10  $\mu\text{M}$ ). Moreover, the GSH concentration in tumor cells has been described to be higher than in normal cells, which has been exploited in the design of nanocarriers with sensitiveness to redox environments. One of the most frequent approaches to achieve this effect is by inserting disulfide bonds in the polymer shell of the nanocarriers<sup>135,150,151</sup> (**Figure 26**).

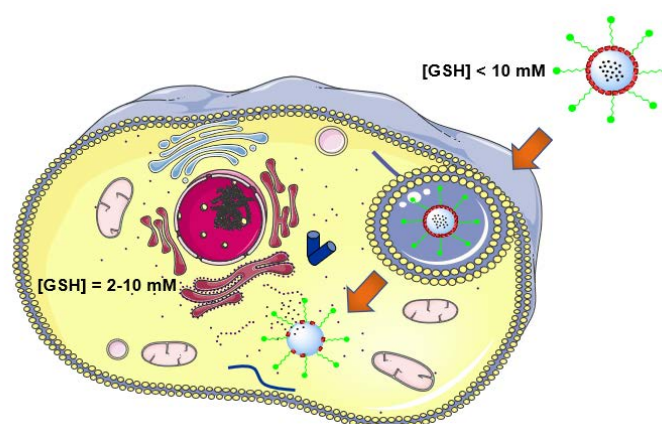


**Figure 26.** Redox-responsive DDS. Adapted from reference 135

Redox responsiveness is mainly achieved by inserting disulfide bonds in amphiphilic copolymers that self-assemble to form degradable micelles or by connecting two different polymer blocks by this redox-cleavable bond.<sup>152</sup> Other approaches are based on the use of crosslinking agents incorporated on the shell or the core of micelles, allowing rapid nanostructure disassembly under reductive conditions, followed by intracellular release of hydrophobic drugs.

#### 4.3.2.3. Enzymatically responsive systems

The altered expression of proteases, phospholipases or glycosidases observed in cancer or inflammation events can be exploited to achieve an enzyme-triggered release.<sup>135,137</sup> For instance, in a study conducted by Law *et al.*<sup>153</sup> a polymer matrix developed and assembled with two different peptide sequences was destabilized and disassembled to release the drug in the presence of these enzymes. However, when the sensitive sequence was scrambled, the degradation did not occur.

Another example is cathepsin, which is an enzyme that can degrade proteins and is also upregulated in cancer.<sup>135</sup> In a study carried out by Vicent *et al.*<sup>154</sup> cathepsin-sensitive *N*-(2-hydroxypropyl)methacrylamide copolymers were conjugated with doxorubicin and the release of this drug was demonstrated under the presence of this enzyme.

Multisensitive nanocarriers have also been developed combining pH and enzymatic degradable moieties for different applications.<sup>155</sup> For instance, Naeem *et al.*<sup>156</sup> reported an efficient drug release achieved at pH > 7.4 in the presence of azo-

reductase enzymes. Under these conditions, burst release was demonstrated *in vitro* and *in vivo*, enhancing the accumulation of the drug in the inflamed colon of rats.

## 5. Clinically approved NP therapies and diagnostics

There is currently a number of NPs intended for therapeutic use that have been approved by the Food and Drug Administration (FDA) in the United States or the European Medicines Agency (EMA). The NPs that have been approved to date are listed in **Table 1**.<sup>47</sup>

**Table 1.** Clinically approved intravenous nanoparticle therapies. From reference 47

Name	Particle type/drug	Approved application/indication	Approval (year)	Investigated application/indication
<b>Cancer Nanoparticle Medicines</b>				
Doxil/Caelyx (Janssen)	Liposomal doxorubicin (PEGylated)	Ovarian cancer (secondary to platinum based therapies) HIV-associated Kaposi's sarcoma (secondary to chemotherapy) Multiple myeloma (secondary)	FDA (1995) EMA (1996)	Various cancers including: solid malignancies, ovarian, breast, leukemia, lymphomas, prostate, metastatic, or liver
DaunoXome (Galen)	Liposomal daunorubicin (non-PEGylated)	HIV-associated Kaposi's sarcoma (primary)	FDA (1996)	Various leukemias
Myocet (Teva UK)	Liposomal doxorubicin (non-PEGylated)	Treatment of metastatic breast cancer (primary)	EMA (2000)	Various cancers including: breast, lymphoma, or ovarian
Abraxane (Celgene)	Albumin-particle bound paclitaxel	Advanced nonsmall cell lung cancer (surgery or radiation is not an option) Metastatic breast cancer (secondary) Metastatic pancreatic cancer (primary)	FDA (2005) EMA (2008)	Various cancers including: solid malignancies, breast, lymphomas, bladder, lung, pancreatic, head and neck, prostate, melanoma, or liver
Marqibo (Spectrum)	Liposomal vincristine (non-PEGylated)	Philadelphia chromosome-negative acute lymphoblastic leukemia (tertiary)	FDA (2012)	Various cancers including: lymphoma, brain, leukemia, or melanoma
MEPACT (Millennium)	Liposomal mifamurtide (non-PEGylated)	Treatment for osteosarcoma (primary following surgery)	EMA (2009)	Osteosarcomas
Onivyde MM-398 (Merrimack)	Liposomal irinotecan (PEGylated)	Metastatic pancreatic cancer (secondary)	FDA (2015)	Various cancers including: solid malignancies, breast, pancreatic, sarcomas, or brain
<b>Iron-replacement nanoparticle therapies</b>				
CosmoFer/INFeD/Ferrisat (Pharmacosmos)	Iron dextran colloid	Iron deficient anemia	FDA (1992) Some of Europe	Iron deficient anemia
DexFerrum/DexIron (American Regent)	Iron dextran colloid	Iron deficient anemia	FDA (1996)	Iron deficient anemia
Ferrlecit (Sanofi)	Iron gluconate colloid	Iron replacement for anemia treatment in patients with chronic kidney disease	FDA (1999)	Iron deficient anemia
Venofer (American Regent)	Iron sucrose colloid	Iron replacement for anemia treatment in patients with chronic kidney disease	FDA (2000)	Iron deficient anemia Following autologous stem cell transplantation
Feraheme (AMAG)/Rienso (Takeda)/Ferumoxytol	Iron polyglucose sorbitol carboxymethylether colloid	Iron deficiency in patients with chronic kidney disease	FDA (2009)	Iron deficient anemia Imaging: brain metastases, lymph node metastases, neuroinflammation in epilepsy, head and neck cancer, myocardial infarction, or multiple sclerosis
Injectafer/Ferinject (Vifor)	Iron carboxymaltose colloid	Iron deficient anemia	FDA (2013)	Iron deficient anemia
Monofer (Pharmacosmos)	10% Iron isomaltoside 1000 colloid	Treating iron deficiency and anemia when oral methods do not work or when iron delivery is required immediately	Some of Europe	Iron deficient anemia
Diafer (Pharmacosmos)	5% Iron isomaltoside 1000 colloid	Iron deficient anemia	Some of Europe	Iron deficient anemia

Doxil is a PEG-functionalized liposomal doxorubicin that constituted the first FDA-approved nanomedicine. Afterwards, liposomal daunorubicin (DaunoXome), liposomal vincristine (Marqibo) and liposomal irinotecan (Onivyde) were approved by the FDA, whereas non-PEGylated liposomal doxorubicin (Myocet) and liposomal mifamurtide (MEPACT) were approved by EMA. The only non-liposomal NP system currently approved is Abraxane, which is based on albumin-bound NPs loading PTX. Surprisingly, the majority of these formulations are not PEGylated, except for Foxil and Onivyde, given the known advantages of PEG that have shown to confer to delivery systems. Moreover, all these formulations are passively targeted, meaning that none of them exhibit any chemical-based targeting ligand. Finally, it is possible that their reduced toxicity is due to their preferential accumulation at tumor sites via the EPR effect, resulting in an increased efficacy of these formulations over the free drugs.

Iron-replacement NP therapies have also made an impact in the treatment of anemia. The goal of these formulations is to increase the Fe concentration in the body and reduce toxicity issues that arise from the injection of free Fe. By using colloidal Fe coated with polysaccharides these drawbacks can be overcome.<sup>46,47,157</sup>

Micro- and nanoparticles developed for diagnosis and approved by the FDA and EMA are listed below (**Table 2**).<sup>47</sup>

**Table 2.** Clinically approved intravenous nanoparticle diagnostics. From reference 47

Name	Particle type/drug	Approved application/indication	Approval (year)	Investigated application/indication
<b>Nanoparticle/microparticle imaging agents</b>				
Definity (Lantheus Medical Imaging)	Perflutren lipid microspheres	Ultrasound contrast agent	FDA (2001)	Ultrasound enhancement for: liver or breast or intraocular or pancreatic tumors, pulmonary diseases, heart function, transcranial injuries, strokes, or liver cirrhosis
Feridex LV. (AMAG/ Endorem)	Iron dextran colloid	Imaging of liver lesions	FDA (1996) Discontinued (2008)	N/A: No current studies
Optison (GE Healthcare)	Human serum albumin stabilized perflutren microspheres	Ultrasound contrast agent	FDA (1997) EMA (1998)	Ultrasound enhancement for: lymph node, renal cell carcinoma, myocardial infarction, pulmonary transit times, or heart transplant rejections
SonoVue (Bracco Imaging)	Phospholipid stabilized microbubble	Ultrasound contrast agent	EMA (2001)	Ultrasound enhancement for: liver neoplasms, prostate or breast or pancreatic cancer, or coronary/pulmonary disease
Resovist (Bayer Schering Pharma)/ Clivast	Iron carboxydextran colloid	Imaging of liver lesions	Some of Europe Discontinued (2009)	N/A No current studies
Ferumoxtran-10/ Combidex/Sinerem (AMAG)	Iron dextran colloid	Imaging lymph node metastases	Only available in Holland	Imaging lymph node metastases
<b>Nanoparticle vaccines</b>				
Epaxal (Cruceil)	Liposome with hepatitis A virus	Hepatitis A vaccine	Some of Europe (Discontinued)	Safety and immunogenicity of hepatitis A vaccine
Inflexal V (Cruceil)	Liposome with trivalent-influenza	Influenza vaccine	Some of Europe (Discontinued)	Safety and immunogenicity of influenza vaccine
<b>Particle anesthetics</b>				
Diprivan	Liposomal propofol	Induction and maintenance of sedation or anesthesia	FDA (1989)	General anesthesia in specific situations: morbidly obese patients, open heart surgery, or spinal surgery
<b>Nanoparticles for fungal treatments</b>				
AmBisome (Gilead Sciences)	Liposomal amphotericin B	Cryptococcal Meningitis in HIV-infected patients Aspergillus, Candida, and/or Cryptococcus species infections (secondary) Visceral leishmaniasis parasite in immunocompromised patients	FDA (1997) Most of Europe	Preventing or treating invasive fungal infections
<b>Nanoparticles for macular degeneration</b>				
Visudyne (Bausch and Lomb)	Liposomal verteporfin	Treatment of subfoveal choroidal neovascularization from age-related macular degeneration, pathologic, or ocular histoplasmosis	FDA (2000) EMA (2000)	Macular degeneration

Some iron oxide NPs have been approved as contrast agents for imaging applications, given their inherent magnetic properties. The combination of these characteristics along with small size, provides a preferential uptake in tumors and a precise imaging of the cancer tissues. In addition, other particles such as Definity, SonoVue and Optison have been also used as intravenous ultrasound enhancing agents. Basically, they are formulations of lipid shells or albumin containing fluorocarbons or SF<sub>6</sub>.<sup>46,47,157</sup>

## 6. Bibliography

- 1 M. Ferrari, *Nat. Rev. Cancer*, 2005, **5**, 161-171.
- 2 J. D. Kingsley, H. Dou, J. Morehead, B. Rabinow, H. E. Gendelman and C. J. Destache, *J. Neuroimmune Pharmacol.*, 2006, **1**, 340-350.
- 3 W. Li, Y. Yang, C. Wang, Z. Liu, X. Zhang, F. An, X. Diao, X. Hao and X. Zhang, *Chem. Commun.*, 2012, **48**, 8120-8122.
- 4 S. Singh, A. Sharma and G. P. Robertson, *Cancer Res.*, 2012, **72**, 5663-5668.
- 5 Z. Cao, Q. Yu, H. Xue, G. Cheng and S. Jiang, *Angew. Chem., Int. Ed.*, 2010, **49**, 3771-3776.
- 6 A. De, R. Bose, A. Kumar and S. Mozumdar, *Targeted Delivery of Pesticides Using Biodegradable Polymeric Nanoparticles*, Springer India, New Delhi, 2014.
- 7 C. Cusco, J. Garcia, E. Nicolas, P. Rocas and J. Rocas, *Polym. Chem.*, 2016, **7**, 6457-6466.
- 8 E. M. Persson, A. S. Gustafsson, A. S. Carlsson, R. G. Nilsson, L. Knutson, P. Forsell, G. Hanisch, H. Lennernäs and B. Abrahamsson, *Pharm. Res.*, 2005, **22**, 2141-2151.
- 9 D. F. Veber, S. R. Johnson, H. Y. Cheng, B. R. Smith, K. W. Ward and K. D. Kopple, *J. Med. Chem.*, 2002, **45**, 2615-2623.
- 10 T. Vasconcelos, B. Sarmiento and P. Costa, *Drug Discovery Today*, 2007, **12**, 1068-1075.
- 11 A. G. Cuenca, H. Jiang, S. N. Hochwald, M. Delano, W. G. Cance and S. R. Grobmyer, *Cancer*, 2006, **107**, 459-466.
- 12 P. Boisseau and B. Loubaton, *C. R. Phys.*, 2011, **12**, 620-636.
- 13 P. A. Wender, D. J. Mitchell, K. Pattabiraman, E. T. Pelkey, L. Steinman and J. B. Rothbard, *Proc. Natl. Acad. Sci.*, 2000, **97**, 13003-13008.
- 14 S. E. McNeil, *Characterization of Nanoparticles Intended for Drug Delivery*, Humana Press, Totowa, 2011.
- 15 M. Ding, N. Song, X. He, J. Li, L. Zhou, H. Tan, Q. Fu and Q. Gu, *ACS Nano*, 2013, **7**, 1918-1928.
- 16 V. P. Torchilin and A. N. Lukyanov, *Drug Discovery Today*, 2003, **8**, 259-266.

- 17 L. Brannon-Peppas and J. O. Blanchette, *Adv. Drug Delivery Rev.*, 2004, **56**, 1649-1659.
- 18 J. Kost and R. Langer, *Adv. Drug Delivery Rev.*, 2012, **64**, **Supplement**, 327-341.
- 19 H. Wei, R. X. Zhuo and X. Z. Zhang, *Prog. Polym. Sci.*, 2013, **38**, 503-535.
- 20 Z. Zuo, V. H. L. Lee and T. P. Begley, *Wiley Encyclopedia of Chemical Biology*, John Wiley & Sons, 2007.
- 21 L. Zhu and V. P. Torchilin, *Integr. Biol.*, 2013, **5**, 96-107.
- 22 P. Workman and S. B. Kaye, *Trends Mol. Med.*, 2002, **8**, S1-S9.
- 23 A. Sharma and U. S. Sharma, *Int. J. Pharm.*, 1997, **154**, 123-140.
- 24 R. Gref, A. Domb, P. Quellec, T. Blunk, R. H. Müller, J. M. Verbavatz and R. Langer, *Adv. Drug Delivery Rev.*, 2012, **64**, **Supplement**, 316-326.
- 25 N. Mody, R. K. Tekade, N. K. Mehra, P. Chopdey and N. K. Jain, *AAPS PharmSciTech*, 2014, **15**, 388-399.
- 26 D. K. Sahana, G. Mittal, V. Bhardwaj and M. N. V. R. Kumar, *J. Pharm. Sci.*, 2008, **97**, 1530-1542.
- 27 A. Zanutto-Filho, K. Coradini, E. Braganhol, R. Schröder, C. M. de Oliveira, A. Simões-Pires, A. M. O. Battastini, A. R. Pohlmann, S. S. Guterres, C. M. Forcelini, R. C. R. Beck and J. C. F. Moreira, *Eur. J. Pharm. Biopharm.*, 2013, **83**, 156-167.
- 28 J. H. Fang, Y. H. Lai, T. L. Chiu, Y. Y. Chen, S. H. Hu and S. Y. Chen, *Adv. Healthcare Mater.*, 2014, **3**, 1250-1260.
- 29 J. M. Klostranec and W. C. W. Chan, *Adv. Mater.*, 2006, **18**, 1953-1964.
- 30 T. Jamieson, R. Bakhshi, D. Petrova, R. Pocock, M. Imani and A. M. Seifalian, *Biomaterials*, 2007, **28**, 4717-4732.
- 31 TAO Patch Human Upgrade Device, Quantum dots entangled with single photons, <http://www.taopatch.com/blog/quantum-dots-entangled-with-single-photons/>, (accessed 20th January 2017).
- 32 H. S. Choi, W. Liu, P. Misra, E. Tanaka, J. P. Zimmer, B. I. Ipe, M. G. Bawendi and J. V. Frangioni, *Nat. Biotechnol.*, 2007, **25**, 1165-1170.
- 33 X. Meshik, S. Farid, M. Choi, Y. Lan, S. Mukherjee, D. Datta, M. Dutta and M. A. Stroschio, *CRC Crit. Rev. Bioeng.*, 2015, **43**, 277-296.
- 34 J. Zhou, Y. Yang and C. y. Zhang, *Chem. Rev.*, 2015, **115**, 11669-11717.
- 35 S. Svenson, *Chem. Soc. Rev.*, 2015, **44**, 4131-4144.

- 36 W. J. Feast, S. P. Rannard and A. Stoddart, *Macromolecules*, 2003, **36**, 9704-9706.
- 37 E. R. Gillies and J. M. J. Frechet, *Drug Discovery Today*, 2005, **10**, 35-43.
- 38 A. M. Caminade, D. Yan and D. K. Smith, *Chem. Soc. Rev.*, 2015, **44**, 3870-3873.
- 39 C. C. Lee, J. A. MacKay, J. M. J. Fréchet and F. C. Szoka, *Nat. Biotechnol.*, 2005, **23**, 1517-1526.
- 40 E. Caló and V. V. Khutoryanskiy, *Eur. Polym. J.*, 2015, **65**, 252-267.
- 41 N. A. Peppas, J. Z. Hilt, A. Khademhosseini and R. Langer, *Adv. Mater.*, 2006, **18**, 1345-1360.
- 42 D. Seliktar, *Science*, 2012, **336**, 1124-1128.
- 43 A. Samad, Y. Sultana and M. Aqil, *Curr. Drug Delivery*, 2007, **4**, 297-305.
- 44 T. M. Allen and P. R. Cullis, *Adv. Drug Delivery Rev.*, 2013, **65**, 36-48.
- 45 Institute of longlife learning, University of New Dehli, Lipid aggregates: micelles, bilayers and liposomes, <http://vle.du.ac.in/mod/book/view.php?id=13513&chapterid=30151>, (accessed 20th January 2018).
- 46 D. Bobo, K. J. Robinson, J. Islam, K. J. Thurecht and S. R. Corrie, *Pharm. Res.*, 2016, **33**, 2373-2387.
- 47 A. C. Anselmo and S. Mitragotri, *Bioeng. Transl. Med.*, 2016, **1**, 10-29.
- 48 H. Daraee, A. Etemadi, M. Kouhi, S. Alimirzalu and A. Akbarzadeh, *Artif. Cells, Nanomed., Biotechnol.*, 2016, **44**, 381-391.
- 49 J. O. Eloy, M. Claro de Souza, R. Petrilli, J. P. A. Barcellos, R. J. Lee and J. M. Marchetti, *Colloids Surf., B*, 2014, **123**, 345-363.
- 50 T. Garg and A. K. Goyal, *Drug Delivery Lett.*, 2014, **10**, 62-71.
- 51 J. Conde, G. Doria and P. Baptista, *J. Drug Delivery*, 2012, **2012**, 1-12.
- 52 M. Rai, A. P. Ingle, I. Gupta and A. Brandelli, *Int. J. Pharm.*, 2015, **496**, 159-172.
- 53 J. Conde, J. T. Dias, V. Grazú, M. Moros, P. V. Baptista and J. M. de la Fuente, *Front. Chem.*, 2014, **2**, 1-27.
- 54 H. Sharma, P. K. Mishra, S. Talegaonkar and B. Vaidya, *Drug Discovery Today*, 2015, **20**, 1143-1151.
- 55 C. E. Mora-Huertas, H. Fessi and A. Elaissari, *Int. J. Pharm.*, 2010, **385**, 113-142.
- 56 J. P. Rao and K. E. Geckeler, *Prog. Polym. Sci.*, 2011, **36**, 887-913.

- 57 G. Suffredini, J. E. East and L. M. Levy, *Am. J. Neuroradiol.*, 2014, **35**, 1246-1253.
- 58 S. Cammas, K. Suzuki, C. Sone, Y. Sakurai, K. Kataoka and T. Okano, *J. Controlled Release*, 1997, **48**, 157-164.
- 59 C. Pinto Reis, R. J. Neufeld, A. J. Ribeiro and F. Veiga, *Nanomed. Nanotech. Biol. Med.*, 2006, **2**, 8-21.
- 60 I. Brigger, C. Dubernet and P. Couvreur, *Adv. Drug Delivery Rev.*, 2012, **64**, **Supplement**, 24-36.
- 61 P. N. Ezhilarasi, P. Karthik, N. Chhanwal and C. Anandharamakrishnan, *Food Bioprocess Technol.*, 2013, **6**, 628-647.
- 62 S. Ortelli and A. L. Costa, *Nano-Struct. Nano-Objects*, 2016, DOI: 10.1016/j.nanoso.2016.03.006
- 63 C. Vauthier and K. Bouchemal, *Pharm. Res.*, 2009, **26**, 1025-1058.
- 64 D. Tuncel and H. V. Demir, *Nanoscale*, 2010, **2**, 484-494.
- 65 B. N. V. Nagavarma, K. S. H. Yadav, A. Ayaz, L. S. Vasudha and H. G. Shivakumar, *Asian J. Pharm. Clin. Res.*, 2012, **5**, **Suppl 3**, 16-23.
- 66 Y. Wang, P. Li, T. Truong-Dinh Tran, J. Zhang and L. Kong, *Nanomaterials*, 2016, **6**, 1-18.
- 67 I. Katouzian and S. M. Jafari, *Trends Food Sci. Technol.*, 2016, **53**, 34-48.
- 68 C. C. West and J. H. Harwell, *Environ. Sci. Technol.*, 1992, **26**, 2324-2330.
- 69 C. Bindschaedler, R. Gurny and E. Doelker, US Pat US4968350, 1990.
- 70 H. Fessi, F. Puisieux, J. P. Devissaguet, N. Ammoury and S. Benita, *Int. J. Pharm.*, 1989, **55**, R1-R4.
- 71 P. Pathak, M. J. Mezirani, T. Desai and Y. P. Sun, *J. Supercrit. Fluid.*, 2006, **37**, 279-286.
- 72 V. J. Mohanraj and Y. Chen, *Trop. J. Pharm. Res.*, 2006, **5**, 561-573.
- 73 V. Freger, *Langmuir*, 2003, **19**, 4791-4797.
- 74 H. Gao, T. Jiang, B. Han, Y. Wang, J. Du, Z. Liu and J. Zhang, *Polymer*, 2004, **45**, 3017-3019.
- 75 B. H. Jeong, E. M. V. Hoek, Y. Yan, A. Subramani, X. Huang, G. Hurwitz, A. K. Ghosh and A. Jawor, *J. Membr. Sci.*, 2007, **294**, 1-7.
- 76 K. Landfester, *Angew. Chem., Int. Ed.*, 2009, **48**, 4488-4507.

- 77 F. Tiarks, K. Landfester and M. Antonietti, *J. Polym. Sci., Part A: Polym. Chem.*, 2001, **39**, 2520-2524.
- 78 K. Bouchemal, S. Briançon, E. Perrier, H. Fessi, I. Bonnet and N. Zydowicz, *Int. J. Pharm.*, 2004, **269**, 89-100.
- 79 L. Torini, J. F. Argillier and N. Zydowicz, *Macromolecules*, 2005, **38**, 3225-3236.
- 80 G. Morral-Ruíz, P. Melgar-Lesmes, M. L. García, C. Solans and M. J. García-Celma, *Polymer*, 2012, **53**, 6072-6080.
- 81 N. Song, M. Ding, Z. Pan, J. Li, L. Zhou, H. Tan and Q. Fu, *Biomacromolecules*, 2013, **14**, 4407-4419.
- 82 J. S. Wang and K. Matyjaszewski, *J. Am. Chem. Soc.*, 1995, **117**, 5614-5615.
- 83 W. A. Braunecker and K. Matyjaszewski, *Prog. Mater. Sci.*, 2007, **32**, 93-146.
- 84 C. E. Wang, P. S. Stayton, S. H. Pun and A. J. Convertine, *J. Controlled Release*, 2015, **219**, 345-354.
- 85 P. B. Zetterlund, S. C. Thickett, S. b. Perrier, E. Bourgeat-Lami and M. Lansalot, *Chem. Rev.*, 2015, **115**, 9745-9800.
- 86 P. Rocas, C. Cuscó, J. Rocas and F. Albericio, *Curr. Drug Delivery*, 2017, **15**, 37-43.
- 87 K. Landfester, A. Musyanovych and V. Mailänder, *J. Polym. Sci., Part A: Polym. Chem.*, 2010, **48**, 493-515.
- 88 R. A. Jain, *Biomaterials*, 2000, **21**, 2475-2490.
- 89 Y. L. Uscátegui, F. R. Arévalo, L. E. Díaz, M. I. Cobo and M. F. Valero, *J. Biomater. Sci., Polym. Ed.*, 2016, **27**, 1860-1879.
- 90 C. W. Ou, C. H. Su, U. S. Jeng and S. h. Hsu, *ACS Appl. Mater. Interfaces*, 2014, **6**, 5685-5694.
- 91 S. Yu, J. Ding, C. He, Y. Cao, W. Xu and X. Chen, *Adv. Healthcare Mater.*, 2014, **3**, 752-760.
- 92 M. Ding, X. Zeng, X. He, J. Li, H. Tan and Q. Fu, *Biomacromolecules*, 2014, **15**, 2896-2906.
- 93 M. Jabbarzadegan, H. Rajayi, M. A. Mofazzal Jahromi, H. Yeganeh, M. Yousefi, Z. Muhammad Hassan and J. Majidi, *Artif. Cells, Nanomed., Biotechnol.*, 2017, **45**, 808-816.

- 94 E. Ajorlou, A. Y. Khosroushahi and H. Yeganeh, *Pharm. Res.*, 2016, **33**, 1426-1439.
- 95 N. M. Matsumoto, D. C. González-Toro, R. T. Chacko, H. D. Maynard and S. Thayumanavan, *Polym. Chem.*, 2013, **4**, 2464-2469.
- 96 M. Goldberg, R. Langer and X. Jia, *J. Biomater. Sci., Polym. Ed.*, 2007, **18**, 241-268.
- 97 P. P. Shah, P. R. Desai, A. R. Patel and M. S. Singh, *Biomaterials*, 2012, **33**, 1607-1617.
- 98 S. Mavuso, T. Marimuthu, E. Y. Choonara, P. Kumar, L. C. du Toit and V. Pillay, *Curr. Pharm. Des.*, 2015, **21**, 2801-2813.
- 99 F. Y. Hsieh, H. H. Lin and S. h. Hsu, *Biomaterials*, 2015, **71**, 48-57.
- 100 H. H. Lin, F. Y. Hsieh, C. S. Tseng and S. h. Hsu, *J. Mater. Chem. B*, 2016, **4**, 6694-6705.
- 101 H. Freichels, M. Wagner, P. Okwieka, R. G. Meyer, V. Mailänder, K. Landfester and A. Musyanovych, *J. Mater. Chem. B*, 2013, **1**, 4338-4348.
- 102 B. Kang, P. Okwieka, S. Schöttler, S. Winzen, J. Langhanki, K. Mohr, T. Opatz, V. Mailänder, K. Landfester and F. R. Wurm, *Angew. Chem., Int. Ed.*, 2015, **54**, 7436-7440.
- 103 D. Xu, K. Wu, Q. Zhang, H. Hu, K. Xi, Q. Chen, X. Yu, J. Chen and X. Jia, *Polymer*, 2010, **51**, 1926-1933.
- 104 E. Blanco, H. Shen and M. Ferrari, *Nat. Biotechnol.*, 2015, **33**, 941-951.
- 105 F. Danhier, O. Feron and V. Préat, *J. Controlled Release*, 2010, **148**, 135-146.
- 106 A. Giakoustidis, S. Mudan and T. Hagemann, *Cancer Microenviron.*, 2015, **8**, 177-186.
- 107 J. Fang, H. Nakamura and H. Maeda, *Adv. Drug Delivery Rev.*, 2011, **63**, 136-151.
- 108 V. Torchilin, *Adv. Drug Delivery Rev.*, 2011, **63**, 131-135.
- 109 H. Maeda, H. Nakamura and J. Fang, *Adv. Drug Delivery Rev.*, 2013, **65**, 71-79.
- 110 B. A. Webb, M. Chimenti, M. P. Jacobson and D. L. Barber, *Nat Rev Cancer*, 2011, **11**, 671-677.
- 111 I. Böhme and A. K. Bosserhoff, *Pigm. Cell Melanoma Res.*, 2016, **29**, 508-523.
- 112 V. P. Torchilin, *Drug Delivery*, Springer, Berlin, 2010.
- 113 S. Biswas and V. P. Torchilin, *Adv. Drug Delivery Rev.*, 2014, **66**, 26-41.

- 114 N. Bertrand, J. Wu, X. Xu, N. Kamaly and O. C. Farokhzad, *Adv. Drug Delivery Rev.*, 2014, **66**, 2-25.
- 115 X. Xu, W. Ho, X. Zhang, N. Bertrand and O. Farokhzad, *Trends Mol. Med.*, 2015, **21**, 223-232.
- 116 Z. Ghotbi, A. Haddadi, S. Hamdy, R. W. Hung, J. Samuel and A. Lavasanifar, *J. Drug Targeting*, 2011, **19**, 281-292.
- 117 B. S. Brown, T. Patanam, K. Mobli, C. Celia, P. E. Zage, A. J. Bean and E. Tasciotti, *Cancer Biol. Ther.*, 2014, **15**, 851-861.
- 118 K. Maruyama, O. Tomoko and T. Kunikazu Moribe, *Adv. Drug Delivery Rev.*, 1999, **40**, 89-102.
- 119 B. R. Liu, S. Y. Lo, C. C. Liu, C. L. Chyan, Y. W. Huang, R. S. Aronstam and H. J. Lee, *PLoS ONE*, 2013, **8**, 1-12.
- 120 A. Akinc and G. Battaglia, *Cold Spring Harbor Perspect. Biol.*, 2013, **5**, 1-24.
- 121 L. M. Bareford and P. W. Swaan, *Adv. Drug Delivery Rev.*, 2007, **59**, 748-758.
- 122 F. Zhao, Y. Zhao, Y. Liu, X. Chang, C. Chen and Y. Zhao, *Small*, 2011, **7**, 1322-1337.
- 123 L. Y. T. Chou, K. Ming and W. C. W. Chan, *Chem. Soc. Rev.*, 2011, **40**, 233-245.
- 124 H. Gao, Z. Yang, S. Zhang, S. Cao, S. Shen, Z. Pang and X. Jiang, *Sci. Rep.*, 2013, **3**, 1-8.
- 125 L. Kou, J. Sun, Y. Zhai and Z. He, *Asian J. Pharm. Sci.*, 2013, **8**, 1-10.
- 126 N. Oh and J. H. Park, *Int. J. Nanomed.*, 2014, **9**, 51-63.
- 127 M. S. H. Akash, K. Rehman and S. Chen, *Pharm. Dev. Technol.*, 2016, **21**, 367-378.
- 128 Ž. Krpetić, F. Porta, E. Caneva, V. Dal Santo and G. Scari, *Langmuir*, 2010, **26**, 14799-14805.
- 129 I. Canton and G. Battaglia, *Chem. Soc. Rev.*, 2012, **41**, 2718-2739.
- 130 S. Ganta, H. Devalapally, A. Shahiwala and M. Amiji, *J. Controlled Release*, 2008, **126**, 187-204.
- 131 S. E. Paramonov, E. M. Bachelder, T. T. Beaudette, S. M. Standley, C. C. Lee, J. Dashe and J. M. J. Fréchet, *Bioconjugate Chem.*, 2008, **19**, 911-919.
- 132 E. M. Bachelder, T. T. Beaudette, K. E. Broaders, S. E. Paramonov, J. Dashe and J. M. J. Fréchet, *Mol. Pharmaceutics*, 2008, **5**, 876-884.

- 133 P. F. Innominato, V. P. Roche, O. G. Palesh, A. Ulusakarya, D. Spiegel and F. A. Lévi, *Ann. Med.*, 2014, **46**, 191-207.
- 134 Y. Li, K. Xiao, W. Zhu, W. Deng and K. S. Lam, *Adv. Drug Delivery Rev.*, 2014, **66**, 58-73.
- 135 W. Cheng, L. Gu, W. Ren and Y. Liu, *Mater. Sci. Eng. C*, 2014, **45**, 600-608.
- 136 A. P. Blum, J. K. Kammeyer, A. M. Rush, C. E. Callmann, M. E. Hahn and N. C. Gianneschi, *J. Am. Chem. Soc.*, 2015, **137**, 2140-2154.
- 137 S. Mura, J. Nicolas and P. Couvreur, *Nat. Mater.*, 2013, **12**, 991-1003.
- 138 S. Louguet, B. Rousseau, R. Epherre, N. Guidolin, G. Goglio, S. Mornet, E. Duguet, S. Lecommandoux and C. Schatz, *Polym. Chem.*, 2012, **3**, 1408-1417.
- 139 B. Priya, P. Viness, E. C. Yahya and C. d. T. Lisa, *Biomed. Mater.*, 2009, **4**, 1-15.
- 140 E. M. Rosenbauer, M. Wagner, A. Musyanovych and K. Landfester, *Macromolecules*, 2010, **43**, 5083-5093.
- 141 C. Lv, Z. Wang, P. Wang and X. Tang, *Langmuir*, 2012, **28**, 9387-9394.
- 142 D. Schmaljohann, *Adv. Drug Delivery Rev.*, 2006, **58**, 1655-1670.
- 143 K. E. Broaders, S. J. Pastine, S. Grandhe and J. M. J. Frechet, *Chem. Commun.*, 2011, **47**, 665-667.
- 144 K. M. Huh, H. C. Kang, Y. J. Lee and Y. H. Bae, *Macromol. Res.*, 2012, **20**, 224-233.
- 145 H. Wu, L. Zhu and V. P. Torchilin, *Biomaterials*, 2013, **34**, 1213-1222.
- 146 F. Huang, R. Cheng, F. Meng, C. Deng and Z. Zhong, *Biomacromolecules*, 2015, **16**, 2228-2236.
- 147 Y. Liu, W. Wang, J. Yang, C. Zhou and J. Sun, *Asian J. Pharm. Sci.*, 2013, **8**, 159-167.
- 148 A. Pompella, A. Visvikis, A. Paolicchi, V. D. Tata and A. F. Casini, *Biochem. Pharmacol.*, 2003, **66**, 1499-1503.
- 149 B. Ketterer, B. Coles and D. J. Meyer, *Environ. Health Perspect.*, 1983, **49**, 59-69.
- 150 N. Ma, Y. Li, H. Xu, Z. Wang and X. Zhang, *J. Am. Chem. Soc.*, 2010, **132**, 442-443.
- 151 A. Latorre and A. Somoza, *Curr. Top. Med. Chem.*, 2014, **14**, 2662-2671.
- 152 N. R. Ko and J. K. Oh, *Biomacromolecules*, 2014, **15**, 3180-3189.
- 153 B. Law, R. Weissleder and C. H. Tung, *Biomacromolecules*, 2006, **7**, 1261-1265.

- 154 M. J. Vicent, F. Greco, R. I. Nicholson, A. Paul, P. C. Griffiths and R. Duncan, *Angew. Chem.*, 2005, **117**, 4129-4134.
- 155 W. Chen, P. Zhong, F. Meng, R. Cheng, C. Deng, J. Feijen and Z. Zhong, *J. Controlled Release*, 2013, **169**, 171-179.
- 156 M. Naeem, W. Kim, J. Cao, Y. Jung and J. W. Yoo, *Colloids Surf., B*, 2014, **123**, 271-278.
- 157 G. Pillai, *SOJ Pharmacy & Pharmaceutical Sciences*, 2014, **2**, 1-13.



## ***General Objectives***



## **General objectives**

The main objective for this Thesis is the development of a synthetic methodology that allows the preparation of multifunctional and multisensitive polyurethane/polyurea NCs for smart drug delivery. In this regard, the general objectives can be further split into four main goals:

- **The development of a potentially scalable synthetic method** to prepare the NCs that is based on a one-pot process and that proceeds under mild conditions.
- **The thorough study of the physicochemical properties of the NCs** in terms of morphology, size, surface charge, entrapment efficiency, drug loading and stability under different conditions.
- **The biological characterization of the NCs** in different cancer cell lines to determine their cytotoxicity, internalization mechanism and cell uptake efficiency.
- **The study of the *in vivo* biodistribution of the NCs** in a mice model to evaluate the accumulation of the NCs in tumor, organs and plasma.



# **CHAPTER 2**

*Multisensitive and smart nanocapsules  
for tumor-targeted drug delivery*



# 1. Introduction

## 1.1. Polyurethane and polyurea DDS

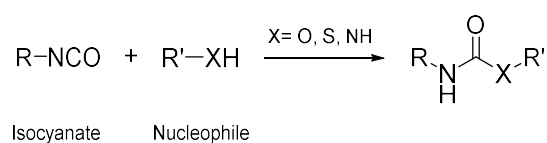
Introduced for the first time in 1967 as implantable materials,<sup>1</sup> polyurethanes have been well established as one of the most versatile materials used for different biomedical purposes, such as heart valves, catheters and wound dressings.<sup>2,3</sup> The straightforward synthetic methodologies,<sup>4-6</sup> the facile preparation and the highly variable chemistries that can be achieved through polyurethanes<sup>7</sup> have allowed the incorporation of different functionalities into the nanoparticulate material. Moreover, polyureas have been described to provide chemical resistance, high stability and biocompatibility to materials destined to biomedical purposes. Overall, the combination of polyurethane and polyurea chemistries offer countless possibilities to develop high performance DDS in terms of selective stimuli responsiveness, targeting capacities, high biocompatibility, specific biodegradability and stability in physiological conditions. Therefore, polyurethane- and polyurea-based nanoassemblies exhibiting diverse physicochemical properties have become appealing candidates in the clinical exploration of next generation of nanotherapeutics for smart drug delivery.<sup>2</sup>

51

## 1.2. Chemistry of polyurethanes and polyureas

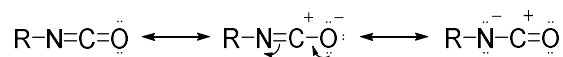
### 1.2.1. Chemistry of isocyanates

Isocyanates are ideal precursors of polyurethanes and polyureas due to their fast kinetics and quantitative reactions, which proceed with complete atom economy<sup>7-12</sup> (**Scheme 1**).



**Scheme 1.** Example of a reaction involving an isocyanate

According to the figure, all the atoms involved in the reaction take part in the final product. This quality allows the introduction of different kind of functionalities into a polymer in very high efficiency. The reactivity of NCO group is governed by the electrophilic character of the carbon atom (**Scheme 2**), which is susceptible to nucleophilic attack.<sup>4,10,11</sup>



**Scheme 2.** Resonance structures of isocyanate group

Generally, if steric factors are neglected, any electron-withdrawing group attached on the NCO increases the positive charge of the carbon atom and therefore enhances the reactivity. According to this effect, the relative reactivity of different types of isocyanates can be listed as in **Figure 1**.

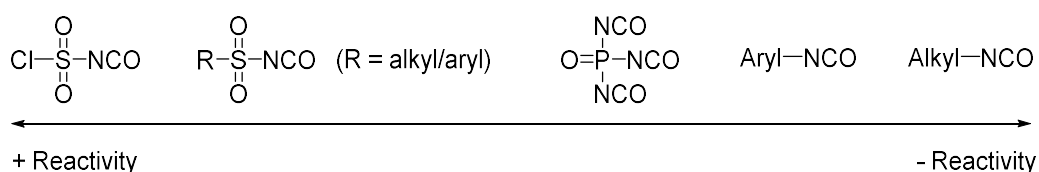
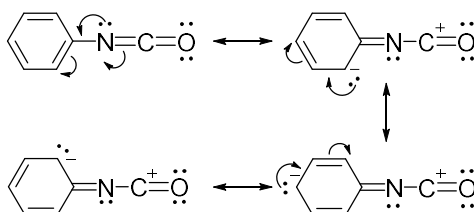


**Figure 1.** Reactivity of different types of isocyanates

According to the list, aromatic isocyanates are generally more reactive than aliphatic or cycloaliphatic analogues.<sup>13,14</sup> In fact, Sato *et al.*<sup>15</sup> showed that phenyl isocyanate was fifty times more reactive than ethyl isocyanate with respect to methanol. Such effect can be explained by the delocalization of the negative charge in the aromatic ring<sup>4</sup> (**Scheme 3**).



**Scheme 3.** Delocalization of the negative charge in aromatic isocyanates

As expected, the type and position of the substituents on the aromatic ring affect the reactivity. It is observed that electron withdrawing groups in *ortho* or *para* positions increase the reactivity whereas the opposite holds for electron donating groups.<sup>16</sup> In the case of aromatic diisocyanates, the electron withdrawing nature of this group, increases the reactivity of the other one.<sup>4</sup>

A similar effect occurs in aliphatic isocyanates such as isophorone diisocyanate (IPDI), with the peculiarity that the difference between the two NCO groups becomes more accentuated due to the steric hindrance of the primary isocyanate.<sup>17,18</sup> The structure of IPDI and other common isocyanates is shown in

**Figure 2.**

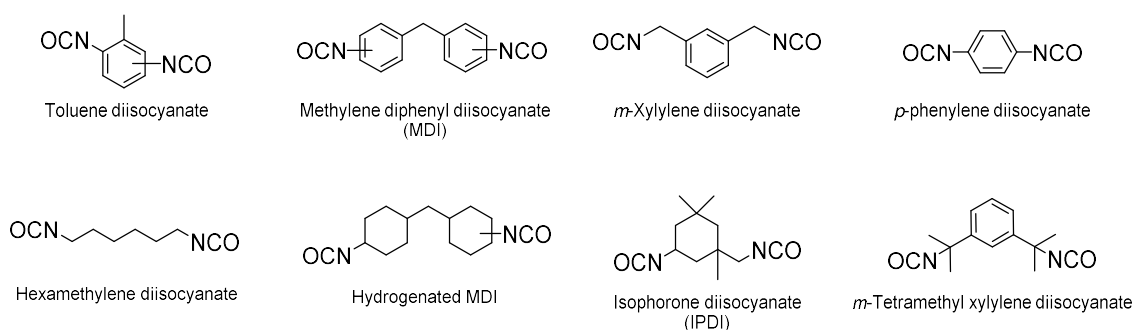


**Figure 2.** Chemical structure of some of the most common isocyanates

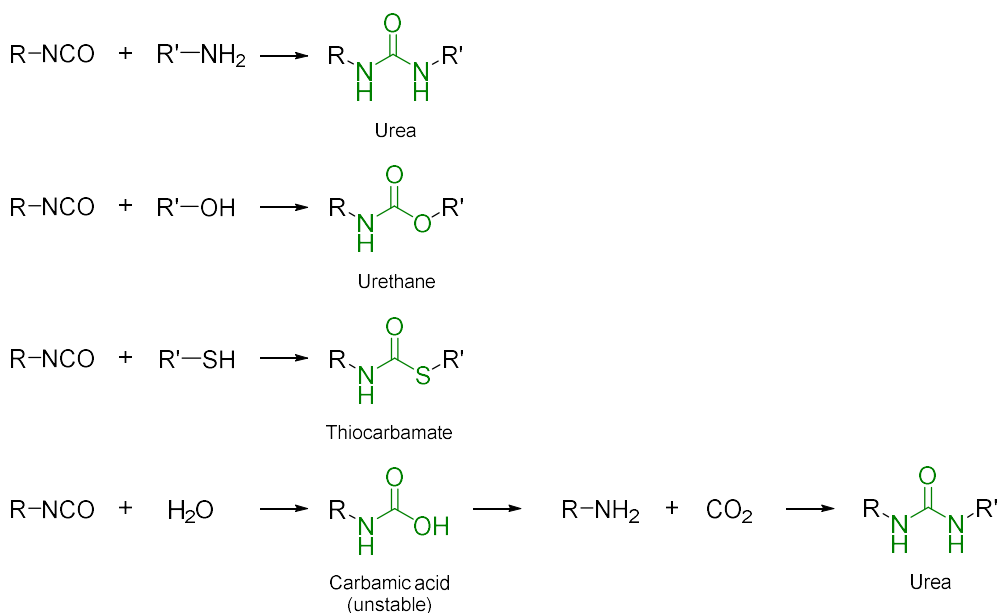
As seen in the figure, the molecules on the top are aromatic diisocyanates, whereas the ones on the bottom are aliphatic. These are some of the most widely used diisocyanates for the production of polyurethanes and polyureas. However, aromatic isocyanates have been reported to be substantially more reactive and toxic than their aliphatic counterparts<sup>7</sup> and their use has been limited. Both types can easily bind proteins such as albumin at physiological conditions, especially in mucous membranes and in the respiratory tract. In fact, a wide variety of toxicological studies have demonstrated that occupational exposure to toluene diisocyanate induces bronchial asthma, non-obstructive bronchitis and rhinitis<sup>19-21</sup> In addition, the type of exposure to these chemicals (vapor or liquid) does play an important role in their toxicity, since volatile isocyanates such as hexamethylene diisocyanate having a high vapor pressure ( $\sim 5 \cdot 10^{-2}$  mmHg, 20 °C) cause a stronger immune response than IPDI, which has a vapor pressure two orders of magnitude lower ( $\sim 3 \cdot 10^{-4}$  mmHg, 20 °C).<sup>20,21</sup> This suggests that volatile isocyanates induce

higher toxicity when they are in vapor phase, rather than in the liquid form. In fact, while a large number of workers in contact with these chemicals develop severe occupational health issues, few cases of allergic contact dermatitis have been reported.<sup>22</sup>

In order to overcome volatility problems, MDI, with a vapor pressure of  $5 \cdot 10^{-6}$  mmHg (20 °C), has become an alternative for the manufacturing of flexible and rigid foams, coatings, adhesives, elastomers, sealants, lacquers and resins.<sup>23-26</sup> However, despite of its lower volatility, MDI, which is presented as a mixture of 4,4', 2,4' and 2,2' isomers, is highly reactive and leads to a toxic aminated form when in contact with moisture. The generated aromatic amines are the indirect responsible for the MDI biological toxicity, as it has been reported to cause several dermatological allergies.<sup>25,26</sup>

### 1.2.2. Main reactions derived from isocyanates

The reactions with isocyanates are quite simple, leading to a wide variety of addition products, along with the migration of the active hydrogen atom to the nitrogen atom of the isocyanate (**Scheme 4**).<sup>4,7,8,10,11,23,27-29</sup>



**Scheme 4.** Most common reactions involving isocyanates and a nucleophile

Among these reaction products, ureas and urethanes, which are prepared from amines and alcohols, respectively, are the most commonly found in coatings, sealants, adhesives.<sup>7</sup> Thiocarbamates, and specially *S*-alkyl thiocarbamates, are widely used as herbicides and pesticides.<sup>30,31</sup> Finally, the reaction of isocyanates with water generates a unstable carbamic acid, which decomposes into gaseous CO<sub>2</sub> and a primary amine, a common way to produce a wide range of materials with different densities such as foams.<sup>4,7,11</sup>

The reactivity of some nucleophiles is listed in **Table 1**.

**Table 1.** Relative reactivity of isocyanates with compounds containing an active hydrogen atom<sup>7</sup>

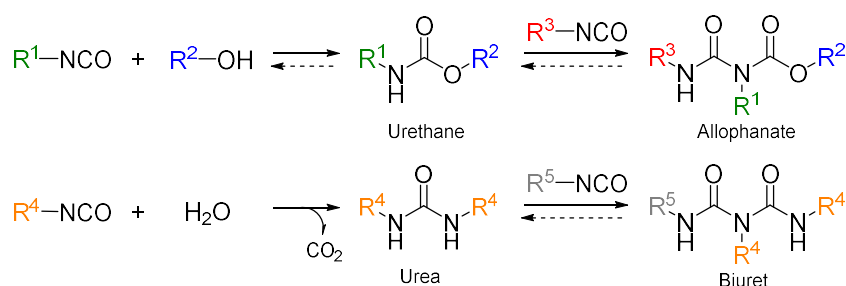
Hydrogen compound	Simplified structure	Relative reaction rate (uncatalyzed, 25 °C)
Primary aliphatic amine	R-NH <sub>2</sub>	1000
Secondary aliphatic amine	R <sub>2</sub> -NH	200–500
Primary aromatic amine	Ar-NH <sub>2</sub>	2–3
Primary alcohol	R-CH <sub>2</sub> -OH	1
Water	H <sub>2</sub> O	1
Secondary alcohol	R <sub>2</sub> -CH-OH	0.3
Urea	R-NH-CO-NH-R	0.15
Tertiary alcohol	R <sub>3</sub> -C-OH	0.005
Phenolic alcohol	Ar-OH	0.001–0.005
Urethane	R-NH-COOR	0.001

The reactivity increases with the nucleophilicity of the molecule having the active hydrogen.<sup>4,7,9,12,28,32</sup> Thus, primary and secondary amines react readily with isocyanates without the need of adding catalysts due to their inherent nucleophilicity. Among them, primary amines are generally more reactive than secondary ones because of the steric hindrance. Aromatic amines react slower than aliphatic ones due to electron delocalization and in contrast to isocyanates, electron-withdrawing groups in *ortho* or *para* reduce nucleophilicity. Regarding alcohols, primary, secondary and tertiary alcohols exhibit decreasing reactivity due to increasing steric hindrance, as expected. In fact, tertiary alcohols can be several orders of magnitude less reactive than primary ones but are barely used in synthetic

processes. Catalysts and/or high temperatures are usually required for reaction completion between isocyanates and alcohols.<sup>10,28,33</sup>

### 1.2.3. Side-reactions derived from isocyanates

Besides the most common reactions detailed in the previous section, a number of side-reactions can be given depending on the conditions, especially if catalysts and/or high temperatures are used.<sup>7,12,29</sup> Indeed, these secondary reactions occur because the products of isocyanates and nucleophiles still have active hydrogen atoms than can further react with a second equivalent of NCO groups, leading mainly to allophanates and biurets<sup>27-29</sup> (**Scheme 5**).



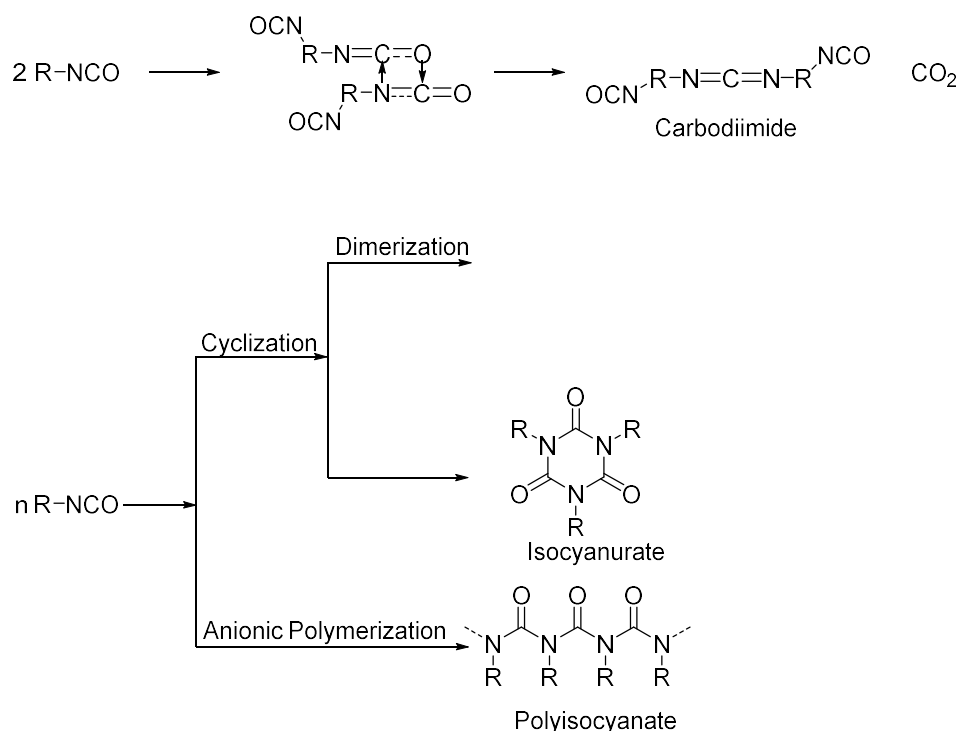
**Scheme 5.** Most common side-reactions involving isocyanates

Under mild conditions and without catalysts, the formation of allophanates and biurets is limited due to the electron withdrawing effect of the carbonyl group attached to the nitrogen atom.<sup>34</sup> Therefore, the use of special reaction conditions (temperature, catalysts, high NCO:nucleophile ratio) are required.<sup>7,29</sup> In this line, according to Spirkova *et al.*,<sup>35</sup> allophanates are formed at very slow rates under temperatures below 60 °C without catalysts. Similarly, Schwetlick *et al.*<sup>36</sup> demonstrated that the reaction between isocyanates and alcohols did not lead to allophanate-based products at 50 °C, using equimolar NCO:OH ratios and regardless the presence of catalysts.<sup>29</sup>

The formation of biurets from isocyanates and water should not be neglected, since traces of water are frequently present in commercial starting materials, such as polyols. In fact, since the molecular weight of water is very low compared to the polyol precursors, the presence of traces become important on molar scale. According to Dusek *et al.*,<sup>37</sup> the formation of biuret is much faster than generation of

allophanate in organotin-catalyzed reactions but the contribution of these side-products is very low at temperatures below 60 °C.<sup>35</sup>

There are other well-known types of isocyanate by-products that are formed from self-condensation reactions. Depending on the conditions used, different products can be obtained, such as carbodiimides, isocyanurates (cyclo trimer), uretdiones (cyclodimer) and polyisocyanates<sup>7,10,11,27,28,34,38</sup> (**Scheme 6**).



**Scheme 6.** Isocyanate self-addition reactions

Although most of the times side-reactions are undesired, the generation of these by-products can also be intentional. In fact, isocyanurates, uretdiones and carbodiimides are frequently used to modify the physicochemical properties of certain isocyanates, such as increasing their functionality, lowering their melting point or decreasing their volatility.<sup>28,36</sup>

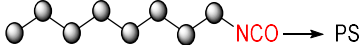
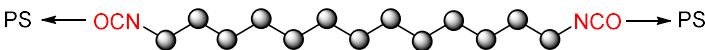
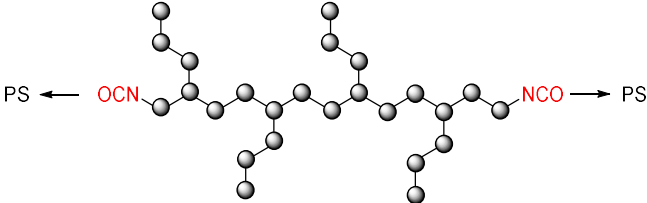
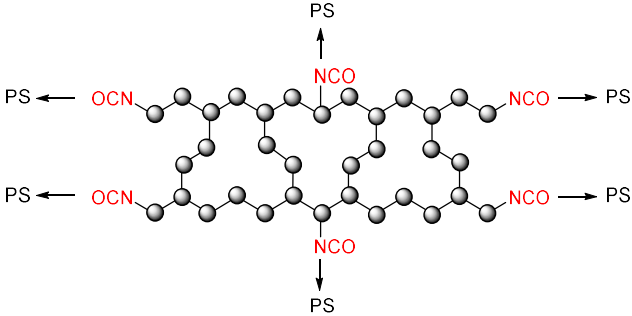
Carbodiimides can be obtained from isocyanates by prolonged heating (temperatures around 200 °C) with elimination of carbon dioxide. Aromatic uretdiones are easily prepared at high temperatures with the presence of catalysts such as trialkylphosphines, substituted pyridines or trialkylamines. Trimerization of alkyl or aryl isocyanates is catalyzed mainly by alkali metal alkoxides, although tertiary amines or tin-based compounds also promote the reaction but at slower

rates.<sup>7,12,28</sup> Finally, polyisocyanates are synthesized at low to intermediate temperatures (from  $-40\text{ }^{\circ}\text{C}$  to  $100\text{ }^{\circ}\text{C}$ ) by anionic chain polymerization.<sup>7,39</sup>

#### 1.2.4. Polymer functionality

The concept of functionality is one of the main properties of monomers used in polycondensation reactions and was established for the first time by Wallace H. Carothers.<sup>40</sup> He related this notion to the structure of the resulting polymers, as shown in **Table 2**.

**Table 2.** Relationship between the functionality and possible polymer configurations

F	Spatial disposition (PS = polymerization site)	Configuration
1		End-capped polymer
2		Linear polymer
2		Branched polymer
> 2		Crosslinked polymer

With his study concluded that linear polymers are formed from difunctional monomers whereas highly-functionalized polymers yield to crosslinked gels. Nevertheless, the experimental conditions and the differences on the reactivity of the groups involved allow to control the final polymer structure.<sup>41</sup> For instance, IPDI

presents two NCO groups with different reactivity, since one of them is primary and the other is a secondary group and both present different steric hindrances (**Figure 2**). Therefore, their reaction rates are not the same, providing a higher reaction control and favoring linear configurations rather than crosslinked ones.<sup>17,18</sup> In this line, hexamethylene diisocyanate (**Figure 2**) is more prone to lead to uncontrolled reactions due to the presence of two equal NCO groups with the same reactivity.

### 1.3. Important considerations in DDS design

In order to develop a DDS with an improved performance, there are several properties that have to be thoroughly considered (**Figure 3**).

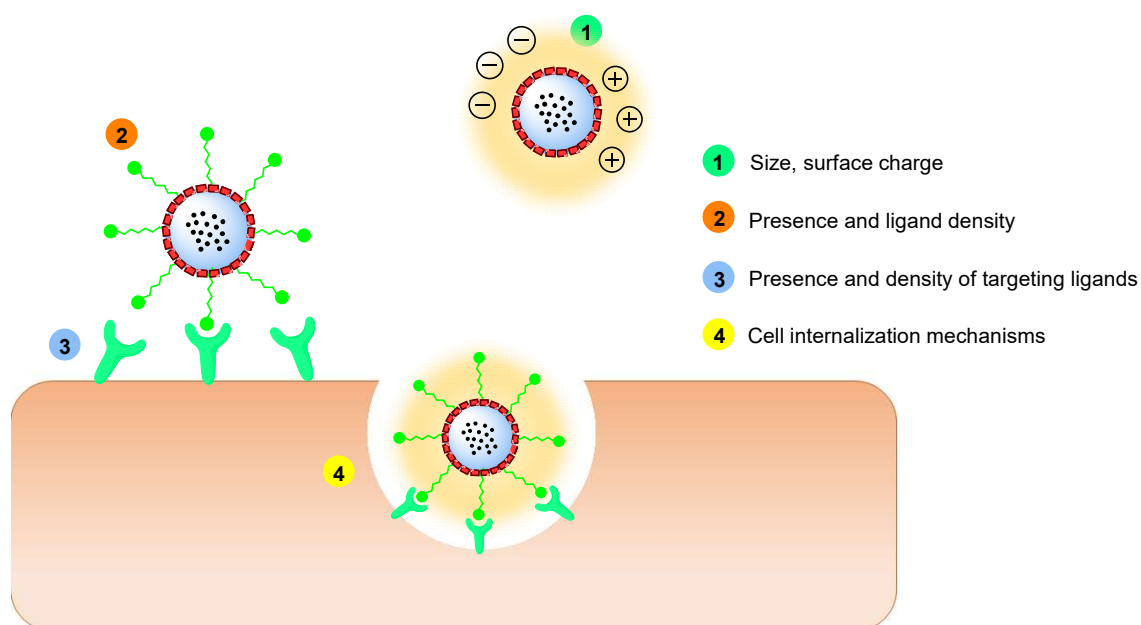


**Figure 3.** Some of the parameters influencing DDS performance

The generated nanosystems have to be designed according to the biocompatibility of the material of choice, the tunability of the polymers that will allow the incorporation of different functionalities and the hydrophobic effects that will take place with the lipophilic drug and will stabilize a micellar form.<sup>42,43</sup> Other parameters involve the interactions that will occur with the external aqueous medium,<sup>44,45</sup> and the presence of ligands or chemical moieties that will display a targeting effect and promote the DDS accumulation at the desired site.<sup>46,47</sup> Finally, the control of the nanoencapsulation efficiency and stability,<sup>48</sup> the optimal size to

promote tumor permeation<sup>49,50</sup> and the biodegradation of the system at the site of action are also important.<sup>51</sup> All of these features will be explained in detail in the following sections.

### 1.3.1. *Biocompatibility*

The development of nanomaterials in scientific and technologic fields has grown significantly during the past decades and has brought significant concerns about their safety, biocompatibility and toxicity. The biocompatibility is defined as the ability of a substance to present an appropriate host response in a particular application, according to a consensus conference of the European Society for biomaterials in 1986.<sup>52</sup>

The toxicity of nanomaterials has been described to depend mainly on their size, surface area, shape, functional groups, dosage, physicochemical stability and agglomeration state<sup>53,54</sup>. However, the chemical composition of the carrier is, at least, equally important as the former parameters because it is in direct contact with the biological medium and therefore plays an important role in the activation of the complement, coagulation and immune system alteration.<sup>55</sup>

In this regard, polyurethanes have been established as very versatile carriers and polyurea have been described as biocompatible materials<sup>56-59</sup> applied in micelles, dendrimers and nanoparticles.<sup>59-61</sup> Therefore, a merge of both functionalities is an interesting approach to develop high-performance biomaterials, since the excellent chemical resistance offered by polyureas would be combined to the synthetic versatility that can be achieved via polyurethanes.<sup>4-7</sup>

### 1.3.2. *Shell tunability*

The possibility of a polymer to convey multiple functions, tunability, is directly related to its intrinsic reactivity. In the ideal case, the polymer should present high reactivity in intermediate stages to allow its convenient functionalization to introduce different moieties, such as fluorescent tags, targeting ligands, charged groups, cleavable bonds, etc (**Figure 4**).<sup>46,62-66</sup>

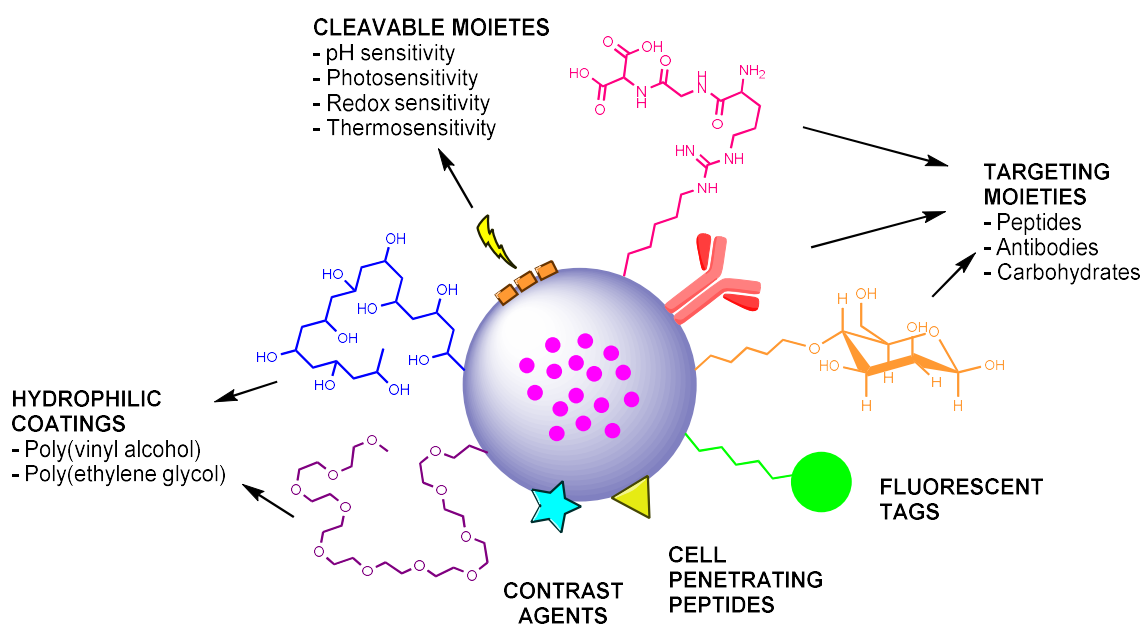


**Figure 4.** Possible chemical functionalities that a nanosystem can exhibit

Besides the possibility of adding multiple functions, the polymer should be able to adopt different morphologies and structures, depending on the final purpose. The existing chemical approaches to generate multifunctional nanoparticles are not able to functionalize them in a straightforward and reproducible manner,<sup>67-69</sup> yet they are based on the subsequent addition of functional monomers that do not participate in the overall nanostructuration. Moreover, most of the times the multiple decoration of the polymer backbone is accompanied by repeated purification cycles that imply a waste of energy and chemical resources.<sup>68,70</sup> This makes it almost impossible for pharmaceutical industry to consider their manufacturing, especially in large amounts, while not making them overly expensive.

The idea of creating architecturally controlled species arises from the need to develop tailored structures with high control at the nanometric level. In this regard, the chemistry of polyurethanes and polyureas offers an attractive approach to achieve such sophisticated nanostructures, due to their well-known chemical versatility and their vast presence in industrial applications.

### **1.3.3. Stratified nanostructured shell**

Although stratification in macromolecular structures has been accepted for a long time,<sup>71-73</sup> its importance was not totally recognized until it was proved that the analysis of o/w interfaces allowed the prediction of structure-property relationships.<sup>43,74</sup> The progress in this field has provided the sufficient understanding on interfacial molecule-molecule interactions to bring a new generation of colloidal nanomaterials with specific interfacial properties. In this regard, both electrostatic and hydrophobic interactions were found to be fundamental in the stratifying capacities of biological systems and nowadays are commonly applied in technological applications.<sup>75,76</sup> In this section, the importance of hydrophobic effects and the control of interfacial nanostructuration will be analyzed in detail.

#### **1.3.3.1. The hydrophobic effect and micelle formation**

The hydrophobic effect, which is the driving force of the nonpolar groups to adhere in aqueous environments to minimize their contact with water,<sup>72,77,78</sup> has been widely studied because of its central role in chemistry and biology.<sup>42</sup> Hydrophobic forces lead to structures that are compact but flexible enough to allow fluidity in the organization of living matter. Cells have to be capable of deformation as part of locomotive activities, when squeezed by neighboring cells or when they have to allow free mobility of metabolites, among others. These essential properties of membranes would be impossible to achieve if the permeability barriers found in biological compartments were only based on attractive forces that normally lead to rigid inflexible structures.<sup>78</sup>

This kind of interactions are manifested in many ways, but the tendency of hydrophobic moieties to aggregate or cluster is observed in all of them (**Figure 5**).

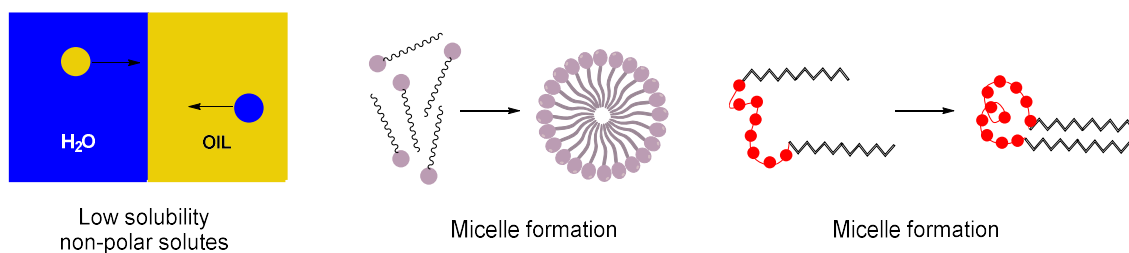


**Figure 5.** Different manifestations of the hydrophobic effect

For instance, hydrophobic interactions are responsible for the low solubility or nonpolar solutes in water<sup>79,80</sup>, self-assembly events, such as micelle formation<sup>81</sup> and protein folding<sup>82,83</sup>, among others.

In the particular case of micelle formation, the opposing thermodynamic preferences of the two ends of an amphiphilic molecule (polar head and hydrophobic tail) are satisfied by self-association to form an aggregate with the carbon chains pointing to the center and the hydrophilic groups on the surface. This kind of entity is named micelle and it typically contains on the order of 100 molecules per particle. Micelle formation strongly depends on monomers concentration, meaning that there is a critical concentration below which no micelles can exist and above which virtually all added amphiphile enters the micellar state.

The size and morphology of micelles is determined by both geometric and thermodynamic factors. One of the geometric factors is the surface/volume ratio, which tends to decrease as the number of hydrophobic tails core becomes larger. Hence, by using less hydrophobic chains but increasing their length in an amphiphile, the size of the resulting nanostructure should decrease. Among the thermodynamic parameters, surface area calculations suggest that very small spherical micelles are thermodynamically unstable due to their large surface/volume ratio. Therefore, a very efficient manner that small micelles have to achieve stability is by varying their shape in one or two dimensions, leading to cylindrical, rod-like or disk-like morphologies. Among them, a disk-like configuration is described as the best way to regain a thermodynamically favored state.

### 1.3.3.2. Self-ordered and compact structures

The formation of self-ordered and self-stratified structures brings a high degree of compaction and the achievement of a more thermodynamically stable state.<sup>77</sup> This concept is crucial in a DDS, since the hydrophobic drug needs to be highly stabilized in the core of the nanoparticle to avoid its premature release. To create self-stratification in polymer nanosystems by hydrophobic effects, both lipophilic and hydrophilic segments of an amphiphile need to be thoroughly designed in order to maximize the favorable interactions and achieve thermodynamic and geometric stability.<sup>77</sup> In this regard, as seen in **Figure 6**, the length and nature of both hydrophobic and hydrophilic chains and their relative position in the polymer backbone (in the main chain or sideways) are relevant parameters that have to be considered.<sup>42,83</sup>

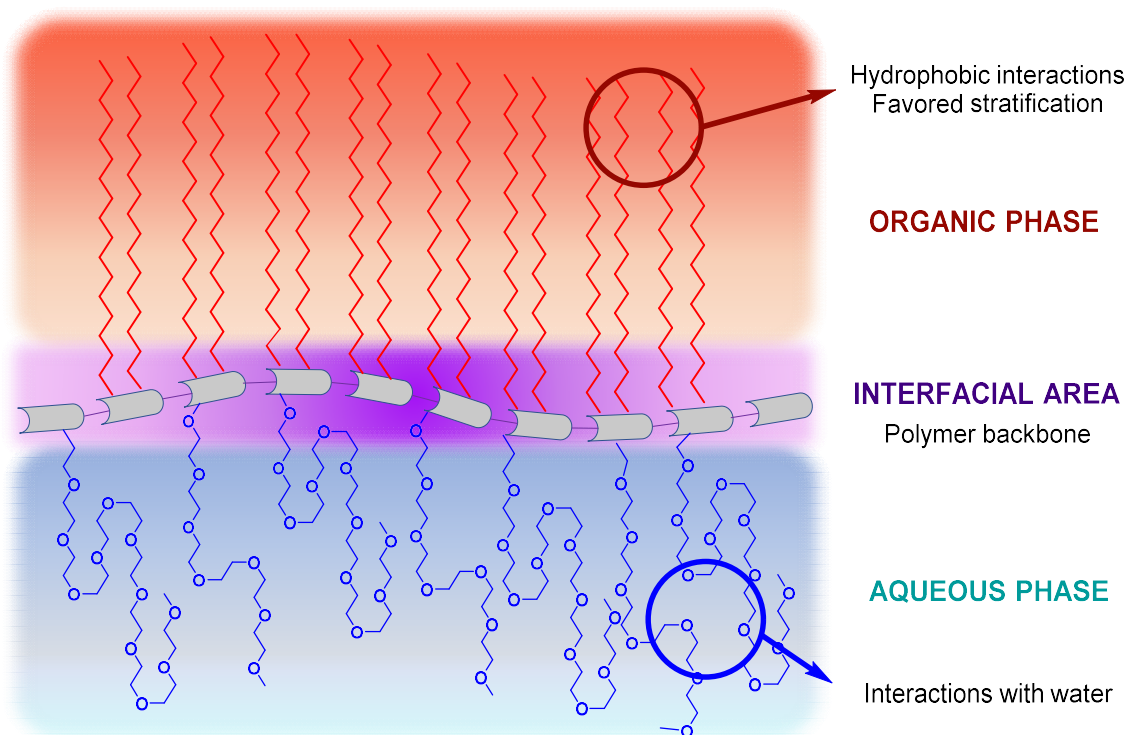


**Figure 6.** Representation of an interface, containing hydrophobic and hydrophilic side chains

As mentioned previously, the critical micelle concentration decreases as the length of the hydrophobic tail increases. This means that the generation of the vesicle is more favored and forms at lower amphiphile concentrations when the hydrocarbon chain is longer. Likewise, the presence of more extended polar groups

instead of short ones also contributes to the overall thermodynamic stability. Finally, relatively long pendant chains anchored to the main polymer backbone also favors more compact and self-stratified structures than shorter ones, since the hydrophobic/hydrophilic gradient created is more accentuated.

#### **1.3.4. Interactions with the biological medium**

The presence of hydrophilic segments has been proved to be relevant in micelle formation, however, its importance goes much further than a favorable interfacial nanostructuration. Hydrophilic chains also participate in the interactions established with the external medium, given their inherent tendency to orient outwards. The interactions between biological macromolecules and the surface occur from the initial contact with blood and are, as a last resort, the responsible for the DDS fate.

Among all the possible interactions between the NPs and the biological environment, their association with blood proteins is considered one of the most critical steps in reaching and releasing the cargo at the target site, determining to a major extent the nanocarrier biodistribution, efficacy and toxicity.<sup>84-86</sup> One of the most common events that occur as a consequence of these interactions is opsonization, defined as the process by which a foreign particle, particularly a microbe, is coated with plasma proteins (opsonins) so as to facilitate the attachment and internalization of that particle by a phagocytic cell.<sup>87</sup>

In general, the process refers to covering the microbe with immunoglobulin molecules (antibodies) that are specific for antigenic determinants on that organism, or with complement proteins deposited on the surface of the organism via either the classical or alternative activation pathways.<sup>87</sup>

The formation of an opsonin corona immediately alerts the phagocyte system thereby promoting rapid clearance of the nanocarrier-opsonin complex from the bloodstream.<sup>88,89</sup> Therefore, macrophage recognition can dramatically reduce the effectiveness of such treatments. Furthermore, the uptake of the nanocarriers by the cells of the phagocytic system can damage the immune system cells due to both drug and nanomaterial.<sup>84</sup>

An effective manner to avoid opsonization and prolong blood circulation is by decorating the surface of the nanocarriers with repelling hydrophilic polymers (**Figure 7**).<sup>89-91</sup>

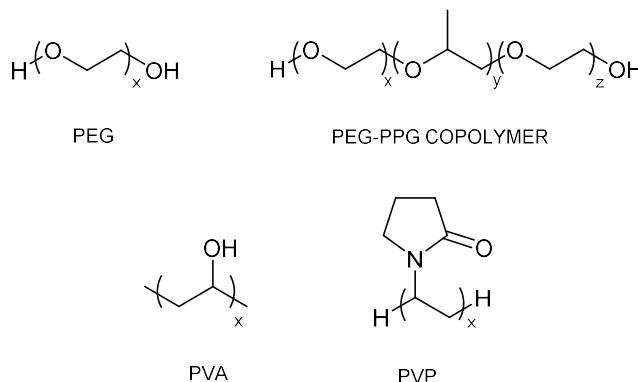


**Figure 7.** Some of the polymer coatings used in nanomedicine

The most common example is long chain PEG,<sup>44,92,93</sup> although other polymers such as PEG-PPG block-copolymers, PVA, dextran and PVP can be used to achieve hydrophilicity and emulsionability.

### 1.3.5. Encapsulation efficiency and stability

#### 1.3.5.1. Preformed amphiphilic shell

Common and commercially available polymers based on PLA,<sup>45,91</sup> PLGA,<sup>92,94,95</sup> PGA,<sup>96,97</sup> PEG-lipid, cholesterol and DPPC, among others.<sup>98,99</sup> All of them are biocompatible and biodegradable materials suitable for different kinds of drugs and, most of them, FDA-approved. Nevertheless, since these structures cannot be easily tuned, some properties such as encapsulation ability, particle size and *in vivo* stability can be compromised.<sup>100</sup>

Nanocarriers generated by self-assembly of amphiphilic polymers have the limitation that they usually present a diffuse and labile compaction. This is a direct consequence of the low nanostructure control at the moment of emulsification that lead to irregularly aggregated and randomly packed walls. This kind of amphiphilic polymers facilitate superficial entrapment of hydrophobic cargos instead of robust encapsulation properties. This causes a rapid burst of cargo release upon interaction with naturally existing biomolecules due to their extracting properties.<sup>101,102</sup>

Alternatively, the loss of shell stability over time can be due to coalescence, aggregation or Ostwald ripening events (**Figure 8**). This effect describes the tendency of small and unstable particles to redeposit their material onto larger droplets to reach higher thermodynamic stability<sup>103-105</sup>

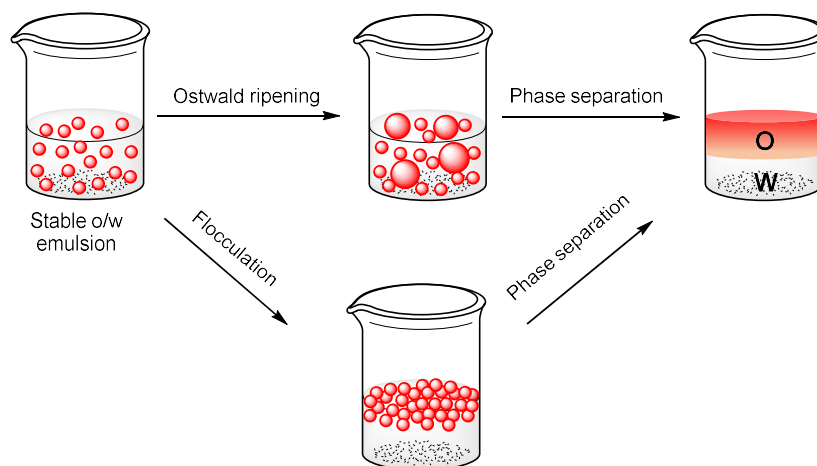


**Figure 8.** Different mechanisms for emulsion destabilization

An common way to increase the solubility of the oil into the aqueous phase is by adding surfactants into the system.<sup>106</sup> However, their presence in the encapsulation matrix create diffusion channels at the polymerization interface, compromising the encapsulation efficiency and stability and lowering the drug entrapped in the shell. Finally, besides altering the o/w interface, the use of emulsifiers also causes toxicity, hypersensitivities and allergies.<sup>107-110</sup>

### 1.3.5.2. Tailor-made polymer shell

In order to avoid such undesired effects, the polymers forming the shell should be tailor-made. This way, a highly packed and nanostructured wall could be achieved and would efficiently retain the encapsulated cargo until the moment of delivery. The formation of a compact shell is mainly due to the hydrophobic forces,<sup>111</sup> as described in the previous section. However, the presence of other amphiphilic and hydrophobic moieties in the external phase can affect negatively the nanostructure integrity, since they can disrupt hydrophobic stratifications *in vitro* and *in vivo*.<sup>101,102</sup> For this reason, chemical crosslinking of the former nanostructures is an interesting approach to avoid destabilization by other

amphiphilic molecules that would jeopardize the specific delivery of the encapsulated cargo (**Figure 9**).

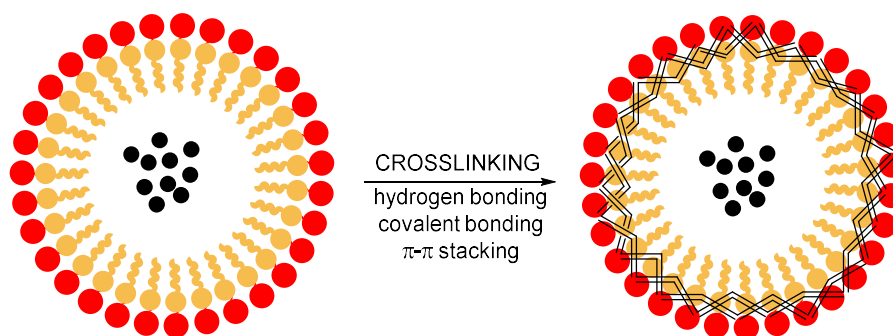


**Figure 9.** Micelle before (left) and after (right) a crosslinking step

The crosslinking can be achieved by covalent bonding, hydrogen bonding or  $\pi$ - $\pi$  stacking.<sup>112-114</sup> Regardless the approach, the crosslinked nanosystems have generally shown better pharmacokinetic profiles due to a better drug retention compared to their non-crosslinked analogs. This improvement has led to the development of novel nanosystems following this direction, with more promising *in vivo* performances and with higher chances to enter clinical trials.<sup>115</sup>

### 1.3.6. Particle size

The structural properties, and especially the size of the nanosystems, have a dramatic effect on its performance, since it dictates the potential accumulation and retention at target sites.

As explained in Chapter 1, tumors possess large fenestrations between endothelial cells of blood vessels as a consequence of angiogenesis events and hence can retain particulates circulating in blood.<sup>116-119</sup> This effect, termed the EPR, allows the nanoparticulate systems to accumulate inside the tumor cells provided that they are not cleared by the liver or spleen or excreted through the kidney.

Throughout the era of the nanotechnology, different size ranges have been studied in order to determine the optimal diameter to allow the nanoparticle navigation between the tumor interstitium after extravasation. In this regard, it was found that liposomal and particulate systems with diameters around 100 nm improved distribution and tumor accumulation only in highly permeable tumors.<sup>120</sup> In addition, they could not extravasate far beyond the blood vessels because they

remained trapped in the extracellular matrix between cells.<sup>121</sup> Moreover, 100 nm micelles showed higher liver accumulation compared to smaller analogs, which caused toxicity in this organ.<sup>120</sup>

In this line, results from intratumoral microdistribution also indicate that sub-30 nm nanomedicines have superior properties in terms of extravasation and tumor penetration among the sub-100 nm nanosystems.<sup>120</sup> Considering that the threshold of renal clearance is 5.5 nm,<sup>122</sup> tumor accumulation and intratumoral distribution of nanomedicines ranging from 6 to 30 nm are theoretically the most promising ones.<sup>120,121</sup> In fact, Cabral *et al.*<sup>120</sup> proved that nanoparticles made of the same carrier material of 30, 50, 70 and 100 nm had an important accumulation in highly permeable tumors but only the 30 nm version could successfully penetrate poorly permeable pancreatic tumors and achieve an antitumor effect.

Another study, conducted by Wang *et al.*,<sup>50</sup> demonstrated indeed that micelle size strongly affected blood clearance rate, tumor accumulation and therapeutic effect. On one hand, 100 nm micelles showed slow blood clearance rates while larger nanocarriers caused a more rapid elimination. Moreover, analyzing organ accumulation, small micelles (35 nm) were mainly cleared by the liver, while large ones (150 nm) were sequestered by spleen. The 100 nm micelles presented 10 to 20 times more accumulation in BCap37 xenografted tumors than the 30 nm analogs, but the latter caused a relatively higher anticancer activity due to their higher ability to penetrate tumors.<sup>50</sup>

### 1.3.7. *Smart targeting*

Translational research seeking cutting-edge effective clinical treatments have increasingly turned to targeted nanoparticle platforms. The ideal nanoparticulate nanosystems should exhibit a specific effect to pathologic tissues, minimizing or avoiding off-target events of the active therapeutic agents on healthy tissues.<sup>123,124</sup> Targeting can be achieved via conjugation or physisorption of different kinds of ligands, such as small molecules, polypeptides, protein domains, antibodies and nucleic acid-based aptamers.<sup>125</sup>

Among the aforementioned targeted nanosystems, antibody therapy is currently the most promising option but owing to their inherent large molecular size and tendency to resist internalization, antibodies have a limited use in NP-based

therapies. Peptides, glycopeptides or protein moieties, given their lower molecular weight, are more suitable for a receptor-mediated endocytosis and therefore have emerged as elegant alternatives for targeted delivery.<sup>123-125</sup>

Although numerous publications highlight the importance of a targeting ligand bound on a nanocarrier *in vitro*,<sup>47,65,66,126-130</sup> the *in vivo* data and the clinical outcome reflect a less encouraging scenario. For instance, the study conducted by Kirpotin *et al.*<sup>131</sup> confirms that the presence of a mAb fragment on the liposomes shell did not affect the biodistribution or long-circulating properties. Moreover, the antibody-conjugated liposomes were not localized in higher concentrations in the tumor, since both targeted and non-targeted versions achieved similar levels in HER2-overexpressing breast cancer xenografts. Another example can be illustrated with the study of Bartlett *et al.*,<sup>132</sup> who concluded that both non-targeted and transferrin-targeted nanoparticles loading siRNA exhibited similar biodistribution patterns by positron emission tomography. In this case, the only advantage that presented the targeted nanoparticles is associated with processes involved in cellular uptake rather than tumor localization.<sup>132</sup>

According to the previous examples, the reality of current targeted nanosystems is that they do not have the ability to lead themselves to the target, yet they reach it as a consequence of blood circulation and extravasation followed by intratumoral retention and distribution.<sup>131,133,134</sup> This explains why an increase of the blood circulation by, for instance, PEGylation can have a deeper effect on the delivery than the presence of a very active ligand. Overall, this may suggest that an active targeting does not automatically translate into an effective delivery,<sup>125</sup> yet it is a consequence of the combination of other multiple and more complex effects.

In this scenario, the development of a next generation of nanosystems with real smart properties is becoming urgent. In this line, the concept 'smart' would not uniquely mean that the nanocarrier possesses certain properties related to triggered self- or dis-assembly, stimuli-responsiveness, magnetic guidance or photo-activation.<sup>67</sup> Yet it would be referred to an ideal nanoconstruct that it would also display variable properties as a direct consequence of their ability to adapt and respond to the external conditions. More specifically, really smart nanobiomaterials should present a tailor-made shell with the ability to turn on and turn off the targeting moiety on demand. On one hand, it should display certain physicochemical

properties to evade RES sequestration and ensure target latency (suppression) in circulation, where it should not cause any effect. On the other hand, after approaching the diseased site, enhanced by the long residence in blood, the latent target would then be activated by the external conditions and be efficiently internalized in the target cells (**Figure 10**).

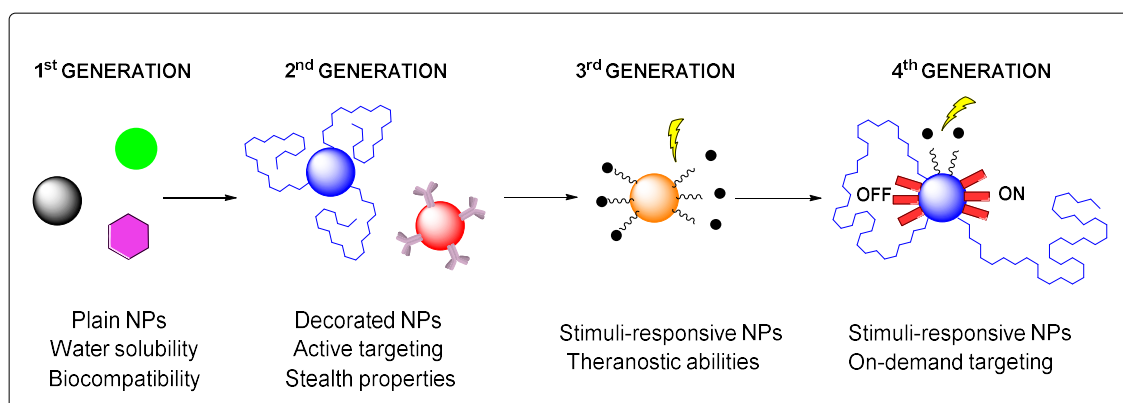


**Figure 10.** The evolution of the different nanomedicine generations

Such a sophisticated behavior is not possible with standard targeting moieties (carbohydrates, peptides, proteins, antibodies...) due to their inherent invariable properties. Therefore, a thorough engineering of the nanoparticle and a very deep control of the encapsulating chemistry is required in this new generation of nanobiomaterials. From this perspective, the selectivity of a DDS would evolve from mere ligand-bearing nanocarriers with unchanging behaviors to more complex and elaborated systems that finely tune their properties as a consequence of their targeting abilities.

### 1.3.8. Biodegradability

Once in the targeted tissue, the nanocarrier should be able to degrade and release its cargo in order to perform its therapeutic effect. In other words, the nanosystem should be sensitive to the external conditions of the targeting site and not to the rest of the organism to ensure a specific drug delivery.

The high reducing potential of the intracellular environment has been extensively applied as a stimulus for the degradation of polyurethane-based NPs for controlled release in cancer cells. For instance, Yu *et al.*<sup>114</sup> developed polyurethane core-crosslinked NPs containing disulfide bonds and they proved the selective

degradation and subsequent release of doxorubicin *in vitro* and *in vivo*. Another example is reported by Ma *et al.*,<sup>135</sup> who developed polyurethane micelles with diselenide bonds in its structure as an approach to achieve a dual effect in both reductive and oxidative environments.

## 2. Objectives

The specific objectives for this Chapter are grouped into two main categories, depending whether they refer to the methodology or to the properties of the NCS:

### Methodology

- **The development of an industrially scalable synthetic methodology to produce polyurethane/polyurea NCs.** In this regard, the process should involve the least number of steps and should proceed through the maximum atom economy. Moreover, the monomers used should be obtained from industrial sources to ensure manufacturing feasibility.
- **The development of an environmentally friendly process** that leads to waterborne products that do not contain external emulsifiers and organic solvents.
- **The development of a robust process** able to compensate batch-to-batch differences. In addition, it should be applicable to different kinds of bioactive ingredients to become more industrially attractive.
- **The development of a chemically versatile method** that allows the insertion of different functionalities on the NCs in a straightforward manner.

### Properties of the NCs:

- **The synthesis of biocompatible NCs** that are composed of materials that do not induce systemic toxicities.
- **The generation of biodegradable NCs** that can be selectively cleaved by GSH and that are stable in physiological conditions.
- **The preparation of NCs that can load different types of molecules** in high concentrations to avoid the unnecessary use of encapsulating material.

- **The synthesis of NCs with a monomodal particle size below 30 nm** to achieve long blood-circulation rates and avoid opsonization *in vivo*.
- **The generation of NCs that can change their surface charge** depending on the pH conditions as a tool to specifically target the tumor microenvironment.

### 3. Results and discussion

#### 3.1. General experimental design

This Chapter is devoted to describing a versatile and potentially scalable synthetic method to produce polyurethane/polyurea NCs conceived to respond to narrow pH changes and be cleaved in reductive environments. The NCs developed were designed to fulfill the requirements described in the objectives, in terms of shell tunability, biocompatibility, redox-triggered release, loading versatility, entrapment efficiency, controlled particle size and smart targeting. To this aim, the polymer forming the NC shell was decorated with the appropriate functional groups that provided the desired properties to the nanosystem. **Figure 11** shows a model nanoparticulate system that includes the necessary functionalities to fulfill the requirements described in the objectives.

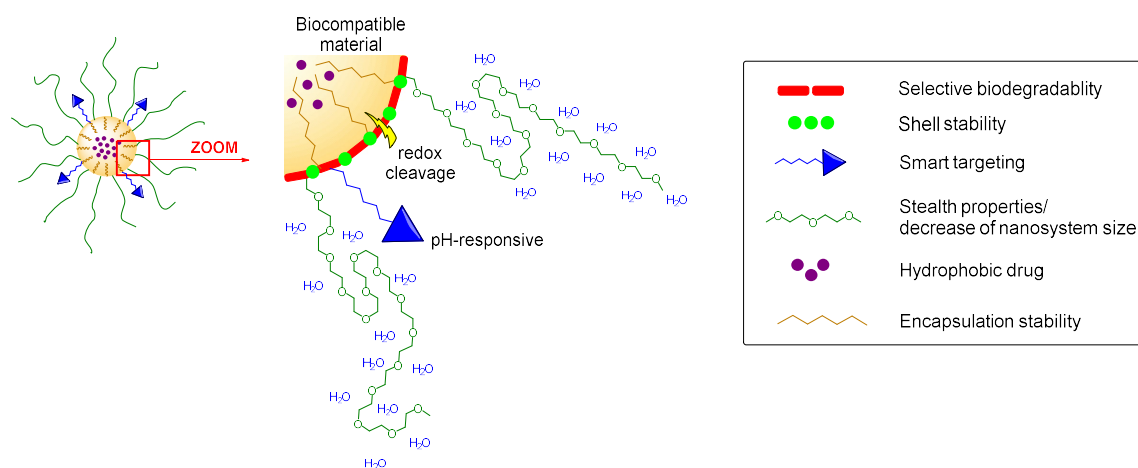
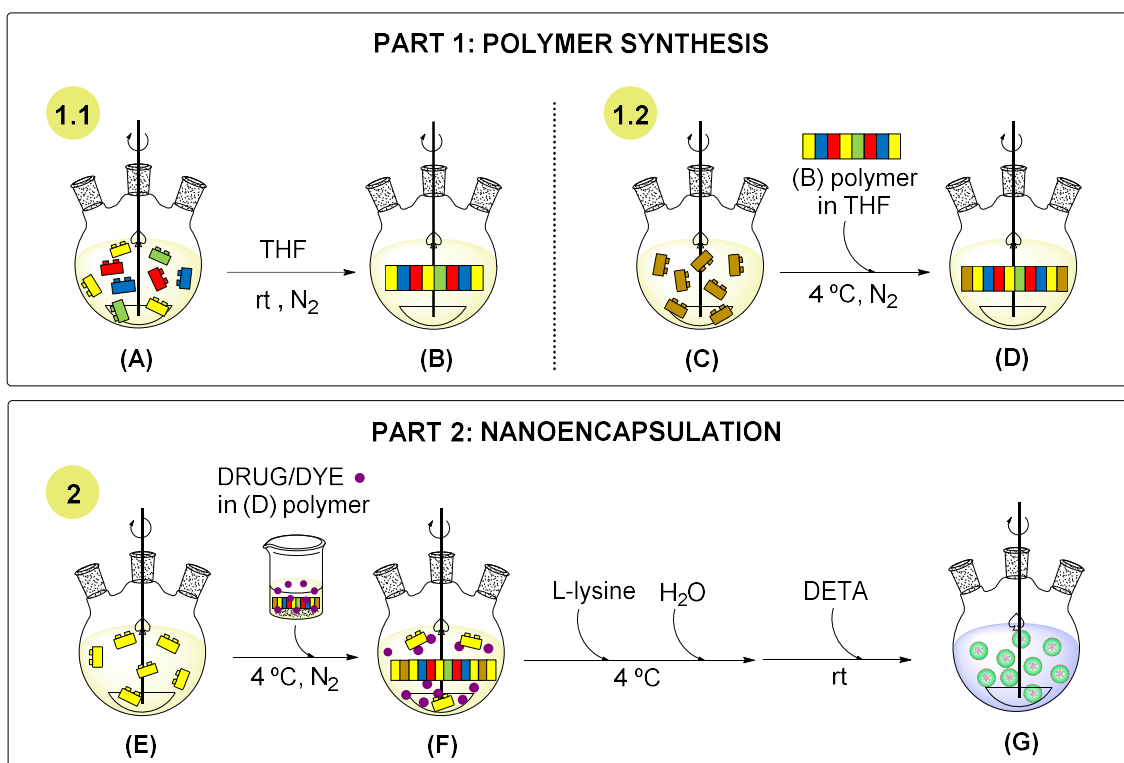


**Figure 11.** Nanosystem of interest exhibiting the desired properties

According to the figure, the polymer forming the shell should contain biodegradable bonds to allow the release of the cargo under reductive conditions. In addition, the polymer shell should be functionalized with specific chemical groups to achieve an on-demand targeting to the tumor microenvironment. Moreover, it should also contain hydrophilic PEG-based side chains to provide stealth properties and contribute to a controlled particle size. Finally, the nanosystem should present a crosslinked shell to prevent premature drug leakage and hydrophobic tails to provide cargo stability.

Given the complexity of the systems to be prepared, the present Chapter is divided into two different parts. The first one describes the synthesis of the polymers that will subsequently be used for the preparation of the NCs, while the second one discusses the nanoencapsulation process and the NCs characterization.

The whole process is schematized in **Scheme 7**, in which the *Lego* pieces represent the different monomers used and the purple dots account for the nanoencapsulated molecules.



**Scheme 7.** Overview of the nanoencapsulation process

As described in the scheme, the first part involved the polymer synthesis (part 1). Accordingly, the method started with the polymerization of the monomers (difunctional nucleophiles in red, green and blue) with a certain diisocyanate (yellow), in THF, under N<sub>2</sub> atmosphere at rt (steps A, B). The reaction led to an intermediate polymer, which was added into another pre-cooled reactor containing the last monomer (brown pieces, step C). The polymerization reaction resulted into an amine-terminated polymer (step D) that was further used in the nanoencapsulation part. This process (part 2) started with the dissolution of the hydrophobic molecule in the former amine-terminated polymer. This mixture was transferred into a reactor containing an excess of the diisocyanate, at 4 °C and under N<sub>2</sub>, and the amines of the polymer reacted with an excess of NCO groups, yielding to a NCO-reactive prepolymer (steps E, F). At that point, L-lysine sodium salt was added as an ionomer and reacted with the NCO-reactive polymer, resulting into an amphiphilic and amphoteric intermediate. Then, the organic phase (drug/dye in the polymer mixture) was emulsified in water, and finally, DETA was added at rt to covalently crosslink the remaining NCO groups and form the final NCs (step G).

## 3.2. Preparation of the polymers

### 3.2.1. Monomers considered

#### 3.2.1.1. Isophorone diisocyanate (IPDI)

The polymers and NCs described were synthesized considering thoroughly the chemistry of isocyanates outlined before. In this regard, isophorone diisocyanate (IPDI) (**Figure 12**) was the isocyanate of choice for two different reasons.

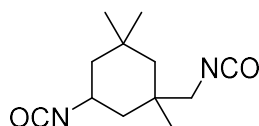


**Figure 12.** Chemical structure of IPDI

Firstly, its reduced toxicity due to the aliphatic structure and relatively high vapor pressure, compared to other isocyanates and, secondly, the presence of two NCO groups with different reactivity that contribute to an improved polyaddition control.<sup>7,22,136,137</sup> Moreover, the polymerization conditions chosen involved low temperatures, generally between 4 °C and rt, no need for catalysts, pre-dried monomers and solvents and the use of NCO:nucleophile ratios below 2, most of the times. These reaction parameters, along with the fact that IPDI presents an exact functionality of 2, make the polymers very likely to show a linear structure with a negligible presence of allophanates, biurets, isocyanurates or uretdione by-products.<sup>7,27,29</sup>

### 3.2.1.2. Genamin TAP100D

Genamin TAP100D (**Figure 13**) was selected due to its aliphatic chain that contributes to the micellar morphology<sup>42,111</sup> and the stabilization of the encapsulated molecules, which are hydrophobic, through hydrophobic interactions.

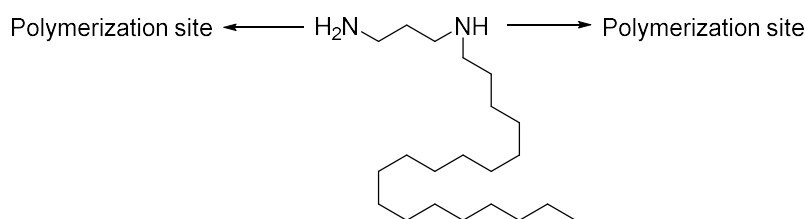


**Figure 13.** Chemical structure of Genamin TAP100D

Moreover, the length of the alkyl side chain (C18) is relevant according to the geometric factors of the theory of the hydrophobic effect.<sup>72,77</sup> Accordingly, by reducing the amount of hydrophobic chains and increasing their length in an amphiphile, the resulting nanostructures become smaller. Therefore, since one of the objectives was to develop very small NCs, the length of the hydrophobic chain could not be shorter, for instance, than C10 because it would result into a non-thermodynamically stabilized system. In addition, the side chain should not be much longer, since larger tails would lead to a higher hydrophobic cargo and would increase the NC diameter.

Another important feature of the chemical structure of Genamin TAP100D is that once this monomer is polymerized, the hydrocarbon tail is likely to be disposed as a side chain and not in the polymer backbone. This favors the hydrophobic interactions between the tails and the drug and promotes a highly packed structuration at the interface. These effects, along with the fact that it can be easily obtained from industrial sources and in bulk volumes, made Genamin TAP 100D the monomer of choice to achieve these properties.

### 3.2.1.3. YMER N-120

YMER N-120 (**Figure 14**) was also present in the polymer backbone and was selected for two main reasons. Firstly, because of its hydrophilic properties as a PEG-based monomer and, secondly, because the multiple ethylene oxide units are organized as side branches and not as a main chain.

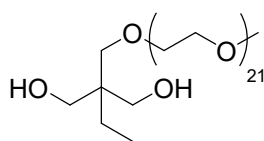


**Figure 14.** Chemical structure of YMER N-120

The incorporation of YMER N-120, along with the hydrophobic side chains of Genamin TAP100D, turned the polymer into an amphiphile. Both monomers gathered in the o/w interface preventing emulsion destabilization, driven by coalescence, flocculation or aggregation.

The self-emulsifying properties of the polymer, in turn, avoid the addition of external surfactants and the need of high speed stirring during emulsification. Self-emulsionability is considered a crucial feature in a nanosystem, because some additives, such as surfactants, are generally difficult to remove from the final product. When the product is either food, cosmetics or pharmaceuticals, this issue becomes more serious, since the remaining emulsifiers can induce contact allergies or hypersensitivities in the consumers.<sup>138-141</sup> Moreover, when the system is not self-emulsifiable, it requires high speed stirring and intensive shearing to be able to emulsify an oily phase in an aqueous medium. Generally, these requirements are difficult to achieve in large-scale productions due to technical limitations.

Besides playing an important role in emulsification, YMER N-120 also provides stealthiness to the NCs to prevent macrophage sequestration and rapid blood clearance. In fact, PEG has been shown to create a brush border around the NCs and provide an impermeable barrier that sterically prevents access to proteins.<sup>89</sup> It is described that every ethylene glycol unit is tightly associated with two or three water molecules, generating the hydrophilic shield.<sup>90</sup> Interestingly, branched PEG coatings are better in cloaking the attached nanocarrier from the immune system and proteolytic enzymes than their lineal analogs.<sup>84,90</sup> Other studies point out that branched PEG also shows increased stability towards denaturant conditions, prolonged body residence times and a reduced antibody recognition.<sup>49,91,142-146</sup>

Thanks to YMER N-120, the synthesized polymers present a sided PEG chain while the two hydroxyl groups are used for the polymerization and remain in the main backbone (**Figure 15**).

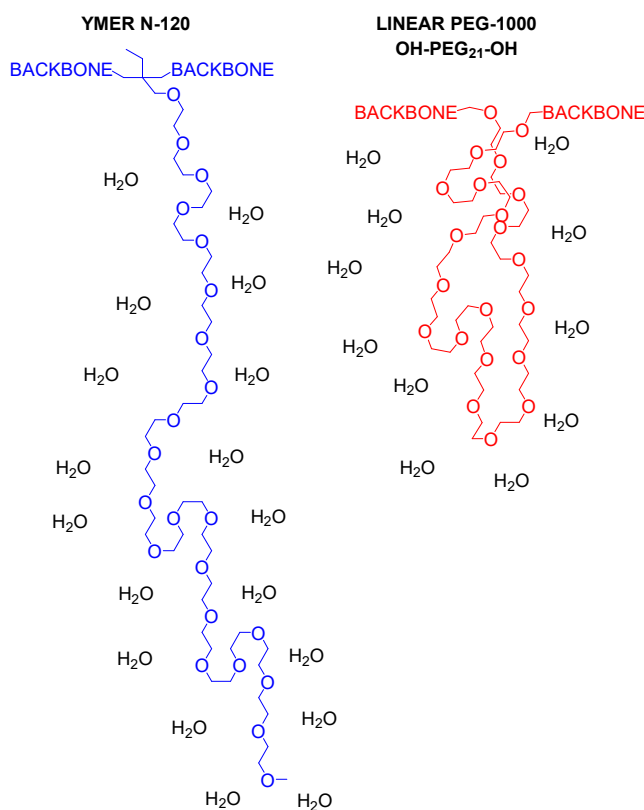


**Figure 15.** Side-chained PEG and lineal PEG of equivalent molecular weight

As it can be seen in the figure, YMER N-120 is more prone of establishing water-PEG interactions due to its free mobility and flexibility compared to its linear PEG-1000 analog, which has a more restricted mobility along with a shorter pendant chain.

#### 3.2.1.4. Jeffcat DPA

Jeffcat DPA (**Figure 16**) was also considered as a monomer for the polymer synthesis because it provides two tertiary amines that participate in the smart targeting properties of the system.

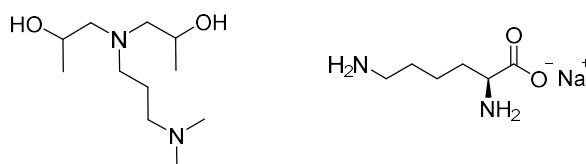


**Figure 16.** Chemical structure of Jeffcat DPA (left) and L-lysine sodium salt (right)

This monomer was selected because one of the tertiary amines presents a specific pK<sub>a</sub> value that allows the NC cationization at the desired pH range to achieve an on-demand targeting. According to our approach, the cooperation between this monomer and L-lysine sodium salt, which is polymerized through the 2 amines during nanoencapsulation, gives the nanosystem the possibility to modulate the surface charge and become be long-circulating in blood and highly permeating in tumor. These aspects will be analyzed in more detail in section 3.3.2.2.

#### 3.2.1.5. 2,2'-Dihydroxyethyl disulfide (DEDS)

Finally, the polymer was decorated with disulfide bonds, introduced through DEDS (**Figure 17**), in order to provide specific biodegradability under reductive conditions.

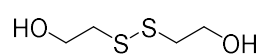


**Figure 17.** Chemical structure of DEDS

Disulfide bonds are prone to rapid cleavage by GSH and thus can be used to confer redox sensitivity. The cytosolic release of cargos can be triggered by the overexpressed GSH concentration found in the intracellular compartments (~2–10 mM) of tumor cells.<sup>97,147-149</sup> DEEDS was selected among other candidates because as a small molecule, it would not significantly affect the amphiphilic properties achieved via Genamin TAP100D/YMER N-120 combination.

### 3.2.2. *Polymers syntheses and characterization*

The polymers synthesized in the present Chapter are named **P1**, **P2** and **P3** and are shown below without revealing the exact structure (**Figure 18**).

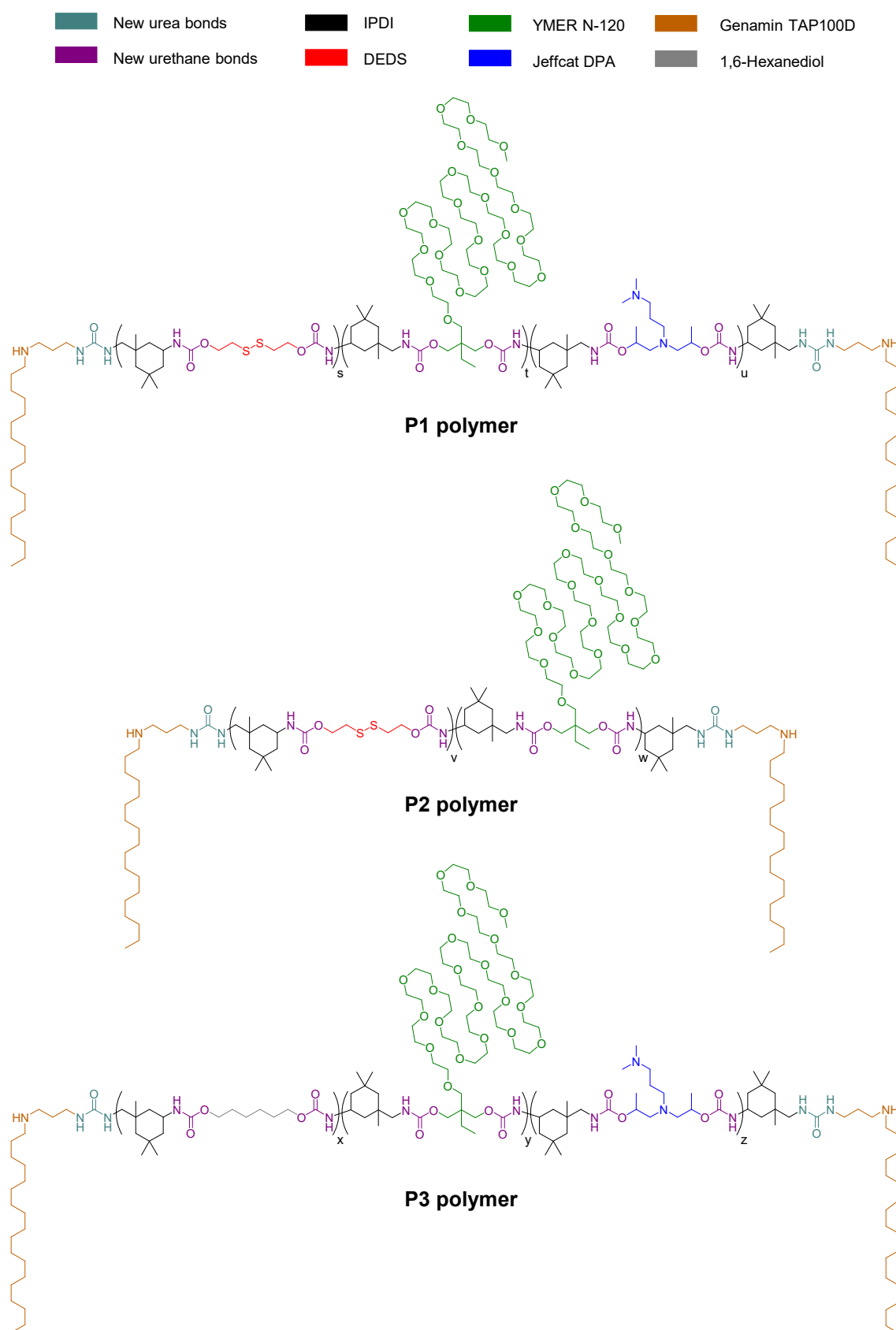
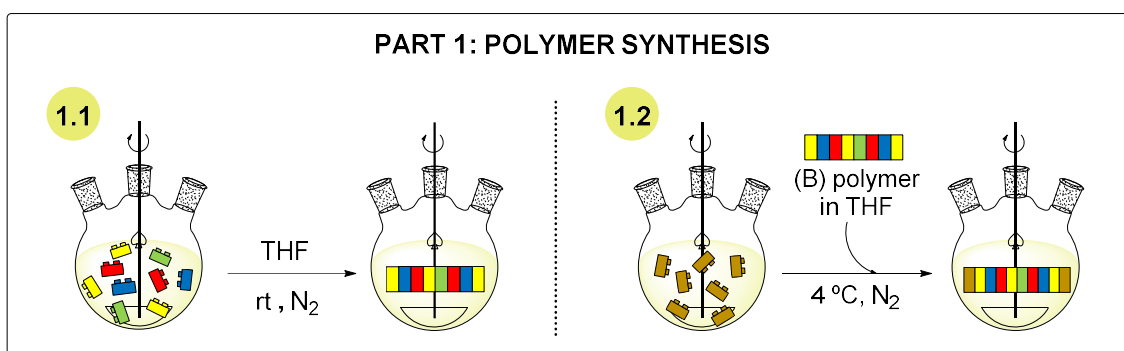


Figure 18. Schematic structure of polymers P1, P2 and P3

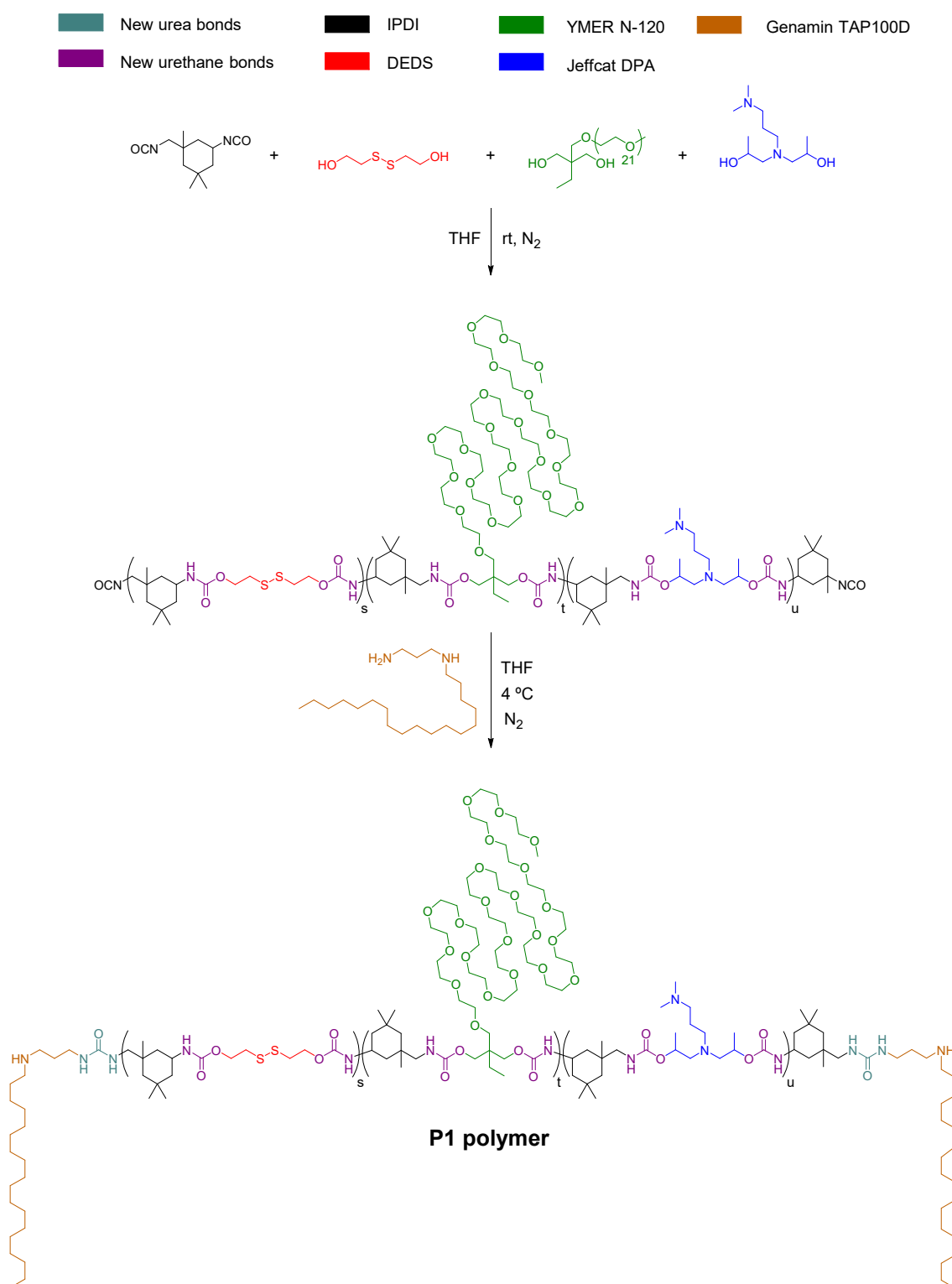
Most of the nanoencapsulation reactions were performed using **P1**, since **P2** and **P3** were prepared as control polymers that lack one of the starting monomers and were only used in sections 3.3.2.2 and 3.3.2.4, respectively. Therefore, the results presented in the present section will be based on **P1**.

These polymers were designed as amine-terminated polymers, since NCO-reactive polymers, and especially those that contain hydrophilic groups such as PEG (in green), are sensitive to hydrolysis and tend to lose NCO content over time.<sup>7</sup> For this reason, **P1–P3** were prepared as amine-reactive polymers susceptible to be reactivated *in situ* during the nanoencapsulation step. The preparation of the polymer is split into two different steps, as shown in **Scheme 8**.



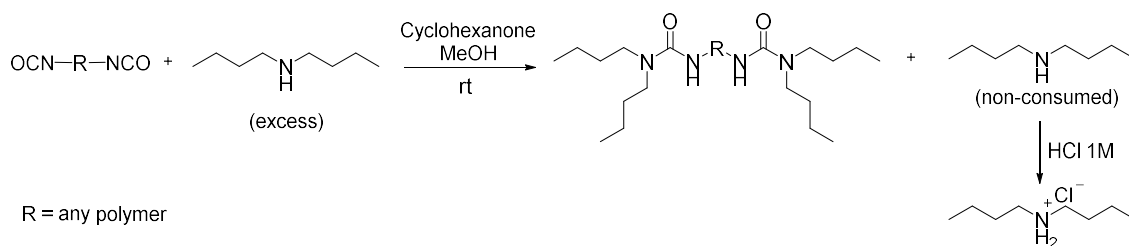
**Scheme 8.** Steps involved in the preparation of the polymer

The first part of the polyaddition reaction (1.1 in the scheme) involved the polymerization between IPDI (yellow), DEDS (red), YMER N-120 (green) and Jeffcat DPA (blue), resulting into a NCO-reactive linear polymer containing new urethane bonds. In the next step (1.2 in the scheme), the polymer was end-capped by Genamin TAP 100D (brown), leaving free amine residues to allow reactivation in the nanoencapsulation step. During the second part, new urea bonds were formed between the polymer and the free IPDI. These two synthetic steps are described in **Scheme 9**, where each part of the polymer is colored according to the corresponding monomer.



**Scheme 9.** The two steps involved in the **P1** synthesis

The monitorization of the polymer synthesis was carried out by IR spectroscopy, since automatic NCO titrations led to erroneous results. These titrations are based on the reaction detailed in **Scheme 10**.<sup>150-152</sup>



**Scheme 10.** Isocyanate titration with *N,N*-dibutylamine

According to the scheme, the NCO-reactive polymer, dissolved in cyclohexanone, reacts with a known excess of *N,N*-dibutylamine (titrant) in dry toluene and methanol, leading to an urea derivative and a non-reacted fraction of the amine. This excess is back-titrated against hydrochloric acid and this reaction is controlled by pH measurements. Given that **P1** contains tertiary amines (from Jeffcat DPA), the total excess of amines is a sum of the non-consumed *N,N*-dibutylamine and the tertiary amines from the polymer. Consequently, the final amine equivalents that were titrated against the acid were so high that exceeded the initial number of equivalents of titrant. Therefore, the calculations performed in basis of this reaction led to a negative NCO content.

Fortunately, the reaction could easily be controlled by IR spectroscopy given that NCO has a very clear and characteristic stretching band at 2280–2230  $\text{cm}^{-1}$ .<sup>7</sup> **Figure 19** contains the IR spectra during the monitoring of the first step of the reaction, while **Figure 20** corresponds to the second step. The IR spectra of **P2** and **P3** were very similar to **P1**, since the amount and nature of the monomers were almost the same, and thus are not enclosed herein.

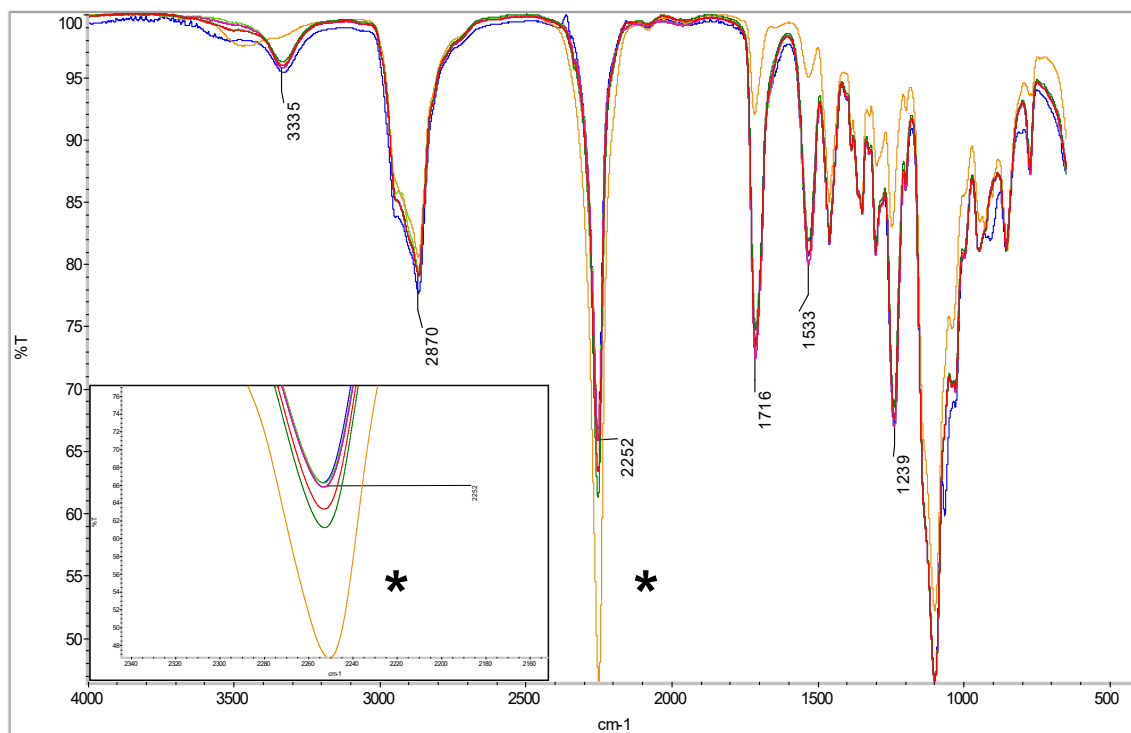


**Figure 19.** IR spectra of the first step of **P1** synthesis

IR spectra of polymer **P1** indicated a successful polyaddition reaction between the diols DEDES, YMER N-120, Jeffcat DPA and the diisocyanate IPDI. The orange line corresponds to the first sample recorded, at the start of the reaction. At that time, the NCO asymmetric stretching band at  $2252\text{ cm}^{-1}$  was very sharp and intense. After 1 h (dark green line), the intensity of the NCO stretching band decreased significantly while the intensities of the CO stretching band at  $1716\text{ cm}^{-1}$ , the CN stretching band at  $1533\text{ cm}^{-1}$ , the NCOO/COC asymmetric stretching band at  $1239\text{ cm}^{-1}$  and the NH stretching band at  $3335\text{ cm}^{-1}$  increased.<sup>7,153,154</sup>

The following samples (red and purple, respectively) were measured after 2 and 3 h of the start of the reaction and the obtained spectra showed a continuous decrease of the intensity of the NCO stretching band, along with a slight increase of the previously mentioned bands. Finally, the two last spectra (light green and blue) were measured after 4 and 5 h and confirmed that the reaction was complete since there were no noticeable changes in the most characteristic bands. Overall, the IR spectra performed during the first step of the synthesis confirmed polyurethane bond formation along with NCO consumption.

The second step was also monitored by IR spectroscopy and **Figure 20** shows the overlapped spectra.

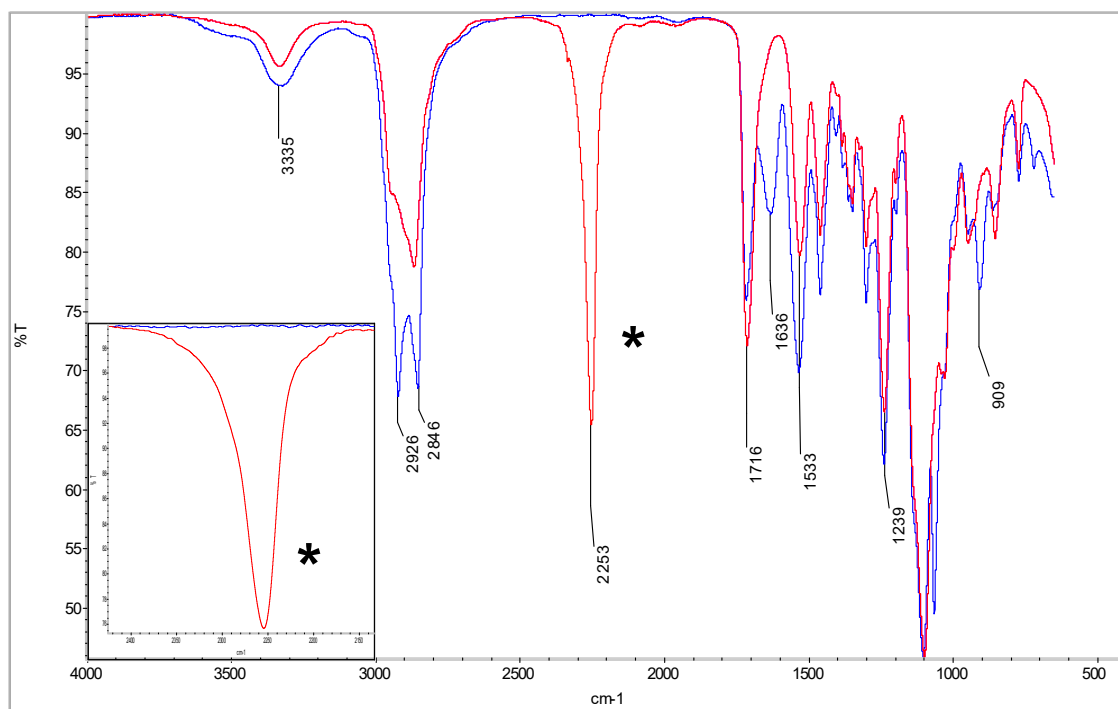
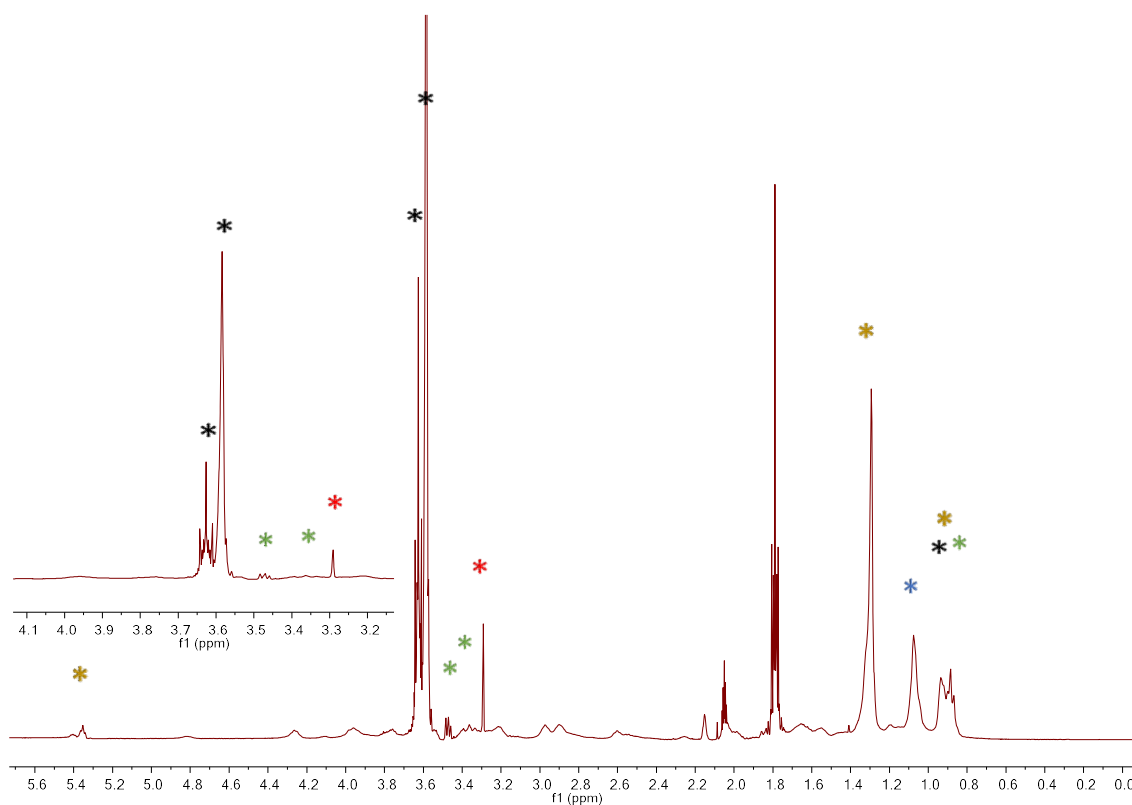


**Figure 20.** IR spectra of the second polyaddition reaction for **P1** preparation

During the second step of the synthesis, two different samples were recorded, just before (red) and after (blue) the addition of Genamin TAP100D. According to the IR spectra, the NCO stretching band at  $2253\text{ cm}^{-1}$  disappeared instantaneously, which was explained by the high reactivity of the amines.<sup>4,7,9,28</sup> Simultaneously, other characteristic bands appeared or changed, such as a new stretching band at  $1636\text{ cm}^{-1}$ , which was associated to the carbonyl of urea bonds, a new wagging band at  $909\text{ cm}^{-1}$  corresponding to the free secondary amine and an increase of the CN stretching band at  $1533\text{ cm}^{-1}$ , which also confirmed polyurea formation.<sup>7,153,154</sup>

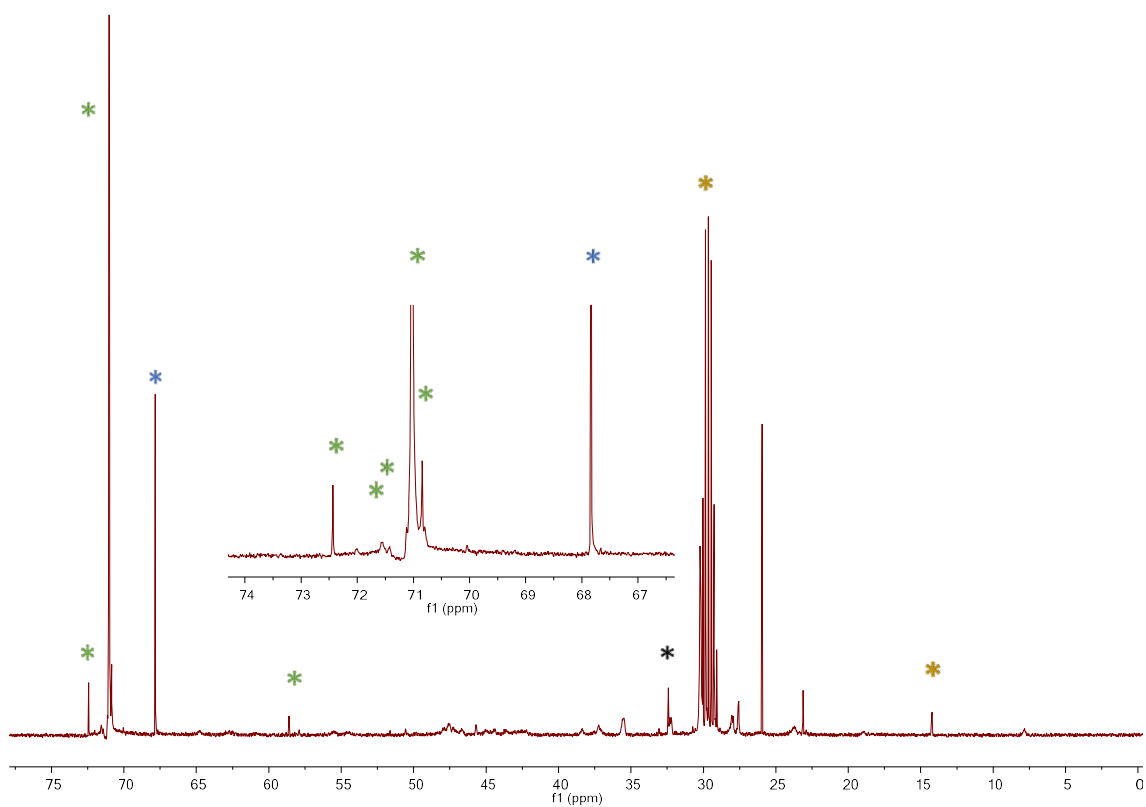
Polymer **P1** was further characterized by  $^1\text{H}$  NMR and  $^{13}\text{C}\{^1\text{H}\}$  NMR spectroscopy. In order to assign the spectra of the polymer,  $^1\text{H}$  NMR and  $^{13}\text{C}\{^1\text{H}\}$  of the monomers had been previously recorded (section 3 of the Annexes). **Figure 21** shows the  $^1\text{H}$  NMR spectrum while **Figure 22** shows the  $^{13}\text{C}\{^1\text{H}\}$  NMR spectrum of **P1**. The multiplicities are not specified because the peaks are broad and ill-defined.



$\delta_H$ (ppm)	Monomer	Moiety
5.35		-NH-
1.29	Genamin TAP100D *	-CH <sub>2</sub> -
0.89		-CH <sub>3</sub>
3.36		-O-CH <sub>2</sub> -CH <sub>2</sub> -O-
3.47	YMER N-120 *	-CH <sub>2</sub> -OH
0.87		-CH <sub>3</sub>
3.29	DEDS *	-CH <sub>2</sub> -OH
1.08	Jeffcat DPA *	-CH <sub>3</sub>
3.64		-CH-NCO
3.58	IPDI *	-CH-NCO
0.94		-CH <sub>3</sub>

**Figure 21.** The most characteristic <sup>1</sup>H NMR peaks of P1

There are characteristic regions in the <sup>1</sup>H NMR spectrum where the presence of the monomers could be identified. Regarding <sup>13</sup>C{<sup>1</sup>H} NMR spectroscopy, the identified shifts were also compared to the peaks assigned to the monomers.



$\delta_c$ (ppm)	Monomer	Moiety
30.23	Genamin TAP100D *	-CH <sub>2</sub> -
14.22		-CH <sub>3</sub>
72.44	YMER N-120 *	-O-CH <sub>2</sub> -CH <sub>2</sub> -O-
71.55		-O-CH <sub>2</sub> -CH <sub>2</sub> -O-
71.42		-O-CH <sub>2</sub> -CH <sub>2</sub> -O-
71.02		-O-CH <sub>2</sub> -CH <sub>2</sub> -O-
70.84		-O-CH <sub>2</sub> -CH <sub>2</sub> -O-
58.61		-O-CH <sub>2</sub> -CH <sub>2</sub> -O-
67.84	Jeffcat DPA *	HO-CH-
32.32	IPDI *	-CH <sub>3</sub>

**Figure 22.** The most characteristic  $^{13}\text{C}\{^1\text{H}\}$  NMR peaks of **P1**

$^{13}\text{C}\{^1\text{H}\}$  NMR spectrum also showed characteristic regions that corresponded to the monomers used, marked with an asterisk.

### 3.3. Nanoencapsulation

#### 3.3.1. Preparation of the NCs

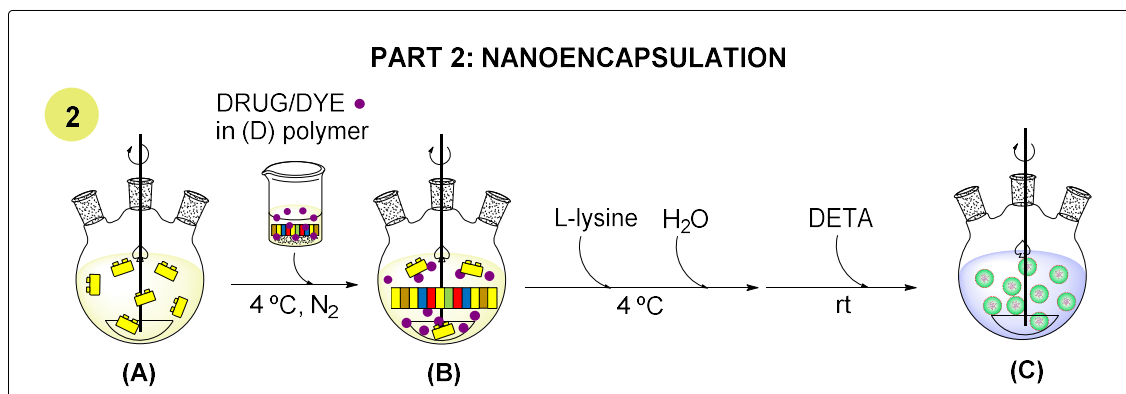
Different types of NCs were synthesized in this Chapter, depending on the cargo, the surface properties and the biodegradability of the shell. In this regard, **Table 3** summarizes the obtained NCs, where the ticks indicate that a certain property is actually found in the NC whereas the crosses denote the opposite.

**Table 3.** Different versions of NCs and the differences between them

Code	Core	Amphoteric	Cationic	Anionic	Redox-labile
<b>PTX-AMP NCs</b>	Paclitaxel	✓	⊗	⊗	✓
<b>CU-AMP NCs</b>	Curcumin	✓	⊗	⊗	✓
<b>HP-AMP NCs</b>	HP	✓	⊗	⊗	✓
<b>HQ-AMP NCs</b>	HQ	✓	⊗	⊗	✓
<b>Unloaded-AMP NCs</b>	Unloaded	✓	⊗	⊗	✓
<b>DiO-AMP NCs</b>	DiO	✓	⊗	⊗	✓
<b>DiI-AMP NCs</b>	DiI	✓	⊗	⊗	✓
<b>PTX-CAT NCs</b>	Paclitaxel	⊗	✓	⊗	✓
<b>PTX-AN NCs</b>	Paclitaxel	⊗	⊗	✓	✓
<b>NL-PTX-AMP NCs</b>	Paclitaxel	✓	⊗	⊗	⊗
<b>NL-DiO-AMP NCs</b>	DiO	✓	⊗	⊗	⊗
<b>NL-DiI-AMP NCs</b>	DiI	✓	⊗	⊗	⊗

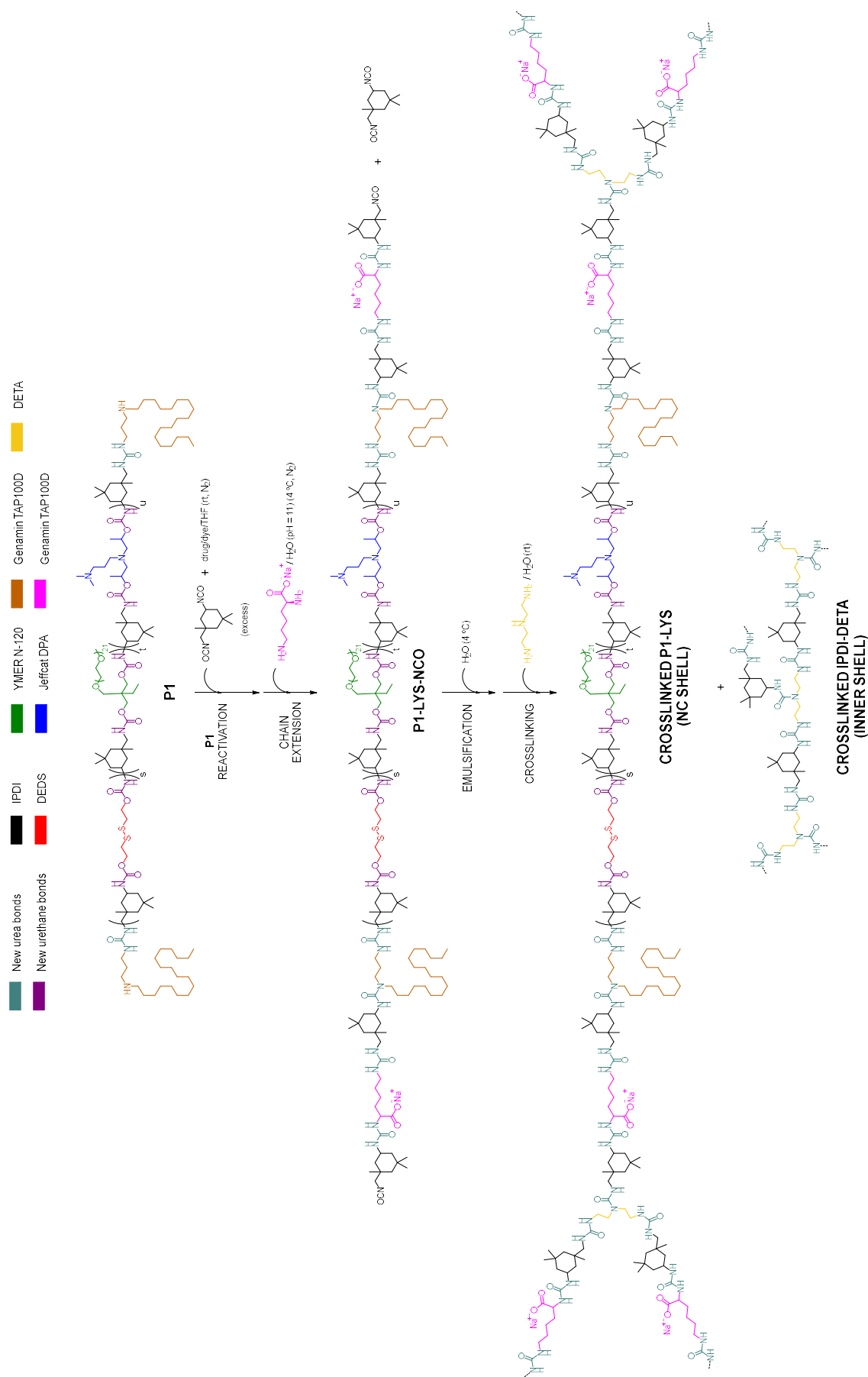
The table highlights some interesting differences among NCs. Regarding the encapsulated material, they loaded either drugs (PTX, CU, HP or HQ), fluorophores (DiO and DiI) or were empty (unloaded). In addition, their surface properties were also modulated depending on the type of NC, leading to products with either amphoteric (AMP), cationic (CAT) or anionic (AN) properties. Finally, some of the

NCs contained a specific moiety (DEDS), which provided redox-triggered biodegradability. Therefore, redox-labile and non-redox labile (NL) versions were also prepared. The general nanoencapsulation process is detailed in **Scheme 11**.



**Scheme 11.** Graphic representation of the nanoencapsulation process

The process started with the mixture of the hydrophobic molecule (drug, dye, oil...) in the polymer (**P1**, **P2** or **P3**) and the addition of the organic phase into a round-bottom flask containing IPDI (A, B), under N<sub>2</sub> atmosphere and cold temperature. Once the polymer reacted with NCO groups, it was reactivated, and L-lysine sodium salt was introduced as an ionomer. Finally, water was added dropwise to turn the organic phase into an o/w nanoemulsion and the process finalized with the addition of, DETA at rt, which rapidly crosslinked the NCO-reactive polymers gathered in the interface to generate the desired NCs (C). The reactions taking place from the start of the nanoencapsulation to the generation of the NCs are given in more detail in **Scheme 12**.



Scheme 12. Reactions taking place during nanoencapsulation

As seen in the scheme, an excess of IPDI was mixed with the polymer (**P1**, **P2** or **P3**), along with the hydrophobic molecule to be encapsulated. Since the polymer was amine-terminated, it reacted with the IPDI and led to an NCO-reactive intermediate (**P1-NCO**). Afterwards, when L-lysine sodium salt was added, **P1-NCO** was extended by incorporating this amino acid residue into the polymer main chain, affording **P1-LYS-NCO**. The addition of water did not imply any reaction, since it was incorporated at low temperature. Finally, DETA reacted in aqueous medium with three different **P1-LYS-NCO** intermediates and led to a crosslinked network, **CROSSLINKED P1-LYS**. Moreover, since IPDI was loaded in excess, part of DETA also reacted with the remaining IPDI to give a crosslinked polymer (**CROSSLINKED IPDI-DETA**) that formed a second, more internal shell. This double wall was intended to better retain the hydrophobic drug and prevent premature drug leakage.

During the nanoencapsulation process, and before the final crosslinking, the components that formed the shell self-assembled and self-organized according to the hydrophobic gradient created from the center of the sphere to the exterior. Thus, the hydrophobic drugs (purple dots) and the hydrocarbon side chains of Genamin TAP 100D (brown bonds) spontaneously pointed to the interior whereas the hydrophilic and potentially charged groups derived from YMER N-120 (green groups), Jeffcat DPA (blue groups) and L-lysine sodium salt (pink groups) oriented outwards. **Figure 23** schematically shows the relative position of these moieties in the core/shell.

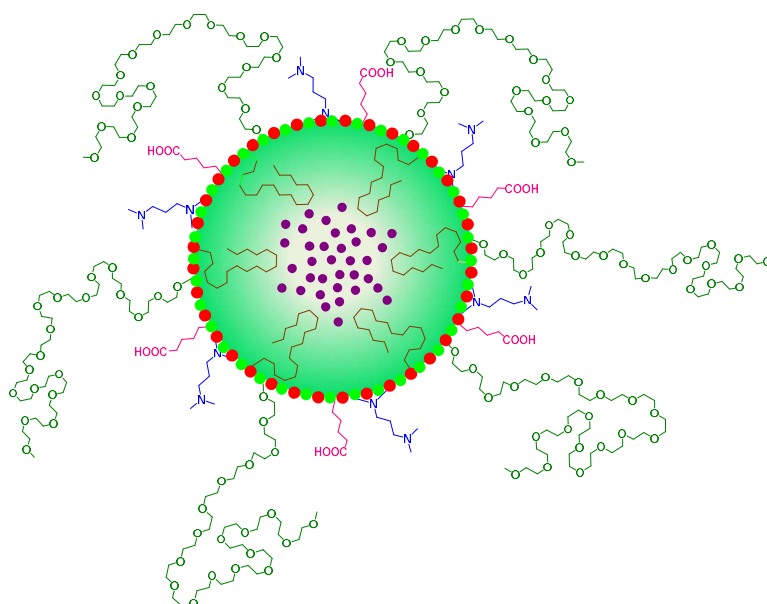


**Figure 23.** Nanocapsule morphology

The nanoencapsulation process was monitored by IR spectroscopy (**Figure 24**) and the final crosslinking step was also tracked by pH measurements (**Figure 25**).

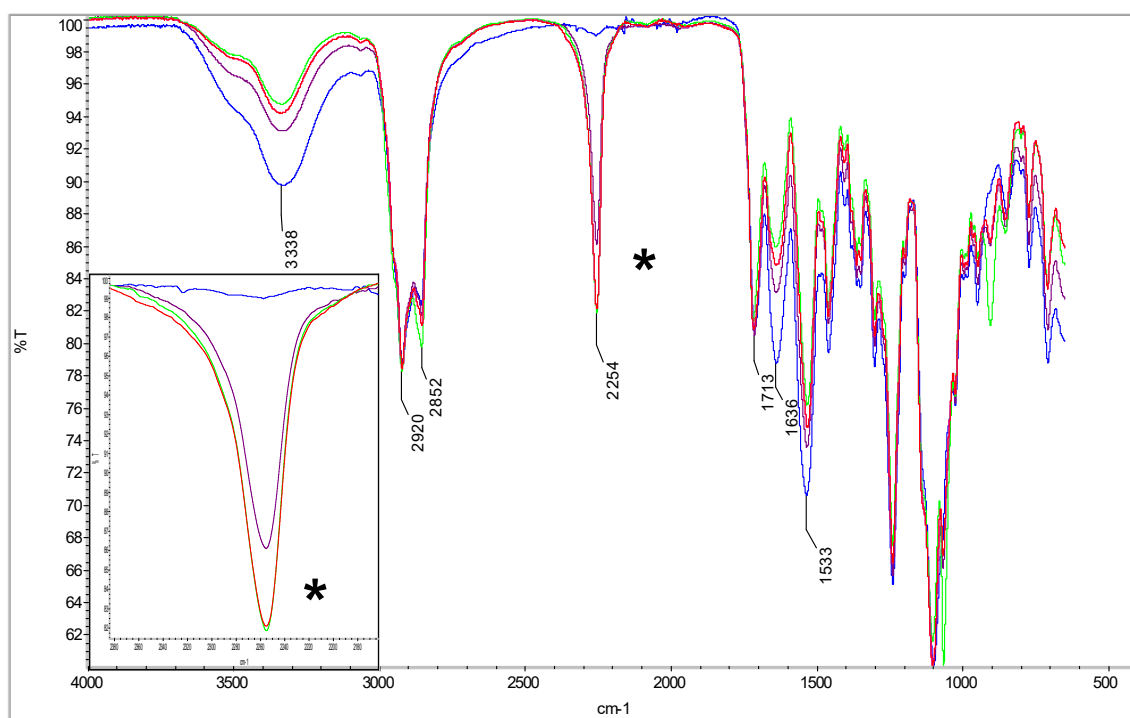


**Figure 24.** IR spectra of three steps of the nanoencapsulation process

The light green line in the IR spectra represents the sample when **P1**, together with the drug, was mixed with IPDI and the red line shows the reaction after 30 min. In this step, the intensity of the NCO stretching band at  $2254\text{ cm}^{-1}$  decreased slightly while the band at  $1636\text{ cm}^{-1}$  and  $1533\text{ cm}^{-1}$  increased, confirming the formation of urea bonds caused by the reactivation of aminic **P1** with IPDI. Afterwards, L-lysine sodium salt was added (purple line) and reacted with the activated **P1**. The sample was analyzed after 45 min and another decrease on the intensity of the NCO stretching band was observed, concomitantly with an increase of the carbonyl and CN stretching bands, confirming urea formation ( $1636\text{ cm}^{-1}$  and  $1533\text{ cm}^{-1}$  respectively). Finally, DETA was added (blue line) and another sample was recorded after 5 min. The NCO stretching band instantaneously disappeared and the urea-associated bands increased their intensity as a result of the rapid reaction between remaining NCO groups and this polyamine.

The monitoring of DETA reaction was performed by periodically measuring the pH of the emulsion, as shown in **Figure 25**.

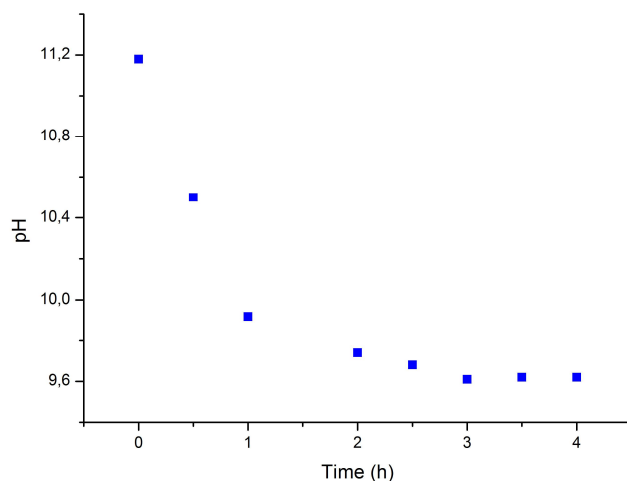


**Figure 25.** Monitorization of the pH of the emulsion after DETA addition

A high pH value was observed upon the addition of the polyamine but steadily decreased as it was consumed to reach a plateau. Once the reaction had finished, the solvent was evaporated under vacuum and the excess of amine was neutralized with HCl to pH 7. When the reaction was finished, it was dialyzed against Milli-Q water for 24 h for further physicochemical characterization.

Noteworthy, the dialysis is the process by which small solutes diffuse from a high concentration solution to a low concentration solution across a semipermeable membrane until the osmotic gradient is in equilibrium (**Figure 26**)<sup>155</sup>.

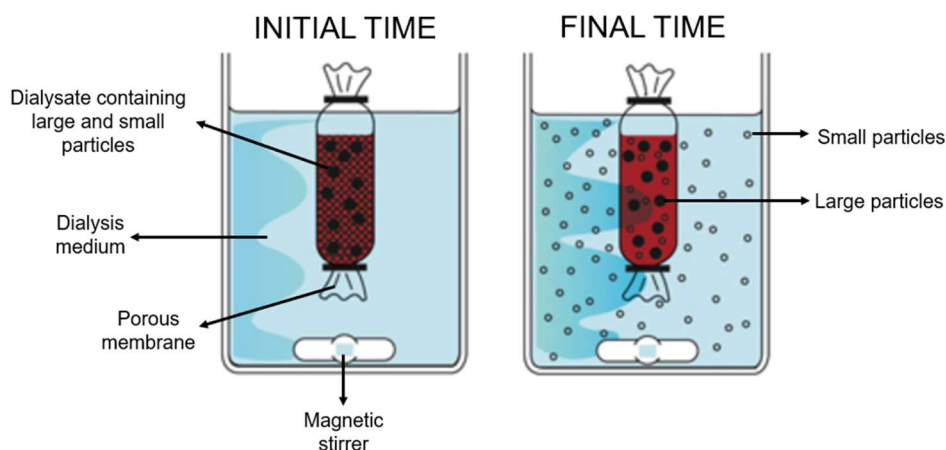


**Figure 26.** Dialysis process using a semipermeable membrane. Adapted from reference 155.

According to the figure, at the initial conditions, the porous membrane contains the product, which consists of large (NCs) and small particles (salts, non-reacted monomers, drugs...). It is stirred for a given period of time in the desired medium (buffer, water...) and during this process the smaller solutes are allowed to migrate to the external medium while the larger species are retained. Therefore, the dialysis can be considered as a separation method based on size rejection. The size is selected depending on the molecular weight of the nanosystems to be purified.

### 3.3.2. Characterization of the NCs

The techniques used to evaluate the properties of the NCs were Transmission Electron Microscopy (TEM), Atomic Force Microscopy (AFM), Dynamic Light Scattering (DLSL,  $\zeta$ -potential ( $\zeta$ -pot), UV/Vis spectroscopy and FRET. Both TEM and AFM provided information about the morphology of the NCs and DLS allowed the study of the particle size distribution.  $\zeta$ -pot measurements were performed to analyze the surface charge of the NCs under different pH conditions. UV/Vis spectroscopy gave information about the encapsulation efficiency and drug loading and finally, FRET studies revealed the release kinetics of the NCs under different environments.

### 3.3.2.1. Morphology and size

The NCs were firstly characterized by TEM (**Figure 27**) and AFM (**Figure 28**) to study their morphology.

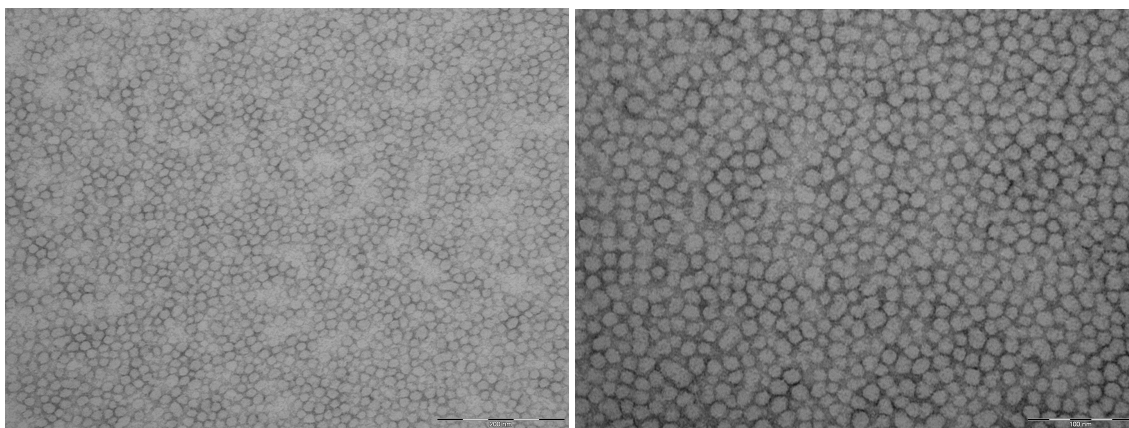


**Figure 27.** TEM micrographs of PTX-AMP NCs. Scale bars: left = 200 nm; right = 100 nm

TEM micrographs showed the presence of roughly round NCs and a homogeneous size distribution.

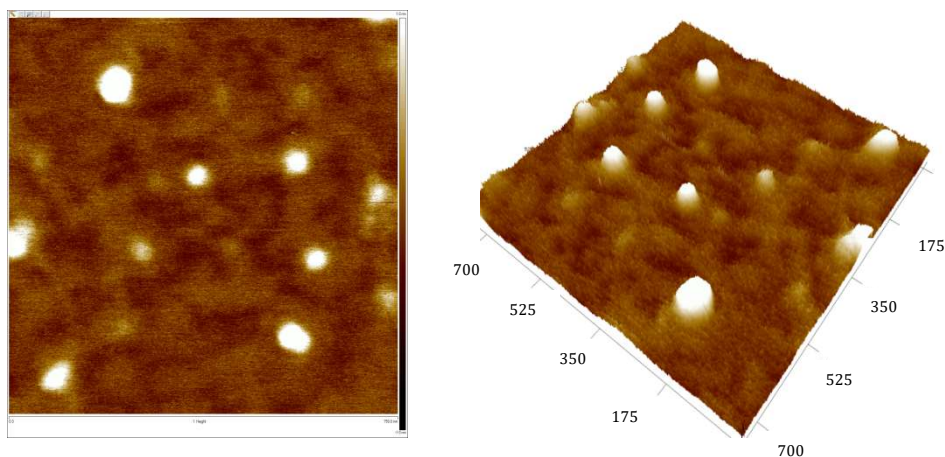
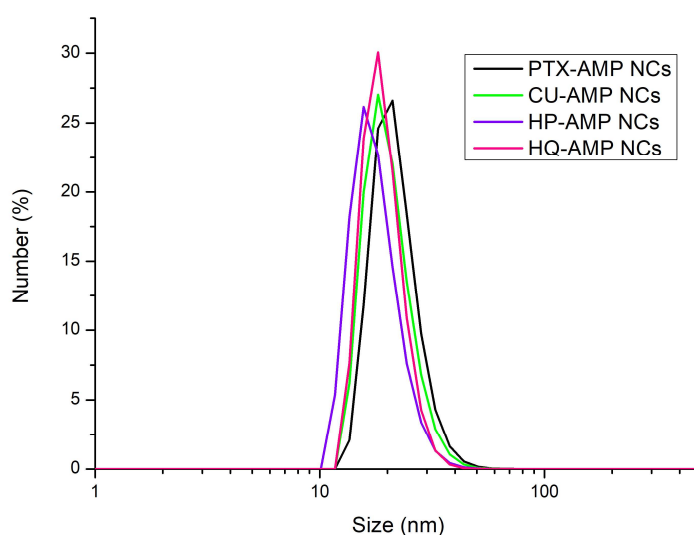


**Figure 28.** AFM micrographs of PTX-AMP NCs in 2D and 3D modes. Scale bar (left) = 750 nm

The AFM analyses corroborated that the NCs presented a roughly round shape. The other versions of NCs exhibited similar morphological properties because they share almost the same composition in terms of hydrophilicity/hydrophobicity.

According to the hydrophobic effect explained previously, the droplet size is dictated by the surfactant type and concentration in the emulsion. Since **P1**, **P2** and **P3** have almost the same amphiphilic properties and are added in approximately the same amount in the emulsion, the resulting NCs present very similar particle sizes and roughly spherical morphologies.

The NCs were analyzed by DLS to determine the influence of the polymer type and the shell decoration on the average particle size distribution. **Figure 29** shows the size distributions for the NCs prepared in this Chapter, the average diameter ( $\emptyset$ ), the standard deviation (SD) and the polydispersity index (PDI).



Sample code	Mean $\emptyset$ (nm)	SD (nm)	PDI
<b>PTX-AMP NCs</b>	23.25	4.96	0.04
<b>CU-AMP NCs</b>	20.08	5.03	0.05
<b>HP-AMP NCs</b>	20.08	4.15	0.05
<b>HQ-AMP NCs</b>	17.33	4.07	0.05
<b>Unloaded-AMP NCs</b>	12.92	2.56	0.03
<b>DiO-AMP NCs</b>	12.65	3.21	0.04
<b>DiI-AMP NCs</b>	13.54	1.71	0.01
<b>PTX-CAT NCs</b>	21.18	3.97	0.04
<b>PTX-AN NCs</b>	17.39	5.50	0.06
<b>NL-PTX-AMP NCs</b>	24.36	3.72	0.02

<b>NL-DiO-AMP NCs</b>	16.62	2.67	0.02
<b>NL-DiI-AMP NCs</b>	13.31	3.66	0.05

**Figure 29.** Particle size distributions and statistical analysis of different types of NCs

DLS measurements of the NCs show monodispersity with an average size between 12.65 nm and 23.35 nm, with low SD and PDI values. The lowest diameters measured refer to those nanosystems containing no core molecule (**unloaded-AMP NCs**) or a small hydrophobic cargo concentration, below 2 % wt (**DiO-AMP NCs, DiI-AMP NCs, NL-DiO-AMP NCs** and **NL-DiI-AMP NCs**), which can be also related to the hydrophobic effect. For those systems having approximately the same amphiphile amount but low concentration of encapsulating molecules, the droplet size decreases because the system is more emulsified. Therefore, the NCs containing no core or fluorophores, have slightly lower diameters. In addition, the obtained SD and PDI values can be associated with a small variation between the measurements and can indicate monodispersity with a narrow size distribution, respectively.

### 3.3.2.2. *Surface properties*

One of the aims of the present Chapter was to develop a nanocarrier with microenvironment-targeting abilities independent from ligands (peptides, protein fractions, antibodies...), which present invariable properties. In this regard, the ideal targeting molecule should be able to adapt to external conditions, being stealth in blood and highly permeating in the tumor microenvironment. One of the possible approaches to achieve an on-demand targeting without ligands is the response of the surface charge to the external conditions. According to previous reports,<sup>44,88,91,156</sup> neutral to slightly anionic NCs have longer blood life-times and a lower mononuclear phagocyte system uptake than their positively charged analogs. In contrast, cationic NCs have been described to bind the negatively charged groups on the cell surface (sialic acid, phospholipids...) via electrostatic interactions, causing translocation across the cell membrane and high levels of cell penetration.<sup>157-160</sup> Therefore, the nanosystems were designed to have dynamic amphoteric properties, being anionic or neutral at physiological conditions (pH = 7.4) and cationic at the typical tumor pH (pH = 5.8–6.9).<sup>161</sup> The tumor

microenvironment presents differential pH characteristics as a result of a high glycolysis rate under both aerobic and anaerobic conditions, poor lymphatic drainage, high interstitial pressure and inadequate blood supply near the tumor tissues.<sup>51,161</sup> Therefore, this pH shift between physiological conditions and the tumor microenvironment can be the basis for the design of the amphoteric properties of the nanosystem.

According to this approach, the requirements for the shell cationization in such a narrow pH range are highly dependent on the acid/base properties of the monomers involved. To achieve this behavior, the shell should be amphiprotic, which means that it should act either as an acid or a base depending on the medium. On one hand, in physiological conditions, the NCs should behave as an acid, since they should donate all their protons to become globally neutral or anionic. On the other hand, in more acidic conditions (the tumor microenvironment) the NCs should accept protons to turn into cationic entities. To this end, a thorough research was performed to select potential monomers prone to accept and donate protons in a pH range between 6.5 (an intermediate value between 5.8 and 6.9) and 7.4. Besides the presence of acid and basic moieties, the monomer should also present nucleophilic groups (alcohols or amines) to be able to polymerize with IPDI. Two building blocks considered are shown in **Figure 30**.

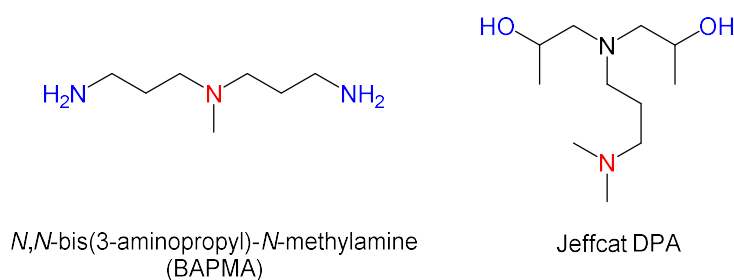


**Figure 30.** Chemical structures of two candidates

The monomers shown in the figure contain amine groups (marked in red) that can protonate/deprotonate in the pH range of interest<sup>162</sup> and all of them present nucleophilic groups (marked in blue) to allow polymerization with isocyanates. BAPMA and Jeffcat DPA present only two reactive sites and therefore are suitable for their incorporation into the polymer chain through lineal polymerization. The NCs having BAPMA in the shell were evaluated by  $\zeta$ -pot measurements in a pH range

of 5.5–8.0 and the results showed that the NCs were invariably anionic in the pH range studied and that the expected change on the surface charge did not occur (section 4 of the Annexes). This could be explained by the fact that BAPMA could not accept any proton at these specific conditions and the anionicity observed was due to the carboxylate group of L-lysine sodium salt present on the polymer shell.

Another trial was performed by using Jeffcat DPA in the synthesis of **P1** and their  $\zeta$ -pot was also studied at the same pH conditions. The results are shown in **Figure 31**.

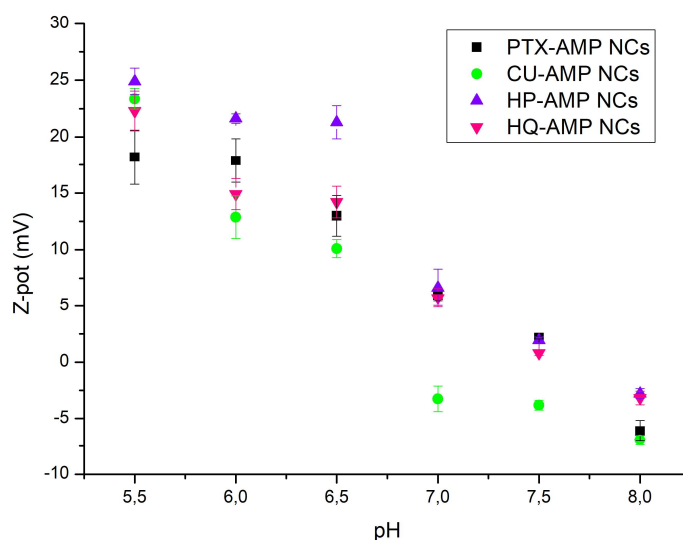


**Figure 31.**  $\zeta$ -pot of four types of amphoteric NCs at different pH conditions

According to the  $\zeta$ -pot analyses, the four types of the NCs tended to become cationic when the pH of the medium decreased while they presented neutral to anionic properties at physiological conditions. From the chemical point of view, these observations could be explained by the selective protonation of Jeffcat DPA and its synchronized effect with L-lysine sodium salt (**Figure 32**).

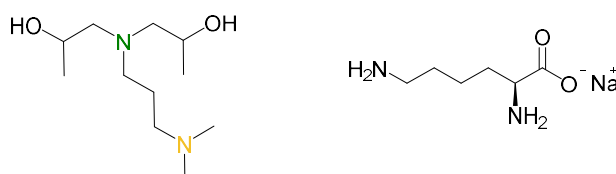


**Figure 32.** Chemical structures of Jeffcat DPA and L-lysine sodium salt

On one hand, Jeffcat DPA contains a tertiary amine with a  $pK_a$  value of 7.2<sup>162</sup> (in orange), which modulates the surface charge at the pH range studied. The other amino group (marked in green), presents a  $pK_a$  value of 9.7<sup>162</sup> and thus is protonated at the pH interval of interest (5.5–8.0). On the other hand, L-lysine, which is added as a sodium salt to stabilize the emulsion during the nanoencapsulation process, provides anionicity due to its carboxylate group. On the overall, this negative charge can form a zwitterion with the most basic tertiary amine of Jeffcat DPA, which is protonated (green), and become a neutral internal salt. Then, the second amine (orange) would modulate the global surface charge because it would selectively accept and donate a proton at a  $pH \sim 7.2$ . This Jeffcat DPA/L-lysine synchronized effect is described in **Figure 33**.

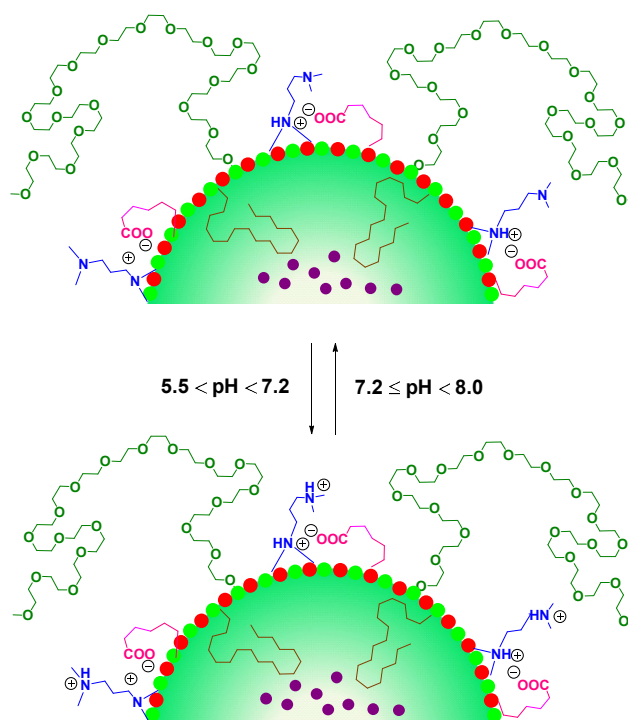


**Figure 33.** Representation of the protonation state of the NC under each condition

According to this figure, when the pH of the medium is between 7.2 and 8, the predominant species is neutral, since one of the tertiary amines is neutralized with the carboxylate group, while the other one is uncharged. However, when the pH becomes more acidic, with values between 5.5 and 7.2, the main species is cationic, given that the second amine accepts a proton, promoting a switch from neutral to positively charged nanosystems.

In order to further confirm that a synchronized effect existed between Jeffcat DPA and L-lysine sodium salt, control NCs were prepared by using only one of the amphoteric pair and their  $\zeta$ -pot was evaluated again. In this regard, **PTX-CAT NCs** were generated by skipping the chain extension step (addition of L-lysine sodium salt) and **PTX-AN NCs** were prepared by removing Jeffcat DPA from the polymerization reaction (**P2**). The NCs were loaded with PTX as a reference drug, were dialyzed and characterized. The results of the  $\zeta$ -pot measurements are shown in **Figure 34**.

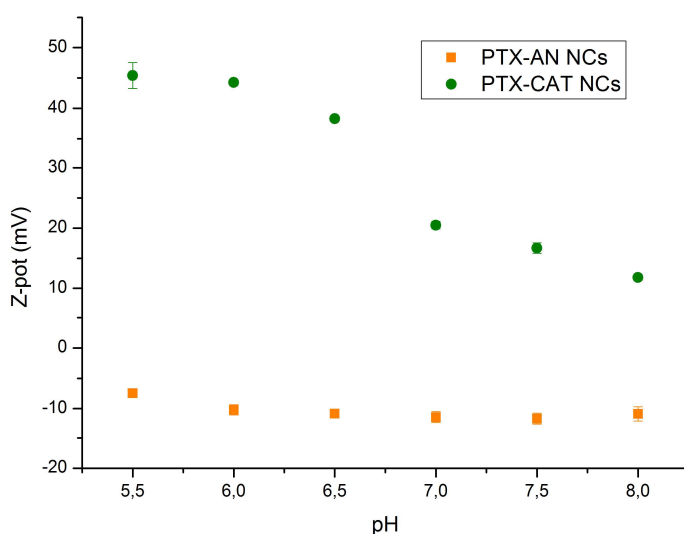


**Figure 34.**  $\zeta$ -pot of **PTX-AN NCs** and **PTX-CAT NCs** at different pH conditions

In this case, regardless the pH, **PTX-AN NCs** presented an invariable anionic surface, while **PTX-CAT NCs** exhibited cationic properties in the entire pH interval studied. In the latter case, an abrupt change on the  $\zeta$ -pot state of the NC could be observed probably due to the protonation of the second amine. The acid/base equilibrium of these NCs in the pH range established is described in **Figure 35**.

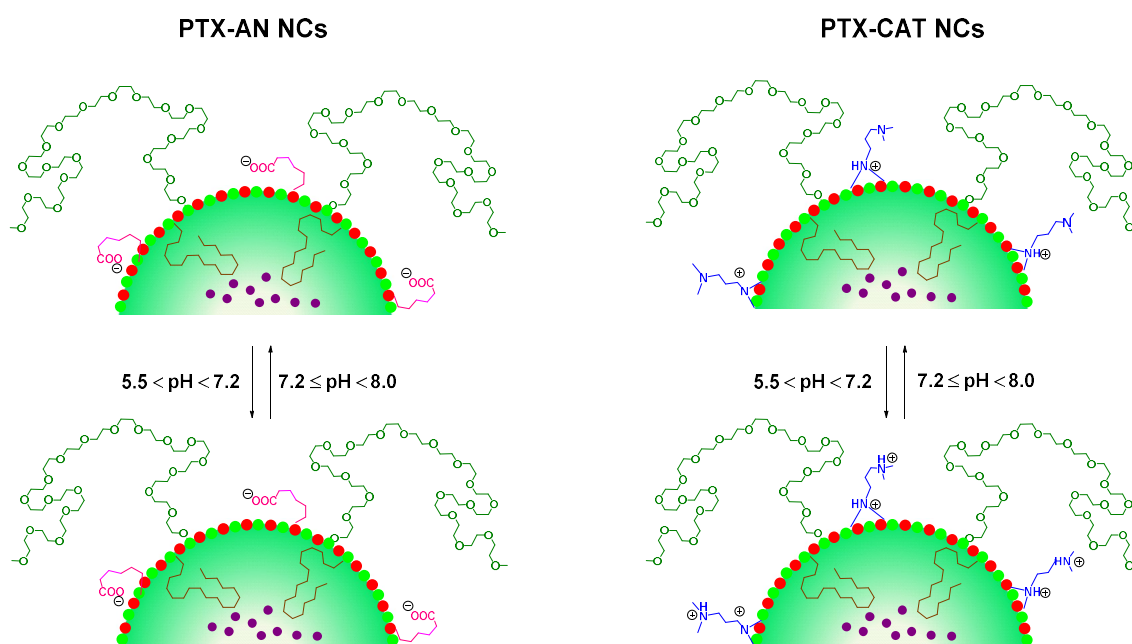


**Figure 35.** Protonation state of **PTX-AN NCs** and **PTX-CAT NCs** in the pH conditions studied

According to the figure, the predominant species in **PTX-AN NCs** is anionic in the pH range 5.5–8, since the carboxylate groups usually protonate at lower pH values. In contrast, the main species of **PTX-CAT NCs** is cationic, since one of the amines is protonated at the whole pH range, but when the medium reaches pH values between 5.5 and 7.2, the second amine accepts a proton and the whole system becomes doubly cationic.

Finally, the rest of the NCs shown in **Table 3** were also characterized by  $\zeta$ -pot measurements and led to similar protonation patterns as in **Figure 31** and thus are not included here.

### 3.3.2.3. Encapsulation efficiency and drug loading

As it has been seen throughout this Chapter, the design of the polymer dictates the properties of the resulting nanocarriers, also in terms of encapsulation ability. In this regard, an amphiphilic polymer with a well-balanced composition is advantageous because the cargo can be incorporated inside the NC without any emulsifier that would decrease the drug concentration and could induce toxicity. In this sense, a well-known example of a surfactant causing serious health issues is Cremphor EL (**Figure 36**), which has been commonly used in the formulation of hydrophobic drugs such as PTX.

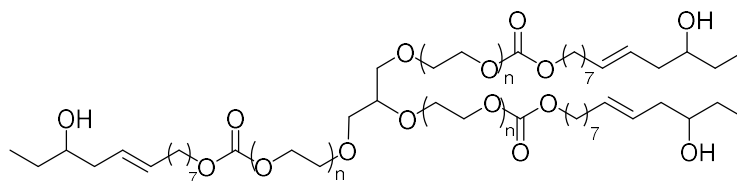


**Figure 36.** Chemical structure of Cremophor EL

This molecule helps the solubilization of poorly soluble drugs, but has been reported to cause severe anaphylactoid hypersensitivity reactions, hyperlipidaemia, abnormal lipoprotein patterns, aggregation of erythrocytes and peripheral neuropathy, among other effects.<sup>109,163,164</sup>

As a consequence, if surfactants are avoided, the derived toxicological issues can be prevented and the encapsulation efficiency (EE) and the drug loading (DL) can be enhanced.

In the present case, the parameters EE and DL, shown in **Table 4**, were determined for the 4 nanoencapsulated hydrophobic drugs using the formulae described in section 2.11 of Chapter 5.

**Table 4.** EE and DL values (and their standard deviations) for drug-loaded amphoteric NCs

Sample code	EE (% wt)	DL (% wt)
PTX-AMP NCs	87.84 ± 4.20	13.19 ± 0.63
CU-AMP NCs	79.12 ± 4.00	11.88 ± 0.06
HP-AMP NCs	96.97 ± 0.83	9.71 ± 0.05
HQ-AMP NCs	85.21 ± 5.47	11.76 ± 0.05

The EE and the DL were higher for all the cases analyzed than other common amphiphilic nanosystems. For instance, Song *et al.*<sup>48</sup> reported PLGA NPs loading vincristine sulfate and quercetin with DL values of only 0.0037% and 1.36%, respectively. Another example was described by Hu *et al.*,<sup>165</sup> who developed multifunctional NCs made of poly(styrene allyl alcohol) encapsulating doxorubicin, leading to an EE of 20–53%. Finally, Graf *et al.*<sup>92</sup> reported PLGA-PEG NPs loading cisplatin and showing a DL of 1% and an EE of 3%.

In all the cases of the present study, the EE was higher than 75%, which directly meant that most of the drug was incorporated inside the NC and a very low amount was discarded. This turned out to be advantageous in the scale-up of nanosystems because when the drug is not efficiently introduced into the nanocarrier, part of the cargo is wasted, more purification steps are required and the whole process becomes costlier and less environmentally friendly. In fact, this issue is also found in liposomal formulations, because even though they are considered as one of the most biocompatible materials, their leaky walls result into low entrapments and systemic toxicities due to premature drug migrations *in vivo*.<sup>100,156,166</sup>

Likewise, a high DL is equally important since it reduces the excessive use of carrier material and the risk to induce systemic toxicity. This is particularly important for those carriers that regardless being biocompatible, their accumulation in excretion organs is a serious issue.<sup>55</sup>

#### 3.3.2.4. NC degradation and release

Besides size, morphology, surface properties, encapsulation efficiency and drug loading, shell biodegradability and specific cargo release are other essential aspects of a DDS. To this aim, the polymer forming the NC wall was decorated with disulfide bonds introduced via the monomer DEDS. This kind of bonds can be selectively cleaved by reductive enzymes and peptides overexpressed in the cytosolic environment of tumor cells, such as reduced GSH. This reduced tripeptide was chosen as a reference molecule in the degradation experiments.

The *in vitro* degradation of the NCs was assessed by TEM, DLS and FRET in a time-course mode. The first two techniques were useful to provide information about changes on the morphology, the size and aggregation state of the NCs, while the last one was used to elucidate the release dynamics of the cargo under different conditions. TEM and DLS measurements were carried out in parallel. The first sample was performed as a control of a prefiltered (0.22  $\mu\text{m}$ ) untreated emulsion of NCs and subsequent aliquots were withdrawn after 24, 48, 72 and 96 h of incubation with 10 mM of GSH at 37 °C. In order to prove that the size alterations were exclusively due to the presence of the enzyme, an extra study was carried out by

incubating another sample of NCs under the same conditions but in the absence of GSH and the size was measured at the same time periods (**Figure 37**).

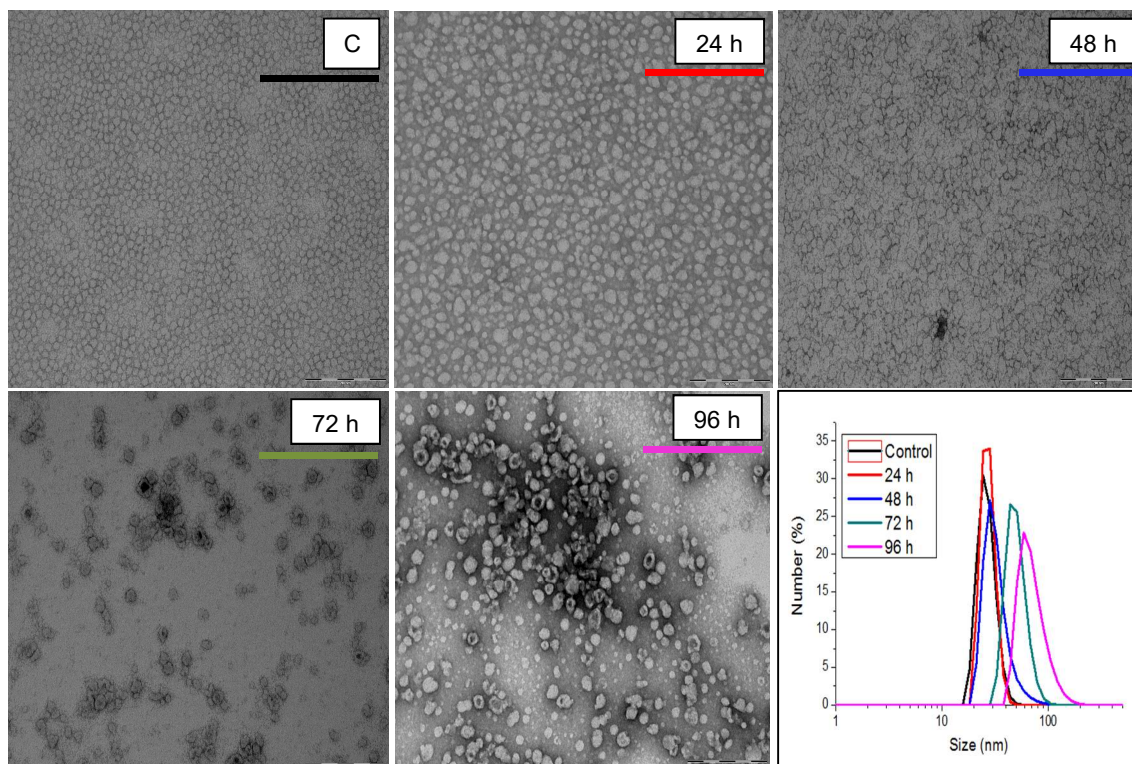


**Figure 37.** Study of the biodegradation of the NCs by TEM and DLS. Scale bars = 200 nm

TEM micrographs showed that after 24 h of the addition of the enzyme the NCs started losing their homogeneity and began to form larger entities. At 48 h, the sample became more heterogeneous and the NCs lost their initial roughly round shape, leading to a non-structured polymer material. At 72 h, the unstructured shells started self-organizing into aggregates, some of them exhibiting holes that indicated extensive degradation. The last sample studied showed more accentuated physical alterations and the aggregates evolved to a larger size.

In addition, a parallel study was carried out by DLS by incubating at 37 °C the NCs under a reductive environment (GSH 10mM) and under control conditions (PBS pH 7.4) and the average particle size was monitored at the start of the assay and after 24, 48, 72 and 96 h. **Figure 38** shows the evolution of the NCs size over time.

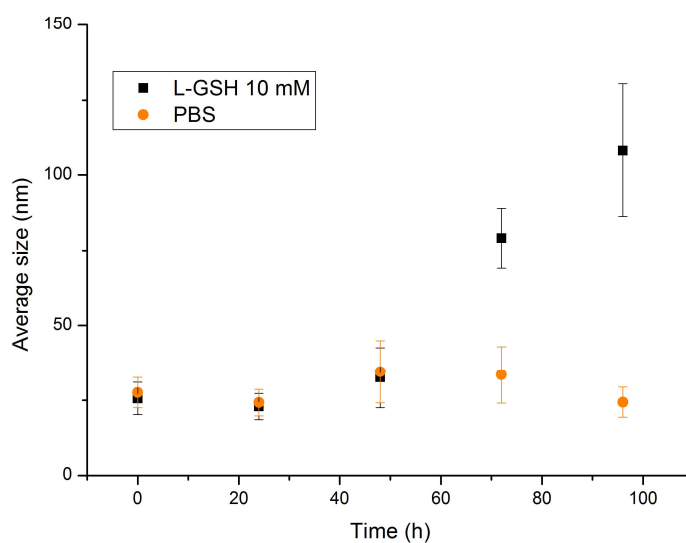


**Figure 38.** Average particle size of the NCs incubated with GSH 10 mM and in PBS (control)

According to the image, the assay confirmed that the aggregation of the sample was a direct consequence of the action of GSH, since the same nanoemulsion incubated in physiological conditions did not show significant size variations.

In order to confirm these results and study the release dynamics of hydrophobic molecules from the NCs, time-course FRET experiments were carried out. FRET is a technique of particular interest due to its intrinsic sensitivity to small variations in molecular distance and orientation between two fluorescent molecules, a donor and an acceptor.<sup>167,168</sup> To this end, two different lipophilic fluorescent tags, DiO and DiI, shown in **Figure 39** were nanoencapsulated to yield **DiO-AMP NCs** and **DiI-AMP NCs**.

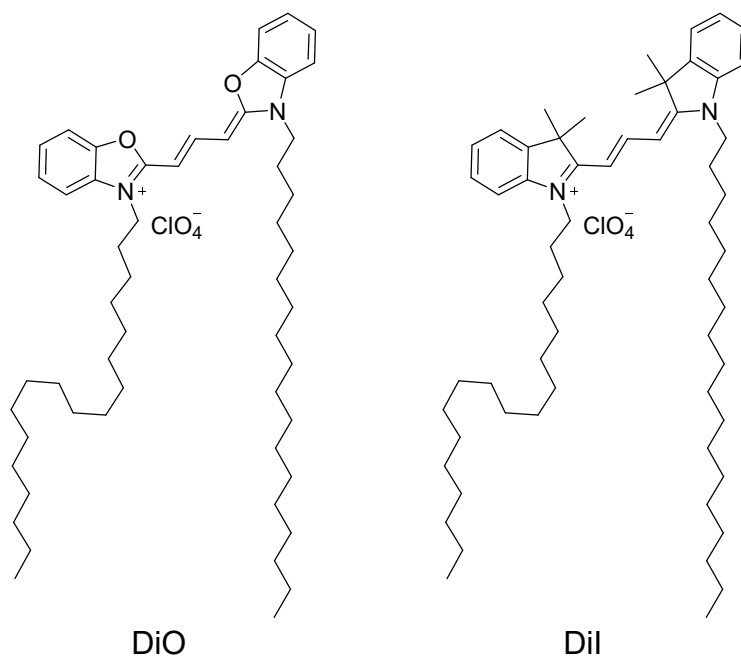


**Figure 39.** Chemical structures of DiO and DiI fluorophores

After their physicochemical characterization, the leakage of these dyes from the NCs was analyzed under four different conditions: PBS (control), BSA- and HSA-rich environments and a reductive medium containing 10 mM of GSH.

**DiO-AMP NCs** and **DiI-AMP NCs** were mixed in the cuvette and the fluorescence was recorded at 37 °C under constant stirring by exciting the sample at 484 nm and measuring the emission from 498 nm to 650 nm. The FRET ratio was calculated as  $I_a/(I_a+I_d)$ ,  $I_a$  being the maximum intensity of the acceptor (DiI) and  $I_d$  the maximum intensity of the donor (DiO). The first measurements were performed in PBS as a control experiment and then two other assays were carried out using BSA and HSA, respectively, to mimic blood plasma conditions. These two proteins were selected due to their high abundance in plasma and their exceptional binding capabilities. They can bind steroid hormones, thyroxine, tryptophan, several vitamins, metal ions and drugs, among others, facilitating their transportation around the body or delivery to disposal sites.<sup>169</sup> In fact, it has been reported that amphiphilic molecules, such as proteins like albumins, can negatively affect the nanostructuration of a system, by disrupting hydrophobic stratifications and compromising the nanocarrier integrity *in vitro* and *in vivo*.<sup>101,102</sup> It was deemed interesting to study the potential release of the dyes out of the NCs as a possible consequence of the interaction between these kind of proteins and the nanocarriers. Under these

conditions (PBS, BSA and HSA), the measurements were continuously performed every 30 min for the first 2 h, then every hour until 10 h of experiment and finally the recordings were carried out once a day to the end of the assay. In order to prove that any fluorescence change occurring would be due to the tripeptide, a few spectra were carried out before its addition (up to 2 h). After this time, the measurements were performed every hour with a longer delay between two consecutive days. The fluorescence profiles are shown in **Figure 40**.

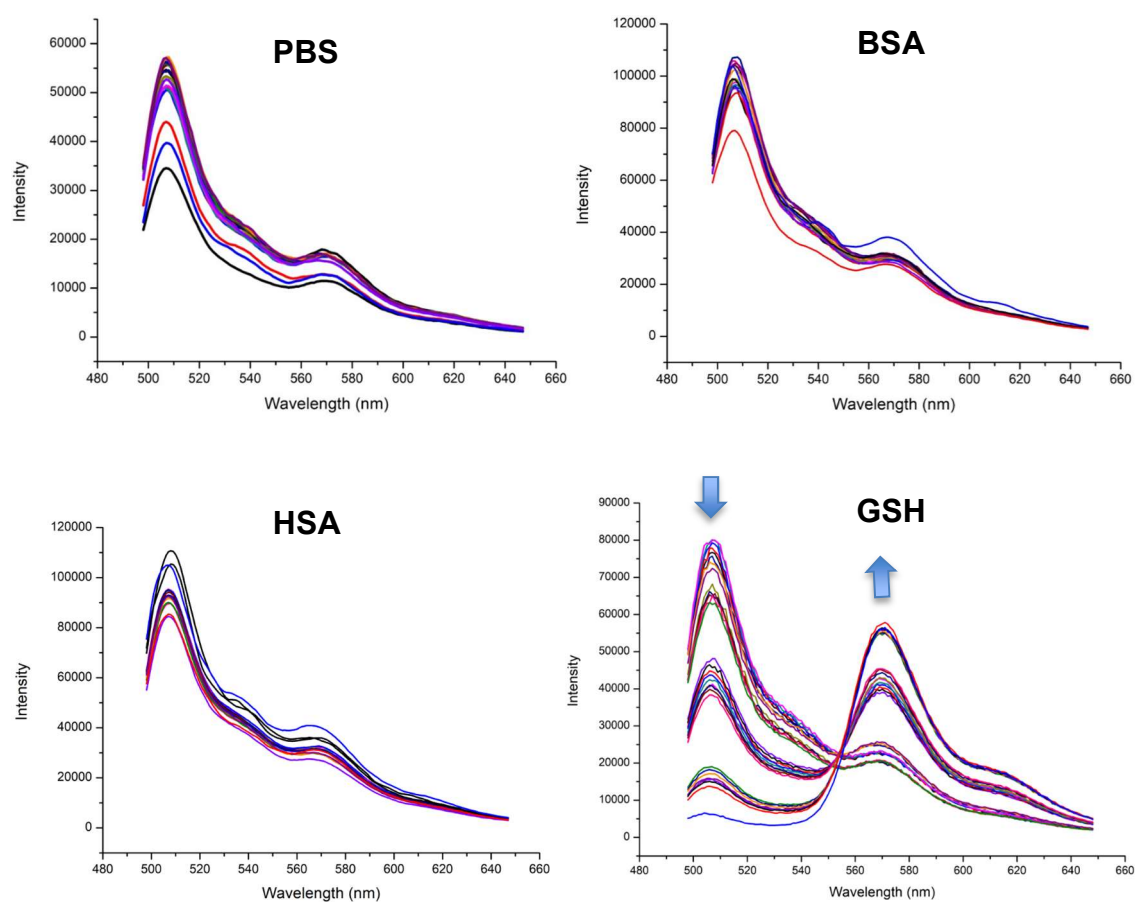


**Figure 40.** Fluorescence spectra of DiO-AMP NCs and DiI-AMP NCs in PBS, BSA, HSA and GSH

According to the first, second and third graphic of the figure, the fluorescence of the sample did not significantly change over the time. Small variations were observed in the emission band at 506 nm (associated with DiO) but they were not accompanied by any increase at 572 nm (corresponding to DiI), ruling out FRET effects. However, in the last graphic, the DiO emission band decreased dramatically whereas the DiI emission band increased, which was a direct consequence of FRET events between the donor fluorophore and the acceptor.

After recording the fluorescence spectra for all the conditions tested, the FRET ratio was calculated over time and resulted into **Figure 41**.

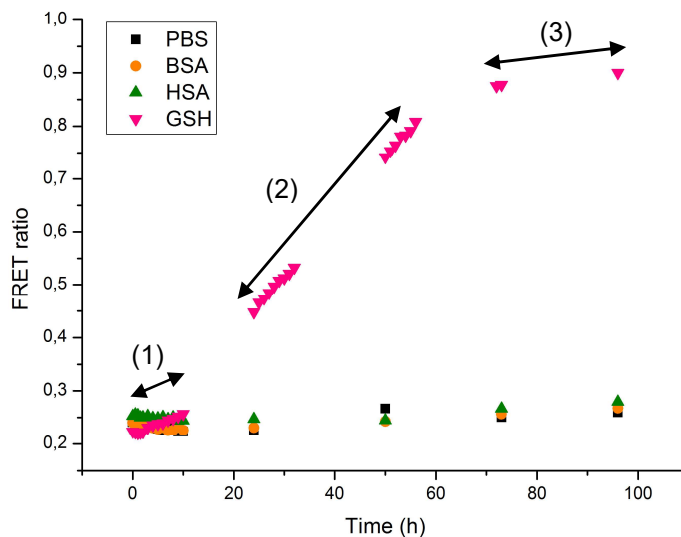


**Figure 41.** FRET ratio of the NCs over time for different conditions

According to the figure, two different profiles could be observed. For the experiments carried out in PBS, BSA and HSA, the FRET ratio was low and almost constant. However, FRET ratio increased following three different tendencies for the reductive medium. These results are analyzed deeper in **Figure 42**.

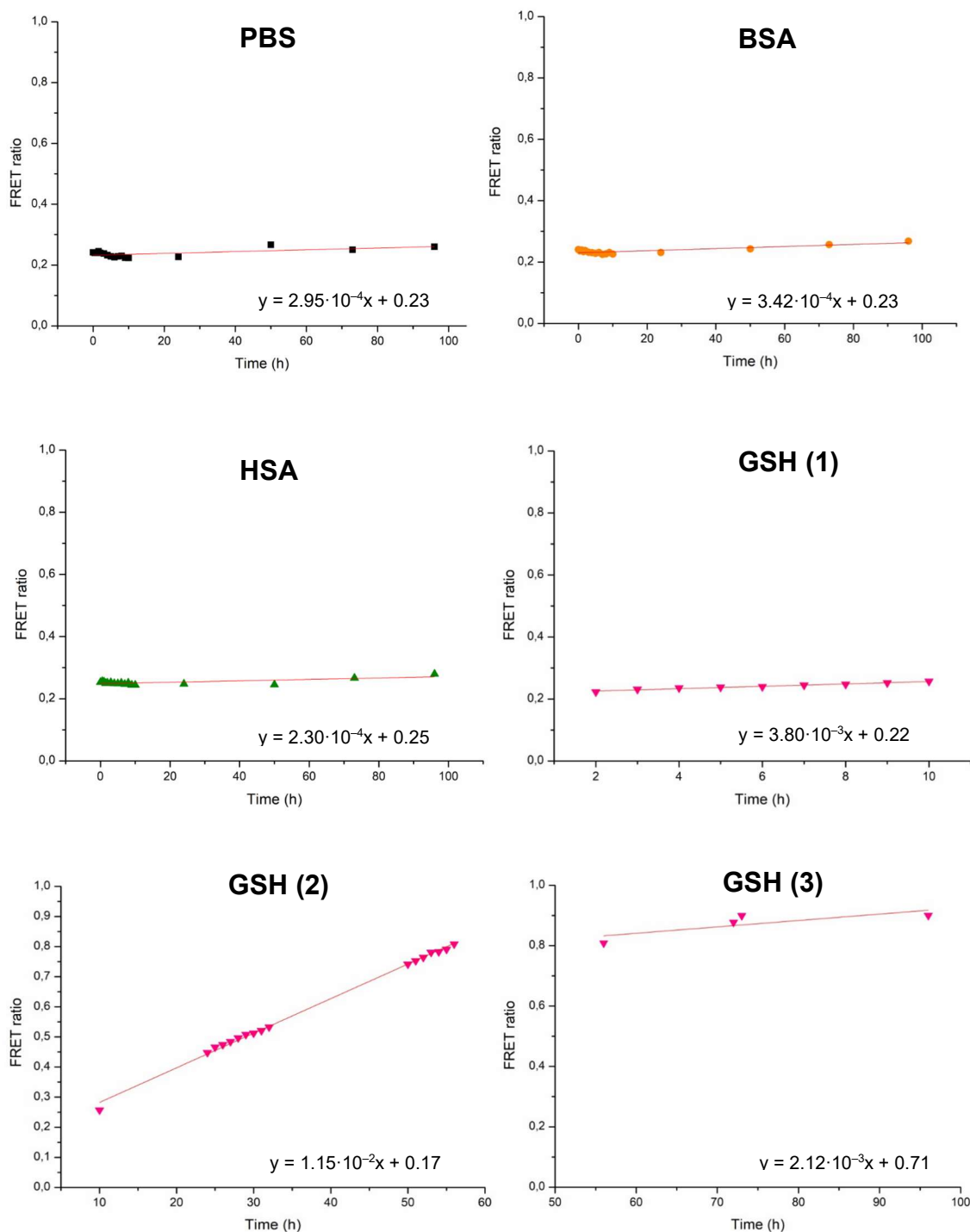


**Figure 42.** FRET ratios under different conditions: PBS, BSA, HAS and GSH

The slopes calculated for control conditions (PBS) and BSA- and HSA-rich solutions were very low ( $2.95 \cdot 10^{-4} \text{ h}^{-1}$ ,  $3.42 \cdot 10^{-4} \text{ h}^{-1}$  and  $2.30 \cdot 10^{-4} \text{ h}^{-1}$ , respectively) and almost invariable during the whole experiment. This meant that no significant release of the tracers occurred under these conditions. However, for the reductive medium, three different profiles could be identified. The release kinetics started

with a slope of  $3.80 \cdot 10^{-3} \text{ h}^{-1}$  and became more accentuated after GSH addition, reaching a value of  $1.15 \cdot 10^{-2} \text{ h}^{-1}$ . Finally, the degradation profile reached a plateau with a slope of  $2.12 \cdot 10^{-3} \text{ h}^{-1}$ , indicating that the cargo had been virtually released. With these results, it can be stated that the NCs specifically releases their content in a reductive medium based on GSH 10 mM and that their crosslinked shell was robust enough to remain stable and retain the encapsulated molecules in buffered or protein-rich environments. These results were expected, since it is known that polyurethane and polyurea bonds are very stable against degradation,<sup>4,7,34</sup> especially if they are forming a crosslinked network.

Another FRET experiment was carried out to support that GSH was only cleaving disulfide bridges and not urethane or urea bonds. In this case, the non-labile cationic amphiphilic polymer (**P3**) was synthesized and was used to nanoencapsulate the lipophilic dyes yielding non-labile versions of the NCs (**NL-DiO-AMP NCs** and **NL-DiI-AMP NCs**). The difference between **P3** and **P1** was basically the replacement of DEDS for an equivalent molecule lacking disulfide bonds: 1,6-hexanediol. The assay was repeated following the same procedure as for the reductive medium and the results are shown in **Figure 43**.

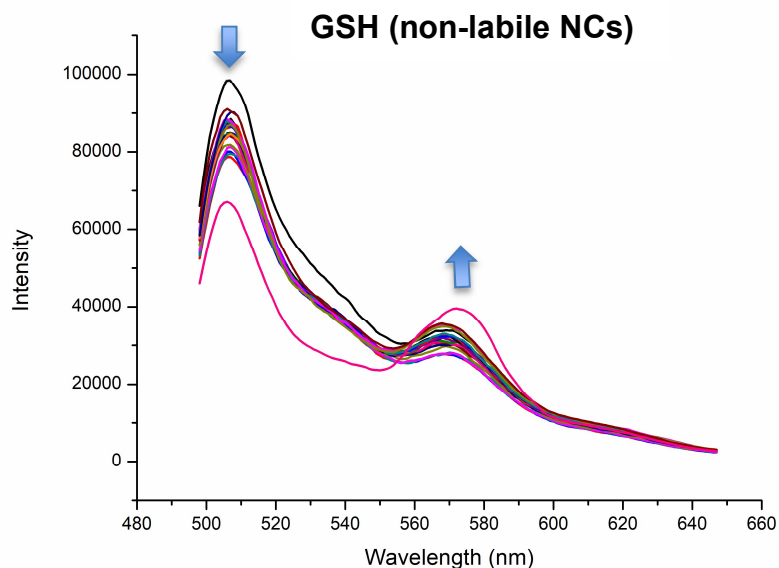


**Figure 43.** Fluorescence spectra of **NL-DiO-AMP NCs** and **NL-DiI-AMP NCs** under GSH conditions

The fluorescence spectra showed only a differentiated change on the intensity in both emission bands after 4 days of assay, as depicted by the pink line. The rest of the profiles were very similar and ruled out any important release of the hydrophobic tracers out of the NCs. Moreover, the FRET ratios were calculated and compared with the ones obtained with the labile NCs under reductive conditions (**Figure 44**).

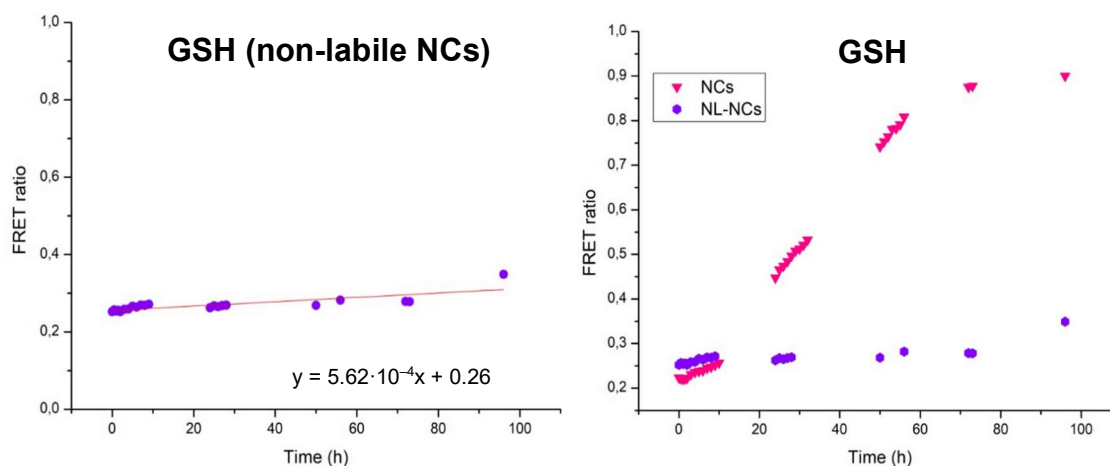


**Figure 44.** FRET ratio over time with redox-labile and non-redox-labile under GSH

The FRET ratio observed with non-labile NCs (purple marker) was almost flat and had a slope of  $5.62 \cdot 10^{-4} \text{ h}^{-1}$ . The profile only increased slightly after 4 days of the start of the assay and was clearly different from pattern marked in pink (redox-labile NCs). In fact, the difference between the two FRET ratios after 24 h is already considerably different, since the value obtained for labile NCs almost doubles the one derived from non-labile analogs. This means that although the complete release is not achieved until 3–4 days, the degradation of the nanosystems starts right when a reductive medium is applied.

#### 4. Conclusions

According to the results obtained, the methodology developed in this Chapter allowed the preparation of multifunctional NCs in almost a straightforward manner. The syntheses of the NCs proceeded with the minimum use of organic solvents and involved few steps. No purification cycles were needed, except for the final dialysis

to remove non-encapsulated drugs, non-reacted monomers or salts generated in the nanoencapsulation step.

The NCs were synthesized from biocompatible polymers, polyurethanes and polyureas. In this scenario, the versatility and reactivity offered by the isocyanate chemistry allowed the successful introduction of multiple functionalities. In this regard, hydrophilic pendant chains, hydrophobic side tails, potentially protonable functional groups, anionic moieties and redox-labile bonds were almost simultaneously incorporated into the polymer chain. All these functionalities were introduced during the polymer synthesis, except for the anionic groups, that were conjugated during the nanoencapsulation step via L-lysine sodium salt.

In addition, the NCs presented a roughly round shape, confirmed by TEM and AFM, and a controlled size below 30 nm, studied by DLS. These properties were observed in all the versions of NCs prepared, regardless the encapsulated cargo and the surface charge. Moreover, the samples showed monomodal particle size distributions, confirming the stability of o/w emulsions.

Regarding the  $\zeta$ -pot measurements, the NCs responded to pH changes as expected, given the Jeffcat DPA/L-lysine sodium salt synchronized effect. Accordingly, the surface charge was neutral at physiological pH and became cationic as the medium became more acidic. These results confirmed the selective protonation of the shell in the range between physiologic and tumor microenvironment pH. Other versions of NCs, lacking one of the amphoteric pairs, presented invariable anionic or cationic properties, depending on the case. This modulation of the surface charge was intended for a smart targeted delivery without targeting ligands.

Finally, as proven by TEM, DLS and FRET, the NCs were selectively degraded under reductive conditions (GSH) and did not show any significant release in aqueous and albumin-rich solutions. This suggests that the nanosystems were stable under physiological conditions and that they only released their content when a reductive molecule such as GSH was present. With these assays, the chemical hydrolytic resistance of polyurethanes and polyureas forming crosslinked systems was confirmed. Moreover, the NCs did not aggregate or coalesce when incubated for a few days, proving their chemical stability and suggesting long shelf-lives.

## 5. Bibliography

- 1 J. W. Boretos and W. S. Pierce, *Science*, 1967, **158**, 1481-1482.
- 2 M. Ding, J. Li, H. Tan and Q. Fu, *Soft Matter*, 2012, **8**, 5414-5428.
- 3 J. L. A. Perales-Alcacio, J. Santa-Olalla Tapia, C. Mojica-Cardoso, R. F. Vargas-Coronado, L. H. Chan-Chan, D. M. Headen, A. J. García, J. M. Cervantes-Uc and J. V. Cauich-Rodríguez, *J. Biomater. Sci., Polym. Ed.*, 2013, **24**, 1601-1617.
- 4 E. Sharmin and F. Zafar, *Polyurethanes*, InTech, 2012.
- 5 B. Fernández-d'Arlas, J. A. Ramos, A. Saralegi, M. Corcuera, I. Mondragon and A. Eceiza, *Macromolecules*, 2012, **45**, 3436-3443.
- 6 G. Morral-Ruíz, P. Melgar-Lesmes, M. L. García, C. Solans and M. J. García-Celma, *Polymer*, 2012, **53**, 6072-6080.
- 7 E. Delebecq, J. P. Pascault, B. Boutevin and F. Ganachaud, *Chem. Rev.*, 2013, **113**, 80-118.
- 8 J. H. Saunders and R. J. Slocombe, *Chem. Rev.*, 1948, **43**, 203-218.
- 9 R. G. Arnold, J. A. Nelson and J. J. Verbanc, *Chem. Rev.*, 1957, **57**, 47-76.
- 10 A. Lowe, *Proc. R. Soc. Med.*, 1970, **63**, 367-368.
- 11 S. Ozaki, *Chem. Rev.*, 1972, **72**, 457-496.
- 12 A. A. Caraculacu and S. Coseri, *Prog. Polym. Sci.*, 2001, **26**, 799-851.
- 13 I. C. Kogon, *J. Am. Chem. Soc.*, 1956, **78**, 4911-4914.
- 14 I. Kogon, *J. Org. Chem*, 1958, **23**, 1594-1594.
- 15 M. Sato, *J. Org. Chem.*, 1962, **27**, 819-825.
- 16 I. Kogon, *J. Org. Chem*, 1961, **26**, 3004-3005.
- 17 H. K. Ono, F. N. Jones and S. P. Pappas, *J. Polym. Sci., Polym. Lett. Ed.*, 1985, **23**, 509-515.
- 18 N. Bialas, H. Höcker, M. Marschner and W. Ritter, *Makromol. Chem.*, 1990, **191**, 1843-1852.
- 19 J. M. Peters, *Proc. roy. Soc. Med.*, 1970, **63**, 372-375.
- 20 C. B. McKerrow, H. J. Davies and A. P. Jones, *Proc. roy. Soc. Med.*, 1970, **63**, 376-378.
- 21 Y. M. Ye, C. W. Kim, H. R. Kim, H. M. Kim, C. H. Suh, D. H. Nahm, H. S. Park, C. A. Redlich and A. V. Wisnewski, *J. Allergy Clin. Immunol.*, 2006, **118**, 885-891.
- 22 A. Goossens, T. Detienne and M. Bruze, *Contact Dermatitis*, 2002, **47**, 304-308.

- 23 M. Szycher, *Szycher's Handbook of Polyurethanes*, CRC Press, Florida, 1999.
- 24 A. N. Papadopoulos, C. A. S. Hill, E. Traboulay and J. R. B. Hague, *Holz Roh-Werkst.*, 2002, **60**, 81-83.
- 25 H. Hamada, Doctoral Thesis, Lund University, 2017.
- 26 N. C. Schaal, W. J. Brazile, K. L. Finnie and J. P. Tiger, *Ann Work Expo Health*, 2017, **61**, 872-882.
- 27 J. H. Saunders, *Rubber Chem. Technol.*, 1959, **32**, 337-345.
- 28 M. E. Rogers and T. E. Long, *Synthetic methods in step-growth polymers*, John Wiley & Sons, New Jersey, 2003.
- 29 A. Lapprand, F. Boisson, F. Delolme, F. Méchin and J. P. Pascault, *Polym. Degrad. Stab.*, 2005, **90**, 363-373.
- 30 E. P. Fuerst, *Weed Technol.*, 1987, **1**, 270-277.
- 31 P. Bolton and J. L. Harwood, *Phytochemistry*, 1976, **15**, 1507-1509.
- 32 E. Dyer, J. F. Glenn and E. G. Lendrat, *J. Org. Chem*, 1961, **26**, 2919-2925.
- 33 D. Kincal and S. Özkar, *J. Appl. Polym. Sci.*, 1997, **66**, 1979-1983.
- 34 M. Ionescu, *Chemistry and Technology of Polyols and Polyurethanes*, Smithers Rapra Press, UK, 2005.
- 35 M. Špírková and K. Dušek, *Polym. Bull.*, 1989, **22**, 191-198.
- 36 K. Schwetlick and R. Noack, *J. Chem. Soc., Perkin Trans. 2*, 1995, **0**, 395-402.
- 37 K. Dusek, M. Spirkova and I. Havlicek, *Macromolecules*, 1990, **23**, 1774-1781.
- 38 G. Kabas and H. C. Rutz, *Tetrahedron*, 1966, **22**, 1219-1226.
- 39 A. J. Bur and L. J. Fetters, *Chem. Rev.*, 1976, **76**, 727-746.
- 40 W. H. Carothers, *Trans. Faraday Soc.*, 1936, **32**, 39-49.
- 41 V. V. Korshak, *Polym. Sci. U.S.S.R.*, 1982, **24**, 1783-1797.
- 42 N. T. Southall, K. A. Dill and A. D. J. Haymet, *J. Phys. Chem. B*, 2002, **106**, 521-533.
- 43 D. Chandler, *Nature*, 2005, **437**, 640-647.
- 44 R. Pignatello, A. Leonardi, R. Pellitteri, C. Carbone, S. Caggia, A. C. E. Graziano and V. Cardile, *Colloids Surf., A*, 2013, **434**, 136-144.
- 45 J. M. Rabanel, J. Faivre, S. F. Tehrani, A. Lalloz, P. Hildgen and X. Banquy, *ACS Appl. Mater. Interfaces*, 2015, **7**, 10374-10385.
- 46 E. S. Lee, Z. Gao and Y. H. Bae, *J. Controlled Release*, 2008, **132**, 164-170.
- 47 M. Martin, H. Wei and T. Lu, *Oncotarget*, 2016, **7**, 52575-52583.

- 48 X. Song, Y. Zhao, S. Hou, F. Xu, R. Zhao, J. He, Z. Cai, Y. Li and Q. Chen, *Eur. J. Pharm. Biopharm.*, 2008, **69**, 445-453.
- 49 C. J. Fee, *Biotechnol. Bioeng.*, 2007, **98**, 725-731.
- 50 J. Wang, W. Mao, L. L. Lock, J. Tang, M. Sui, W. Sun, H. Cui, D. Xu and Y. Shen, *ACS Nano*, 2015, **9**, 7195-7206.
- 51 K. T. Oh, H. Yin, E. S. Lee and Y. H. Bae, *J. Mater. Chem.*, 2007, **17**, 3987-4001.
- 52 M. Adabi, M. Naghibzadeh, M. Adabi, M. A. Zarrinfard, S. S. Esnaashari, A. M. Seifalian, R. Faridi-Majidi, H. Tanimowo Aiyelabegan and H. Ghanbari, *Artif. Cells, Nanomed., Biotechnol.*, 2017, **45**, 833-842.
- 53 M. Foldvari and M. Bagonluri, *Nanomedicine: Nanotechnology, Biology and Medicine*, 2008, **4**, 183-200.
- 54 Y. Yoshioka, K. Higashisaka and Y. Tsutsumi, *Nanomaterials in Pharmacology*, Springer, New York, 2016.
- 55 A. Kunzmann, B. Andersson, T. Thurnherr, H. Krug, A. Scheynius and B. Fadeel, *Biochim. Biophys. Acta, Gen. Subj.*, 2011, **1810**, 361-373.
- 56 W. Yin, S. M. Venkitachalam, E. Jarrett, S. Staggs, N. Leventis, H. Lu and D. A. Rubenstein, *J. Biomed. Mater. Res., Part A*, 2010, **92A**, 1431-1439.
- 57 F. Sabri, J. D. Boughter Jr, D. Gerth, O. Skalli, T. C. N. Phung, G. R. M. Tamula and N. Leventis, *PLoS One*, 2012, **7**, 1-7.
- 58 R. B. Restani, P. I. Morgado, M. P. Ribeiro, I. J. Correia, A. Aguiar-Ricardo and V. D. B. Bonifácio, *Angew. Chem., Int. Ed.*, 2012, **51**, 5162-5165.
- 59 F. Xiang, M. Stuart, J. Vorenkamp, S. Roest, H. Timmer-Bosscha, M. C. Stuart, R. Fokkink and T. Loontjens, *Macromolecules*, 2013, **46**, 4418-4425.
- 60 K. Laumann, U. Boas, H. M. Larsen, P. M. H. Heegaard and A. L. Bergström, *Biomacromolecules*, 2015, **16**, 116-124.
- 61 T. Berthold, C. R. Castro, M. Winter, G. Hoerpel, M. Kurttepli, S. Bals, M. Antonietti and N. Fechner, *ChemNanoMat*, 2017, **3**, 311-318.
- 62 V. A. Sethuraman and Y. H. Bae, *J. Controlled Release*, 2007, **118**, 216-224.
- 63 V. Fievez, L. Plapied, A. des Rieux, V. Pourcelle, H. Freichels, V. Wascotte, M. L. Vanderhaeghen, C. Jérôme, A. Vanderplasschen, J. Marchand-Brynaert, Y. J. Schneider and V. Préat, *Eur. J. Pharm. Biopharm.*, 2009, **73**, 16-24.
- 64 N. M. Sakhrani and H. Padh, *Drug Des., Dev. Ther.*, 2013, **7**, 585-599.

- 65 B. S. Brown, T. Patanam, K. Mobli, C. Celia, P. E. Zage, A. J. Bean and E. Tasciotti, *Cancer Biol. Ther.*, 2014, **15**, 851-861.
- 66 B. Kang, P. Okwieka, S. Schöttler, S. Winzen, J. Langhanki, K. Mohr, T. Opatz, V. Mailänder, K. Landfester and F. R. Wurm, *Angew. Chem., Int. Ed.*, 2015, **54**, 7436-7440.
- 67 T. Lammers, *Int. J. Pharm.*, 2013, **454**, 527-529.
- 68 R. Paliwal, R. J. Babu and S. Palakurthi, *AAPS PharmSciTech*, 2014, **15**, 1527-1534.
- 69 C. Cusco, J. Garcia, E. Nicolas, P. Rocas and J. Rocas, *Polym. Chem.*, 2016, **7**, 6457-6466.
- 70 J. M. Asua, *Prog. Polym. Sci.*, 2014, **39**, 1797-1826.
- 71 H. J. Hamilton, *Zygon*, 1977, **12**, 289-335.
- 72 C. Tanford, *Science*, 1978, **200**, 1012-1018.
- 73 N. Muller, *Acc. Chem. Res.*, 1990, **23**, 23-28.
- 74 O. Félix, Z. Zheng, F. Cousin and G. Decher, *C. R. Chim.*, 2009, **12**, 225-234.
- 75 M. W. Urban, *Prog. Polym. Sci.*, 2009, **34**, 679-687.
- 76 M. W. Urban, *Curr. Opin. Colloid Interface Sci.*, 2014, **19**, 66-75.
- 77 L. R. Pratt and D. Chandler, *J. Chem. Phys.*, 1977, **67**, 3683-3704.
- 78 R. S. Spolar, J. H. Ha and M. T. Record, *Proc. Natl. Acad. Sci.*, 1989, **86**, 8382-8385.
- 79 K. Lum, D. Chandler and J. D. Weeks, *J. Phys. Chem. B*, 1999, **103**, 4570-4577.
- 80 A. Wallqvist and B. J. Berne, *J. Phys. Chem.*, 1995, **99**, 2885-2892.
- 81 E. E. Meyer, K. J. Rosenberg and J. Israelachvili, *Proc. Natl. Acad. Sci.*, 2006, **103**, 15739-15746.
- 82 S. H. White and W. C. Wimley, *Biochim. Biophys. Acta*, 1998, **1376**, 339-352.
- 83 A. Ben-Naim. *Hydrophobic Interactions*, Plenum Press: New York, 1980; 1-24.
- 84 P. P. Karmali and D. Simberg, *Expert Opin. Drug Delivery*, 2011, **8**, 343-357.
- 85 C. Sacchetti, K. Motamedchaboki, A. Magrini, G. Palmieri, M. Mattei, S. Bernardini, N. Rosato, N. Bottini and M. Bottini, *ACS Nano*, 2013, **7**, 1974-1989.
- 86 B. Pelaz, P. del Pino, P. Maffre, R. Hartmann, M. Gallego, S. Rivera-Fernández, J. M. de la Fuente, G. U. Nienhaus and W. J. Parak, *ACS Nano*, 2015, **9**, 6996-7008.

- 87 C. J. Czuprynski, *Encyclopedic Reference of Immunotoxicology*, Springer, Berlin, Heidelberg, 2005.
- 88 V. C. F. Mosqueira, P. Legrand, J. L. Morgat, M. Vert, E. Mysiakine, R. Gref, J. P. Devissaguet and G. Barratt, *Pharm. Res.*, 2001, **18**, 1411-1419.
- 89 R. Michel, S. Pasche, M. Textor and D. G. Castner, *Langmuir*, 2005, **21**, 12327-12332.
- 90 J. M. Harris and R. B. Chess, *Nat. Rev. Drug Discovery*, 2003, **2**, 214-221.
- 91 Y. Sheng, Y. Yuan, C. Liu, X. Tao, X. Shan and F. Xu, *J. Mater. Sci.: Mater. Med.*, 2009, **20**, 1881-1891.
- 92 N. Graf, D. R. Bielenberg, N. Kolishetti, C. Muus, J. Banyard, O. C. Farokhzad and S. J. Lippard, *ACS Nano*, 2012, **6**, 4530-4539.
- 93 R. Gref, A. Domb, P. Quellec, T. Blunk, R. H. Müller, J. M. Verbavatz and R. Langer, *Adv. Drug Delivery Rev.*, 2012, **64**, **Supplement**, 316-326.
- 94 D. K. Sahana, G. Mittal, V. Bhardwaj and M. N. V. R. Kumar, *J. Pharm. Sci.*, 2008, **97**, 1530-1542.
- 95 Z. Ghotbi, A. Haddadi, S. Hamdy, R. W. Hung, J. Samuel and A. Lavasanifar, *J. Drug Targeting*, 2011, **19**, 281-292.
- 96 R. Zhang, S. Xu, J. Luo and X. Liu, *Microchim. Acta*, 2015, **182**, 175-183.
- 97 S. Pillarisetti, S. Maya, S. Sathianarayanan and R. Jayakumar, *Colloids Surf., B*, 2017, **159**, 809-819.
- 98 C. Wan, T. M. Allen and P. R. Cullis, *Drug Delivery Transl. Res.*, 2014, **4**, 74-83.
- 99 J. C. Kraft, J. P. Freeling, Z. Wang and R. J. Y. Ho, *J. Pharm. Sci.*, 2014, **103**, 29-52.
- 100 A. Sharma and U. S. Sharma, *Int. J. Pharm.*, 1997, **154**, 123-140.
- 101 H. Chen, S. Kim, L. Li, S. Wang, K. Park and J. X. Cheng, *Proc. Natl. Acad. Sci.*, 2008, **105**, 6596-6601.
- 102 P. Zou, H. Chen, H. J. Paholak and D. Sun, *Mol. Pharmaceutics*, 2013, **10**, 4185-4194.
- 103 P. W. Voorhees, *J. Stat. Phys.*, 1985, **38**, 231-252.
- 104 J. Weiss, N. Herrmann and D. J. McClements, *Langmuir*, 1999, **15**, 6652-6657.
- 105 L. V. Ratke, P.W., *Growth and Coarsening Ostwald Ripening in Material Processing*, Springer, Berlin, 2002.
- 106 P. Taylor, *Adv. Colloid Interface Sci.*, 1998, **75**, 107-163.

- 107 D. Dye and J. Watkins, *Br. Med. J.*, 1980, **280**, 1353-1353.
- 108 J. Szebeni, C. R. Alving and F. M. Muggia, *J. Natl. Cancer Inst.*, 1998, **90**, 300-306.
- 109 K. Iwase, Y. Oyama, T. Tatsuishi, J. y. Yamaguchi, Y. Nishimura, A. Kanada, M. Kobayashi, Y. Maemura, S. Ishida and Y. Okano, *Toxicol. Lett.*, 2004, **154**, 143-148.
- 110 S. T. Kim, K. Saha, C. Kim and V. M. Rotello, *Acc. Chem. Res.*, 2013, **46**, 681-691.
- 111 L. Maibaum, A. R. Dinner and D. Chandler, *J. Phys. Chem. B*, 2004, **108**, 6778-6781.
- 112 C. K. Simi and T. Emilia Abraham, *Bioprocess Biosyst. Eng.*, 2007, **30**, 173-180.
- 113 S. Shu, X. Zhang, Z. Wu, Z. Wang and C. Li, *Biomaterials*, 2010, **31**, 6039-6049.
- 114 S. Yu, J. Ding, C. He, Y. Cao, W. Xu and X. Chen, *Adv. Healthcare Mater.*, 2014, **3**, 752-760.
- 115 M. Talelli, M. Barz, C. J. F. Rijcken, F. Kiessling, W. E. Hennink and T. Lammers, *Nano Today*, 2015, **10**, 93-117.
- 116 P. Carmeliet and R. K. Jain, *Nature*, 2000, **407**, 249-257.
- 117 J. L. Yu, L. May, P. Klement, J. I. Weitz and J. Rak, *Semin. Thromb. Hemostasis*, 2004, **30**, 21-30.
- 118 N. Ferrara and R. S. Kerbel, *Nature*, 2005, **438**, 967-974.
- 119 N. Nishida, H. Yano, T. Nishida, T. Kamura and M. Kojiro, *Vasc. Health Risk Manage.*, 2006, **2**, 213-219.
- 120 H. Cabral, Y. Matsumoto, K. Mizuno, Q. Chen, M. Murakami, M. Kimura, Y. Terada, M. R. Kano, K. Miyazono, M. Uesaka, N. Nishiyama and K. Kataoka, *Nat Nano*, 2011, **6**, 815-823.
- 121 A. Albanese, P. S. Tang and W. C. W. Chan, *Annu. Rev. Biomed. Eng.*, 2012, **14**, 1-16.
- 122 H. S. Choi, W. Liu, P. Misra, E. Tanaka, J. P. Zimmer, B. I. Ipe, M. G. Bawendi and J. V. Frangioni, *Nat. Biotechnol.*, 2007, **25**, 1165-1170.
- 123 S. Franzen and S. A. Lommel, *Nanomedicine*, 2009, **4**, 575-588.
- 124 A. D. Friedman, S. E. Claypool and R. Liu, *Curr. Pharm. Des.*, 2013, **19**, 6315-6329.
- 125 Y. H. Bae and K. Park, *J. Controlled Release*, 2011, **153**, 198-205.

- 126 J. M. Irache, H. H. Salman, C. Gamazo and S. Espuelas, *Expert Opin. Drug Delivery*, 2008, **5**, 703-724.
- 127 W. Chung-Hao, H. Yao-Jhang, C. Chia-Wei, H. Wen-Ming and P. Ching-An, *Nanotechnology*, 2009, **20**, 1-7.
- 128 A. Tivnan, W. S. Orr, V. Gubala, R. Nooney, D. E. Williams, C. McDonagh, S. Prenter, H. Harvey, R. Domingo-Fernández, I. M. Bray, O. Piskareva, C. Y. Ng, H. N. Lode, A. M. Davidoff and R. L. Stallings, *PLoS ONE*, 2012, **7**, 1-12.
- 129 K. Landfester and V. Mailänder, *Expert Opin. Drug Delivery*, 2013, **10**, 593-609.
- 130 H. Freichels, M. Wagner, P. Okwieka, R. G. Meyer, V. Mailänder, K. Landfester and A. Musyanovych, *J. Mater. Chem. B*, 2013, **1**, 4338-4348.
- 131 D. B. Kirpotin, D. C. Drummond, Y. Shao, M. R. Shalaby, K. Hong, U. B. Nielsen, J. D. Marks, C. C. Benz and J. W. Park, *Cancer Res.*, 2006, **66**, 6732-6740.
- 132 D. W. Bartlett, H. Su, I. J. Hildebrandt, W. A. Weber and M. E. Davis, *Proc. Natl. Acad. Sci.*, 2007, **104**, 15549-15554.
- 133 K. F. Pirollo and E. H. Chang, *Trends Biotechnol.*, 2008, **26**, 552-558.
- 134 A. S. Mikhail and C. Allen, *J. Controlled Release*, 2009, **138**, 214-223.
- 135 N. Ma, Y. Li, H. Xu, Z. Wang and X. Zhang, *J. Am. Chem. Soc.*, 2010, **132**, 442-443.
- 136 H. Sardon, L. Irusta and M. J. Fernández-Berridi, *Prog. Org. Coat.*, 2009, **66**, 291-295.
- 137 K. Aalto-Korte, K. Suuronen, O. Kuuliala, M. L. Henriks-Eckerman and R. Jolanki, *Contact Dermatitis*, 2012, **67**, 78-88.
- 138 D. Roux, C. Degert and R. Laversanne, WO Pat. WO/1997/000623, 1999.
- 139 C. Fruijtier-Pöllöth, *Toxicology*, 2005, **214**, 1-38.
- 140 I. Kralova and J. Sjöblom, *J. Dispersion Sci. Technol.*, 2009, **30**, 1363-1383.
- 141 A. Goossens, *J. Allergy*, 2011, **2011**, 1-6.
- 142 F. M. Veronese, C. Monfardini, P. Caliceti, O. Schiavon, M. D. Scrawen and D. Beer, *J. Controlled Release*, 1996, **40**, 199-209.
- 143 F. M. Veronese, P. Caliceti and O. Schiavon, *J. Bioact. Compat. Polym.*, 1997, **12**, 196-207.
- 144 L. Zhang, F. X. Gu, J. M. Chan, A. Z. Wang, R. S. Langer and O. C. Farokhzad, *Clin. Pharmacol. Ther.*, 2008, **83**, 761-769.

- 145 C. Pinholt, J. T. Bukrinsky, S. Hostrup, S. Frokjaer, W. Norde and L. Jorgensen, *Eur. J. Pharm. Biopharm.*, 2011, **77**, 139-147.
- 146 G. Morral-Ruíz, C. Solans, M. L. García and M. J. García-Celma, *Langmuir*, 2012, **28**, 6256-6264.
- 147 Y. Tang, Z. Gu and M. Zhao, WO Pat. WO2012/142410A2, 2012.
- 148 J. Wang, X. Sun, W. Mao, W. Sun, J. Tang, M. Sui, Y. Shen and Z. Gu, *Adv. Mater.*, 2013, **25**, 3670-3676.
- 149 S. Mura, J. Nicolas and P. Couvreur, *Nat. Mater.*, 2013, **12**, 991-1003.
- 150 S. Siggia and J. G. Hanna, *Anal. Chem.*, 1948, **20**, 1084-1084.
- 151 J. E. Dumas, K. Zienkiewicz, S. A. Tanner, E. M. Prieto, S. Bhattacharyya and S. A. Guelcher, *Tissue Eng., Part A*, 2010, **16**, 2505-2518.
- 152 ASTM Standard D2572, 2010, *Standard Test Method for Isocyanate Groups in Urethane Materials or Prepolymers*, West Conshohocken, PA.
- 153 A. K. Mishra, D. K. Chattopadhyay, B. Sreedhar and K. V. S. N. Raju, *Prog. Org. Coat.*, 2006, **55**, 231-243.
- 154 K. K. Jena, D. K. Chattopadhyay and K. V. S. N. Raju, *Eur. Polym. J.*, 2007, **43**, 1825-1837.
- 155 Spectrum Labs, Fundamentals of Membrane Dialysis, <http://spectrumlabs.com/dialysis/Fund.html>, (accessed 14<sup>th</sup> October, 2017).
- 156 M. L. Immordino, F. Dosio and L. Cattell, *Int. J. Nanomed.*, 2006, **1**, 297-315.
- 157 A. Verma and F. Stellacci, *Small*, 2010, **6**, 12-21.
- 158 M. Wang, A. D. Miller and M. Thanou, *J. Drug Targeting*, 2013, **21**, 684-692.
- 159 P. R. Leroueil, S. A. Berry, K. Duthie, G. Han, V. M. Rotello, D. Q. McNerny, J. R. Baker, B. G. Orr and M. M. Banaszak Holl, *Nano Lett.*, 2008, **8**, 420-424.
- 160 N. Oh and J. H. Park, *Int. J. Nanomed.*, 2014, **9**, 51-63.
- 161 V. Estrella, T. Chen, M. Lloyd, J. Wojtkowiak, H. H. Cornell, A. Ibrahim-Hashim, K. Bailey, Y. Balagurunathan, J. M. Rothberg, B. F. Sloane, J. Johnson, R. A. Gatenby and R. J. Gillies, *Cancer Res.*, 2013, **73**, 1524-1535.
- 162 ChemAxon, <https://chemicalize.com/> (accessed 15<sup>th</sup> November, 2015).
- 163 H. Gelderblom, J. Verweij, K. Nooter and A. Sparreboom, *Eur. J. Cancer*, 2001, **37**, 1590-1598.

- 
- 164 J. y. Yamaguchi, Y. Nishimura, A. Kanada, M. Kobayashi, K. Mishima, T. Tatsuishi, K. Iwase and Y. Oyama, *Toxicology*, 2005, **211**, 179-186.
- 165 S. H. Hu, S. Y. Chen and X. Gao, *ACS Nano*, 2012, **6**, 2558-2565.
- 166 A. A. Date, M. D. Joshi and V. B. Patravale, *Adv. Drug Delivery Rev.*, 2007, **59**, 505-521.
- 167 R. M. Clegg, *Curr. Opin. Biotechnol.*, 1995, **6**, 103-110.
- 168 T. Ha, T. Enderle, D. F. Ogletree, D. S. Chemla, P. R. Selvin and S. Weiss, *Proc. Natl. Acad. Sci.*, 1996, **93**, 6264-6268.
- 169 S. Curry, *Vox Sang.*, 2002, **83**, 315-319.



# **CHAPTER 3**

*Application of ionophore-loaded  
nanocapsules to lung cancer and  
neuroblastoma*



# 1. Introduction

## 1.1. Lung cancer

### 1.1.1. Epidemiology and risk factors

Cancer is nowadays the second major cause of death in developed countries, following coronary diseases and stroke. According to the World Health Organization, more than 14 million new cases were diagnosed and more than 8 million deaths occurred in 2012. Moreover, the prognostics suggest an ever-increasing cancer burden in low and middle-income countries, reaching 20 million of new cases by 2030, due to a higher incidence of the risk factors and a longer life expectancy.<sup>1-5</sup>

The risk factors associated with cancer can come from external causes, such as smoking, atmospheric pollution, sedentarism, unbalanced food habits, alcohol consumption, sun exposure, stress, obesity... or internal factors, such as inherited genetic mutations or personal immunologic state.<sup>6,7</sup>

Lung, breast and colorectal cancers are the most frequently diagnosed, while lung, stomach and kidney cancers cause the major number of deaths.<sup>3</sup> In fact, lung cancer (LC) has emerged as the most common cause of cancer-related death worldwide, affecting millions of individuals. In 2012, LC was diagnosed in approximately 1.8 million of new cases and led to 1.6 million of deaths, accounting to approximately 19% of total deceases. In the male population, LC is the first cause of cancer death worldwide, while in females, it is the leading cause of cancer death only in less developed countries.<sup>8-10</sup>

Epidemiological studies have identified different risk factors from environmental, behavioral or lifestyle causes and have associated them to patterns of cancer occurrence (**Figure 1**).

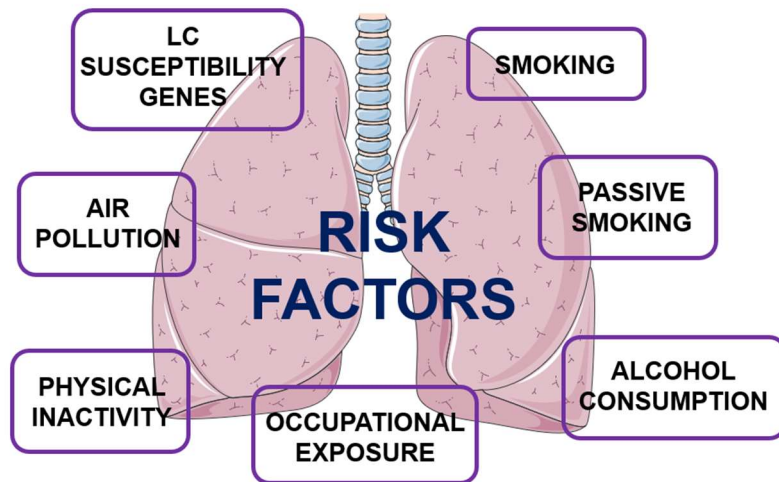


**Figure 1.** Relevant risk factors for lung cancer

The most important risk factor attributed to lung carcinogenesis is smoking, both active and passive.<sup>11</sup> Tobacco smoke contains more than 5,000 identified constituents that contribute to carcinogenesis through multiple pathways,<sup>12-14</sup> including DNA binding, inflammation, oxidative stress, mutations and other changes in crucial genes such as tumor protein 53 (p53).<sup>15,11</sup>

Other risk factors involve the exposure to air pollution from unventilated coal-fueled stoves and cooking fumes, exposure to occupational and environmental carcinogens such as asbestos, arsenic, radon and polycyclic hydrocarbons.<sup>8</sup> Outdoor pollution and alcohol consumption play also an important role, while sedentarism and unbalanced diets increase the risks to contract this disease.<sup>16</sup> Finally, intrinsic host factors, such as genetic heredity, susceptibility and instability are also relevant mechanisms in LC development.<sup>17</sup>

### **1.1.2. Histology**

LC is classified by its histologic appearance into small cell lung cancer (SCLC) or non-small cell lung cancer (NSCLC), the latter being further divided into adenocarcinoma, squamous cell carcinoma and large-cell carcinoma.<sup>14</sup> About 80–85% of LC cases belong to NSCLC type,<sup>18</sup> for which the predicted 5-year survival rate is around 16%<sup>19</sup> and the rest are associated to SCLC.

#### **1.1.2.1. *Small cell lung cancer (SCLC)***

SCLC is a carcinoma of neuroendocrine origin and is one of the most distinctive malignancies in the field of oncology, due to its high proliferative rates.<sup>20</sup> This type of cancer usually starts in the bronchial tubes and tend to spread quickly to other parts of the body. In fact, most of the patients present hematogenous metastasis while only one third of them present limited-stage disease confined to the chest. SCLC is highly sensitive to initial chemotherapy and radiotherapy but most of the patients eventually die of recurrent disease.<sup>21</sup> The main cause for this type of carcinomas is tobacco smoking.

#### **1.1.2.2. *Non-small cell lung cancer (NSCLC)***

The major part of NSCLC are adenocarcinomas, squamous cell carcinomas or large-cell carcinomas (90–95%), while the rest are classified as mixed tumors. Adenocarcinomas are present in about 40% of the cases and occur in both current and former smokers and in non-smokers. It typically appears as small peripheral lesions that have a high propensity to metastasize to regional lymph nodes and distant sites.<sup>22</sup> Squamous cell carcinomas account for 25–30% of the cases and are associated to active smokers. This type of cancer arises from bronchial epithelium and spreads to regional lymph nodes. Finally, large-cell carcinomas occur in 10–15% of LC cases and can be found in any part of the lung. They tend to grow and spread rapidly, worsening its diagnosis and treatment.<sup>23</sup>

#### **1.1.3. *Treatments***

Several types of therapies are currently available to treat LC. The most suitable treatment is selected by considering the histological type of cancer, molecular characteristics of the tumor, general health of the patient and level of fitness.<sup>18</sup> Another important parameter is the tumor stage at the moment of diagnosis. There are four main phases in cancer development, I to IV. In phase I, the cancer is still small and has not grown deeply into nearby tissues. In stages II and III, the tumor has invaded adjacent tissues or lymph nodes. Finally, in phase IV, the cancer has metastasized to other parts of the body.<sup>24</sup>

### 1.1.3.1. Conventional treatments

Therapies for NSCLC, which cover the main part of LC cases, strongly depend on the stage of the disease. For patients with stage I to III, the goal is the cure, whereas those facing a IV phase disease, the aim is palliation of the symptoms and life prolongation.<sup>18</sup> With patients with NSCLC in stage I or II, with or without metastases, the primary curative modality is surgical resection. When the LC is in a more advanced phase but presents no invasion to other organs, a preoperative radiotherapy or chemotherapy are used. By doing this, the spread of cancer cells during surgery can be reduced or prevented.<sup>25</sup> When the tumor is unresectable or after surgical practice, the patients start a treatment care plan with the combination of radiotherapy and/or drug therapy (chemotherapy, targeted therapy or immunotherapy).

Pt-based compounds, and more specifically cisplatin (**Figure 2**), have been long administered as primary cytotoxic chemotherapeutics for LC, since they have been associated to acceptable response and survival rates.<sup>26</sup>

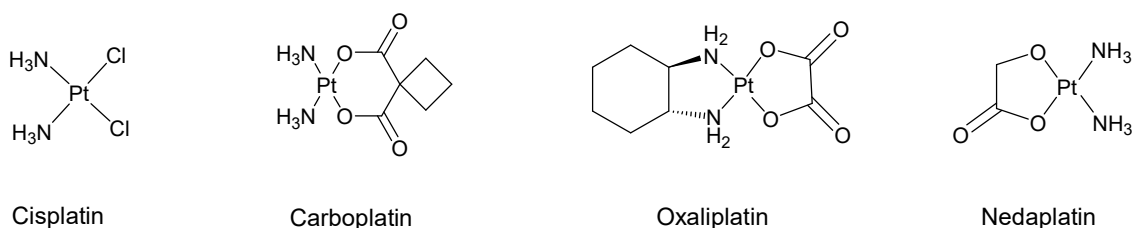
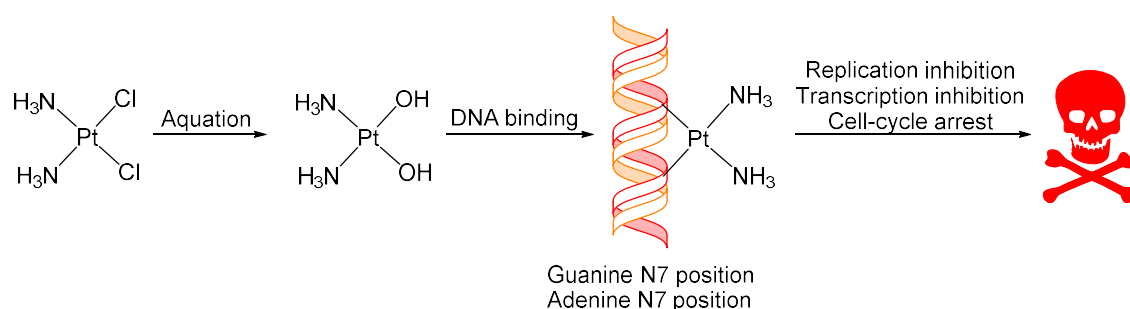


**Figure 2.** The most commonly used Pt-based drugs in LC

After the synthesis of cisplatin in 1978, more than 3,000 Pt analogs were developed and tested in cancer cells, but less than 15 succeeded in reaching clinical trials and only a few of them were accepted for clinical use. Among them, cisplatin and carboplatin are used worldwide, oxaliplatin is available in few countries and nedaplatin is only accepted in Japan.<sup>27</sup> They are all Pt(II) complexes bound to two amino groups with different hydrophobicities and reactivity.<sup>27-29</sup>

The mechanism of action of Pt-based complexes is shown in **Scheme 1** and proceeds through different steps.



**Scheme 1.** Mechanism of action of cisplatin

There is overwhelming evidence that cisplatin becomes activated after an aquation step, in which the two chloride leaving groups are replaced by two hydroxides.<sup>27,30</sup> This intermediate can subsequently react with DNA bases, preferentially with the N7 position of guanine or adenine, leading to crosslinked adducts between the same and opposite strands. This activates DNA-damage recognition and repair pathways, cell-cycle arrest and programmed cell death or apoptosis.<sup>31,32</sup> Thus, the efficacy of the Pt-based complexes is related to the cellular saturation to repair Pt adducts of DNA. *Trans*-adducts are more easily repaired than *cis*-analogs, and therefore the *cis* configuration of the diaquo- intermediates are reported to be more toxic than the *trans* isomer.<sup>27</sup>

Besides Pt-based drugs, there is a broad range of therapeutic modalities, depending on the subtype of LC. Given the wide variety of parameters to be considered, the selection of drug therapy strategy, dosing and administration can be a complex endeavor. To facilitate this process, the National Comprehensive Cancer Network has generated some guidelines with the currently accepted approaches for NSCLC and SCLC treatment (**Figure 3**).

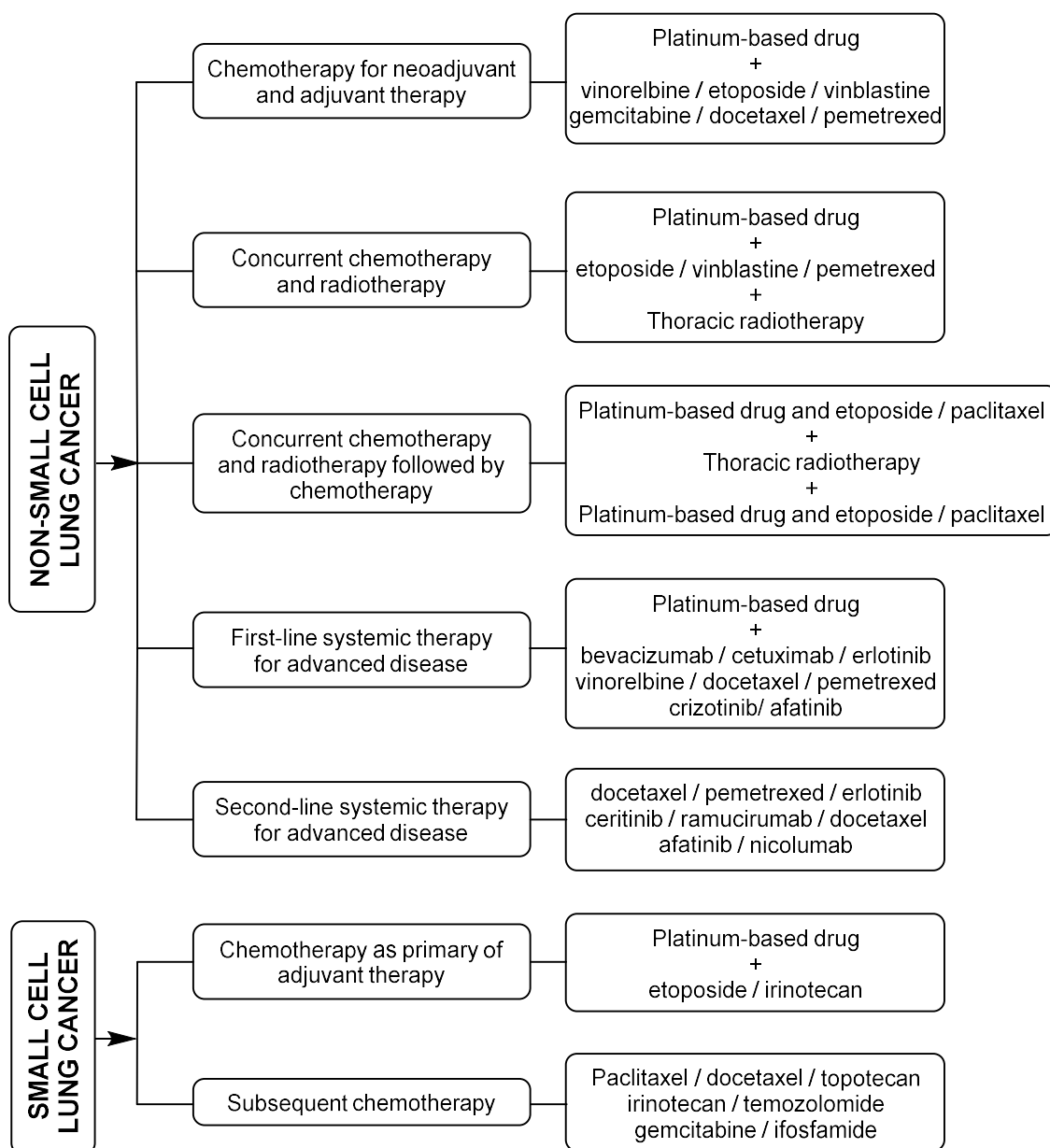


**Figure 3.** Guidelines for NSCLC and SCLC treatment. Adapted from reference 33

For patients diagnosed with LC, chemotherapy is the mainstay therapy and can be applied as a neoadjuvant/adjuvant therapy or as a first/second line-systemic treatment. The most common chemotherapeutic agents are Pt-based compounds, etoposide, vinblastine, paclitaxel, docetaxel, pemetrexed and irinotecan. The application of chemotherapy and radiotherapy, however, is limited because of drug resistance and serious adverse effects, such as renal problems, hair loss, deafness, neurotoxicity and decrease of the immunity towards infections.<sup>32,34</sup> Therefore, new research lines have involved the use of novel therapies that can overcome side effects and offer a better life quality. This is the case of targeted therapeutic agents,

which are based on discovering genetic variations and the signaling pathways altered in cancer as an inhibition tool. The firstly approved molecularly-targeted drug was trastuzumab and was followed by gefitinib, erlotinib and bevacizumab.<sup>35</sup> Systemic treatment with targeted therapies, however, present some disadvantages related to drug resistance developed by most patients after 1 year of treatment and also the variability obtained in the clinical response.<sup>36</sup>

For those patients with inoperable locally advanced NSCLC, thoracic radiotherapy in combination with chemotherapy is considered the best option.<sup>37</sup> Nevertheless, the target tumor motion limits the efficacy of this treatment because geometrical errors in dose delivery easily lead to high exposure of healthy tissues to high doses.

Altogether, despite the advances achieved, the prognosis and clinical outcome are not satisfactory for LC patients. Therefore, the research on the development of new drugs and alternative therapies should address the current limitations and particularly the acquired drug resistance in patients.

#### 1.1.3.2. *Experimental treatments: ionophores*

Marine-derived compounds have gained a considerable degree of attention in the last decades due to their promising properties in the healthcare area.<sup>38</sup> In fact, oceans, which cover two third parts of the planet, offer a huge opportunity to discover and isolate new molecules. Among all the described products of marine origin, almost 20% present active properties and around 600 are included in the pipeline of drug discovery programs and in clinical trials.<sup>39</sup> In line with this potential, prodiginines, red pigments produced by the aquatic bacterium *Serratia marcescens*, have shown interesting biological activities, such as immunosuppressive, antiviral, antibiotic and anticancer effects both *in vitro* and *in vivo*.<sup>40-43</sup>

Prodiginines are characterized by a common pyrrolyl dipyrromethene skeleton. There are two main structural types of prodiginines, depending whether the substituent is linear (i.e. prodigiosin) or cyclic (i.e. streptorubin B)<sup>40,42</sup> (**Figure 4**).

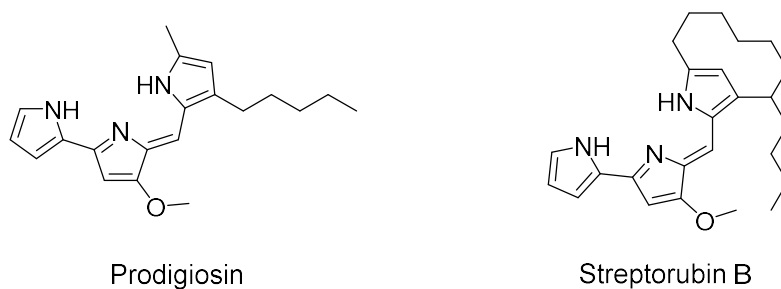


**Figure 4.** Chemical structure of two prodiginines

Prodiginines show promising anticancer activities, for instance, prodigiosin has an average  $IC_{50}$  (half inhibitory concentration) of  $2.1 \mu\text{M}$ , tested in more than 60 cancer cell lines. They are classified as proapoptotic drugs that induce cellular stress through different mechanisms and have proven to be unaltered by multidrug resistance pumps.<sup>40,44,45</sup> Such an outstanding biological activity is related to their capacity to change the  $pH_i$ , which is an essential parameter to guarantee cell homeostatic maintenance and correct functioning, including endocytosis, exocytosis, intracellular trafficking as well as cell differentiation, cell growth and cell death. There is considerable evidence that prodiginines can disrupt this pH gradient and induce an increase in  $pH_i$  by rapidly and reversibly importing and exporting  $H^+$  and  $Cl^-$  ions across the lipid bilayer.<sup>46,47</sup> Such behavior is typically found in ionophores, which are molecules that reversibly bind to cations or anions to facilitate their passage across hydrophobic membranes (**Figure 5**).

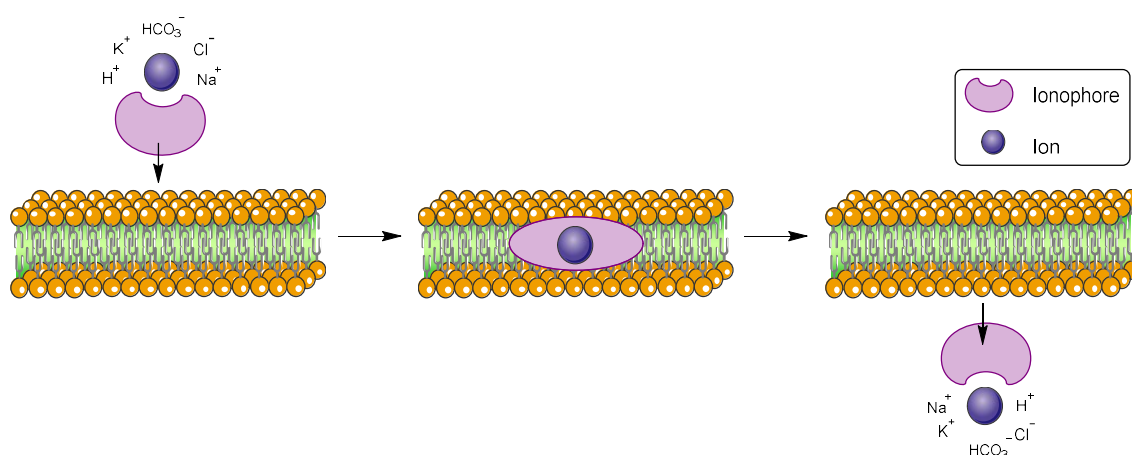


**Figure 5.** Graphic representation of the activity of an ionophore

There are two main types of ionophores: cationophores and anionophores. The first group comprises all those molecules that bind cationic entities, including protons and different types of metal ions to assist their transport across the membranes. These cationic species are essential for living organisms and their local concentration must be accurately controlled. For instance, proton concentration must be different depending on the cell compartment, since in lysosomes hydrolytic enzymes work at acidic pH while in cytosol the environment has to be closer to neutrality. Therefore, the proton efflux should be maintained within specific levels to guarantee the correct functioning of the cell. Besides regulation of the concentration of specific positively charged species, cationophores stand out for their antibiotic properties due to their high affinity for ions like  $\text{Na}^+$  or  $\text{K}^+$ .<sup>47</sup>

Structurally speaking, cationophores usually consist of an array of oxygen atoms or other heteroatoms with a suitable binding pocket surrounded by a hydrophobic envelope (**Figure 6**).

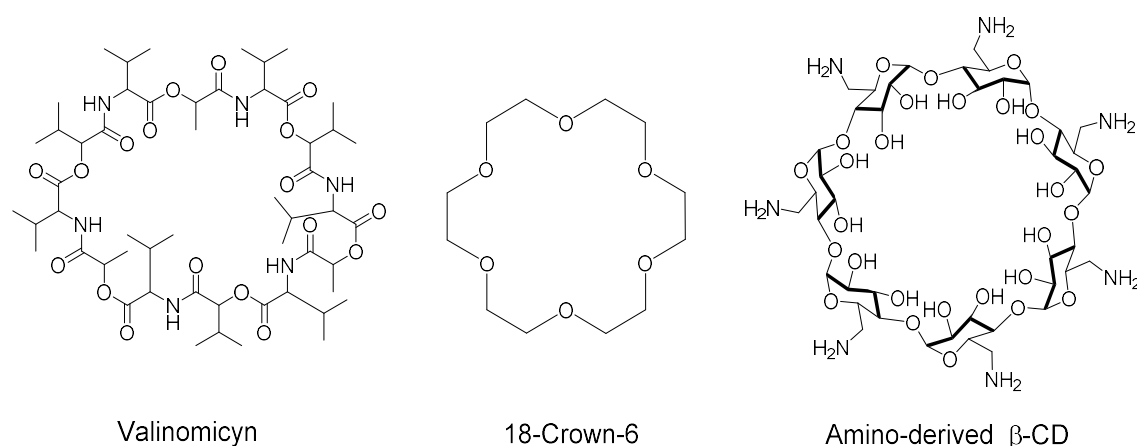


**Figure 6.** Some examples of cationophores

For instance, imidazole derivatives are well-known for their ability to dissipate pH gradients. Moreover, macrocyclic peptides or depsipeptides, such as valinomycin, selectively form an inner polar binding site with  $\text{K}^+$ , transporting it across the membrane thanks to an external hydrophobic shell. Other examples are crown ethers, which specifically bind alkali and earth alkali metal cations, or certain amino-derived cyclodextrins, which have the ability to solubilize  $\text{K}^+$  in their polar pocket.<sup>47</sup>

The second group of ionophores are the less commonly studied anionophores, which as their name suggests, act as anion transporters.<sup>48</sup> Among them, there are specific short peptides that have shown efficient insertion into membranes and self-association to generate Cl<sup>-</sup> channels (**Figure 7**).<sup>47</sup>

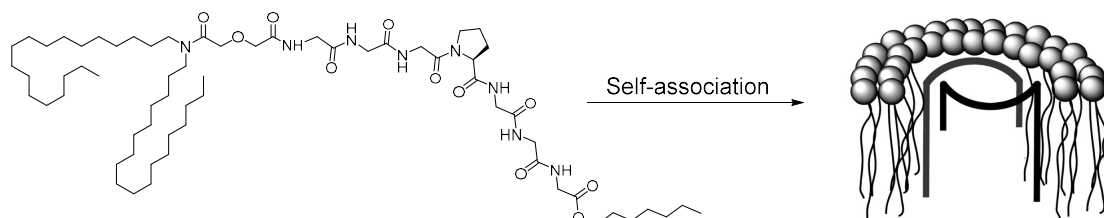


**Figure 7.** Small peptides that self-assemble into ion channels. Adapted from reference 47

Some isophthalamide-based derivatives have demonstrated the same effect,<sup>45</sup> while other examples have been inspired in aminosterol squalamine, anion receptors derived from bile acids (cholapods) and the previously described prodiginines (**Figure 8**).

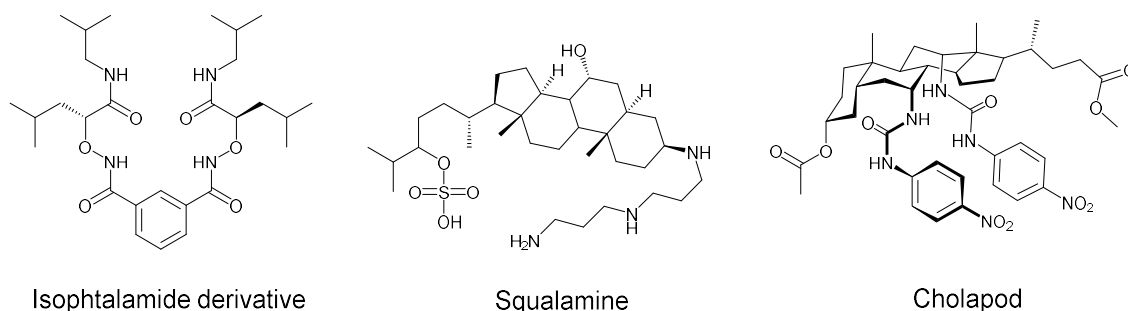


**Figure 8.** Some examples of anionophores

Squalamine has been described to form a positively charged pathway across the membrane as a tool to selectively bind  $\text{SO}_3^-$  groups. Cholapods are able to allow the  $\text{Cl}^-/\text{NO}_3^-$  exchange and prodiginines have been described to successfully promote  $\text{HCl}$  co-transport and  $\text{Cl}^-/\text{HCO}_3^-$  exchange in model liposomes.<sup>45</sup>

Recently, the synthetic hydrophobic prodiginine obatoclax (**Figure 9**) has generated particular interest due to its promising results in preclinical and phase II clinical trials in different types of cancer and has shown encouraging outcomes in combination with carboplatin, etoposide in front-line extensive-stage SCLC.<sup>42,45,49</sup>

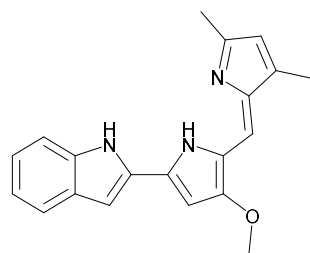


**Figure 9.** Chemical structure of obatoclax

This molecule is described to efficiently promote  $\text{Cl}^-$ ,  $\text{HCO}_3^-$  and  $\text{NO}_3^-$  transport and such a potent anion binding ability correlates well with its outstanding anticancer activity. In fact, other analogs of obatoclax were synthesized by modifying the number of hydrogen bond donors and resulted into poorer anion-carrier abilities and therefore non-cytotoxic properties.<sup>49</sup>

### 1.1.3.3. *Tambjamines*

Synthetic prodiginin analogues have shown potential anticancer effects but their non-straightforward preparation and the difficulties to improve their bioactivity have limited their development. Therefore, other prodiginine-based molecules have emerged, such as tambjamines.<sup>40,42,44,48,49</sup> Similarly to prodiginines, tambjamines have shown interesting antimicrobial and anticancer activity that have been related to their role as anion transporters. The first tambjamine molecules that Quesada's group studied<sup>48</sup> are shown in **Figure 10**.

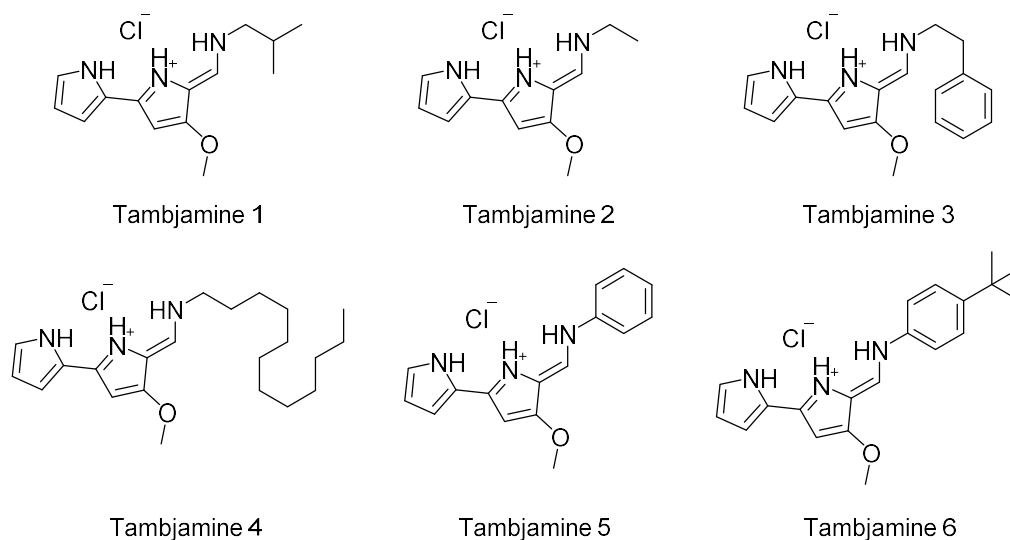


**Figure 10.** Some examples of tambjamine analogs

Tambjamines 1–4 are secondary naturally occurring analogs, while tambjamines 5 and 6 are synthetic molecules with aromatic groups as amine substituents.

Solid state structures of hydrochloride salts of tambjamines 2 and 6 were determined by X-ray diffraction studies and revealed a flat bipyrrrolenamine core with the chloride anion interacting with the tambjamine.<sup>48</sup>

The anion transport properties of these molecules were tested in model liposomes by loading them with NaCl and measuring the chloride release promoted by tambjamines 1–6 with a Cl<sup>-</sup>-selective electrode. The results pointed out that tambjamines were very potent NO<sub>3</sub><sup>-</sup> and HCO<sub>3</sub><sup>-</sup>/Cl<sup>-</sup> exchangers, with 6 being the best candidate and 2 the worst one, due to its low hydrophobicity. In addition, their *in vitro* ionophoric activity was studied in a SCLC cell line using vital staining with acridine orange. This fluorophore shows orange fluorescence in acidic compartments (lysosomes) and green fluorescence at sites with higher pH (**Figure 11**).

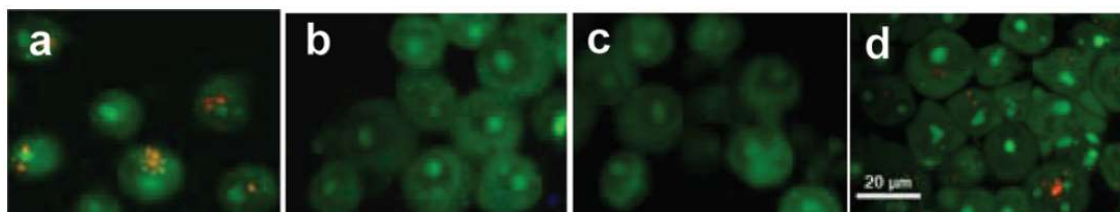


**Figure 11.** (a) Control; (b) exposure to tambjamine 4; (c) tambjamine 6; (d) tambjamine 2.

Reproduced from reference 48

On one hand, those analogs with better ionophoric properties (4 and 6) led to a general green fluorescence in the entire cell, indicating a deacidification of the lysosomes, probably promoted by a hydrogencarbonate influx. On the other hand, the molecules showing low exchange abilities did not alter the lysosomal pH and therefore this compartment remained orange.

Other studies carried out with tambjamines bearing different aromatic enamine substituents (**Figure 12**) also supported outstanding anion exchange properties, deacidification of acidic organelles and cytotoxicity values in the lower micromolar range in different cancer cell lines.<sup>50</sup>

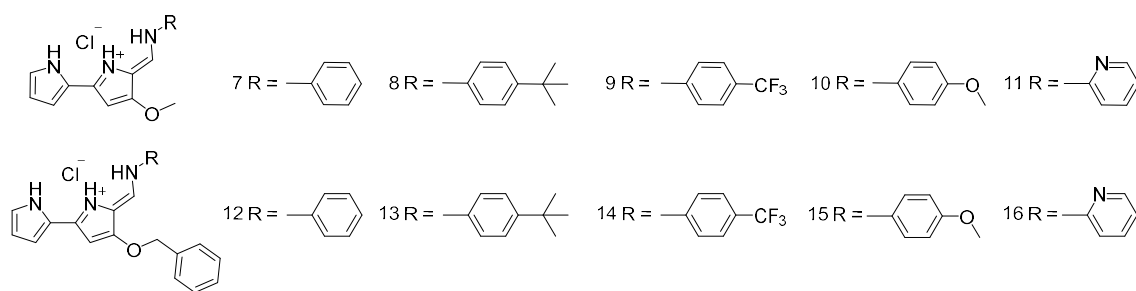
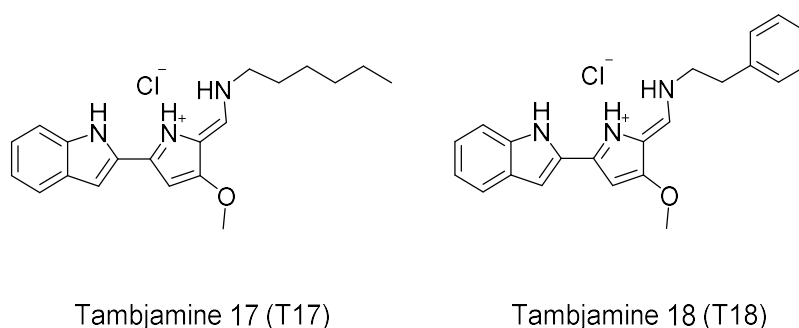


**Figure 12.** Tambjamines bearing aromatic substituents

Finally, Soto-Cerrato *et al.*, characterized the effect of two other types of tambjamines (**Figure 13**) in cancer stem cells (CSCs).<sup>51</sup>



Tambjamine 17 (T17)

Tambjamine 18 (T18)

**Figure 13.** Chemical structures of T17 and T18

As mentioned previously, cancer cells present a reversed pH gradient compared to normal differentiated cells, with a  $\text{pH}_i$  higher than  $\text{pH}_e$ . This feature is regulated by ion channels and pumps and is directly related to the acquisition of sustained proliferative signaling or resistance to cell death. Likewise, membrane potential ( $V_m$ ) is another parameter that is altered in cancer cells compared to healthy ones.  $V_m$  is depolarized in rapidly proliferating cells and hyperpolarized in non-proliferating terminally differentiated cells. In this regard, CSC, a tumor cell subpopulation that shows tumor initiating capacities and contributes to its acquired chemotherapy resistance, shows a depolarized  $V_m$  as a tool to maintain their stemness capacities. Therefore, pH modulation and alteration of  $V_m$  can be viewed as two interesting therapeutic approaches for cancer treatment.

In Soto-Cerrato's study,<sup>51</sup> tambjamine analogs 17 and 18 (T17 and T18) were developed by carefully calculating their relative hydrophobicity as a key parameter to enhance their performance as anion transporters. The experimental data fully supported that hydrophobicity favorably contributed to a high transport activity,

since a more hydrophilic version caused insignificant anion transportation. They exhibited a remarkable exchange of  $\text{Cl}^-$  and  $\text{HCO}_3^-$  in model liposomes that correlated with their high cytotoxicity. Cell viability was tested in differentiated and CSC and the results showed that the most active anion transporters were able to significantly reduce CSC viability. In addition, these two molecules induced cytoplasmic pH acidification after 1 h of treatment, being a sufficient change to trigger apoptotic processes in cells. Finally, these tambjamines also proved to induce plasma membrane hyperpolarization, leading to suppression of stemness properties, which caused cell differentiation and effective elimination of this cell population.

#### 1.1.3.4. FDA-approved nanosystems applied to LC

Among the targeted therapies, there are also nanosystems in the market, approved by the FDA, to treat different types of LC. However, despite of the intensive research specifically focused on this disease, there are only two of them that have reached the market to date, Genexol-PM and Abraxane (**Figure 14**).

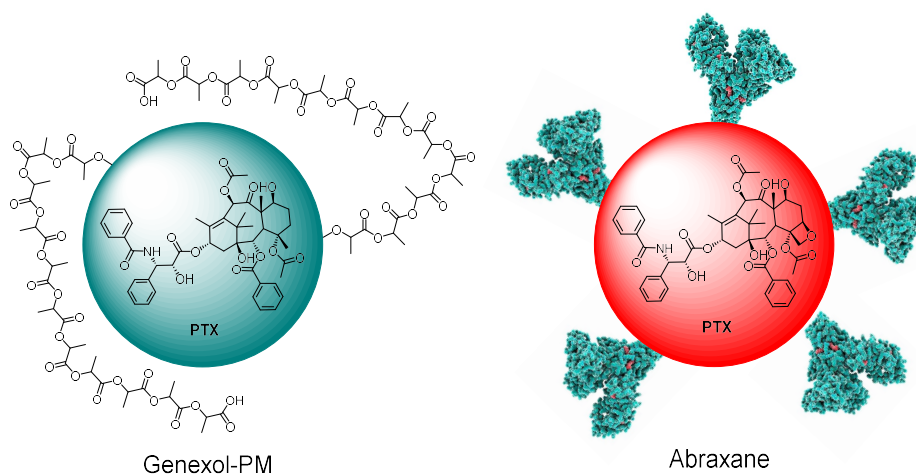


**Figure 14.** Graphic representations of Genexol-PM and Abraxane

On one hand, Genexol-PM is based on 20–50 nm PTX-loaded micelles formed by self-assembly of PEG and polylactide polymers for the treatment of SCLC. This copolymer increases the water-solubility of the drug and allows the delivery of a higher doses than the drug alone.<sup>52,53</sup>

On the other hand, Abraxane is based on albumin-bound paclitaxel nanospheres of around 130 nm, developed for the treatment of NSCLC. Albumin serves as a carrier and is highly appropriate due to its preferential uptake in tumors and inflamed tissues. In previous reports, the benefits of Abraxane have been associated with fewer acute adverse reactions and a significant reduction in healthcare resources rather than a successful performance in improving survival.<sup>52,53</sup>

## 1.2. Neuroblastoma

### 1.2.1. Origin

Neuroblastoma (NB) is the most common malignancy found in childhood. It is diagnosed at the average age of 17 months and affects 10.2 cases per million children under the age of 15.<sup>54,55</sup> NB is an embryonal solid tumor of the autonomic nervous system, which is originated in the neural crest tissues. The neural crest is a critically important structure that is present only during embryogenesis and gives rise to diverse cell types, including peripheral neurons, enteric neurons and glia, melanocytes, Schwann cells, and cells of the craniofacial skeleton and adrenal medulla.<sup>55</sup>

The tumors typically arise in the adrenal medulla (70% of the cases) or paraspinal ganglia, and can be presented as mass lesions in the chest (20%), neck (5%), abdomen or pelvis (5%) (**Figure 15**).<sup>56</sup>

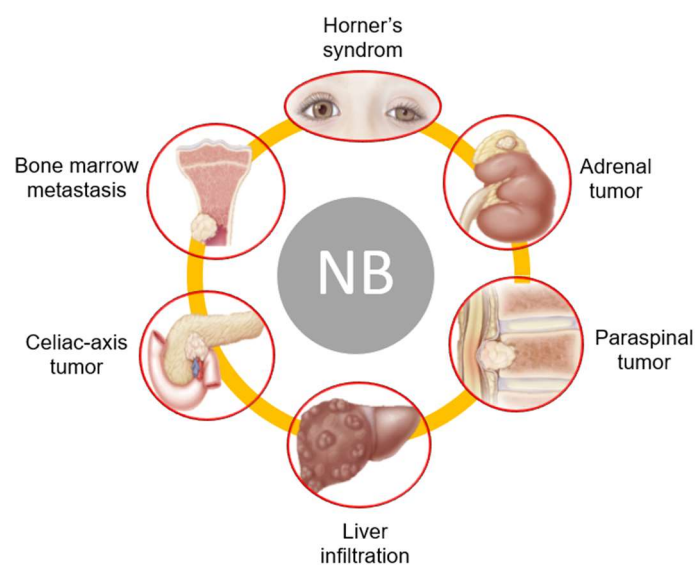


**Figure 15.** Different clinical presentations of NB. Adapted from reference 56

Primary tumors in the neck or upper chest can cause the Horner's syndrome and those along the spinal column can lead to cord compression, resulting in paralysis. Although several cases of lower-stage NB are encapsulated and can be surgically excised, higher-stage tumors often infiltrate local organs like the liver, surround critical nerves, such as the celiac axis and are largely unresectable at the time of diagnosis. NB typically metastasizes to regional lymph nodes and to the bone marrow and these tumor cells can infiltrate cortical bone.<sup>55,56</sup>

The clinical presentation is highly variable, ranging from a mass that causes no symptoms to a primary tumor that leads to a critical illness as a result of local invasion, widely disseminated disease or both.<sup>56</sup>

Four categories are established in terms of 5-year event-free survival rates: very low risk (>85%), low risk (75–85%), intermediate (50–75%) and high risk (<50%). These groups are based on the age, tumor stage, histologic category, grade of tumor differentiation and DNA-ploidy, among others.

### **1.2.2. *Epidemiology and prognostics***

The prevalence of NB is about one case in 7,000 live births and there are about 700 new cases per year in the US, although this incidence is relatively uniform throughout the developed countries.<sup>54</sup>

On one hand, NB accounts for very high morbidity and mortality among the cancers of childhood and, on the other hand, it is associated with one of the highest proportions of spontaneous and complete regression of all human cancers. The outcomes in patients with NB have improved in the last years, with 5-year survival rates increasing from 52% to 74% in approximately 10 years. However, such an improvement has not been observed with children suffering from high-risk NB, despite receiving dramatic escalations in the intensity of the therapy provided.

Most children experience complete regression of the disease by minimal therapy, even with metastatic disease. However, older patients frequently have a metastatic disease that grows relentlessly, despite of the most invasive multimodality therapy. Whether a patient will evolve to one or the other direction primarily depends on age, the stage of the disease at diagnosis and the molecular, cellular and genetic features of the tumor.

### 1.2.3. Treatments

#### 1.2.3.1. Conventional treatments

The treatment applied in each case is based on the stage and risk group of the patient. For instance, surgery is often applied in low-risk NB when the tumor is localized, not located near vital structures and not wrapped around large blood vessels. In this case, as much of the tumor as possible is removed and usually, chemotherapy or radiotherapy are applied afterwards in order to eliminate the remaining cancer cells.<sup>57</sup>

In contrast, current treatments for intermediate- to high-risk NB depend mainly on medium to high-dose chemotherapy and can be divided into three different phases: induction of remission, consolidation of the remission and a maintenance phase to eradicate residual disease.<sup>56,58</sup> Chemotherapy for NB usually includes dose-intensive cycles of cisplatin or carboplatin (**Figure 2**) and etoposide alternating with vincristine, doxorubicin and cyclophosphamide. Recently, topotecan was also added due to its anti-NB activity in cases of relapse<sup>54,56,57</sup> (**Figure 16**).

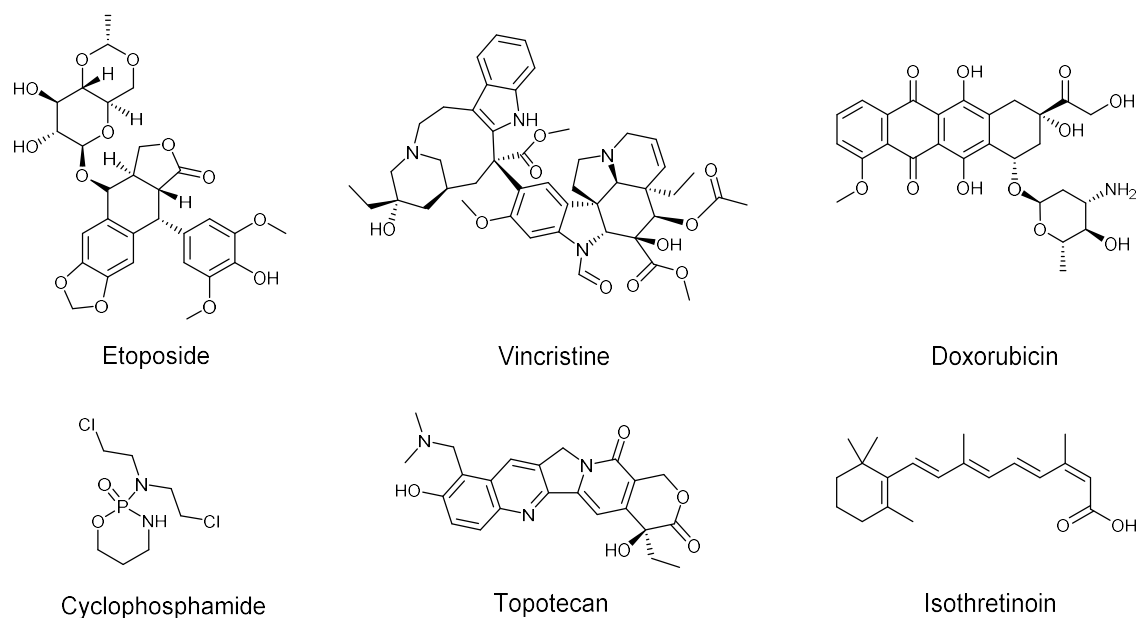


**Figure 16.** The most common chemotherapeutic agents for NB treatment

In addition, external-beam radiotherapy is most of the times applied in high-risk patients in order to shrink the tumor before surgery or to destroy remaining NB cells.

Giving higher doses of chemotherapeutics (and sometimes radiation) might be more effective in treating high-risk NB, but unfortunately, such an invasive treatment often causes severe damage to the bone marrow, leading to life-threatening shortages of blood cells. The only solution is to replace the patient's bone marrow cells by new ones through the so-called stem cell transplant.<sup>57</sup>

Most of the high-risk NB initially respond to chemotherapy, but ultimately relapse. Therefore, there is a growing interest in developing agents that can attack residual NB cells. Well-known examples are retinoic compounds, which induce NB cell lines terminal differentiation into normal cells upon their exposure. In fact, 13-*cis*-retinoic acid (isotretinoin) (**Figure 16**) decreases NB cells proliferation<sup>54,59</sup> and when applied after high-dose chemotherapy and stem cell transplant, the risk of relapse is significantly reduced.<sup>56,58</sup>

#### 1.2.3.2. Targeted therapies

Among the targeted therapies, the treatment with the antiGD2 mAb to prevent NB relapse after a cytotoxic therapy is maybe the most extended one.<sup>56,58,60</sup>

GD2 is a disialoganglioside antigen that is expressed in tumors of neuroectodermal origin, including NB and melanoma, with relatively little heterogeneity between cells. Moreover, GD2 expression in normal tissues is restricted to skin melanocytes, peripheral pain fibers and the brain, which is inaccessible to circulating antibodies.<sup>58,61</sup>

AntiGD2 mAbs, such as chimeric 14.18 (Ch14.18) and 3F8, have been tested in clinical trials for NB for over the past two decades and have shown antitumor activity via antibody-directed cellular cytotoxicity and complement-mediated cytotoxicity.<sup>58,62</sup> However, antiGD2 mAb requires the co-administration of other agents, such as interleukin-2 and granulocyte-macrophage colony-stimulating factor, in order to result in a therapeutic effect. In addition, other disadvantages that limit the use of the antiGD2 are the acute pain associated with GD2 expression on peripheral nerves and the inability of antibodies to treat bulky tumors.<sup>56,60</sup> Despite

these hurdles, antiGD2 mAb has still been exploited as a potential targeting agent to specifically detect and deliver chemotherapeutics in NB cell lines.<sup>60,62,63</sup>

Other examples of targeted therapies are related to the presence of norepinephrine on the cell surface of NB. Scientists have taken advantage of this molecular target to deliver high levels of radiation to NB cells. Finally, the discovery of NB-predisposition genes, such as *ALK*, has allowed the exploration of their inhibition of a targeted therapeutic approach. In fact, preclinical data has shown high effectivity in cell models that harbor *ALK* mutations or amplifications and are providing the basis for an early-phase clinical trial.<sup>56,64</sup>

## 2. Objectives

The objectives of the present Chapter are:

- **The nanoencapsulation of tambjamines T17 and T18** through the methodology presented in Chapter 2 and its optimization.
- **The physicochemical characterization** of the resulting NCs, in terms of morphology, average particle size, surface charge modulation in different pH conditions, EE and DL.
- **The biological characterization** of the most promising NCs in terms of cell viability (LC cell lines, NB cell lines and a normal cell line), cell uptake and cell internalization in physiological conditions and slightly acidic conditions that mimic the tumor microenvironment.
- **The study of the *in vivo* biodistribution** of two types of NCs, amphoteric and antiGD2-functionalized NCs, in a mouse NB model. Determination of the relative accumulation of the nanosystems in tumor, organs and plasma.

## 3. Results and discussion

T17 and T18 were selected due to their outstanding biological activity in different types of LC and NB cell lines and CSC. In addition, they were preferred among other analogs because of their increased hydrophobicity, a feature that should made amenable to nanoencapsulation though the methodology described in

Chapter 2. The strategy followed to study the nanoencapsulation of T17 and T18 is depicted in **Figure 17**.

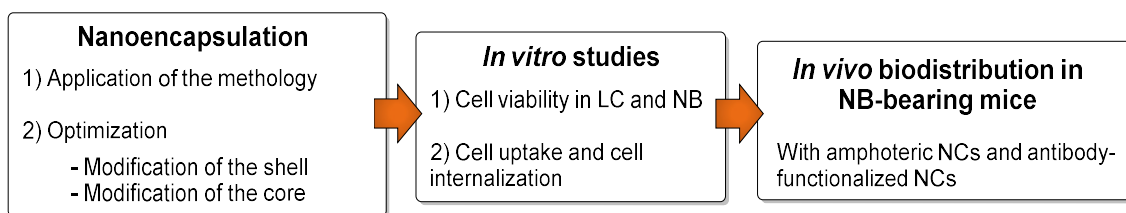


**Figure 17.** Nanoencapsulation and biological studies of T17 and T18

The approach started with the nanoencapsulation of both tambjamines, firstly by just applying the methodology presented in the previous Chapter and, secondly, by modifying the process, regarding the NC shell and the NC core. Some changes had to be introduced into the design because tambjamines are not purely hydrophobic entities, but amphiphilic. It should be recalled that ionophores change their hydrophobicity when coordinating ions or penetrating membranes. Thus, this dynamic behavior can hamper their encapsulation by the process presented previously.

Once the NCs were synthesized, they were analyzed according to their morphology, size, surface characteristics, DL and EE through different analytical techniques. The best nanoencapsulated candidates were further studied *in vitro* with LC and NB cell lines, determining their cytotoxicity, cell uptake and internalization mechanisms. Finally, *in vivo* biodistribution studies were carried out in a NB mice model with amphoteric and antiGD2-functionalized NCs.

It should be noted that part of the work shown in the present Chapter is the result of a collaboration with the Department of Chemistry of the University of Burgos (UBU), who kindly provided **T17** and **T18** for their nanoencapsulation. In addition, the *in vitro* studies performed in both LC and NB resulted from another well-established collaboration with the Department of Pathology and Experimental Therapeutics of the University of Barcelona (UB). Finally, the *in vivo* biodistribution studies were performed at the Functional Validation and Preclinical Research laboratory of Vall d'Hebron Research Institute (VHIR).

### 3.1. Application of Chapter 2 methodology

#### 3.1.1. Preparation of the NCs

The first set of nanocapsules were prepared in three different loading capacities, in terms of % wt: low ( $5 < DL < 7$ ), medium ( $7 \leq DL < 9$ ) and high ( $DL > 9$ ), as shown in **Table 1**.

**Table 1.** Summary of the first trials using the developed methodology

Sample code	Tambjamine	Drug concentration
<b>T17-AMP-L NCs</b>	17	Low (L)
<b>T18-AMP-L NCs</b>	18	Low (L)
<b>T17-AMP-M NCs</b>	17	Medium (M)
<b>T18-AMP-M NCs</b>	18	Medium (M)
<b>T17-AMP-H NCs</b>	17	High (H)
<b>T18-AMP-H NCs</b>	18	High (H)

The first two trials, **T17-AMP-L NCs** and **T18-AMP-L NCs**, were performed as preliminary tests to study the ability of **P1** polymer to nanoencapsulate these amphiphilic compounds in low concentration and the drug content was increased in the rest of the trials.

The preparation of these NCs was performed according to the process described in **Scheme 11** of Chapter 2. Briefly, polymer **P1** was used to dissolve **T17** or **T18** and the resulting mixture was transferred into a reactor containing IPDI. Since **P1** is an amine-reactive polymer, it instantaneously reacted with an excess of IPDI, becoming an NCO-reactive polymer (**P1** reactivation). Then, L-lysine sodium salt was added and the organic phase was emulsified with water to yield an o/w nanoemulsion. Finally, DETA ended the process by crosslinking the NCO-reactive sites along the polymer micelles and forming polyurethane/polyurea NCs. The nanoencapsulation reaction was monitored by IR spectroscopy (**Figure 18**) as reported in the experiments of Chapter 2.

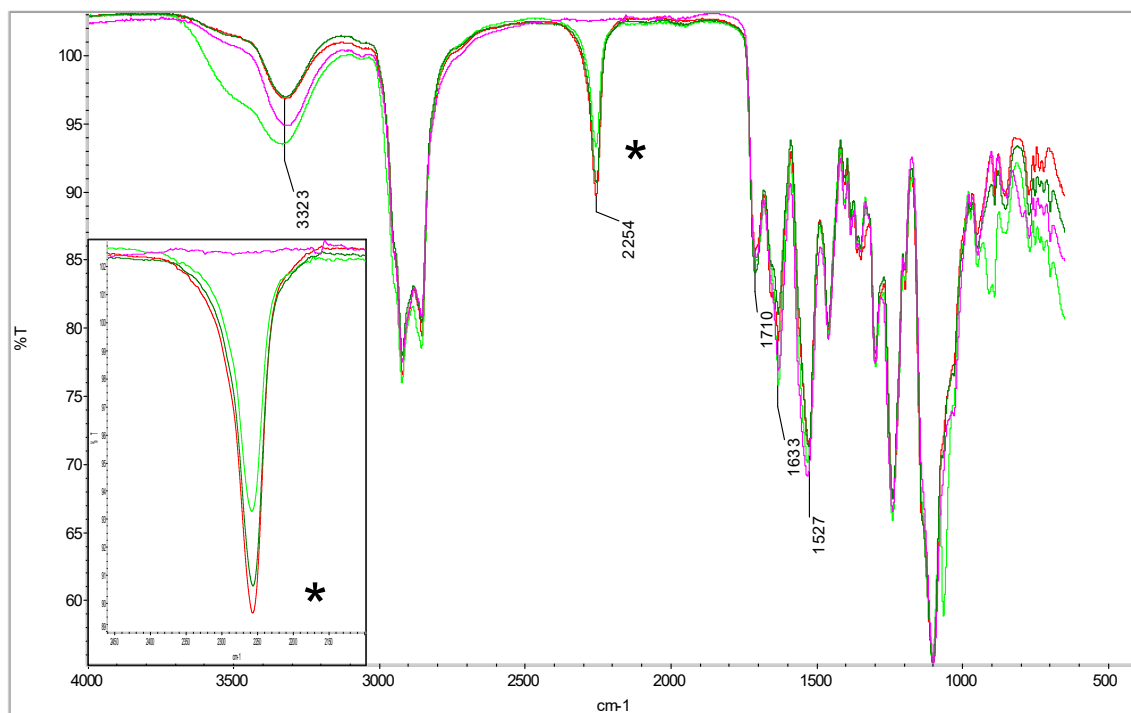


**Figure 18.** IR spectra showing the different steps of the nanoencapsulation process

The red line in the IR spectra corresponds to the sample when **P1**, along with the drug, was mixed with IPDI and the dark green line represents this reaction after 30 min. In this step, the intensity of the NCO stretching band at  $2254\text{ cm}^{-1}$  decreased slightly, confirming the isocyanate consumption. Afterwards, L-lysine sodium salt was added and reacted with the previously activated **P1** polymer. The sample was analyzed after 45 min (light green line) and another decrease on the intensity of the NCO stretching band was observed, concomitantly with the increase of the carbonyl and CN stretching bands, confirming urea formation ( $1633\text{ cm}^{-1}$  and  $1527\text{ cm}^{-1}$  respectively). Finally, DETA was added and the sample was recorded after 5 min (pink line). The NCO stretching band instantaneously disappeared and the urea-associated bands increased their intensity as a result of the rapid reaction between remaining NCO groups and this polyamine.

The last stage of the nanoencapsulation, the crosslinking step, was also monitored by measuring the pH changes in the nanoemulsion (**Figure 19**).

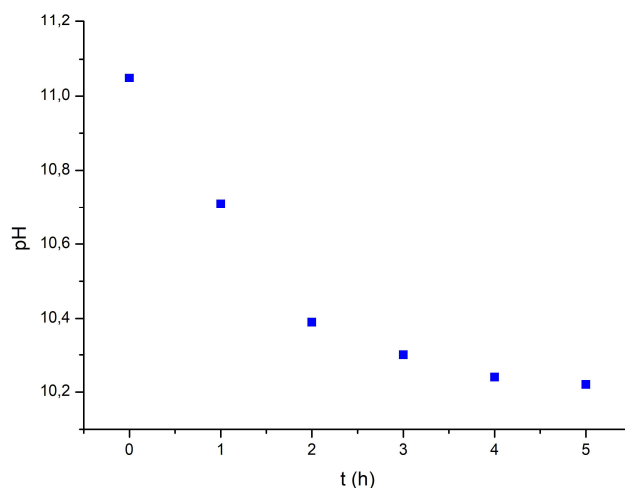


**Figure 19.** pH of the nanoemulsion after the addition of DETA

The pH of the medium was high at the moment DETA was added but it rapidly decreased indicating the reaction between the amines from DETA and the remaining NCO groups from the NCs. After crosslinking the NCs, they were dialyzed in order to remove the non-reacted monomers, salts and other small molecules present in the nanoemulsion.

### 3.1.2. Characterization of the NCs

#### 3.1.2.1. Morphology and size

After confirming that the nanoencapsulation proceeded as expected, the morphology and the size of this set of NCs was studied by TEM and DLS, respectively. **T17-AMP-L NCs** and **T18-AMP-L NCs** were not characterized in detail because they uniquely served as preliminary tests to validate these tambjamines could be nanoencapsulated. The morphology of **T17-AMP-M NCs**, which was taken as a reference, was studied by TEM (**Figure 20**).

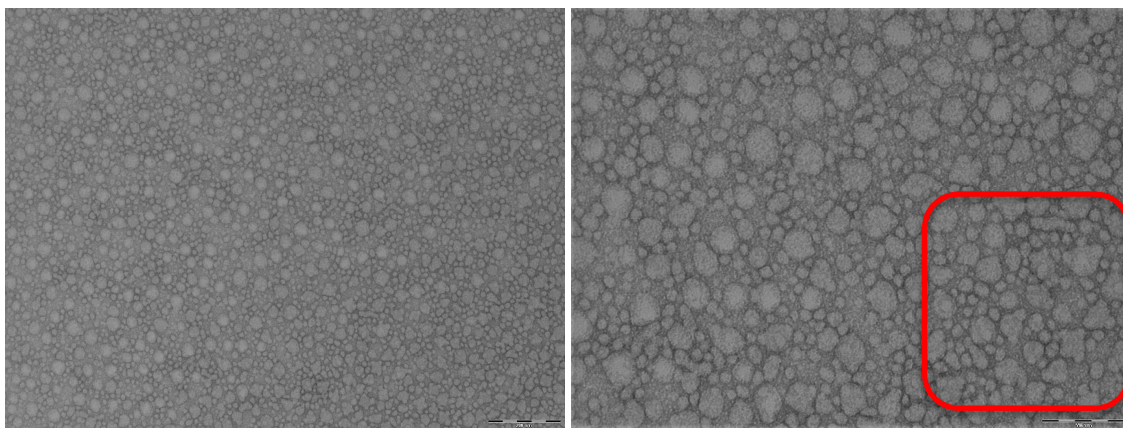
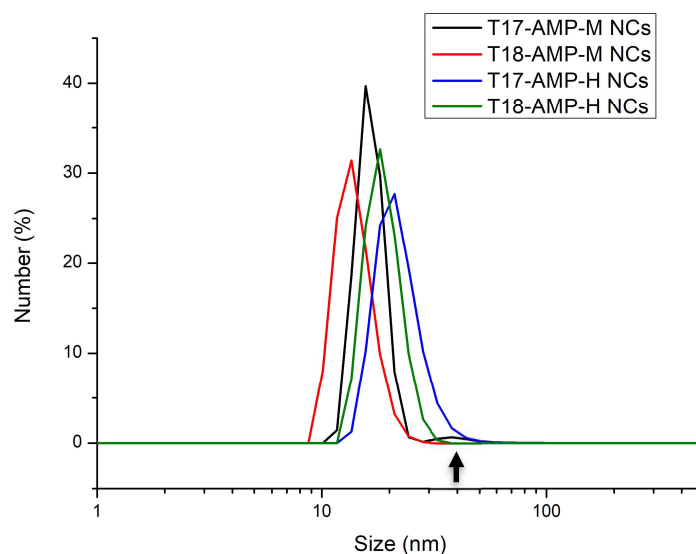


**Figure 20.** TEM micrographs of **T17-AMP-M NCs**. Scale bars: left = 200 nm; right = 100 nm

The image on the left showed a panoramic view of the sample while the one on the right was the zoom of a random zone. The results indicated a heterogeneous sample consisting of two differentiated particle populations. Both particle sizes presented irregular shapes, with the larger ones being roughly double in diameter than the smaller ones. Moreover, some of the large NCs seemed to be composed of the aggregation of the small particles, as highlighted in the red square. These observations could be the result of Ostwald ripening effects,<sup>65-67</sup> where the small drops dissolve and redeposit their material onto larger entities to reach a higher thermodynamic stability. The results obtained by TEM analyses were further confirmed with the study of the particle size distribution of the NCs by DLS (**Figure 21**).



Sample code	Mean $\bar{\phi}$ (nm)	SD (nm)	PDI
T17-AMP-M NCs	15.69	3.95	0.06
T18-AMP-M NCs	13.55	3.12	0.05
T17-AMP-H NCs	21.03	6.29	0.09
T18-AMP-H NCs	18.17	3.30	0.03

**Figure 21.** Particle size distribution of four different versions of NCs containing T17 and T18

The particle size distributions of the samples were not as homogeneous as the ones obtained with purely hydrophobic cargos (Chapter 2). **Figure 21** shows the appearance of a larger subpopulation of NCs in the **T17-AMP-M NCs** sample, highlighted with the arrow.

The average particle sizes were comprised between 13.55 nm and 21.03 nm. It can be observed that the higher the drug loading (**T17-AMP-H NCs** and **T18-AMP-H NCs**), the larger the diameter of the NCs. SDs and PDIs values were acceptable, although the distributions were fairly broad, probably because of the coexistence of two different particle populations.

### 3.1.2.2. Surface properties

The surface charge was studied in the four versions of NCs and a control sample (**BLANK-AMP-2 NCs**) that consisted on unloaded NCs. The study was performed by measuring the  $\zeta$ -pot of diluted samples at two different pH values, 6.50 and 7.50 (**Figure 22**). These two values were selected because the shell cationization due to Jeffcat DPA monomer was expected to occur between this pH range.

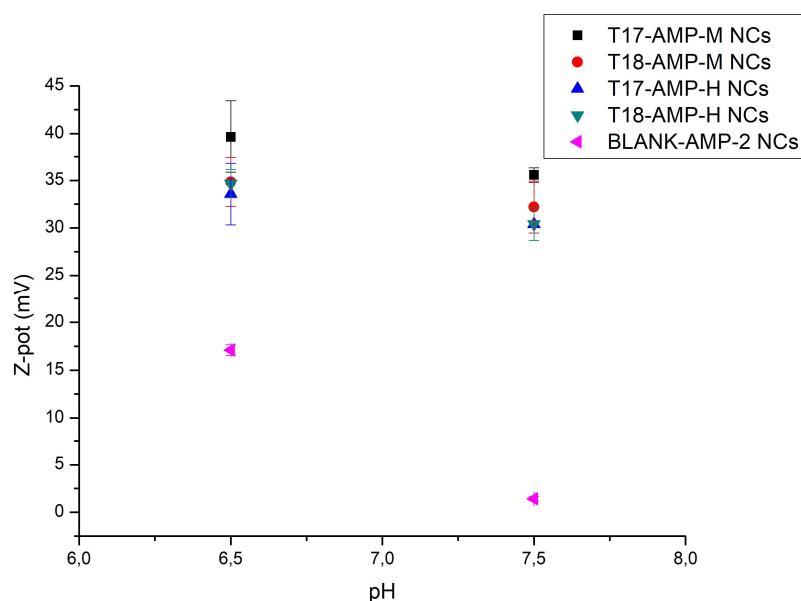


**Figure 22.**  $\zeta$ -pot of some of the NCs including the blank NCs

As seen in this figure, the  $\zeta$ -pot of the tambjamine-loaded NCs was much higher than the unloaded NCs, regardless the pH conditions. These results suggest that the nanosystems were invariably cationic and did not respond to the selective shell protonation observed in Chapter 2. Furthermore, the error bars associated to these results were considerable, indicating unhomogeneous NCs surface.

In contrast, blank NCs showed very different patterns of cationization, which were very similar to those observed with NCs loading purely hydrophobic drugs (Chapter 2). In this case, the surface showed almost neutral properties at physiological conditions, while it cationized when the pH of the medium decreased, reaching values in the +15 to +20 mV range.

Overall, it can be confirmed that the cationization pattern observed with tambjamine-loaded NCs was due to the physicochemical properties of the drug and its presence close to the NC surface. These conclusions are in line with the nanostructuring of the polymer wall explained in the previous Chapter. According to the hydrophobic/hydrophilic gradient created in the micelles, the hydrophobic elements are placed in the interior in order to avoid their contact with the external aqueous medium. In contrast, hydrophilic molecules tend to orient outwards so that they can establish favorable interactions with water molecules. Therefore, tambjamins, that are composed of a polar protonable moiety and a hydrophobic substituent, do not have a clear location in the NC and they prefer to accommodate close to the interface. **Figure 23** tries to provide a feasible hypothesis of the way tambjamine-loaded NCs are nanostructured.

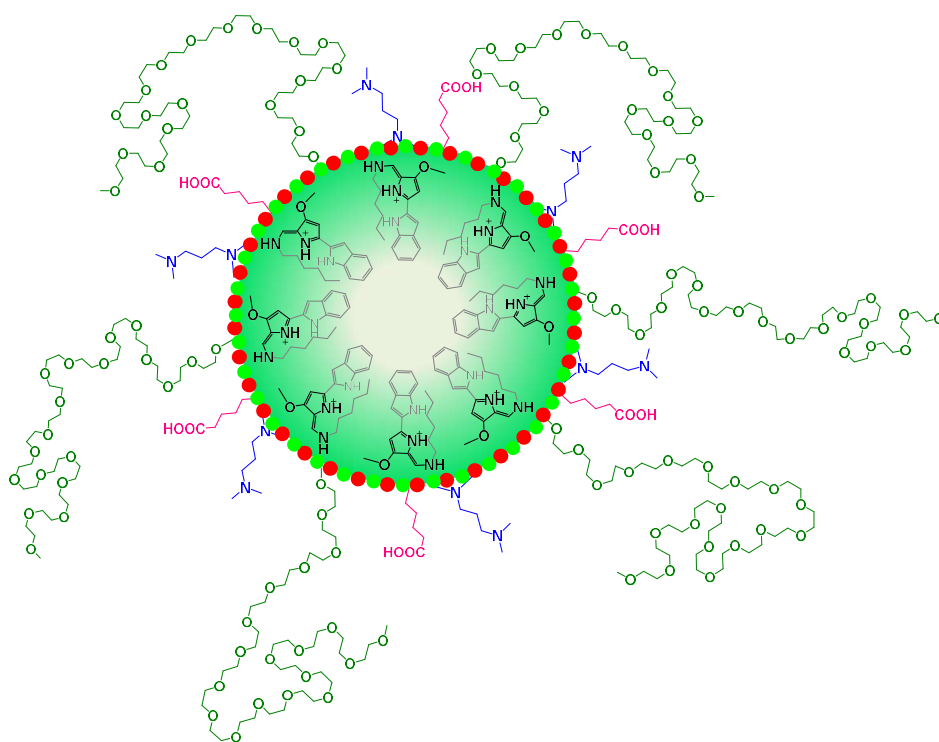


**Figure 23.** NC zoom showing the position of T17 inside the core

As it can be seen in this figure, the more polar groups marked in black tend to approximate the surface, whereas the hydrophobic tails highlighted in grey behave the opposite way and point inwards.

### 3.1.2.3. Encapsulation efficiency and drug loading

Besides the morphology, size and surface properties of tambjamine-loaded NCs, the DL and EE were also analyzed (**Table 2**).

**Table 2.** EE and DL values and their respective SD for tambjamine-loaded NCs

Sample code	EE (% wt)	DL (% wt)
T17-AMP-M NCs	37.39 ± 3.57	3.26 ± 0.31
T18-AMP-M NCs	36.59 ± 1.45	2.87 ± 0.11
T17-AMP-H NCs	38.67 ± 0.98	3.43 ± 0.90
T18-AMP-H NCs	25.87 ± 3.26	2.29 ± 0.29

The EE values were relatively low in all cases, meaning that more than half of tambjamine added did not incorporate into the NC. The most feasible explanation is that tambjamines are initially entrapped into the polymer matrix but once the NCs are crosslinked and dialyzed, they eventually migrate outside the shell. **Figure 24** shows a picture of real example of tambjamine-loaded NCs purification.



**Figure 24.** Dialysis medium after 24 h of purification of tambjamine-loaded NCs

As shown in this image, the dialysis medium becomes yellow after the purification step. This provides a clear evidence of the presence of these drugs, which have a yellow/green color, in the external phase. Therefore, such low EE and

DL values can be the result of the tambjamine migration outside the NC during dialysis.

The physicochemical characterization of tambjamine-loaded NCs in terms of morphology, size, surface properties, EE and DL provided strong evidence that the methodology presented in Chapter 2 was not completely suitable to nanoencapsulate amphiphilic drugs. Therefore, changes on the synthetic procedure were required to better stabilize the tambjamins inside the NCs and prevent the alteration of the NC amphoteric properties and their premature leakage.

## 3.2. Optimization

### 3.2.1. Preparation of the NCs

In order to overcome the issues described in the previous section, some changes were applied to optimize the procedure to nanoencapsulate amphiphilic molecules. The optimization work was divided into two different strategies (**Figure 25**).

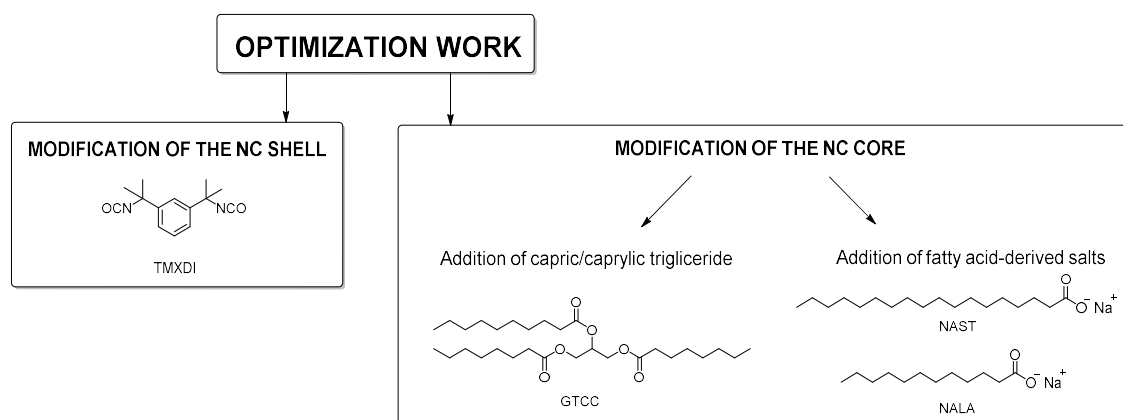


**Figure 25.** Organization of the optimization work

In both approaches, the general methodology developed previously was preserved and minor variations were applied. Firstly, the composition of the shell was modified by replacing the excess of IPDI by tetramethyl-1,3-xylylene diisocyanate (TMXDI). Secondly, the shell was slightly tuned by adding hydrophobizing oils or fatty acid-derived salts.

The first modification was intended to improve the stabilization of the encapsulated cargo by  $\pi$ - $\pi$  stacking interactions between the diisocyanate and the tambjamines. Through the establishment of these new interactions, the drug could be more prone to stay in the NC shell rather than diffuse across the polymer wall.

The second strategy was designed to increase the cargo hydrophobicity in order to be more encapsulable. Different agents were considered, such as medium-chain triglycerides (GTCC) or fatty-acid derived salts (sodium stearate, NAST, and sodium laurate, NALA). GTCC was added at a concentration of 1% wt. of solids and both NAST and NALA were incorporated according to the necessary equivalents to neutralize the positive charges of tambjamines.

**Table 3** classifies the different NCs developed in the optimization part according to the changes applied in the shell and the addition of hydrophobizing agents in the core.

**Table 3.** Shell and core change as part of the optimization work

Code	Tambjamine	Shell change	Core change
<b>T18-TMXDI-AMP NCs</b>	T18	TMXDI	⊗
<b>T18-GTCC-AMP NCs</b>	T18	⊗	GTCC
<b>T18-TMXDI-GTCC-AMP NCs</b>	T18	TMXDI	GTCC
<b>T18-NAST-AMP NCs</b>	T18	⊗	NAST
<b>T17-NAST-AMP NCs</b>	T17	⊗	NAST
<b>T18-NALA-AMP NCs</b>	T18	⊗	NALA

The first trial was performed by replacing IPDI used in the reactivation of **P1** by TMXDI, an aliphatic diisocyanate containing an aromatic moiety. In this case, the NCs only contained T18 as a hydrophobic core. Secondly, a change on the core composition was applied by adding GTCC as a hydrophobizing agent, along with T18. After that, both GTCC and TMXDI were included in the nanoencapsulation and finally the salts derived from fatty acids, NAST and NALA, were tested in the core. Overall, the nanoencapsulation of T17 and T18 was performed by considering these

slight modifications and the resulting nanosystems were characterized by the typical analytical techniques after 24 h of dialysis.

### 3.2.2. Characterization of the NCs

#### 3.2.2.1. Morphology and size

The morphology and size were again studied for two types of optimized NCs, **T18-TMXDI-GTCC-AMP NCs (Figure 26)** and **T18-NAST-AMP NCs (Figure 27)**. These two versions were selected because the first one contained modifications both in the shell and in the core and therefore it was assumed they would lead to more morphological changes than those NCs bearing only one modification. The other sample was considered because it was also interesting to evaluate the effect of salts derived from fatty acids in the core of the NC. Among NAST and NALA, the former was selected because it was more prone to induce size and shape changes due to its longer hydrocarbon chain compared to the latter.

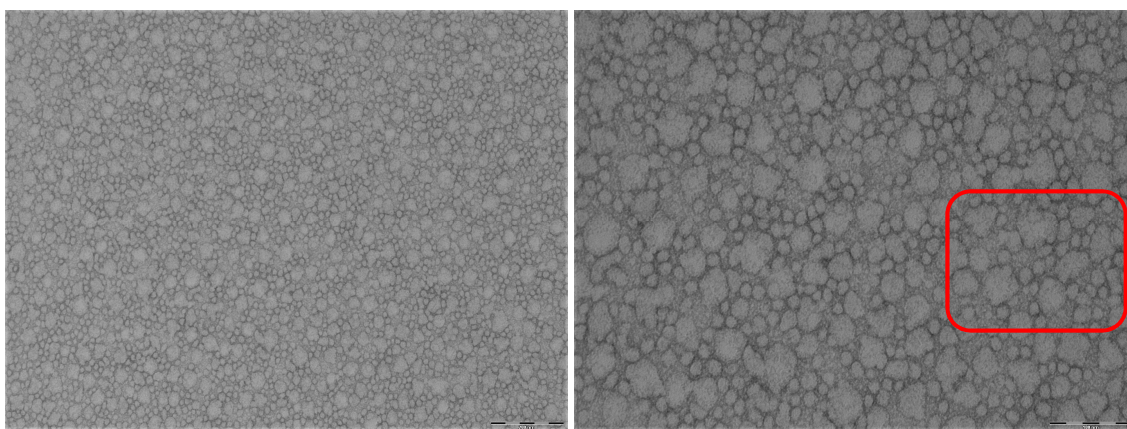


**Figure 26.** TEM micrographs of **T18-TMXDI-GTCC-AMP NCs**. Scale bars: left = 200 nm; right = 100 nm

According to **Figure 26**, the size distribution was not homogeneous, since two clear particle populations could be observed. The appearance of this sample was very similar to the previous one with the NCs without any modification (**Figure 20**). In addition, the large particles appeared as an aggregation of the small ones, suggesting Ostwald ripening events as a consequence of micelle destabilization during emulsion. The red square highlights large particles that have absorbed small

ones in their structure. This contrasts with the morphology of the sample containing NAST, shown in **Figure 27**.

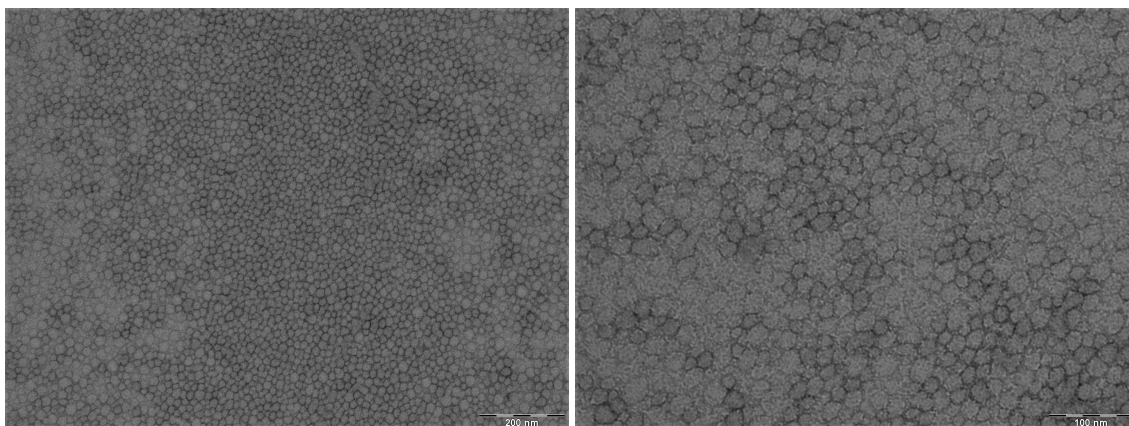
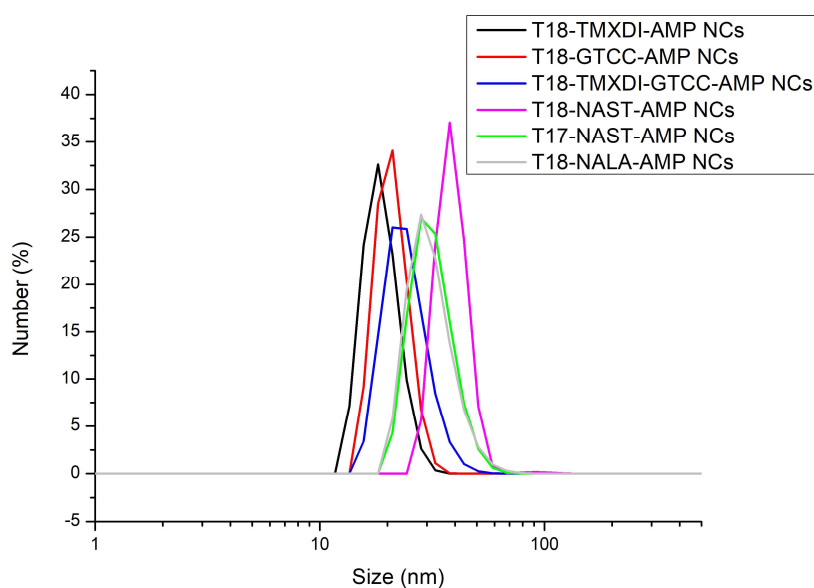


**Figure 27.** TEM micrographs of **T18- NAST-AMP NCs**. Scale bars: left = 200 nm; right = 100 nm

In this case, the micrographs showed more homogeneous particle sizes, since only one differentiated particle size population could be observed. Moreover, the size was similar to the NCs containing hydrophobic drugs (Chapter 2). Therefore, according to the morphological studies performed, NAST seemed to have a more positive effect in stabilizing the o/w interface than GTCC or TMXDI.

The particle size distributions were evaluated for all the optimized samples and a statistical analysis was also performed (**Figure 28**).



Sample code	Mean $\emptyset$ (nm)	SD (nm)	PDI
<b>T18-TMXDI-AMP NCs</b>	15.08	2.74	0.04
<b>T18-GTCC-AMP NCs</b>	16.63	4.09	0.05
<b>T18-TMXDI-GTCC-AMP NCs</b>	15.18	3.11	0.04
<b>T18-NAST-AMP NCs</b>	20.08	3.31	0.02
<b>T17-NAST-AMP NCs</b>	17.47	3.92	0.06
<b>T18-NALA-AMP NCs</b>	17.47	2.72	0.03

**Figure 28.** Particle size distribution of the different samples and statistical analysis

The average particle sizes were comprised between 15.08 nm and 20.02 nm. The samples having the smallest diameters corresponded to the NCs whose shell was composed of TMXDI, regardless the presence of GTCC (**T18-TMXDI-AMP NCs**, **T18-GTCC-AMP NCs** and **T18-TMXDI-GTCC-AMP NCs**). The samples showing larger sizes corresponded to the NCs loading a certain amount of fatty acid-derived salts along with the tambjamins (**T18-NAST-AMP NCs**, **T17-NAST-AMP NCs** and **T18-NALA-AMP NCs**). These results are coherent with previous analyses (Chapter 2), where the nanosystems containing a higher concentration of hydrophobic cargo

led to structures with larger diameters. Regarding the SD and PDI values, they were approximately in the range of the other versions of NCs.

### 3.2.2.2. Surface properties

The surface charge of the NCs bearing a modified shell and/or loading GTCC was evaluated by following the same procedures as described previously. In order to analyze the results more accurately, a sample of blank NCs (**BLANK-TMXDI-GTCC NCs**) was prepared containing both modifications. This was intended to evaluate whether the  $\zeta$ -pot obtained was due to the optimization made on the polymer wall or was attributed to the NC core. Therefore, the surface charge of the nanosystems was analyzed at the two significant pH values, 6.5 and 7.5 (**Figure 29**).

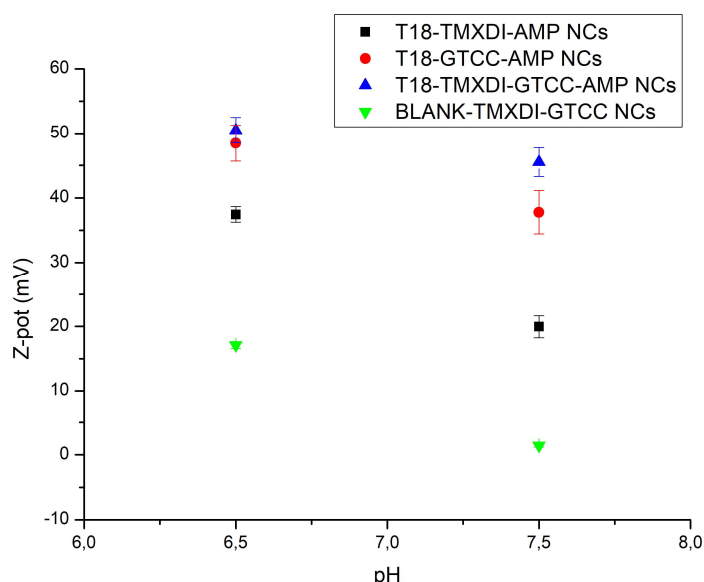


**Figure 29.**  $\zeta$ -pot of the optimized samples containing TMXDI/GTCC with the corresponding blank

According to this analysis, the surface charge of the NCs loading T18 (black, red and blue symbols) was clearly cationic in both pH conditions ( $\zeta$ -pot > +37 mV at pH = 6.5 and  $\zeta$ -pot > +19 mV at pH = 7.5). Such a highly positive charge could be attributed to the effect of T18 in the core of the NCs, since **BLANK-TMXDI-GTCC NCs** (light green symbol) showed the expected amphoteric behavior, with a neutral surface charge at pH 7.5 and slightly cationic properties under acidic conditions. These results suggest that the first attempt to optimize the NCs by introducing

TMXDI and/or GTCC did not lead to any improvement, since T18 was still not stabilized inside the NC core yet. This could be due to the presence of T18, which could be the responsible for the loss of nanostructuration at the o/w interface during emulsification, resulting in a diffuse shell. The higher SD obtained for T18-loaded NCs compared to their blank analogs also supported that the interface was not appropriately stabilized in the emulsion.

The same study was repeated with those NCs containing NAST or NALA, along with T17 or T18. In this particular case, given that the  $\zeta$ -pot values suggested an amphoteric pattern, the results were extended to the whole pH range from 5.5 to 8.0 (**Figure 30**).

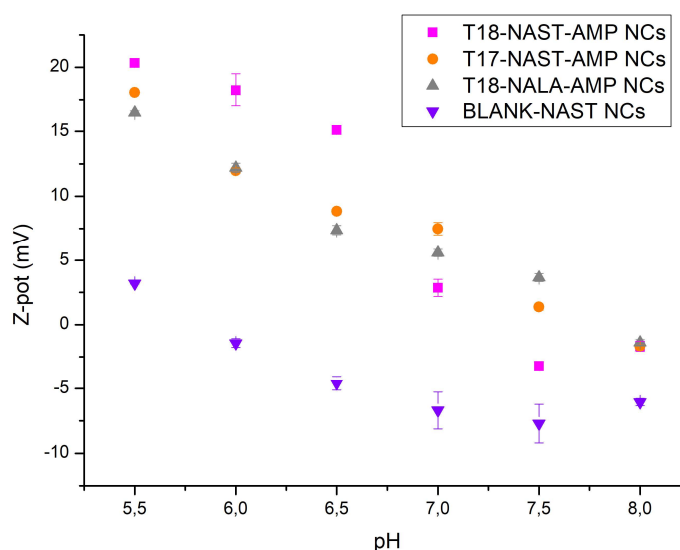


**Figure 30.**  $\zeta$ -pot of the optimized samples containing NAST/NALA with their corresponding blank

On one hand, the NCs containing T17/T18 and NAST/NALA (pink, orange and grey symbols) showed a more evident shell cationization in the pH range studied. At physiological conditions the surface charge was almost neutral ( $-3.5 \text{ mV} < \zeta\text{-pot} < +3.5 \text{ mV}$ ) while it became cationic under slightly acidic pH ( $\zeta\text{-pot} > 7.5 \text{ mV}$ ). On the other hand, the blank NCs loading NAST (**BLANK-NAST NCs**) presented the expected anionic properties in almost the whole pH range, due to the presence of the carboxylate moieties (from NAST) close to the NC surface. In this case, the SD associated to the values were narrower than in the previous studies, suggesting a more stabilized interface.

From the  $\zeta$ -pot studies, it can be concluded that the replacement of IPDI for TMXDI or the addition of GTCC did not lead into an enhanced stabilization of T18 inside the NC core. This resulted in the alteration of the shell nanostructuration by the presence of protonated moieties of the drug and the loss of the specific pH-cationization effect. However, by adding fatty acid-derived salts inside the core, the surface charge was neutralized and followed the amphoteric pattern that they were designed for. From these results, the presence of NAST and NALA could have two roles: firstly, it could serve merely as an anionic counterpart to neutralize the protonated amines of T17 or T18, and secondly, it could also stabilize them into the NC. This question was solved by analyzing the EE and the DL of the NCs.

### 3.2.2.3. Encapsulation efficiency and drug loading

Whether NAST and NALA behaved as anionic counterparts of tambjamins and/or stabilized them into the NCs, was evaluated by measuring the DL and EE, since an appropriate stabilization of the core would translate into an improvement of these parameters (**Table 4**).

**Table 4.** EE and DL values and their respective SD for optimized NCs

Sample code	EE (% wt)	DL (% wt)
<b>T18-TMXDI-AMP NCs</b>	37.79 $\pm$ 1.40	4.11 $\pm$ 0.15
<b>T18-GTCC-AMP NCs</b>	37.15 $\pm$ 3.83	4.00 $\pm$ 0.41
<b>T18-TMXDI-GTCC-AMP NCs</b>	34.47 $\pm$ 1.53	3.75 $\pm$ 0.17
<b>T18-NAST-AMP NCs</b>	43.89 $\pm$ 0.29	4.32 $\pm$ 0.03
<b>T17-NAST-AMP NCs</b>	48.43 $\pm$ 2.44	4.90 $\pm$ 0.25
<b>T18-NALA-AMP NCs</b>	68.28 $\pm$ 0.71	6.90 $\pm$ 0.07

The EE for the first three samples analyzed was relatively low and in the same range as the non-optimized NCs. The values were approximately 35% wt, which meant that 65% of the total amount of drug was discarded during nanoencapsulation and/or the dialysis purification. This resulted into a small concentration of drug entrapped inside the NC and therefore a low DL content.

However, those versions containing NAST and NALA afforded fairly improved values for these parameters. The NCs loading NAST showed an EE > 40% wt, while this value was enhanced until almost 70% wt in those having NALA in the core. The DL of these NCs were accordingly improved, being almost 7% wt the concentration of T18 in the NC after 24 h of dialysis.

### 3.3. *In vitro studies in LC and NB cell lines*

The best tambjamine-loaded NCs in terms of size, surface properties, EE and DL were also evaluated *in vitro* in terms of cell viability, cell uptake and cell internalization. The first one aims to study the concentration of NCs that induces 50% of inhibition of a specific biological or biochemical function, the IC<sub>50</sub> value. The second assay allows the determination of the efficiency by which the NCs permeate the cells after different incubation periods. Finally, the cell internalization aims to determine which penetration mechanism is preferred by the NCs.

The best candidates to be tested *in vitro* were **T18-NAST-AMP NCs**, **T17-NAST-AMP NCs** and **T18-NALA-AMP NCs**, since they showed an amphoteric behavior and they presented improved DL and EE values, compared to the previous versions. In this Chapter, though, the results are based on **T18-NAST-AMP NCs**, since the studies with **T18-NALA-AMP NCs** are still underway and **T18** was a more potent cytotoxic molecule than **T17**.

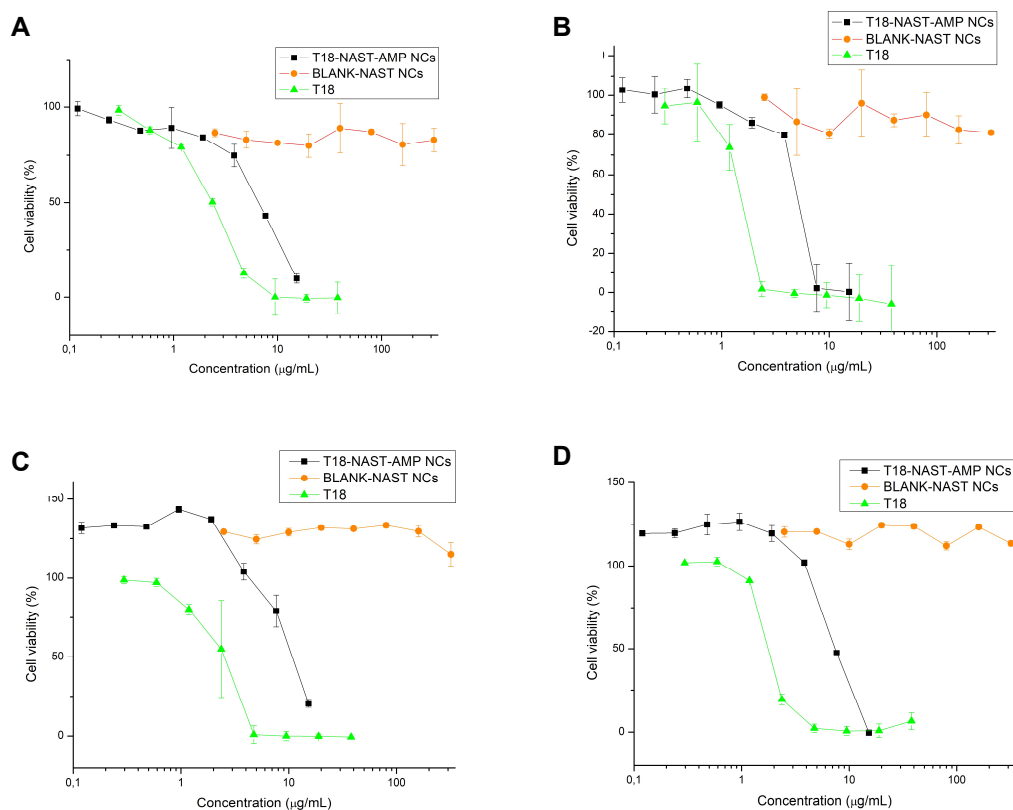
#### 3.3.1. *Cell viability*

##### 3.3.1.1. *LC cell lines*

Both A549 and H520 cancer cell lines belong to the NSCLC histological subtype, which accounts for 80–85% total LC cases. More specifically, A549 cells are adenocarcinomic human alveolar epithelial cells, while H520 are squamous carcinoma cells. DMS53 cell line was also selected because it represents one type of SCLC, which is responsible for the remaining 15–20% of the cases, is the most aggressive, the fastest growing and the most prone to induce metastasis. The cell viability was also studied in a non-cancerous LC cell line, HFL-1, in order to assess

whether the cytotoxicity of the **T18-NAST-AMP NCs** had different responses in cancer cells and in normal cells.

Cell viability in the A549 and H520 cell lines was calculated after 48 and 72 h of treatment with the NCs. These time periods were selected because the cytotoxic effect of the NCs was not expected to be immediate, given their intended controlled release. Therefore, the assays were planned waiting long enough for the cells to internalize the NCs, degrade the polymer shell and finally release the drug. The experiments included the free drug T18 and blank NCs (**BLANK-NAST NCs**) in order to take into account the effect of the polymer wall in the cytotoxicity observed in **T18-NAST-AMP NCs**. The cell viability curves for adenocarcinoma A549 and squamous cell carcinoma H520 cell lines are shown in **Figure 31**.



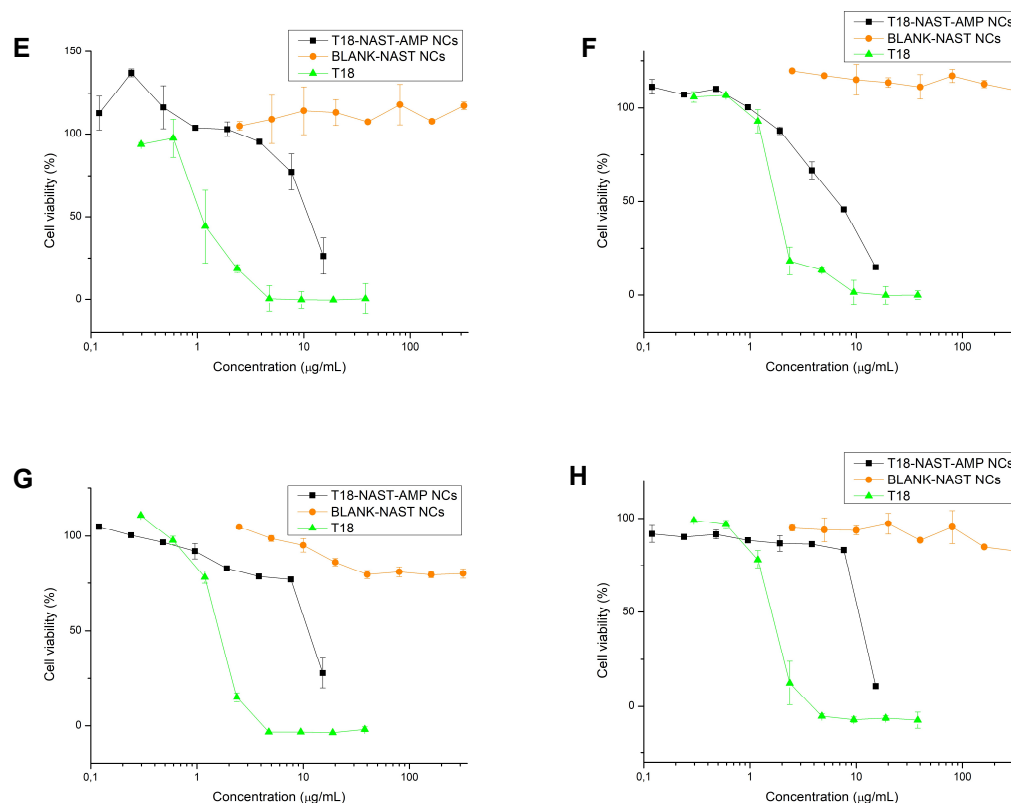


**Figure 31.** Cell viability curves in different cell lines and incubation periods. A) A549, 48 h; B) A549, 72 h; C) H520, 48 h; D) H520, 72 h; E) DMS53, 48 h; F) DMS53, 72 h; G) HFL-1, 48 h; H) HFL-1, 72 h

It can be observed that for **T18-NAST-AMP NCs** and **T18**, the cell viability decreased when the concentration of these substances increased. In contrast, **BLANK-AMP NCs** did not induce any significant cytotoxic effect in the concentration range assayed. The exact  $IC_{50}$  values were calculated for each case from the cell viability curves (**Table 5**).

**Table 5.**  $IC_{50}$  values in the LC and normal cell lines after 48 and 72 h of treatment

TYPE OF SUBSTANCE	MEAN $\pm$ SD ( $\mu\text{g T18/mL}$ )	
	<i>A549 (48 h)</i>	<i>A549 (72 h)</i>
<b>T18-NAST-AMP NCs</b>	$7.03 \pm 0.18$	$5.19 \pm 0.07$
<b>BLANK-NAST NCs</b>	> 320	> 320
<b>T18</b>	$2.61 \pm 0.57$	$1.52 \pm 0.04$
		<i>H520 (48 h)</i>
<b>T18-NAST-AMP NCs</b>	$7.85 \pm 0.22$	$7.47 \pm 0.14$
<b>BLANK-NAST NCs</b>	> 320	> 320
<b>T18</b>	$2.04 \pm 0.57$	$2.45 \pm 0.58$

	<i>DMS53 (48 h)</i>	<i>DMS53 (72 h)</i>
<b>T18-NAST-AMP NCs</b>	9.62 ± 2.11	7.76 ± 0.57
<b>BLANK-NAST NCs</b>	> 320	> 320
<b>T18</b>	1.59 ± 0.61	1.73 ± 0.71
	<i>HFL-1 (48 h)</i>	<i>HFL-1 (72 h)</i>
<b>T18-NAST-AMP NCs</b>	11.00 ± 0.78	10.75 ± 0.28
<b>BLANK-NAST NCs</b>	> 320	> 320
<b>T18</b>	2.10 ± 0.75	1.66 ± 0.05

On one hand, the cell viability in A549 cell line showed that IC<sub>50</sub> values of **T18-NAST-AMP NCs** were barely different between the two incubation times considered. In the case of H520 cell line, these differences were even less significant. However, in all cases studied, T18 showed a lower cytotoxicity when nanoencapsulated, since the IC<sub>50</sub> values were higher than those associated to the free drug. This observation agrees with the fact that the cytotoxic effect of nanoencapsulated T18 is not immediate and is a consequence of a process that involves cell internalization, polymer degradation and drug release. It is also likely that a certain fraction of the drug remains stabilized inside the NC shell and therefore does not induce a cytotoxic effect. Nevertheless, it is very important to emphasize that the therapeutic window with **T18-NAST-AMP NCs** is considerably broad since the **BLANK-NAST NCs** did not induce any important decrease on the cell viability at the concentration range studied.

Cell viabilities in DMS53 cell line showed that IC<sub>50</sub> values of **T18-NAST-AMP NCs** presented slight differences between the two time periods considered. In the case of HFL-1 cell line, these differences were less significant. Nevertheless, in the case of DMS53, T18 resulted into a slightly lower cytotoxicity than the previous cases, since the nanoencapsulated drug is approximately four times less cytotoxic than the free drug. Regarding the non-cancerous cell line, T18 seemed to induce a similar cytotoxic effect than cancerous cell lines but, surprisingly, **T18-NAST-AMP NCs** were less toxic to this normal cell line than in A549, H520 and DMS53. This result could suggest a slight selectivity of the NCs for the cancer cell lines. In all the cases studied, the therapeutic window was also wide, since the **BLANK-NAST NCs** did not induce any important decrease on the cell viability at the concentration range studied.

### 3.3.1.2. NB cell lines

Cell viability of **T18-NAST-AMP NCs** was studied in two different NB cell lines, CHLA90 and SKNB2. The results were compared to the blank NCs, **BLANK-NAST NCs**, and the free drug T18. The results of the cell viability curves are shown in the following graphs (**Figure 32**).

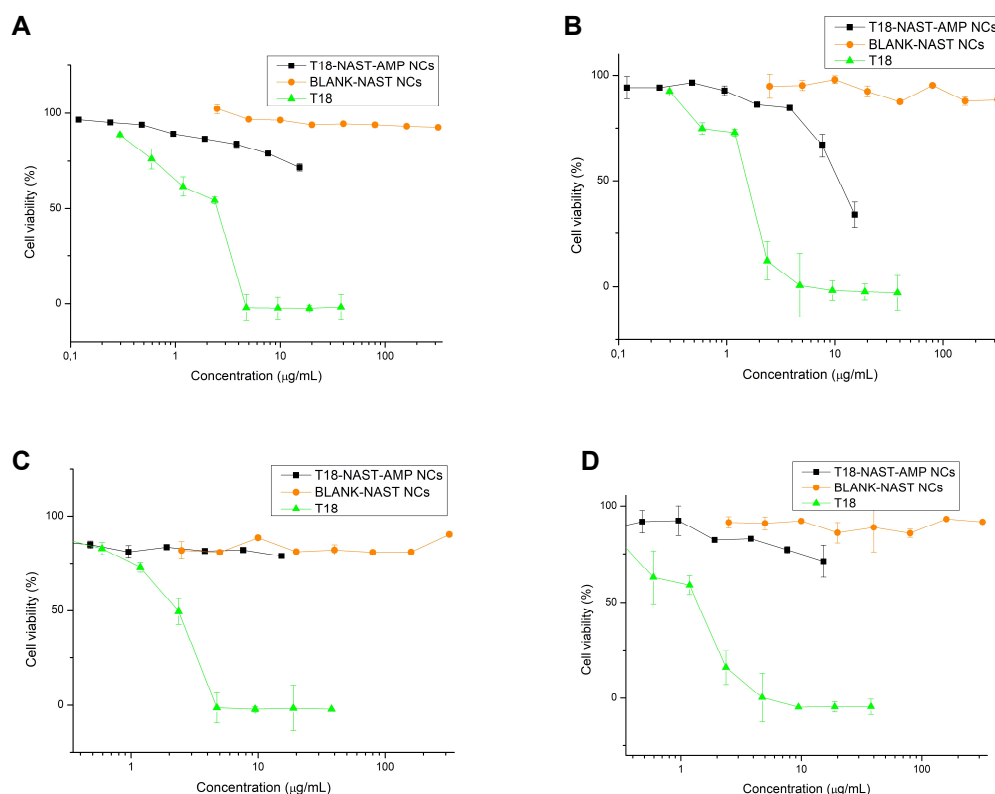


**Figure 32.** Cell viability curves in different cell lines and incubation periods. A) CHLA90, 48 h; B) CHLA90, 72 h; C) SKNB2, 48 h; D) SKNB2, 72 h

As seen in the previous figure, the cell viability for **T18-NAST-AMP NCs** and T18 induced cytotoxicity when the concentration increased. However, in the case of **BLANK-NAST NCs**, the cell viability was almost invariable in the whole concentration range assayed, indicating that the polymer shell is biocompatible. The exact  $IC_{50}$  values derived from these curves are detailed in **Table 6**.

**Table 6.** IC<sub>50</sub> values in CHLA90 and SKNBE2 after 48 and 72 h of treatment

TYPE OF SUBSTANCE	MEAN ± SD (µg T18/mL)	
	CHLA90 (48 h)	CHLA90 (72 h)
<b>T18-NAST-AMP NCs</b>	> 15.30	11.49 ± 0.97
<b>BLANK-NAST NCs</b>	> 320	> 320
<b>T18</b>	2.10 ± 0.74	1.73 ± 0.08
	SKNBE2 (48 h)	SKNBE2 (72 h)
<b>T18-NAST-AMP NCs</b>	> 15.30	> 15.30
<b>BLANK-NAST NCs</b>	> 320	> 320
<b>T18</b>	2.48 ± 0.16	2.52 ± 0.63

In this case, the cytotoxicity of the **T18-NAST-AMP NCs** could not be exactly determined in CHLA90 cell line (48 h) and SKNBE2 cell line (48 and 72 h), due to a technical limitation of the method. However, by analyzing these results, it can be concluded that, in general, NB cell lines were less sensitive to the tambjamine-loaded NCs than LC cell lines, since the IC<sub>50</sub> values obtained were higher. Finally, as observed in the previous *in vitro* cell viability tests, the control NCs (**BLANK-NAST NCs**) did not induce any significant cytotoxic effect.

### 3.3.2. Cell uptake

The second *in vitro* assay performed was the study of the NCs cellular uptake, which is the efficiency of the nanosystems to penetrate cells. In this case, the experiments were carried out with A549 cells, because LC is more common than NB and this specific LC subtype has a high incidence.

To perform the assay, the NCs were loaded with a fluorescent molecule, DiO, **DiO-AMP-2 NCs**, and were incubated with the cells for different periods of time, including unloaded NCs (**BLANK-AMP-3 NCs**) as a control. After each incubation time, they were washed several times to remove non-internalized NCs and were finally fixed with PFA. Therefore, those cells that had uptaken the NCs, the fluorescent-positive cells, could be detected by a specific laser of the flow cytometer. The cell uptake assay was divided into three different conditions regarding the pH used to perform the experiments. In this regard, besides performing the analyses at physiological conditions (pH = 7.4), the experiments were repeated with more acidic pH values (pH = 6.8 and 7.1). These extra measurements were included in order to evaluate whether the NCs were internalized more efficiently in slightly acidic

conditions (mimicking the tumor microenvironment) due to shell cationization as a result of the amphoteric effect.

### 3.3.2.1. Physiological conditions

The first assays were performed following the standard protocols at pH 7.4 in order to determine how efficiently NCs were internalized under normal conditions. Six different time periods were selected (1, 4, 8, 16, 24 and 48 h) and a control condition (non-fluorescent NCs) was included in the assay and applied at the longest time. The initial objective was to monitor the NCs cellular uptake using the same incubation times than cell viability assays (after 48 and 72 h of treatment), but due to technical difficulties, the incubation time had to be shortened, being 48 h the longest time studied.

The fluorescence detected by the cytometer was plotted against the incubation time and the results are shown in **Figure 33**.

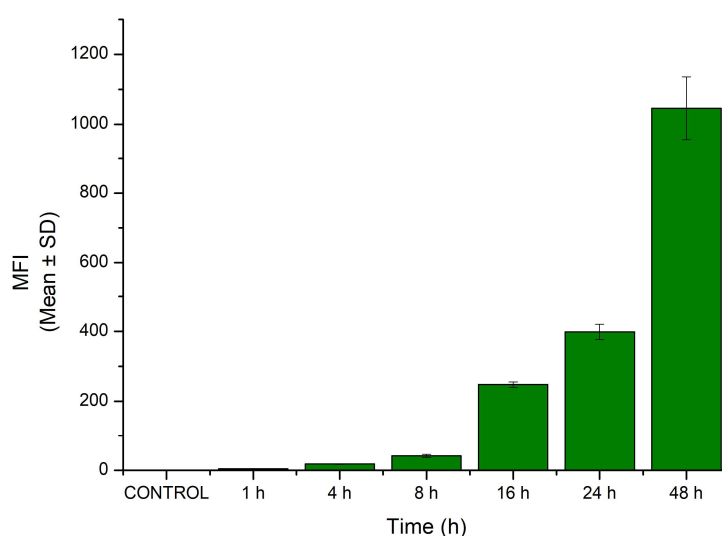


**Figure 33.** NCs cell uptake under physiological conditions

According to the graphic, the internalization of NCs depends on the incubation time, being the fluorescence low after 1 h of treatment and increasing 200-fold after 48 h. Interestingly, this experiment confirmed that the cells were not saturated after the 48 h-treatment, since the fluorescence continued increasing.

Although the fluorescence intensity at the shortest incubation time was low, the entire cell population was DiO-positive, according to the cytometer raw data (graphs shown in section 5 of the Annexes). Accordingly, all the cells had uptaken the NCs after 1 h of treatment, but after 48 h they continued internalizing them without reaching a saturation state or undergoing any toxic effect. Therefore, the physicochemical properties of the NCs are adequate for a long-term treatment.

### 3.3.2.2. *Slightly acidic conditions*

Some modifications of the protocol were applied in order to perform the assay in slightly acidic conditions. In this case, instead of using the standard growing medium, a HEPES buffer (at 15 mM) was prepared in order to keep the pH conditions at the initially established values. Three different volumes were separated and the pH was adjusted to 6.8, 7.1 and 7.4. The cells were seeded in the standard buffer and were let grow in these conditions until the next day, when the medium was removed and replaced by the new one having the desired pH. The cells were allowed to grow and adapt into the new pH conditions for another day and after that the treatment with **DiO-AMP-2 NCs** started. The time course selected was 1, 4, 8 and 24 h and the pH of each well was measured before washing and fixing the cells. By doing this, it could be assessed whether the pH conditions established at the beginning of the experiment were preserved along the treatment or were varied due to cell metabolism.

The results obtained from the cytometer are expressed in fluorescence mean for every incubation time at the three pH values studied (**Figure 34**).

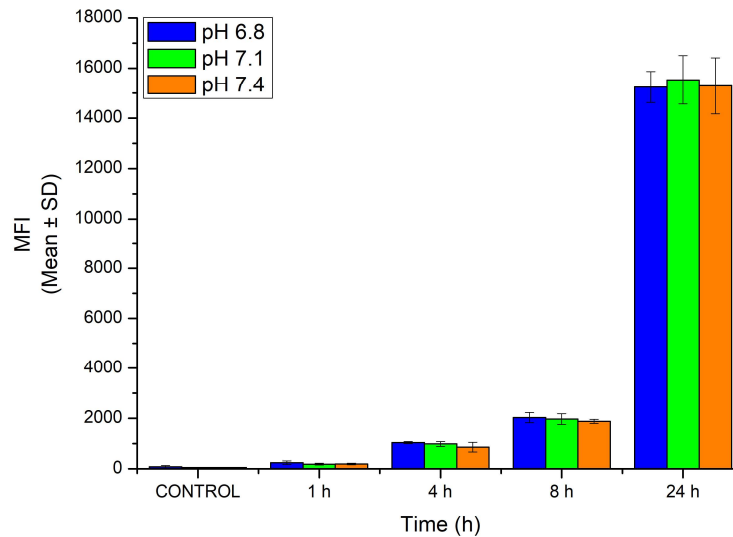


**Figure 34.** NCs cell uptake using media at different pH containing HEPES at 15 mM

The results of NCs cell uptake obtained in this assay were quite similar to those shown in **Figure 33**. The fluorescence mean increased over time and the values obtained in each time period were in the range of the previous studies. However, these results also point out that there was no statistically significant difference between the NCs uptake at each pH. These findings could be explained by analyzing the final pH measurements after each treatment (**Figure 35**).

171

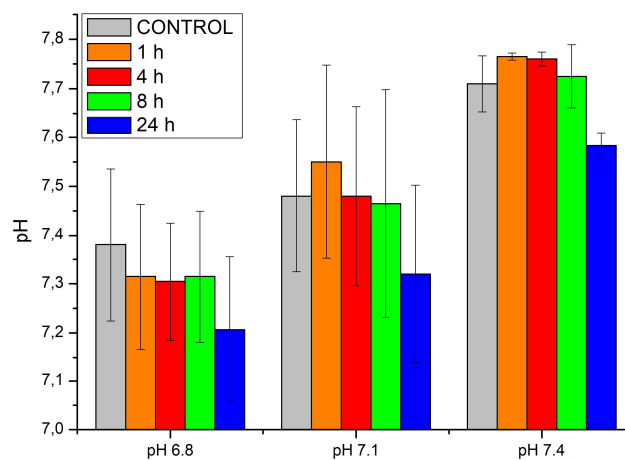


**Figure 35.** pH variation measurements after each treatment

The general trend observed was that the cell culture tended to increase the pH of the medium to reach physiological conditions. For instance, the cells that were set at pH 6.8 raised the pH to approximately pH 7.3 after only 1 h of treatment (orange bar on the left). The same behavior was observed with the other conditions, although the global pH was slightly higher. The fact that the pH was not maintained along the experiment could be due to the cell metabolism and to the incubator working conditions, which include temperature, gas tension ( $\text{CO}_2/\text{O}_2/\text{N}_2$ ) and humidity. These three parameters work in synchrony to provide the optimum cell growth and mimic an *in vivo* state. The  $\text{CO}_2$  gas present in the incubator is combined with  $\text{NaHCO}_3$  of the growth medium to control pH to 7.4 to achieve bloodstream conditions.

Therefore, due to this technical limitation, the acidic pH could not be preserved along the treatments and hence all the results obtained actually correspond to physiological conditions. This explains why there was no statistically significant difference between each type of treatment.

### 3.3.3. *Cell internalization*

The internalization mechanism was also studied with DiO-loaded NCs (**DiO-AMP-2 NCs**) in A549 cells. The NCs were incubated for different time periods (1, 8, 16, 24 and 48 h), including a control condition with unloaded NCs (**BLANK-AMP-3 NCs**). One h before finishing each treatment, LysoTracker red, a fluorescent dye that tags acidic organelles such as lysosomes, was added. Cells were washed several times, fixed with PFA and visualized in a confocal microscope. The images are shown in **Figure 36**.

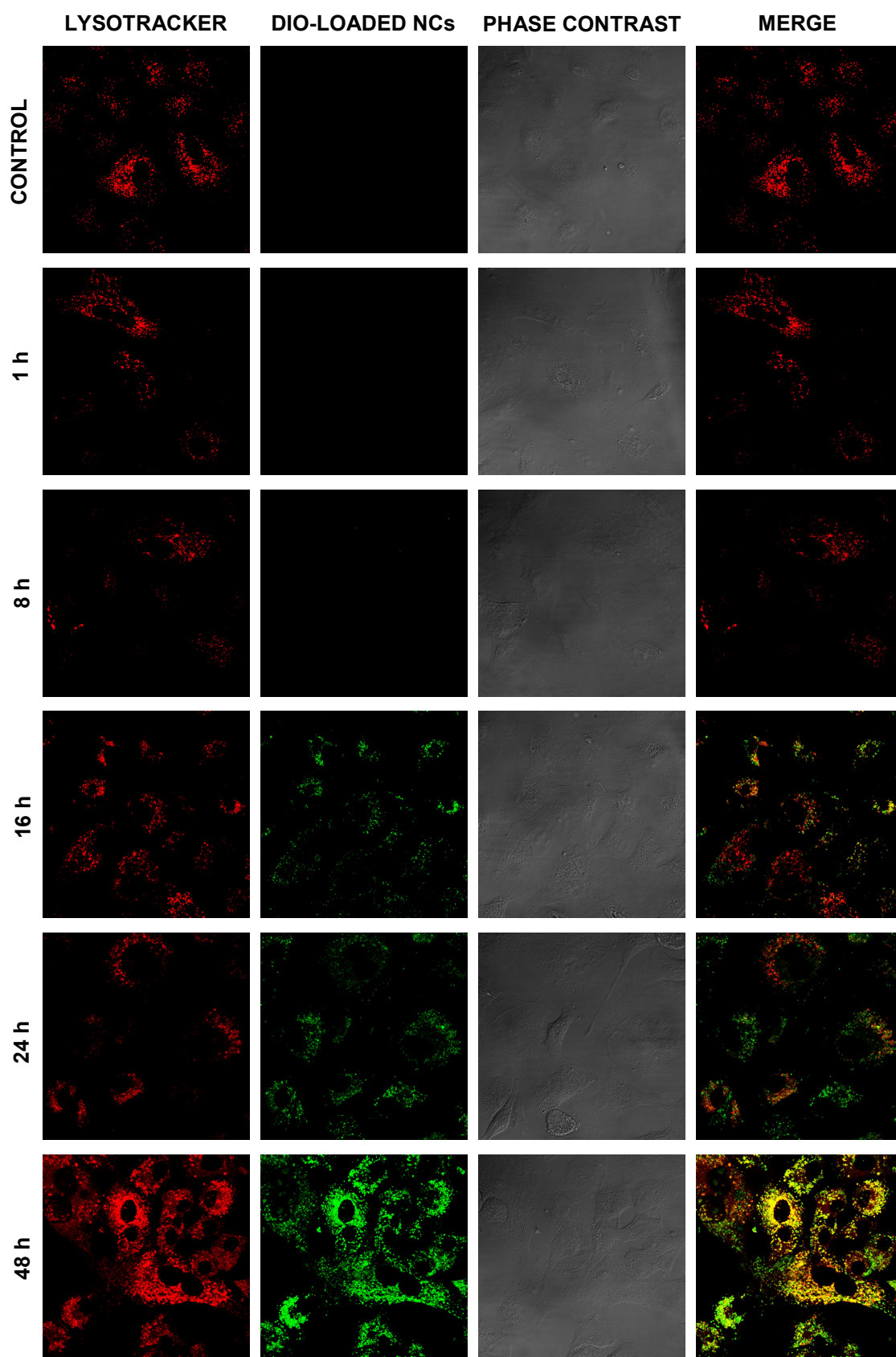


**Figure 36.** Cell internalization in A549 cells during different incubation times

According to **Figure 36**, four different types of images were collected in this assay, depending on the cytometer channel used. In this regard, the pictures on the left column show the acidic organelles, which are stained in red due to the effect of LysoTracker red. The second column highlights the NCs that have been internalized by the cells and they are colored in green because of the DiO fluorophore. The control phase images show the relief of the cells and provide a confirmation that their morphologies do not present significant alterations due to the treatments. Finally, the right column corresponds to the overlaid images showing the LysoTracker red and the NCs in order to determine possible colocalizations.

In general terms, it has been demonstrated that the longer the exposure, the more NCs that are internalized inside the cells. Therefore, the images recorded after 48 h of treatment show a very intense green fluorescence due to the high concentration of NCs that have been able to permeate the cells. Accordingly, shorter incubation times led to a lower fluorescence signals. However, it should be noted that the lack of fluorescence observed in 1 h- and 8 h-treatments is due to the microscope settings. Before starting the visualization of the samples, the parameters were adjusted by using the image having the highest signal and the rest were normalized accordingly. As a result, the green fluorescence observed at 1 h and 8 h was much lower than the one obtained for the longest time.

The samples incubated for 16 and 24 h with the NCs show a large number of green spots inside the cells. When these images are overlaid to study the colocalization with LysoTracker red, a mixture of yellow, orange and red colors appear simultaneously (**Figure 37**).

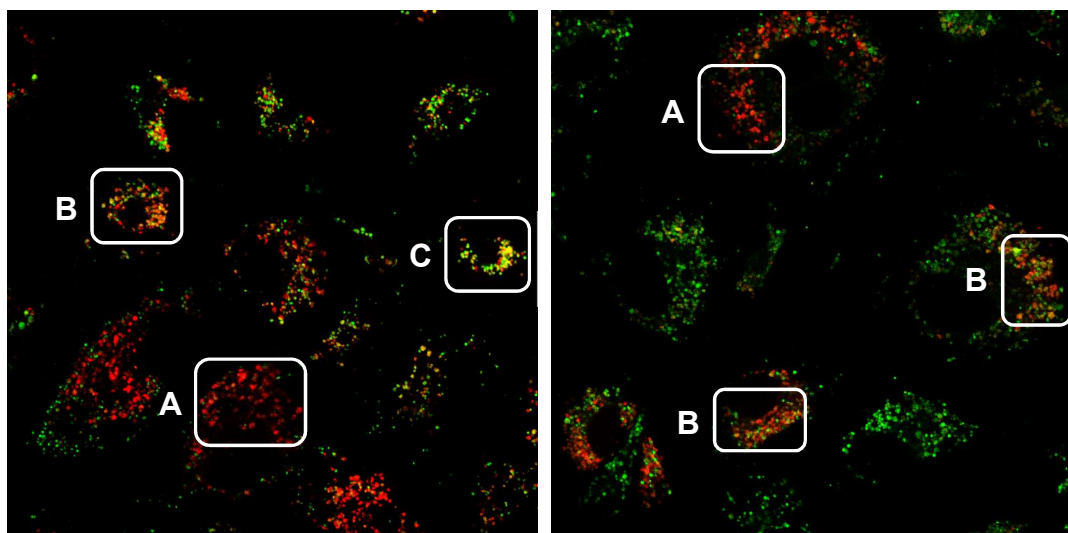


**Figure 37.** Merge image corresponding to 16 h (left) and 24 h (right) of incubation

This figure shows different degrees of colocalization. Regions labeled as *A* highlight the acidic organelles in red and almost no green dots can be distinguished. However, in regions *B*, the merge leads to an orange color, which indicates that more NCs colocalize with the Lysotracker and therefore the red color is not so intense. Finally, areas labeled in *C* clearly show a yellow color that indicates there is a high concentration of green NCs which are localized in the acidic organelles.

After 48 h of exposure, the main part of the NCs are colocalizing with the Lysotracker, since a general yellow color can be observed. Overall, these results suggest that the NCs were internalized through endocytosis and their localization was mainly in acidic organelles, such as the lysosomes.

### 3.4. *In vivo* biodistribution in a NB mouse model

After performing the previous physicochemical and biological characterization, the next step considered was the biodistribution of the NCs in an *in vivo* NB mouse model. This study aimed to elucidate the relative accumulation of the amphoteric NCs (**DiR-AMP NCs**) into the tumor, plasma and organs. In order to evaluate their targeting abilities, a version of antibody-functionalized NCs (**DiR-antiGD2 NCs**) directed to GD2 ganglioside was included in the assay. To perform the experiment, the NCs were loaded with the DiR fluorophore (**Figure 38**), since it allowed their detection using a non-invasive near IR visualization system.

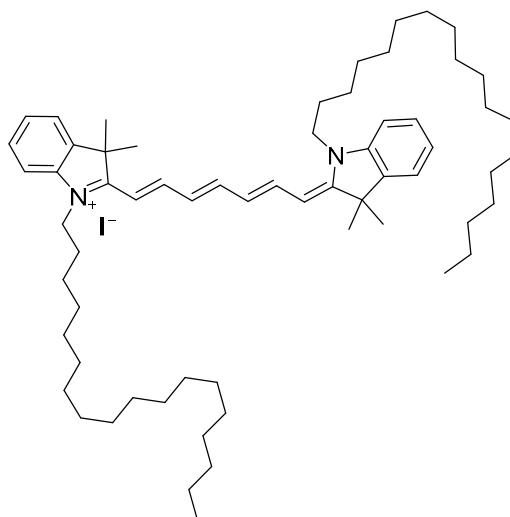


**Figure 38.** Chemical structure of DiR

The *in vivo* biodistribution could only be performed in a NB mouse model because a national funding was given specifically for this disease. Thus, **DiR-AMP NCs** and **DiR-antiGD2 NCs** were prepared, characterized and injected in NB-bearing mice. It should be reminded that GD2 disialoganglioside has been reported to be overexpressed in NB cells and not in normal tissues, except the skin melanocytes, peripheral nerves and the brain, where the antibody does not have access.<sup>62,63,68,69</sup>

#### 3.4.1. Preparation of the NCs

Plain amphoteric NCs, **DiR-AMP NCs**, were prepared as explained previously in Chapter 2 but the NCs bearing the antiGD2 mAb (amino acid sequence shown in **Figure 39**) were synthesized by modifying the encapsulation procedure in order to properly conjugate the antibody.

##### *Amino acid heavy chain (variable and constant domains)*

EVQLLQSGPE	LEKPGASVMI	SCKASGSSFT	GYNMNWVRQN	IGKSLEWIGA
IDPYYGGTSY	NQKFKGRATL	TVDKSSSTAY	MHLKSLTSED	SAVYYCVSGM
EYWGQGTSVT	VSSASTKGPS	VFPLAPSSKS	TSGGTAALGC	LVKDYFPEPV
TVSWNSGALT	SGVHTFPAVL	QSSGLYSLSS	VVTVPSSSLG	TQTYICNVNH
KPSNTKVDKR	VEPKSCDKTH	TCPPCPAPEL	LGGPSVFLFP	PKPKDTLMIS
RTPEVTCVVV	DVSHEDPEVK	FNWYVDGVEV	HNAKTKPREE	QYNSTYRVVS
VLTVLHQDWL	NGKEYKCKVS	NKALPAPIEK	TISKAKGQPR	EPQVYTLPPS
REEMTKNQVS	LTCLVKGFYP	SDIAVEWESN	GQPENNYKTT	PPVLDSDGSF
FLYSKLTVDK	SRWQQGNVFS	CSVMHEALHN	HYTQKSLSL	PGK

*Amino acid light chain (variable and constant domains)*

EIVMTQSPAT	LSVSPGERAT	LSCRSSQSLV	HRNGNTYLHW	YLQKPGQSPK
LLIHKVSNRF	SGVPDRFSGS	GSGTDFTLKI	SRVEAEDLGV	YFCSQSTHVP
PLTFGAGTKL	ELKRTVAAPS	VFIFPPSDEQ	LKSGTASVVC	LLNNFYPREA
KVQWKVDNAL	QSGNSQESVT	EQDSKDSTYS	LSSTLTLSKA	DYEKHKVYAC
EVTHQGLSSP	VTKSFNRGEC			

**Figure 39.** AntiGD2 antibody amino acid sequence. Both chains are duplicated.

There is an array of crosslinkers for protein conjugation on nanocapsules,<sup>70</sup> but the most common ones are *N*-hydroxysuccinimide (NHS)/*N*-(3-dimethylaminopropyl)-*N'*-ethylcarbodiimide (EDC, commercially available as hydrochloride) and maleimide (Mal) (**Figure 40**). These reagents can be used in physiological conditions in order to prevent tertiary and quaternary structure alteration that would cause the loss of the antibody targeting abilities.<sup>71</sup>

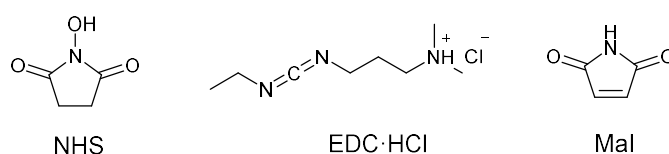
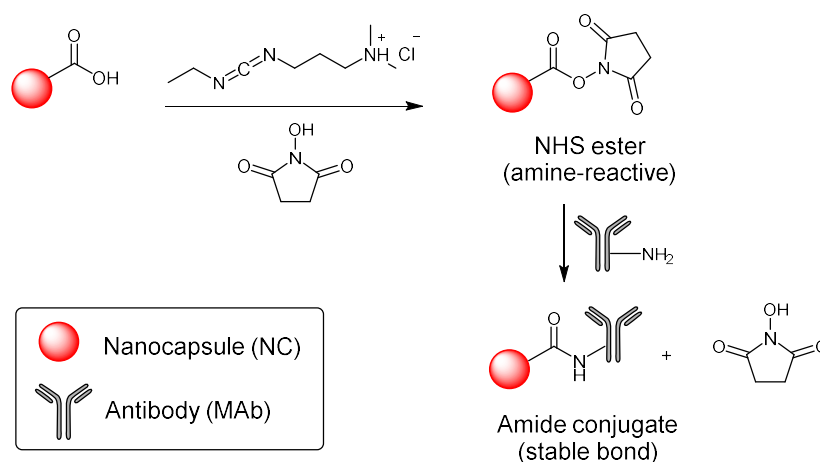


**Figure 40.** Chemical structures of common crosslinkers

Carbodiimides are smooth dehydrating agents that are usually used in peptide synthesis.<sup>72</sup> The crosslinking reaction involving NHS/EDC is shown in **Scheme 2**.<sup>73,74</sup>



**Scheme 2.** EDC/NHS crosslinking reaction scheme between a NC and an antibody

The NCs functionalized with carboxylic moieties react with NHS, after being dehydrated by EDC, yielding a NHS-active ester. This intermediate reacts with the amines of the antibody to form the NC-mAb conjugate via a stable amide bond. However, although the NHS/EDC combination is biologically compatible, the reactions taking place are difficult to control in antibodies due to the high number of amines.<sup>75</sup> To solve this issue, more specific crosslinkers such as Mal are used.

Mal chemistry involves a specific reaction with thiol groups. Since thiols are generally unavailable in proteins due to the tendency of cysteine to form disulfide bonds, prior reduction of this bond has to be performed. In this sense, there are two very common approaches to achieve that. The first one consists of reducing solvent-exposed disulfide bonds with reducing agents, such as dithiothreitol, tris(2-carboxyethyl)phosphine and 2-mercaptoethanol (**Figure 41**).

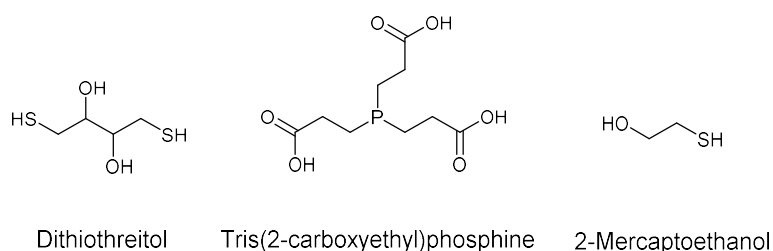


**Figure 41.** Chemical structures of some reducing agents

The second approach is based on the thiolation of primary amine residues with agents such as 2-iminothiolane hydrochloride (Traut's reagent), *N*-succinimidyl *S*-acetylthioacetate or *N*-succinimidyl *S*-acetylthiopropionate (**Figure 42**).

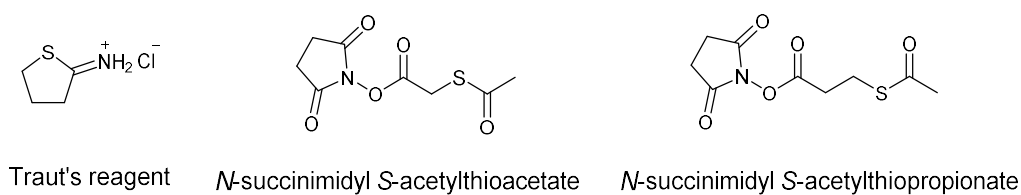
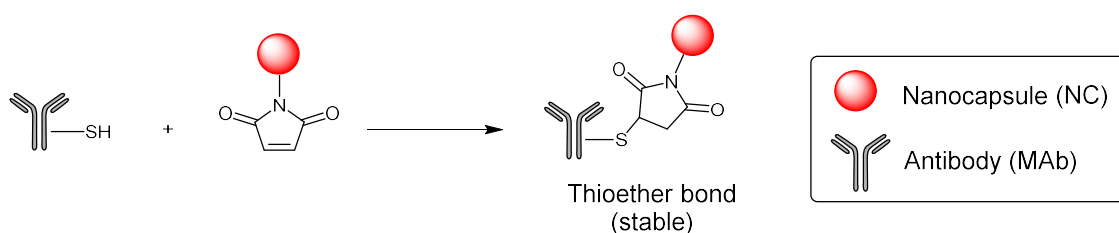


**Figure 42.** Chemical structures of thiolating agents

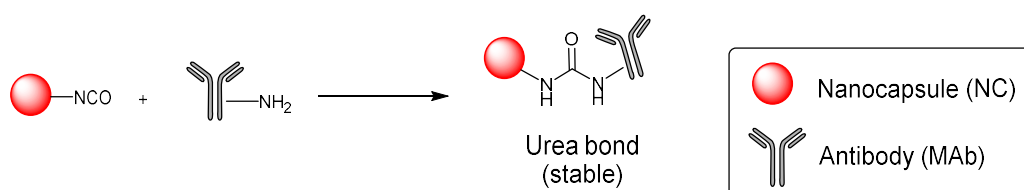
Once the thiol is formed, the reaction with a MaI-functionalized NC proceeds as **Scheme 3** shows.<sup>71</sup>



**Scheme 3.** Conjugation reaction between a mAb and a NC via MaI chemistry

In this case, MaI groups react with thiols to lead to a stable thioether bond, which links the antibody to the NC.<sup>76</sup>

Taking into account that the aforementioned conjugation methods involve various steps and the addition of large excesses of crosslinkers, in our case the conjugation was done via the direct coupling between amines (from lysines of the mAb) and the remaining NCO groups (from the NC). This new approach allowed the preparation of the conjugates more directly, in quantitative yields and avoided the excesses of reagents, given the very high reactivity of NCO groups with amines (**Scheme 4**).<sup>77-80</sup> As a consequence, besides obtaining the conjugates in only one step, there was no need to purify the products.



**Scheme 4.** Conjugation reaction via isocyanate chemistry

The coupling reaction was performed at pH 7.4 and rt and the aim was to modify the least number of lysine residues and preserve protein function. At neutral pH conditions, most of the lysine side chains were protonated, according to their theoretical pK<sub>a</sub> value of 8.95,<sup>81</sup> leading to a more controlled reaction with IPDI and avoiding the generation of highly crosslinked conjugates. In addition, Traut's reagent also involves the lysine primary amines, but requires an extra step with MaI-

derivatives to complete the conjugation reaction. Therefore, the antibody coupling using isocyanate chemistry can be as quantitative and more direct.

### 3.4.2. Characterization

**DiR-AMP NCs** and **DiR-antiGD2 NCs** were fully characterized in terms of morphology, size and surface charge at different pH conditions by the typical analytical techniques. In addition, the antibody conjugation efficiency was determined by amino acid analysis using the AccQ·Tag pre-column derivatization method.<sup>82,83</sup>

#### 3.4.2.1. Morphology and size

The morphology of both types of NCs was studied by TEM and the results are shown in **Figure 43**.

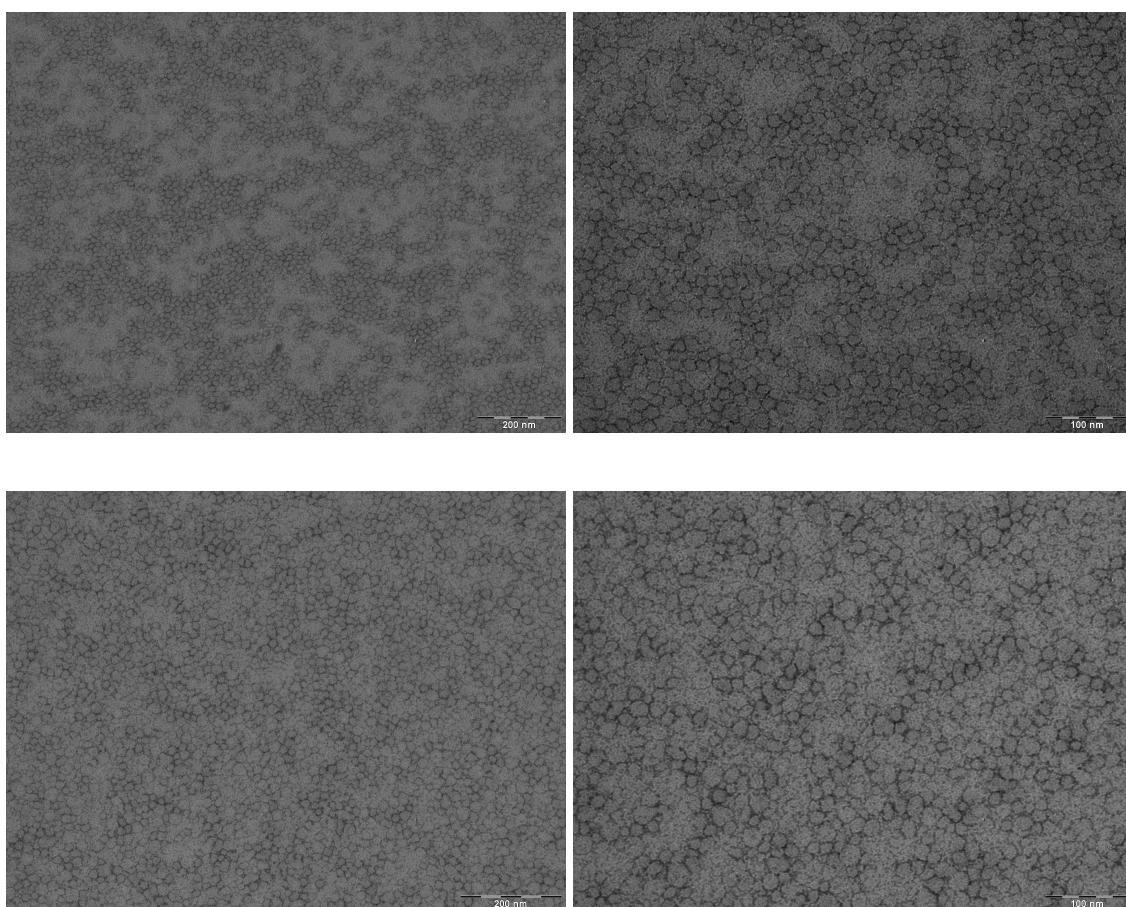
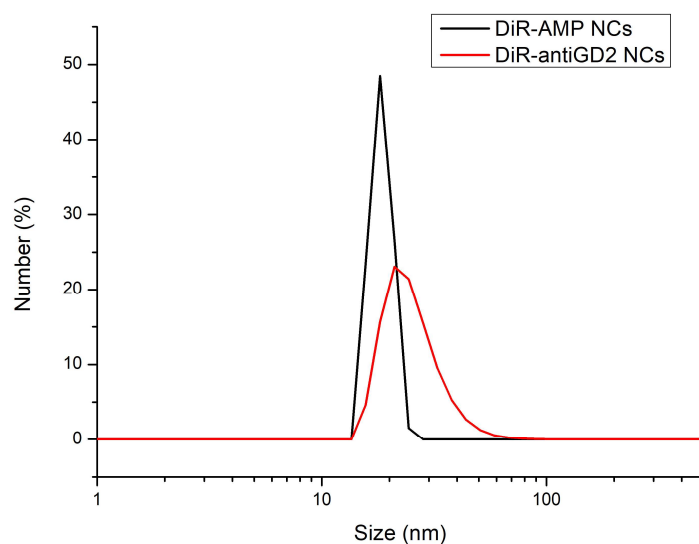


**Figure 43.** TEM micrographs of **DiR-AMP NCs** (top) and **DiR-antiGD2 NCs** (bottom). Scale bars images on the left = 200 nm; images on the right = 100 nm.

The two micrographs on the top correspond to the amphoteric NCs (**DiR-AMP NCs**), while the other two represent the antibody-functionalized NCs (**DiR-antiGD2 NCs**). On one hand, the morphology of **DiR-AMP NCs** was homogeneous and with a roughly round shape. In this sample, only one particle size population could be observed, having an average diameter of around 20 nm. On the other hand, **DiR-antiGD2 NCs** showed a slightly less homogeneous morphology. Despite observing only one particle size population, the diameters observed in the sample presented more variability than the previous case. This could be explained by the presence of the antibody on the surface of the NCs, which would enlarge the size of the particles, due to its high molecular weight (around 150 KDa). According to the micrographs, the approximate size for this sample was also around 20 nm, although more variability could be observed. However, although the sample was not entirely homogeneous, no Ostwald ripening effects could be detected as in the case of tambjamine-loaded NCs.

The size of the NCs was further characterized by DLS, as in the previous cases. **Figure 44** shows the particle size distributions and the statistical analyses derived thereof.



Sample code	Mean $\bar{\phi}$ (nm)	SD (nm)	PDI
DiR-AMP NCs	17.34	2.04	0.01
DiR-antiGD2 NCs	19.65	8.62	0.13

**Figure 44.** Particle size distributions of the samples and statistical analyses

The particle size distribution of **DiR-AMP NCs** sample was narrower than the **DiR-antiGD2 NCs**, probably because of the presence of the antibody in the interface of the NCs. AntiGD2 antibody is a large protein that contains a wide variety of amino acids of different nature (**Figure 39**), both hydrophobic and hydrophilic. Therefore, by considering the hydrophobic/hydrophilic gradient created from the interior of the NC to the exterior, hydrophobic side chains of antiGD2 can cause o/w destabilization because of its inherent tendency to self-allocate inside, with the rest of hydrophobic groups. This could be a reasonable explanation why the particle size distribution of this sample is slightly higher and presents a four-times larger SD than that without the antibody. However, the average sizes of both samples are around 20 nm, in accordance with the TEM observations.

### 3.4.2.2. Surface properties

The study of the surface properties provided in this case a solid confirmation of the different nature of both types of NCs due to the presence of antiGD2. In this regard, in **DiR-AMP NCs**, the amphoteric properties were expected with an increase of a  $\zeta$ -pot with a pH decrease, while in **DiR-antiGD2 NCs**, a different cationization patten was expected. The measurements were performed as in the previous cases, using the diluted solutions of the samples at different pH conditions, ranging from 5.5 to 8.0. The results are shown in **Figure 45**.

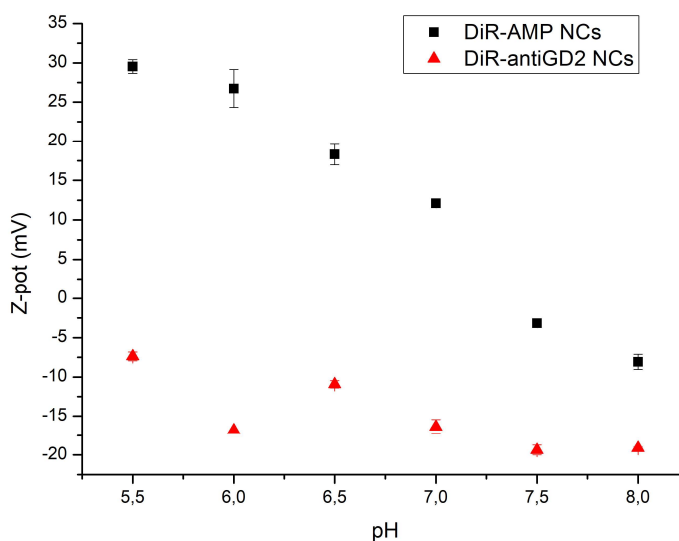


**Figure 45.**  $\zeta$ -pot of DiR-AMP NCs and DiR-antiGD2 NCs at different pH conditions

According to the figure, the black symbols are referred to the amphoteric NCs, while the red ones correspond to the antibody-functionalized NCs. The former showed the typical cationization pattern, which is characterized by an increase of the  $\zeta$ -pot along with the acidification of the medium. On the other hand, **DiR-antiGD2 NCs** followed a different  $\zeta$ -pot profile, since the surface charge of the NCs was invariably anionic regardless the pH conditions. Nevertheless, the charge became slightly more negative when the medium was more alkaline. Taking into account the number of positively-charged amino acid residues present in antiGD2 antibody (arginine and lysine, 132 in total) and those exhibiting negative charges (aspartic acid and glutamic acid, 120 in total), the global  $\zeta$ -pot expected should be slightly positive. A feasible explanation for that could be that part of the lysine residues from antiGD2 reacted with the IPDI during the conjugation process, resulting into less cationic side chains exposed and a decrease of the overall  $\zeta$ -pot.

#### 3.4.2.3. *Antibody conjugation efficiency*

The antiGD2 mAb conjugation efficiency was determined by amino acid analysis, after hydrolyzing the samples under strong acidic conditions. The chromatograms of the control sample (**DiR-AMP NCs**) and the antiGD2-functionalized NCs (**DiR-antiGD2 NCs**) are shown in section 6 of the Annexes.

As seen in the chromatogram from **DiR-AMP NCs**, some of the peaks correspond to the derivatized amino acids, while the others can be attributed to certain molecules coming from the NC shell, including the monomers and the crosslinker DETA. As expected, the area of the amino acid peaks is almost negligible in some cases and therefore leads to very low amount numbers, except for the IS compounds ( $\gamma$ -aminobutyric acid, AABA, and norleucine, NLE). Interestingly, the amount of lysine is relatively high compared to the rest of the amino acids, due to its presence in the NC shell.

In the case of **DiR-antiGD2 NCs**, most of the peaks are attributed to the amino acid residues and, moreover, the amounts derived from the areas are higher than the previous chromatogram. These results are in line with the nature of the sample, since it contains the protein and therefore the concentration of amino acids is higher

than in the control assay. In addition, and as observed before, the amount of lysine exceeds the expected value because of its presence in the NC shell.

Regarding the quantification of the antibody, three different amino acids were considered to make the calculations: Arg, Thr and Ile. They were selected because they were not present into the control sample and therefore their concentrations could unequivocally be derived from the antiGD2 mAb. Additionally, they are among the amino acids that do not undergo degradation events and thus they are more reliable for quantification. In order to determine the conjugation yield (%), the amount per residue was firstly calculated (**Table 7**).

**Table 7.** Previous calculations for the antibody conjugation yield

<b>Amino acid</b>	<b>Number of residues</b>	<b>Amount</b>	<b>Amount/residue</b>
<b>Arg</b>	36	0.031	$8.61 \cdot 10^{-4}$
<b>Thr</b>	102	0.091	$8.92 \cdot 10^{-4}$
<b>Ile</b>	26	0.022	$8.46 \cdot 10^{-4}$

As seen in the previous table, the amount/residue was very similar between the three amino acid residues considered. Therefore, the average value ( $8.66 \cdot 10^{-4}$ ) was fixed as a reference to calculate the total amount of antiGD2 that corresponded to the analyzed sample of lyophilized NCs. The calculations took into account the volume injected to the HPLC, the total volume of derivatized sample, the aliquot that was used for the derivatization reaction, the volume of medium used to resuspend the hydrolyzed amino acids, the molecular weight of the antibody (around 150 KDa) and the amount of AABA added into the initial sample. After the necessary calculations, the average the conjugation yield was:

$$\% \text{ conjugation yield} = \frac{\text{mg antiGD2 (experimental)}}{\text{mg antiGD2 (theoretical)}} * 100 = \mathbf{98.5 \%}$$

Given this high value, it can be confirmed that the antibody was successfully conjugated to the NCs via direct IPDI/lysine coupling under physiological conditions and rt.

### 3.5. *In vivo and ex vivo data*

This *in vivo* assay aimed the study of the accumulation of amphoteric **DiR-AMP NCs** and antibody-functionalized **DiR-antiGD2 NCs** into NB-bearing mice. To do so, tumor-accumulation and whole-body biodistribution of the NCs in mice with subcutaneous CHLA90 human NB cancer tumors was measured by means of *in vivo* and *ex vivo* fluorescence imaging (FLI) with an optical system using a near IR dye, DiR (**Figure 38**), as a probe.

*In vivo* FLI was performed at 24 and 48 h post administration. Plasma, tumor, liver, spleen, kidney and lung samples were collected at 24 and 48 h end time points. Tumors were weighted, measured *ex vivo*, imaged and processed. The plasma and the other tissues were also weighted, imaged and processed. The experimental groups were organized as follows (**Figure 46**).

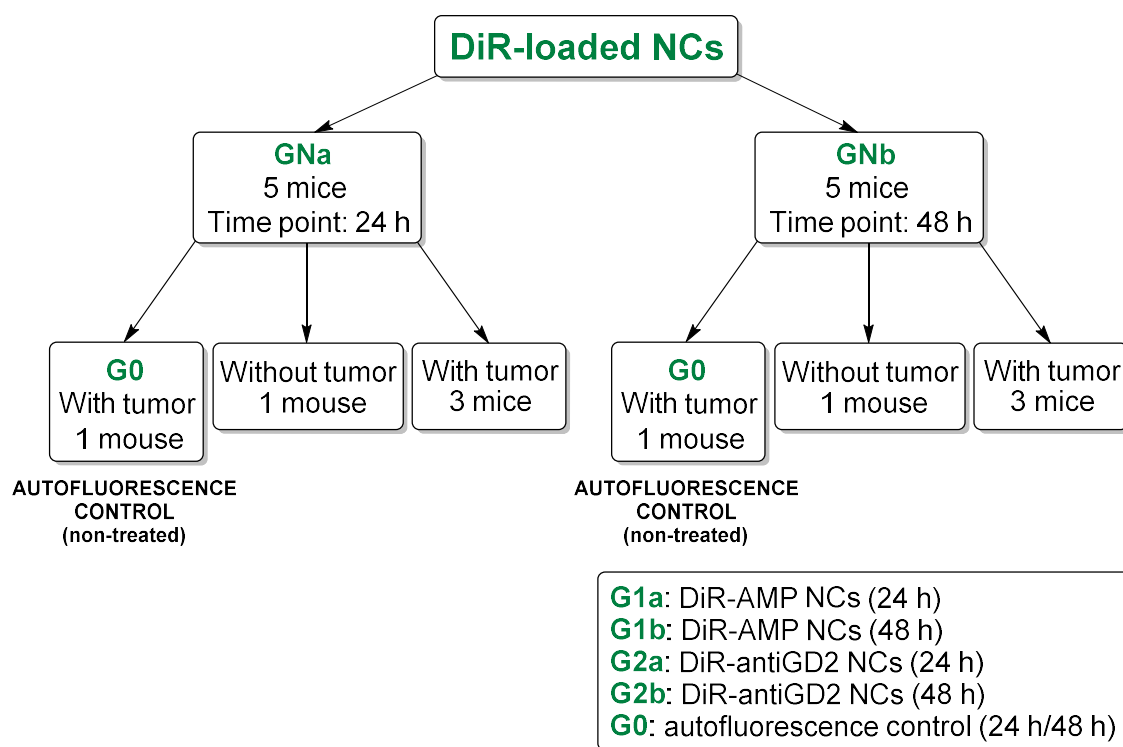


**Figure 46.** Organization of experimental conditions for the *in vivo* biodistribution

According to the experimental design shown in the figure, mice were randomized in two different groups once the tumor reached acceptable volumes (range 90.54 mm<sup>3</sup> to 409.46 mm<sup>3</sup>). The treatments were based on a unique injection at a DiR concentration of 0.8 mg DiR/kg. The first group, which was treated with

**DiR-AMP NCs** for 24 h, consisted of 5 mice that were divided into 1 tumor-bearing mouse non-treated as a control to set the tissue autofluorescence (G0), 1 non-tumor-bearing mouse with the corresponding treatment and three tumor-bearing mice injected with the NCs (G1a). The next group was identical but with the exception that the end time was 48 h instead of 24 h (G0, G1b). The other two groups were treated with **DiR-antiGD2 NCs** for 24 and 48 h, respectively, and were based on the same organization. Therefore, in this case the groups were named G0 (autofluorescence control at 24 and 48 h), G2a (treatment for 24 h for both tumor-bearing and non-tumor bearing mice) and G2b (treatment for 48 h for both tumor-bearing and non-tumor bearing mice).

At 24 and 48 h post administration, tumor-accumulation and whole-body biodistribution were measured non-invasively by DiR FLI monitoring from the dorsal and ventral mouse views. Moreover, at 24 and 48 h post administration end time point, plasma, tumor, liver, spleen, kidneys and lung samples were collected, and the NC plasma and tissue accumulations were determined by *ex vivo* DiR FLI monitoring.

### 3.5.1. Incidences

In the course of the study, some deviations from the study plan occurred. The cell inoculation had to be postponed for weeks because the tumors did not grow sufficiently, therefore, more cells were implanted later without any other incidence. After 49 days post cell implantation, the animals did not develop subcutaneous tumors. This was corrected by implanting again the cells in the left flank with Matrigel, which is a gelatinous protein mixture secreted by Engelbreth-Holm-Swarm mouse sarcoma cells that resembles the complex extracellular environment found in many tissues. Fortunately, the tumors grew correctly and 3 of the whole group of animals also developed tumors at the right flank, corresponding to the cells implanted without Matrigel.

### 3.5.2. Body weight change during treatment

Mice were weighted twice a week in order to detect any important change after cell implantation and once a day during the treatment (**Figure 47**).

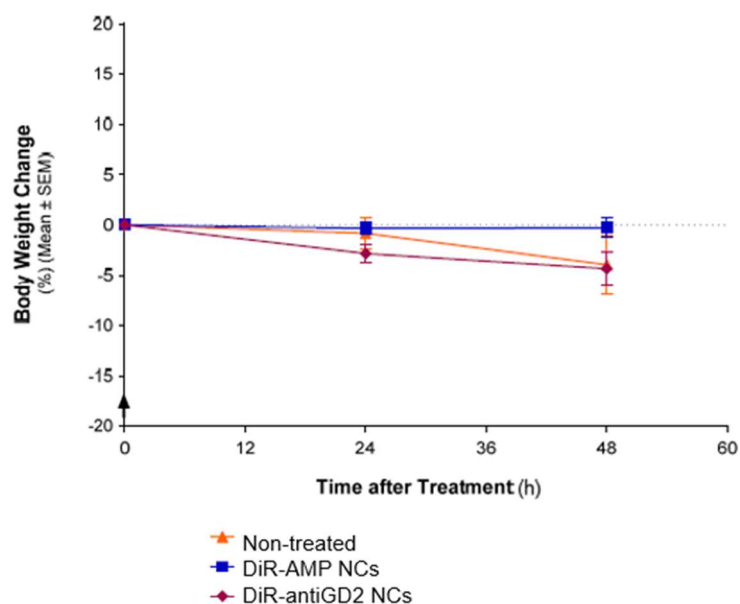


**Figure 47.** Monitoring of body weight change during the treatment

According to the body weight change, a unique intravenous administration dose of **DiR-AMP NCs** and **DiR-antiGD2 NCs** at 0.8 mg DiR/kg was well tolerated and adverse side effects were not observed up to 48 h post administration.

### 3.5.3. *In vivo* whole-body biodistribution kinetics

*In vivo* FLI tissue accumulation of both versions of NCs was monitored after 24 and 48 h post injections. Representative ventral images of mice are shown in **Figure 48**.

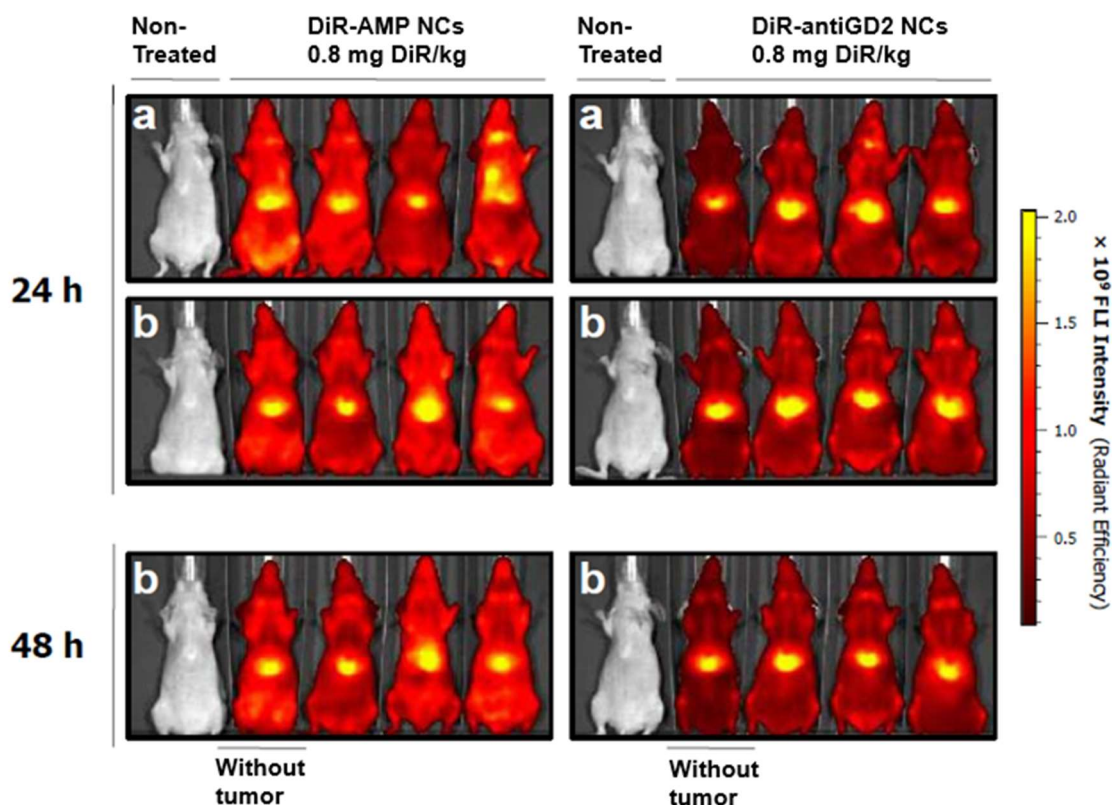


**Figure 48.** Non-invasive monitoring of whole-body tissue-accumulations over time

Control mice on the left of every group did not show any fluorescence signal and therefore all the color observed in the rest of the images was due to DiR accumulation in the tissues. At a first glance, and comparing the fluorescence intensities with the pseudocolor scale bars, the highest accumulation was generally observed in the liver. Undetectable changes could be noticed between the two time points and between untargeted **DiR-AMP NCs** and **DiR-antiGD2 NCs**. Nevertheless, these preliminary observations were further confirmed by *ex vivo* tumor and whole-body tissue analyses.

### 3.5.4. *Ex vivo* tumor and whole-body tissue-accumulation kinetics

After 24 and 48 h post administration, animals were euthanized by cervical dislocation while still anaesthetized, following the euthanasia standard operating procedure. Then, plasma, tumor, liver, spleen, kidneys and lung samples were collected, and plasma and tissue accumulations were determined by *ex vivo* DiR FLI monitoring. Mean values  $\pm$  SEM (standard error of the mean) and individual values were displayed at each corresponding end point.

#### 3.5.4.1. Tumor accumulation

The accumulation of both types of NCs in tumor was measured qualitatively by fluorescence intensity. It was found that some of the mice developed more than one tumor as a consequence of different cell implantations (see section 3.5.1). The results are shown in **Figure 49**.

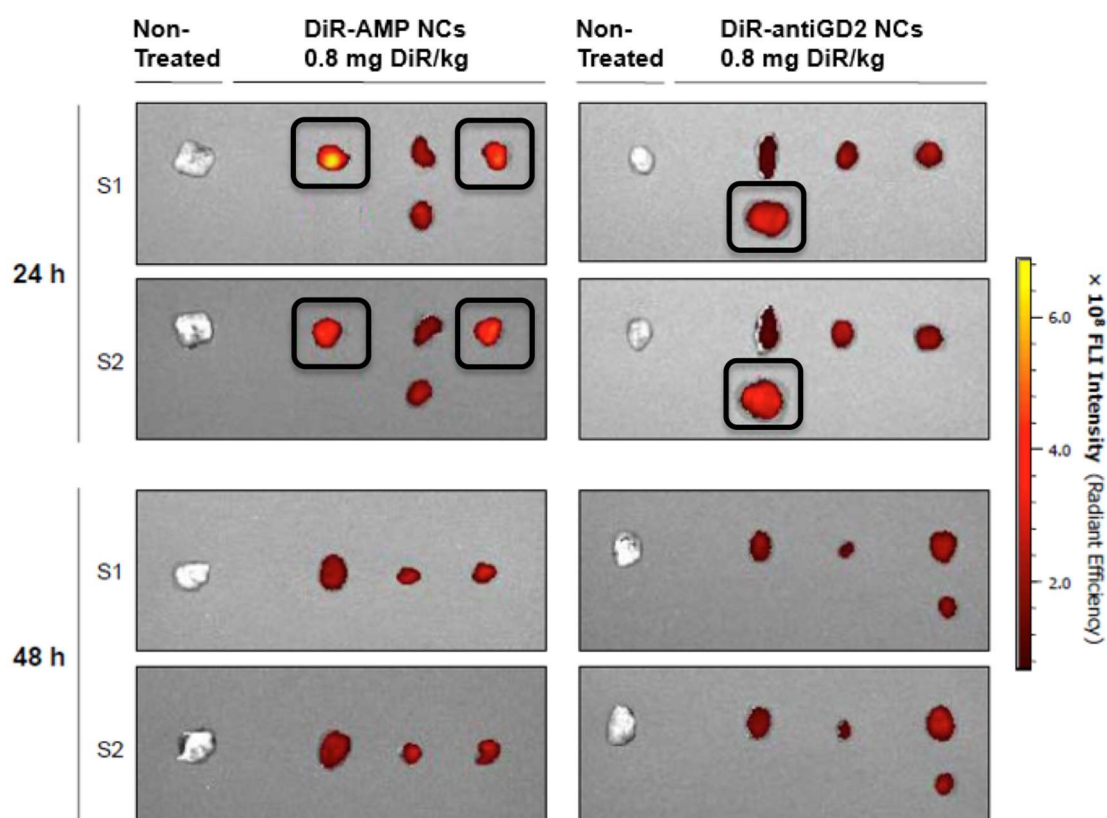


**Figure 49.** Qualitative data of *ex vivo* tumor accumulation of both types of NCs after 24 and 48 h

*Ex vivo* accumulation measurements showed a moderate fluorescence intensity in the tumors, being slightly higher for those treated with **DiR-AMP NCs** than their antibody-targeted analog **DiR-antiGD2 NCs**. Particularly, among the 24 h-treated mice with **DiR-AMP NCs** there were four tumors with a relevant fluorescence intensity, while in those injected with **DiR-antiGD2 NCs**, there were two cases of remarkable fluorescence (highlighted with a square). In contrast to these results, in the 48 h-post injection mice, no NCs showed any significant accumulation enhancement. Quantitative DiR tumor accumulation was measured by taking into account fluorescence intensity and the tumor weight. The results are shown in **Figure 50**.

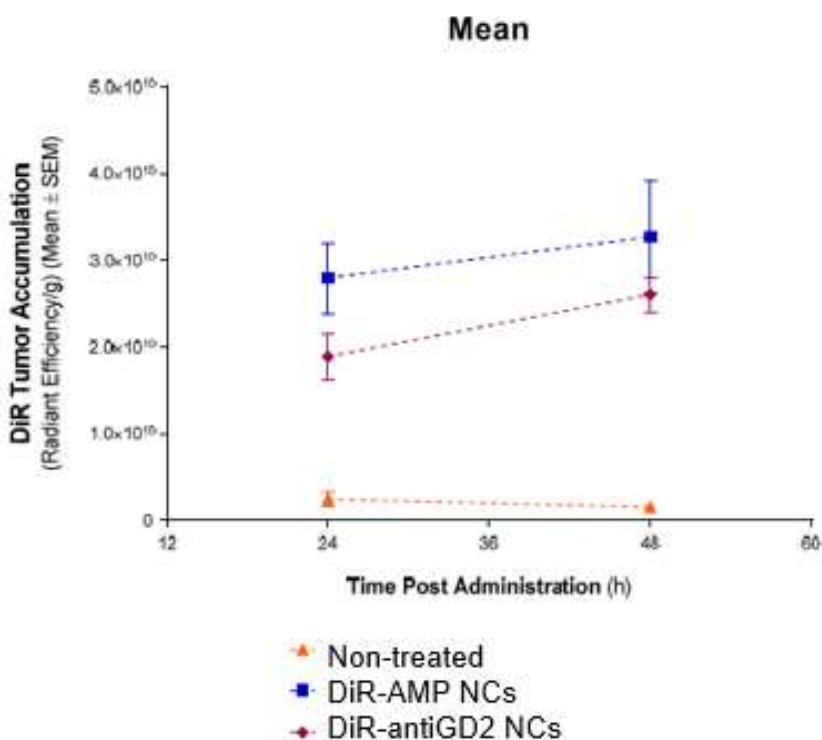


**Figure 50.** Quantitative *ex vivo* tumor accumulation of both types of NCs after 24 and 48 h

In contrast to the previous observations regarding the qualitative data, the DiR tumor accumulation showed higher accumulation rates after 48 h post injection than after only 24 h, proving the slow permeating abilities of the synthesized nanosystems. This result was in line with the nature of the NCs, which were designed to be long circulating and to approach and permeate the tumor in a controlled manner by changing their surface charge. Therefore, a higher accumulation after

longer circulation times was expected and proved that both versions of NCs continued circulating and increasing their accumulation in the tumors. Between the NCs tested, a slightly higher accumulation was observed with **DiR-AMP NCs** (around  $3 \cdot 10^{10}$  radiant efficiency/g) than with **DiR-antiGD2 NCs** (around  $2 \cdot 10^{10}$  radiant efficiency/g).

### 3.5.4.2. Liver accumulation

As in the previous case, the liver accumulation was measured qualitatively by fluorescence intensity (**Figure 51**).

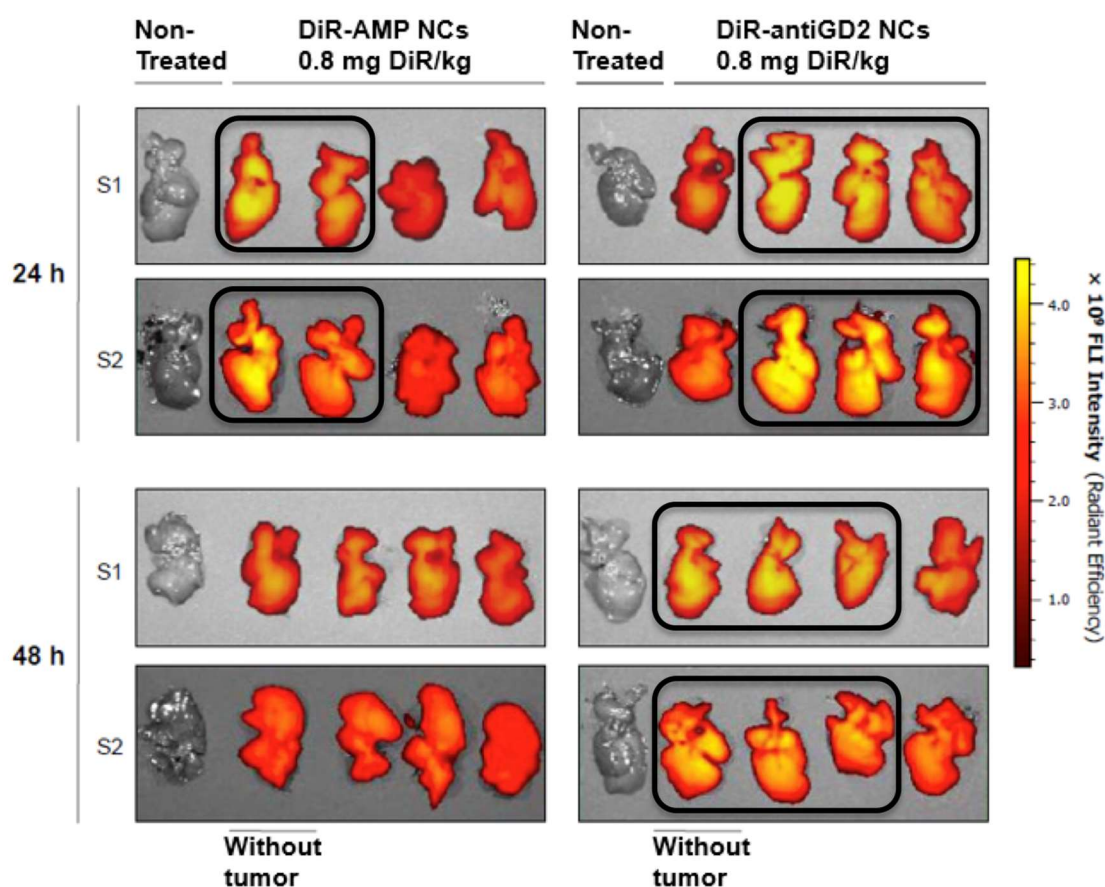


**Figure 51.** Qualitative data of *ex vivo* liver accumulation of both types of NCs after 24 and 48 h

Liver showed an important DiR accumulation, according to the general orange and yellow coloration of this organ in both types of NCs and both end time points. At a first glance, though, amphoteric **DiR-AMP NCs** seemed to have experimented lower liver penetration than **DiR-antiGD2 NCs**, as highlighted by the squares. The

quantitative data obtained from the fluorescence intensities and the weights of these organs is shown in **Figure 52**.

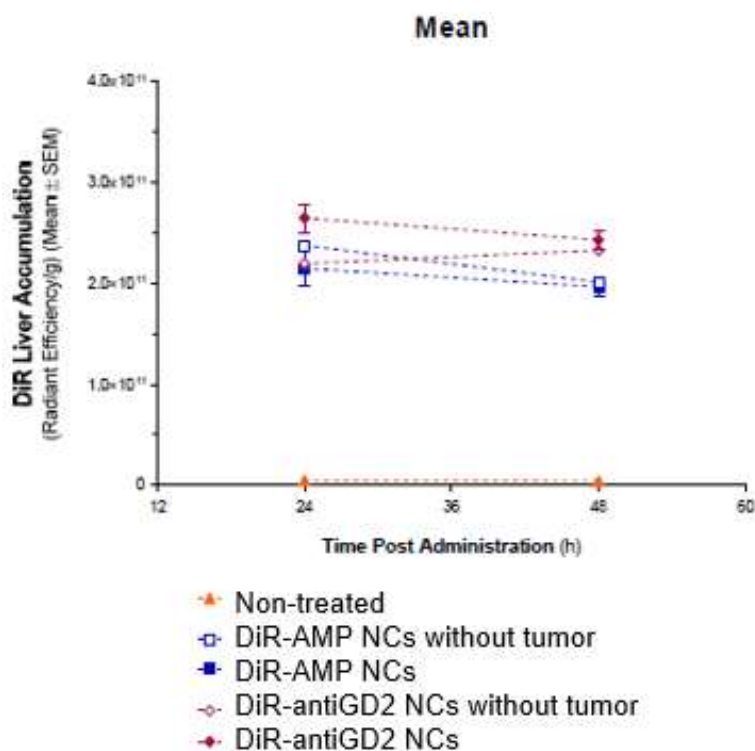


**Figure 52.** Quantitative *ex vivo* liver accumulation of both types of NCs after 24 and 48 h

By analyzing the quantitative data, the accumulation of **DiR-AMP NCs** in the liver ( $2\text{--}2.5 \cdot 10^{11}$  radiant efficiency/g) slightly decreased over time, both in control mice and NB-bearing mice. In the case of **DiR-antiGD2 NCs** injected to control mice, their permeation was in the range of the previous ones, and the accumulation slightly increased from 24 to 48 h. However, the DiR accumulation was a little bit higher ( $2.5\text{--}3 \cdot 10^{11}$  radiant efficiency/g) in mice with tumors, and this tendency slightly decreased after 48 h post injection.

### 3.5.4.3. Spleen accumulation

As with the previous cases, the spleen accumulation was measured qualitatively by fluorescence intensity (**Figure 53**).

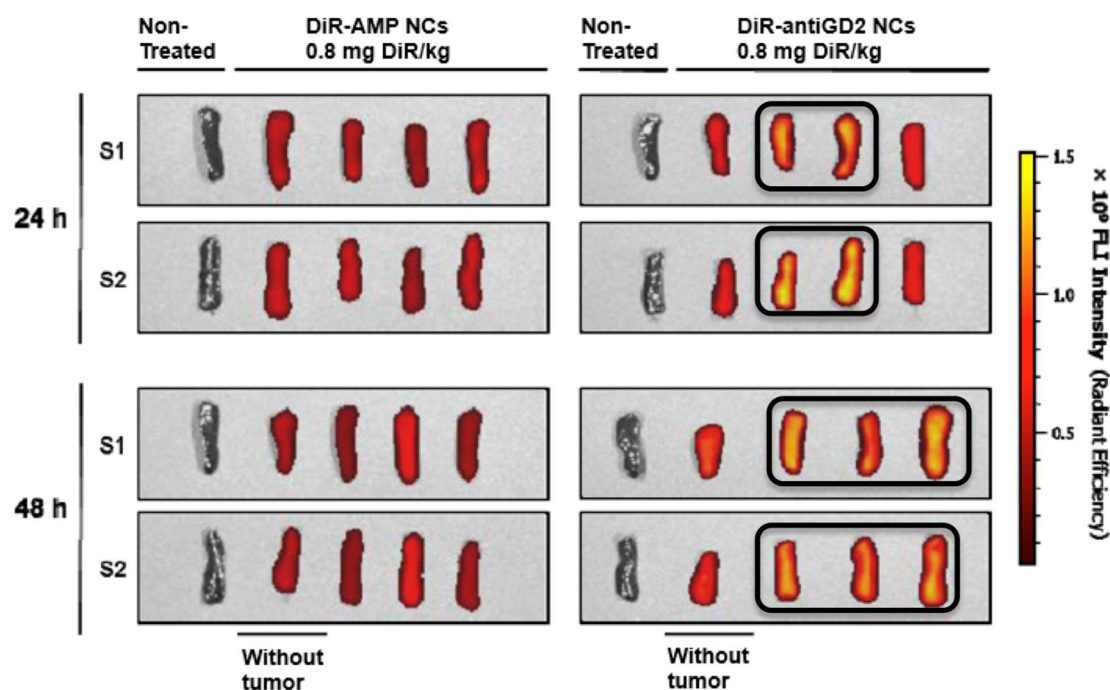


**Figure 53.** Qualitative data of *ex vivo* spleen accumulation of both types of NCs after 24 and 48 h

The fluorescence intensity in the spleens analyzed seemed to be higher for **DiR-antiGD2 NCs** than for **DiR-AMP NCs**, regardless the duration of the treatment. As marked by the squares, the spleens treated with the antibody-functionalized NCs have orange to yellow colorations, while the ones treated with amphoteric NCs are generally red. The quantitative data of these results is shown in **Figure 54**.

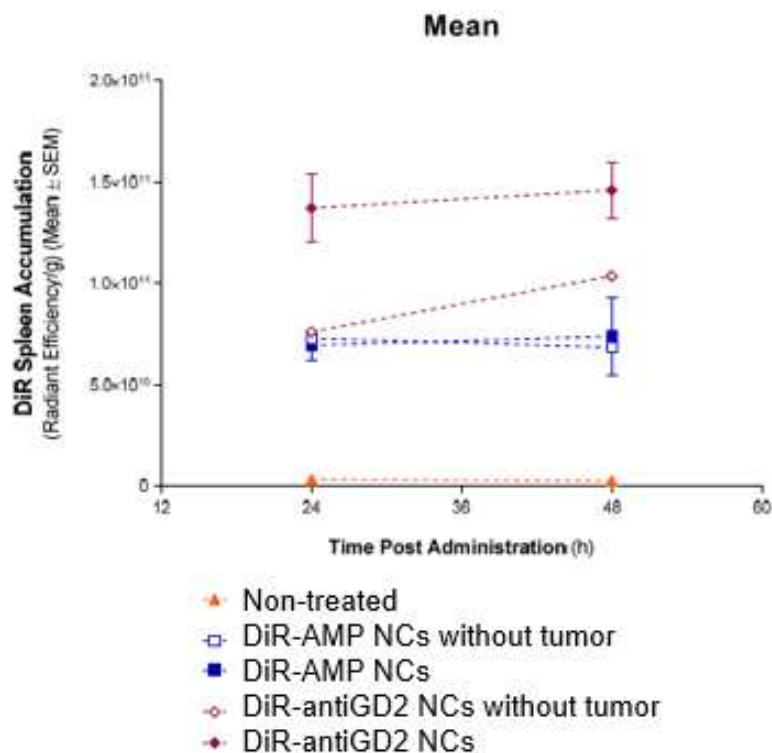


**Figure 54.** Quantitative *ex vivo* spleen accumulation of both types of NCs after 24 and 48 h

According to the quantitative data, spleen accumulation was clearly lower than the values found in liver. Particularly, **DiR-AMP NCs** led to a constant accumulation around  $7 \cdot 10^{10}$  radiant efficiency/g, which was clearly lower than those presented by **DiR-antiGD2 NCs** in NB-bearing mice. However, the second type of NCs had almost the same accumulation than the first one, but it increased after 48 h of treatment.

Overall, **DiR-AMP NCs** resulted into low accumulation rates in this organ and, interestingly, they were not uptaken more intensively at longer circulation times.

### 3.5.4.4. Kidneys accumulation

As with the previous cases, the kidneys accumulation was measured qualitatively by fluorescence intensity (**Figure 55**).

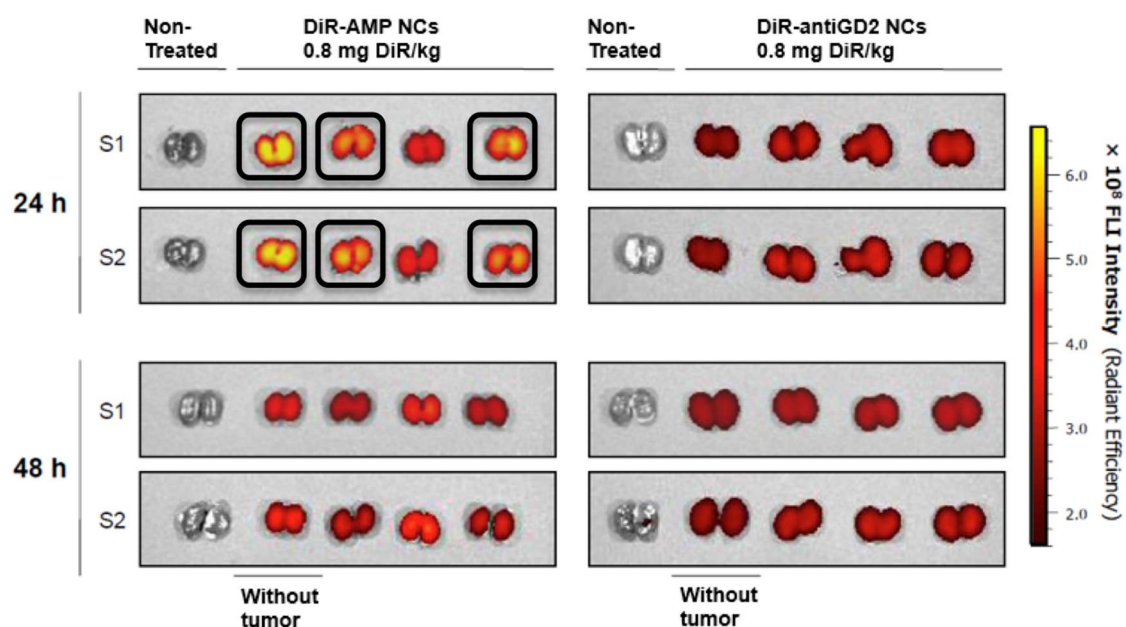


**Figure 55.** Qualitative data of *ex vivo* kidneys accumulation of both types of NCs after 24 and 48 h

The general tendency of the qualitative results indicated that **DiR-AMP NCs** have been more efficiently uptaken by the kidneys than **DiR-antiGD2 NCs**, especially after 24 h. However, the amphoteric NCs were less accumulated after 48 h in this organ, while these differences were not observed in antibody-functionalized NCs. Quantitative results from the fluorescence intensities and the weight of the organs are detailed in **Figure 56**.

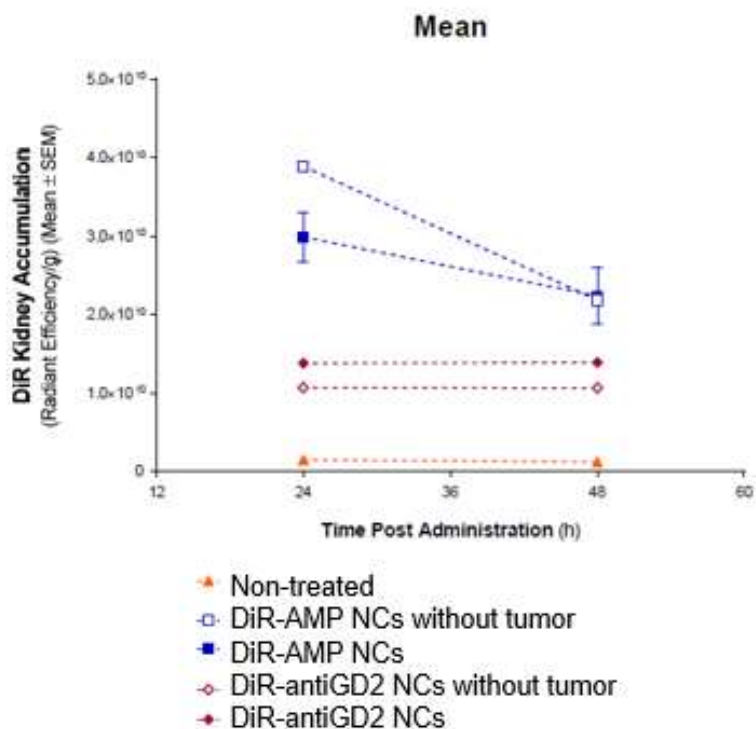


**Figure 56.** Quantitative *ex vivo* kidneys accumulation of both types of NCs after 24 and 48 h

Quantitative data showed that **DiR-AMP NCs** led to a relatively high accumulation in kidneys after 24 h ( $3\text{--}4 \cdot 10^{10}$  radiant efficiency/g), which clearly decreased after 48 h post injection (around  $2 \cdot 10^{10}$  radiant efficiency/g). In contrast, **DiR-antiGD2 NCs** showed a lower and invariable accumulation in kidneys, which was independent on time. These observations could be relate to the size of the nanosystems, since larger particles have been reported to undergo renal clearance less likely than smaller analogs.<sup>84-86</sup> Although both types of NCs have very similar average diameters (Figure 44), the particle size distribution of **DiR-antiGD2 NCs** is broader, meaning that there is a higher number of larger particles. Therefore, the probability of renal elimination of antibody-functionalized NCs is lower than for the other kind of NCs.

### 3.5.4.5. Lungs accumulation

As with the previous cases, the kidneys accumulation was measured qualitatively by fluorescence intensity (**Figure 57**).

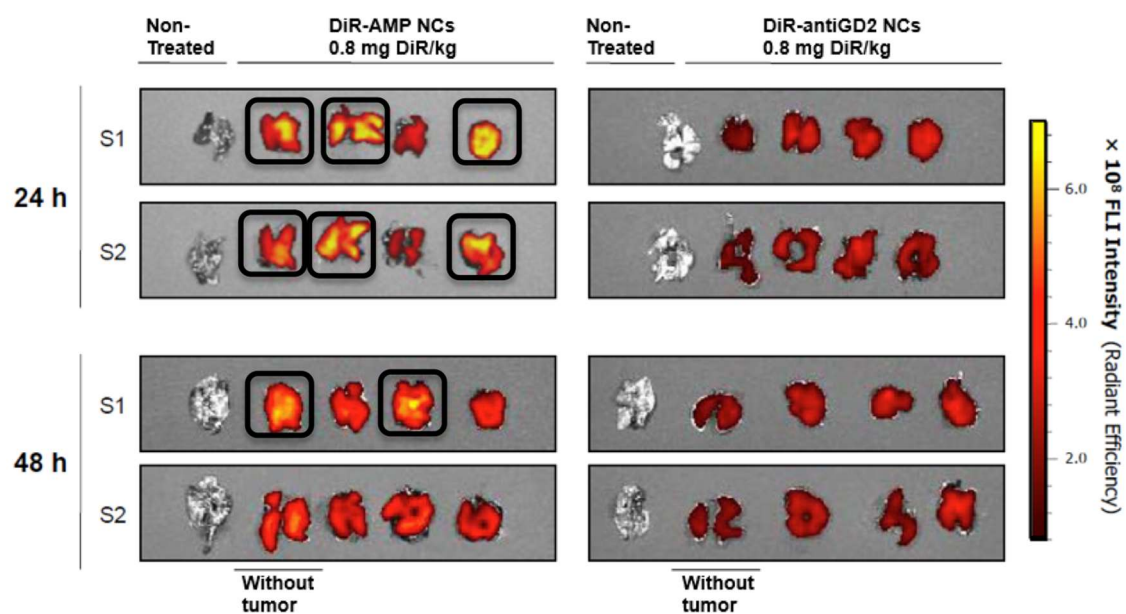


**Figure 57.** Qualitative data of *ex vivo* lungs accumulation of both types of NCs after 24 and 48 h

The qualitative analyses regarding the NCs accumulation in the lungs showed higher permeation by **DiR-AMP NCs** after 24 h post injection than by **DiR-antiGD2 NCs** at any of the two time intervals. The quantitative data is shown in **Figure 58**.

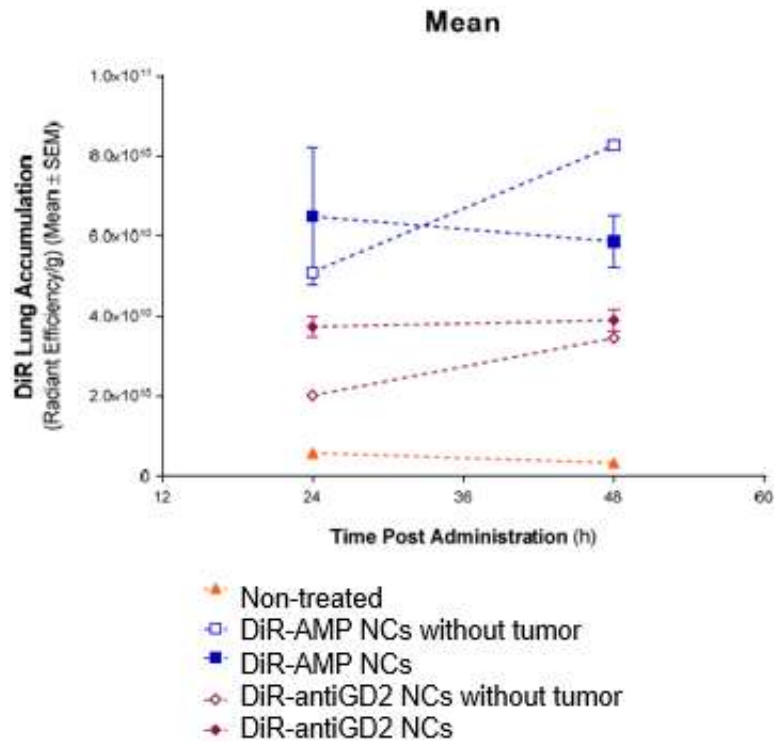


**Figure 58.** Quantitative *ex vivo* lungs accumulation of both types of NCs after 24 and 48 h

Quantitative data showed that **DiR-AMP NCs** presented a higher accumulation in lungs ( $5\text{--}7 \cdot 10^{10}$  radiant efficiency/g) after 24 h post injection, compared to **DiR-antiGD2 NCs** ( $2\text{--}4 \cdot 10^{10}$  radiant efficiency/g). The amphoteric NCs that were injected to control mice increased their accumulation significantly after 48 h, while the inverted behavior was observed in tumor-bearing mice. Among the antibody-targeted NCs, the accumulation increased for both control and NB-bearing mice, although for the control mice, the differences were more accentuated.

### 3.5.4.6. Plasma accumulation

As with the organs, the plasma accumulation was measured qualitatively by fluorescence intensity (**Figure 59**).

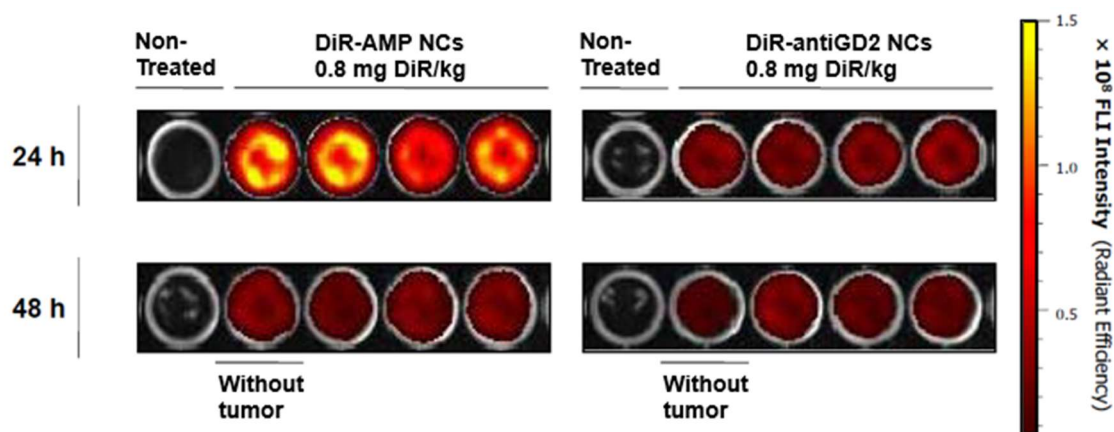


**Figure 59.** Qualitative data of *ex vivo* plasma accumulation of both types of NCs after 24 and 48 h

In this case, a more intense fluorescence was observed in **DiR-AMP NCs** after 24 h post injection than in **DiR-antiGD2 NCs**. However, this trend changed after 48 h, since the fluorescence intensities were lower and at the range of the rest of the samples analyzed. These observations were further confirmed with the quantitative analyses (**Figure 60**).

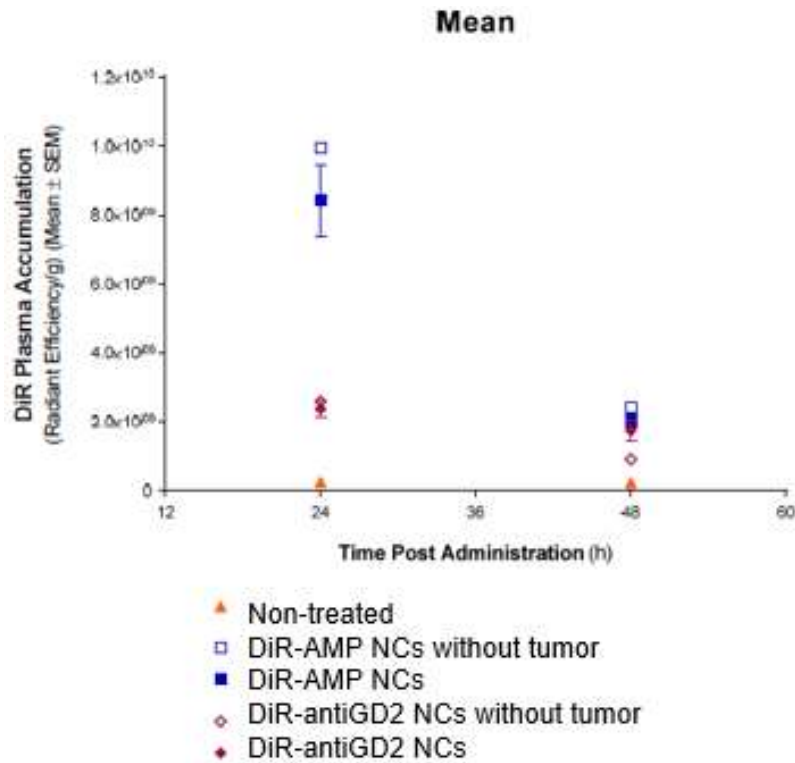


**Figure 60.** Quantitative *ex vivo* plasma accumulation of both types of NCs after 24 and 48 h

Plasma accumulations were generally lower than those found in tumor and in the rest of the organs. The data regarding **DiR-AMP NCs** showed a clear decrease of plasma accumulation from 24 ( $9 \cdot 10^9$  radiant efficiency/g) to 48 h post injection ( $2 \cdot 10^9$  radiant efficiency/g). In the case of **DiR-antiGD2 NCs** the plasma accumulation was clearly lower and constant in the two time points analyzed.

### 3.5.5. Percentage of *ex vivo* tissue-accumulation per tissue weight

The percentage of *ex vivo* **DiR-AMP NCs** and **antiGD2-AMP NCs** FLI tissue-accumulations per tissue weight is represented in **Figure 61**.

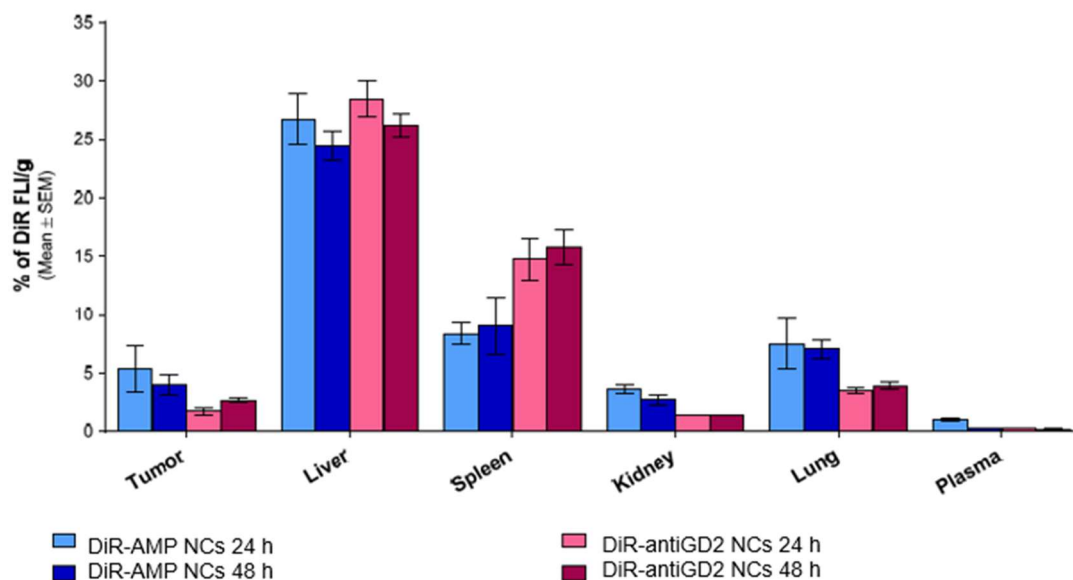


**Figure 61.** *Ex vivo* tumor, liver, spleen, kidney, lung and plasma FLI per tissue weight

The *ex vivo* accumulations were further compared and normalized to the weight of the tissue analyzed. Accordingly, the highest accumulation achieved was found in the liver and was followed by the spleen, which are the two major detoxification organs. In both cases, a higher accumulation in these organs was observed for **DiR-antiGD2 NCs** than **DiR-AMP NCs**. The lungs had a similar uptake of amphoteric NCs than the spleen, but in the case of antibody-functionalized NCs, the accumulation was significantly lower. The tumor targeting abilities of **DiR-AMP NCs** were higher than those of **DiR-antiGD2 NCs**, since the accumulation of the former NCs was almost twice the latter. The kidneys presented low NCs uptake for both types of nanosystems and the plasma did not have any significant accumulation of the NCs.

One observation raising from these results was that the injected dose was probably too high taking into account the low size and weight of the tumors. Therefore, such small tumors could only accept a small fraction of the entire dose and hence the excess was destined to the detoxification organs (liver, spleen). Moreover, the heterogeneity of the tumors also affected the expected performance of the NCs. Since there were different implantation periods (section 3.5.1), the

tumors developed were more heterogeneous and thus the resulting tumor microenvironment was not totally defined. Overall, the non-ideal conditions by which this *in vivo* biodistribution study was carried out should be taken into account to draw conclusions about the real performance of the NCs.

#### 4. Conclusions

Two different tambjamine molecules, T17 and T18, were nanoencapsulated through the methodology described in Chapter 2. Firstly, the process was applied with no modifications and the resulting NCs were characterized by the typical analytical techniques. The morphology of the nanosystems was roughly round but two different particle size populations could be observed and confirmed by DLS. These results indicated that the possible destabilization of the o/w interface could have occurred during nanoemulsion and crosslinking. Additionally, the surface charge analyses supported that both T17 and T18 were interfering the interface, since the  $\zeta$ -pot values were very high regardless the pH conditions. Finally, the calculated EE and DL were relatively low and such discouraging results could be explained by the migration of the drugs from the NC core during the dialysis, as confirmed by the color of the external medium.

Minor changes were applied in the encapsulation reaction to improve the results. TMXDI, GTCC, a combination of both and fatty acid-derived salts, NAST and NALA, were added along with T17 and T18 in order to increase the hydrophobic cargo and make the core more encapsulable. The best results were obtained by including NAST and NALA in the core, as confirmed by the characterization data. In this regard, much more homogeneous samples were obtained, narrower particle size distributions, selective shell-cationization dependent on pH conditions and higher EE and DL values. With these results, it can be confirmed that the nanoencapsulation methodology presented in Chapter 2 could also be extended to amphiphilic molecules, such as tambjamines, preserving the desired properties (size,  $\zeta$ -pot, EE and DL).

The best candidates were further characterized in biological studies. Cell viability of **T18-NAST AMP NCs** was tested in three different LC cell lines, a normal cell fibroblast cell line and two different NB cell lines. The experiments showed that

the NCs were properly degraded, releasing T18 into the cell culture, which performed a controlled cytotoxic effect that was maximum after 72 h of incubation. A slightly lower cytotoxicity was observed with the normal cell fibroblasts, indicating that they were not as sensitive as the cancerous cell lines. Irrespective of the cell line considered, the unloaded NCs did not cause any significant cell inhibition in all the concentration range assayed. Regarding the cell viabilities in the NB cell lines, the results showed that **T18-NAST-AMP NCs** were not as cytotoxic than in LC cell lines, since the obtained IC<sub>50</sub> values were higher. However, the control NCs (unloaded) did not cause any cell viability decrease, confirming the safety and biocompatibility of the polymers used.

Moreover, the NCs uptake was evaluated at short (1 h) and long incubation times (up to 48 h) and the results showed that the NCs were rapidly uptaken, since all the cells were DiO-positive after the shortest time assayed. Expectedly, more NCs were internalized after longer treatments and no saturation was observed after 48 h. Regarding the internalization mechanism, **DiO-AMP-2 NCs** penetrated A549 cells by endosomal entry and colocalized into the lysosomes and acidic compartments of the cells.

Finally, the amphoteric NCs (**DiR-AMP NCs**) were evaluated through *in vivo* biodistribution studies and compared to antiGD2-functionalized NCs (**DiR-antiGD2 NCs**). The results showed that both types of NCs were accumulated in liver and spleen, being the accumulation of antibody-targeted NCs higher than amphoteric NCs. **DiR-antiGD2 NCs** were less accumulated into the lungs than **DiR-AMP NCs**, but this trend was inverted in the tumor. The tumor targeting abilities of the amphoteric NCs were almost twice than those observed for antibody-functionalized NCs. The kidneys presented low NCs uptake of both types of nanosystems and plasma did not show any significant presence of NCs. As mentioned before, the high accumulation of NCs found in liver and spleen could indicate that the dose used in these *in vivo* studies was excessive, especially considering the small size and heterogeneity of the tumors.

Despite these experimental drawbacks, the amphoteric NCs led to good tumor accumulation rates. Such encouraging results could give way to other studies. Firstly, another *in vivo* biodistribution study using a lower dose of NCs (preserving the necessary DiR concentration) in order to assess whether the tumor targeting

abilities could be improved while minimizing the liver and spleen affectation. Secondly, *in vivo* efficacy studies to determine the therapeutic dose of the nanosystems and compare it to the free drug. These studies could be performed in various cancer cell lines, providing that the tumors generated are larger, have more microenvironment and are more homogeneous.

## 5. Bibliography

- 1 F. Bray, A. Jemal, N. Grey, J. Ferlay and D. Forman, *Lancet Oncol.*, 2012, **13**, 790-801.
- 2 R. L. Siegel, K. D. Miller and A. Jemal, *CA Cancer J. Clin.*, 2015, **65**, 5-29.
- 3 J. Ferlay, I. Soerjomataram, R. Dikshit, S. Eser, C. Mathers, M. Rebelo, D. M. Parkin, D. Forman and F. Bray, *Int. J. Cancer*, 2015, **136**, E359-E386.
- 4 D. Farmakis, P. Stafylas, G. Giamouzis, N. Maniadakis and J. Parissis, *Int. J. Cardiol.*, 2016, **203**, 279-281.
- 5 F. Bray, *Cancer Epidemiol., Biomarkers Prev.*, 2016, **25**, 3-5.
- 6 A. Jemal, F. Bray, M. M. Center, J. Ferlay, E. Ward and D. Forman, *CA Cancer J. Clin.*, 2011, **61**, 69-90.
- 7 American Cancer Society, What is cancer?, <https://www.cancer.org/cancer/cancer-basics/what-is-cancer.html>, (accessed 21<sup>st</sup> September, 2017).
- 8 L. A. Torre, F. Bray, R. L. Siegel, J. Ferlay, J. Lortet-Tieulent and A. Jemal, *CA Cancer J. Clin.*, 2015, **65**, 87-108.
- 9 L. A. Torre, R. L. Siegel, E. M. Ward and A. Jemal, *Cancer Epidemiol. Biomarkers Prev.*, 2016, **25**, 16-27.
- 10 K. D. Miller, R. L. Siegel, C. C. Lin, A. B. Mariotto, J. L. Kramer, J. H. Rowland, K. D. Stein, R. Alteri and A. Jemal, *CA Cancer J. Clin.*, 2016, **66**, 271-289.
- 11 S. S. Hecht, *Nat. Rev. Cancer*, 2003, **3**, 733-744.
- 12 S. S. Hecht, *J. Natl. Cancer. Inst.*, 1999, **91**, 1194-1210.
- 13 S. S. Hecht, *Int. J. Cancer*, 2012, **131**, 2724-2732.
- 14 K. Latimer and T. Mott, *Am. Fam. Physician*, 2015 **4**, 250-256.
- 15 G. Pfeifer, M. Denissenko, M. Olivier, N. Tretyakova, S. Hecht and P. Hainaut, *Oncogene*, 2002, **21**, 7435-7451.

- 16 J. R. Molina, P. Yang, S. D. Cassivi, S. E. Schild and A. A. Adjei, *Mayo Clin. Proc.*, 2008, **83**, 584-594.
- 17 K. Ohtsuka, H. Ohnishi, D. Kurai, S. Matsushima, Y. Morishita, M. Shinonaga, H. Goto and T. Watanabe, *J. Clin. Oncol.*, 2011, **29**, e191-e192.
- 18 S. M. Gadgeel, S. S. Ramalingam and G. P. Kalemkerian, *Radiol. Clin. North Am*, 2012, **50**, 961-974.
- 19 Z. Chen, C. M. Fillmore, P. S. Hammerman, C. F. Kim and K. k. Wong, *Nat. Rev. Cancer*, 2014, **14**, 535-546.
- 20 W. D. Travis, *Mod. Pathol.*, 2012, **25**, S18-30.
- 21 G. P. Kalemkerian, W. Akerley, P. Bogner, H. Borghaei, L. Q. M. Chow, R. J. Downey, L. Gandhi, A. K. P. Ganti, R. Govindan, J. C. Grecula, J. Hayman, R. S. Heist, L. Horn, T. Jahan, M. Koczywas, B. W. Loo, R. E. Merritt, C. A. Moran, H. B. Niell, J. O'Malley, J. D. Patel, N. Ready, C. M. Rudin, C. C. Williams, K. Gregory and M. Hughes, *J. Natl. Compr. Cancer Network*, 2013, **11**, 78-98.
- 22 A. C. Society, What is non-small cell lung cancer? , <https://www.cancer.org/cancer/non-small-cell-lung-cancer/about/what-is-non-small-cell-lung-cancer.html>, (accessed 27<sup>th</sup> September, 2017).
- 23 M. Reck, D. F. Heigener, T. Mok, J. C. Soria and K. F. Rabe, *The Lancet*, 2013, **382**, 709-719.
- 24 A. S. o. C. Oncology, Stages of Cancer, <https://www.cancer.net/navigating-cancer-care/diagnosing-cancer/stages-cancer>, (accessed 3<sup>rd</sup> January, 2018).
- 25 N. Horita, T. Woo, N. Miyazawa and T. Kaneko, *Transl. Lung Cancer Res.*, 2014, **4**, 1561-1571.
- 26 V. Georgoulas, E. Papadakis, A. Alexopoulos, X. Tsiafaki, A. Rapti, M. Veslemes, P. Palamidis and I. Vlachonikolis, *The Lancet*, 2001, **357**, 1478-1484.
- 27 B. Desoize and C. Madoulet, *Crit. Rev. Oncol. Hematol.*, 2002, **42**, 317-325.
- 28 J. T. Hartmann and H. P. Lipp, *Expert Opin. Pharmacother.*, 2003, **4**, 889-901.
- 29 M. Shimada, H. Itamochi and J. Kigawa, *Cancer Manage. Res.*, 2013, **5**, 67-76.
- 30 L. Kelland, *Nat. Rev. Cancer*, 2007, **7**, 573-584.
- 31 O. Rixe, W. Ortuzar, M. Alvarez, R. Parker, E. Reed, K. Paull and T. Fojo, *Biochem. Pharmacol.*, 1996, **52**, 1855-1865.
- 32 S. Dasari and P. Bernard Tchounwou, *Eur. J. Pharmacol.*, 2014, **740**, 364-378.

- 33 National Comprehensive Cancer Network, NCCN Guidelines, [https://www.nccn.org/professionals/physician\\_gls/default.asp](https://www.nccn.org/professionals/physician_gls/default.asp), (accessed 2<sup>nd</sup> February, 2018).
- 34 D. Screnci, M. J. McKeage, P. Galettis, T. W. Hambley, B. D. Palmer and B. C. Baguley, *Br. J. Cancer*, 2000, **82**, 966-972.
- 35 L. R. Chirieac and S. Dacic, *Surg Pathol Clin*, 2010, **3**, 71-82.
- 36 P. Maione, P. C. Sacco, A. Sgambato, F. Casaluze, A. Rossi and C. Gridelli, *Ther. Adv. Med. Oncol.*, 2015, **7**, 263-273.
- 37 A. R. Filippi, C. Mantovani and U. Ricardi, *Transl. Lung Cancer Res.*, 2012, **1**.
- 38 A. M. S. Mayer, A. D. Rodríguez, R. G. S. Berlinck and N. Fusetani, *Comp. Biochem. Physiol., Part C: Toxicol. Pharmacol.*, 2011, **153**, 191-222.
- 39 H. Malve, *J. Pharm. BioAllied Sci.*, 2016, **8**, 83-91.
- 40 R. Perez-Tomas and M. Vinas, *Curr. Med. Chem.*, 2010, **17**, 2222-2231.
- 41 K. Papireddy, M. Smilkstein, J. X. Kelly, Shweta, S. M. Salem, M. Alhamadsheh, S. W. Haynes, G. L. Challis and K. A. Reynolds, *J. Med. Chem.*, 2011, **54**, 5296-5306.
- 42 N. Darshan and H. K. Manonmani, *J. Food Sci. Technol.*, 2015, **52**, 5393-5407.
- 43 S. Afra, A. Makhdoumi, M. M. Matin and J. Feizy, *J. Appl. Microbiol.*, 2017, **123**, 1228-1236.
- 44 V. Soto-Cerrato, E. Llagostera, B. Montaner, G. L. Scheffer and R. Perez-Tomas, *Biochem. Pharmacol.*, 2004, **68**, 1345-1352.
- 45 J. T. Davis, P. A. Gale, O. A. Okunola, P. Prados, J. C. Iglesias-Sánchez, T. Torroba and R. Quesada, *Nat. Chem.*, 2009, **1**, 138-144.
- 46 A. Huczyński, *Bioorg. Med. Chem. Lett.*, 2012, **22**, 7002-7010.
- 47 I. Alfonso and R. Quesada, *Chem. Sci.*, 2013, **4**, 3009-3019.
- 48 P. I. Hernandez, D. Moreno, A. A. Javier, T. Torroba, R. Perez-Tomas and R. Quesada, *Chem. Commun.*, 2012, **48**, 1556-1558.
- 49 P. A. Gale, N. Busschaert, C. J. E. Haynes, L. E. Karagiannidis and I. L. Kirby, *Chem. Soc. Rev.*, 2014, **43**, 205-241.
- 50 E. Hernando, V. Soto-Cerrato, S. Cortes-Arroyo, R. Perez-Tomas and R. Quesada, *Org. Biomol. Chem.*, 2014, **12**, 1771-1778.

- 51 V. Soto-Cerrato, P. Manuel-Manresa, E. Hernando, S. Calabuig-Fariñas, A. Martínez-Romero, V. Fernández-Dueñas, K. Sahlholm, T. Knöpfel, M. García-Valverde, A. M. Rodilla, E. Jantus-Lewintre, R. Farràs, F. Ciruela, R. Pérez-Tomás and R. Quesada, *J. Am. Chem. Soc.*, 2015, **137**, 15892-15898.
- 52 G. Pillai, *SOJ Pharmacy & Pharmaceutical Sciences*, 2014, **2**, 1-13.
- 53 D. Bobo, K. J. Robinson, J. Islam, K. J. Thurecht and S. R. Corrie, *Pharm. Res.*, 2016, **33**, 2373-2387.
- 54 G. M. Brodeur, *Nat Rev Cancer*, 2003, **3**, 203-216.
- 55 N. K. V. Cheung and M. A. Dyer, *Nat. Rev. Cancer* 2013, **13**, 397-411.
- 56 J. M. Maris, *N. Engl. J. Med.*, 2010, **362**, 2202-2211.
- 57 American Cancer Society, Neuroblastoma Surgery, <https://www.cancer.org/cancer/neuroblastoma/treating/surgery.html>, (accessed 15<sup>th</sup> November, 2017).
- 58 R. K. Yang and P. M. Sondel, *Drugs Future*, 2010, **35**, 665-278.
- 59 K. K. Matthay, J. G. Villablanca, R. C. Seeger, D. O. Stram, R. E. Harris, N. K. Ramsay, P. Swift, H. Shimada, C. T. Black, G. M. Brodeur, R. B. Gerbing and C. P. Reynolds, *N. Engl. J. Med.*, 1999, **341**, 1165-1173.
- 60 J. E. Adrian, A. Wolf, A. Steinbach, J. Rössler and R. Süß, *Pharm. Res.*, 2011, **28**, 2261-2272.
- 61 M. Ahmed and N. K. V. Cheung, *FEBS Lett.*, 2014, **588**, 288-297.
- 62 B. S. Brown, T. Patanam, K. Mobli, C. Celia, P. E. Zage, A. J. Bean and E. Tasciotti, *Cancer Biol. Ther.*, 2014, **15**, 851-861.
- 63 A. A. Zubareva, A. A. Boyko, I. V. Kholodenko, F. N. Rozov, M. V. Larina, T. K. Aliev, I. I. Doronin, P. A. Vishnyakova, I. M. Molotkovskaya and R. V. Kholodenko, *Russ. J. Bioorg. Chem.*, 2016, **42**, 532-545.
- 64 D. Di Paolo, C. Brignole, F. Pastorino, R. Carosio, A. Zorzoli, M. Rossi, M. Loi, G. Pagnan, L. Emionite, M. Cilli, S. Bruno, R. Chiarle, T. M. Allen, M. Ponzoni and P. Perri, *Mol. Ther.*, 2011, **19**, 1131-1140.
- 65 P. W. Voorhees, *J. Stat. Phys.*, 1985, **38**, 231-252.
- 66 P. Taylor, *Adv. Colloid Interface Sci.*, 1998, **75**, 107-163.
- 67 J. Weiss, N. Herrmann and D. J. McClements, *Langmuir*, 1999, **15**, 6652-6657.
- 68 W. Chung-Hao, H. Yao-Jhang, C. Chia-Wei, H. Wen-Ming and P. Ching-An, *Nanotechnology*, 2009, **20**, 1-7.

- 69 C. A. Peng and C. H. Wang, *Cancers*, 2011, **3**, 227-240.
- 70 G. T. Hermanson, *Bioconjugate Techniques*, Academic Press, Boston, 2013.
- 71 B. S. Brown, PhD, University of Texas, 2014.
- 72 M. Bodanszky, *Principles of peptide synthesis*, Springer Science & Business Media, Berlin, 2012.
- 73 D. Sehgal and I. K. Vijay, *Anal. Biochem.*, 1994, **218**, 87-91.
- 74 M. J. E. Fischer, *Surface Plasmon Resonance: Methods and Protocols*, Humana Press: Totowa, 2010.
- 75 A. J. van der Vlies, C. P. O'Neil, U. Hasegawa, N. Hammond and J. A. Hubbell, *Bioconjugate Chem.*, 2010, **21**, 653-662.
- 76 C. P. Ryan, M. E. B. Smith, F. F. Schumacher, D. Grohmann, D. Papaioannou, G. Waksman, F. W. b, J. R. Baker and S. Caddick, *Chem. Commun.*, 2011, **47**, 5452-5454.
- 77 J. H. Saunders and R. J. Slocombe, *Chem. Rev.*, 1948, **43**, 203-218.
- 78 R. G. Arnold, J. A. Nelson and J. J. Verbanc, *Chem. Rev.*, 1957, **57**, 47-76.
- 79 S. Ozaki, *Chem. Rev.*, 1972, **72**, 457-496.
- 80 E. Delebecq, J. P. Pascault, B. Boutevin and F. Ganachaud, *Chem. Rev.*, 2013, **113**, 80-118.
- 81 J. R. Rumble, *Handbook of Chemistry and Physics*, 98<sup>th</sup> Edition, CRC Press, Boca Raton, 2017.
- 82 S. A. Cohen and D. P. Michaud, *Anal. Biochem.*, 1993, **211**, 279-287.
- 83 S. A. Cohen and K. M. De Antonis, *J. Chromatogr. A*, 1994, **661**, 25-34.
- 84 H. S. Choi, W. Liu, P. Misra, E. Tanaka, J. P. Zimmer, B. I. Ipe, M. G. Bawendi and J. V. Frangioni, *Nat. Biotechnol.*, 2007, **25**, 1165-1170.
- 85 A. A. Burns, J. Vider, H. Ow, E. Herz, O. Penate-Medina, M. Baumgart, S. M. Larson, U. Wiesner and M. Bradbury, *Nano Lett.*, 2008, **9**, 442-448.
- 86 J. H. Park, L. Gu, G. Von Maltzahn, E. Ruoslahti, S. N. Bhatia and M. J. Sailor, *Nat. Mater.*, 2009, **8**, 331-336.

# **CHAPTER 4**

*Application of peptide-functionalized  
nanocapsules to breast cancer*



# 1. Introduction

## 1.1. Breast cancer

### 1.1.1. Epidemiology and risk factors

Breast cancer (BC) is the most frequently occurring cancer in women<sup>1,2</sup> and represents a major public health problem, being responsible for approximately half a million deaths per year.<sup>3-8</sup> The World Health Organization shows that nearly 1.7 million women were diagnosed with BC in 2012, leading to 522,000 related deaths, which represented an increase in BC incidence and mortality of approximately 18% from 2008. Moreover, such an alarming increase is expected to be even more accentuated in upcoming years, since 3.2 million new cases are predicted to occur in 2050.<sup>2,5,9</sup>

BC is one of the most heterogeneous cancers and therefore it cannot be considered as a single disease, but a group of malignancies developing from a single organ. In fact, the different BC types show important biological and pathological disparities that encompass from slow growing tumors with excellent prognosis, to very aggressive untreatable tumors.<sup>2,6,10,11</sup>

There are several risk factors and lifestyle habits that have been attributed to BC development (**Figure 1**).

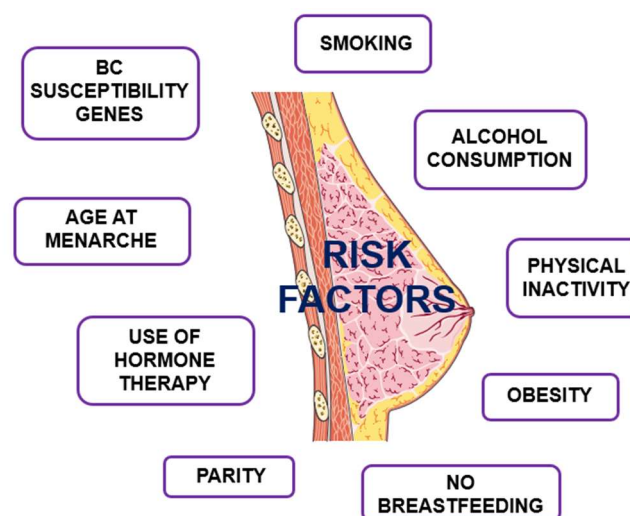


**Figure 1.** Risk factors for BC

Regarding the risk factors related to the woman's biology and parity, early age at menarche, late age at first birth, nulliparity, no breastfeeding, late age at menopause and use of combined estrogen and progestin postmenopausal hormone therapy have been commonly reported. About the lifestyle habits, alcohol and tobacco consumption, exposure to ionizing radiation, leanness in early life, obesity in later life and sedentarism have been identified.<sup>3,4,10,12-15</sup>

These risk factors may promote the development of specific types of BC and it is possible that, besides influencing the course of the disease, they have an effect on survival. For instance, some studies point out that nulliparous women have a better prognosis and an early age at first full-term pregnancy results in an adverse prognostic factor.<sup>2,5,12,16</sup> Likewise, smoking has been associated with a less favorable prognosis and this fact becomes more accentuated with increasing number of cigarettes per day.<sup>17</sup> Alcohol consumption also goes in that direction, since different studies have demonstrated a dose-response relationship between ethanol intake and risk to contract this disease.<sup>12,18</sup> Moreover, a statistically significant association has been found between sedentarism and obesity and survival from BC. However, some uncertainty surrounds the link between exogenous estrogen use and survival. Several investigations show no association, whereas other point out adverse prognostics or an improved survival among users of the oral contraceptive pill.<sup>6,19</sup>

### 1.1.2. Subtypes

There are different strategies for classifying BC, focusing on tumor morphological characteristics, histological grade and the expression of specific receptors, such as the estrogen receptor (ER), progesterone receptor (PR) and human epidermal growth factor receptor type 2 (HER2).<sup>2</sup> Among these classification criteria, the last one is most interesting, since it gives an idea about the clinical options for each of them.

Using RNA expression arrays, different molecular types of BC could be identified by Perou *et al.*<sup>20</sup> in 2000: two ER/PR-positive subgroups and three ER-negative subtypes<sup>2-4,10,15,16,21-23</sup> (**Figure 2**).

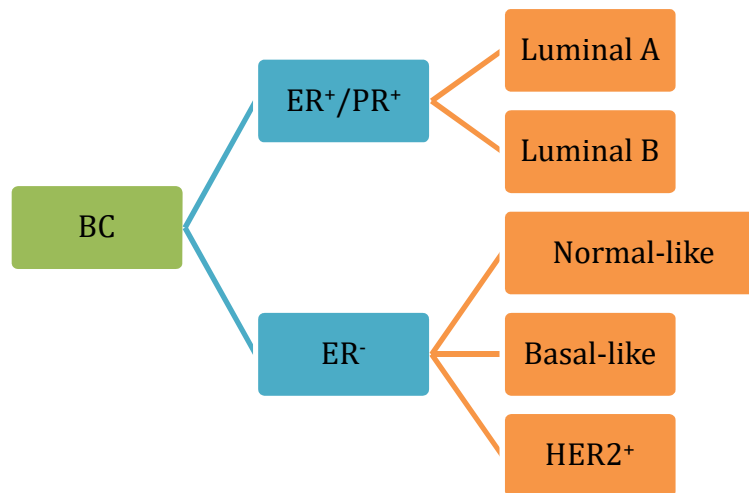


**Figure 2.** BC subtypes depending on the expression of specific receptors

ER<sup>+</sup> and PR<sup>+</sup> tumors can be further classified into luminal A and the less endocrine-responsive luminal B. Among the ER<sup>-</sup> tumors, normal-like BC are usually enriched for genes expressed in adipose tissue<sup>24</sup> and basal-like tumors present high expression of genes normally identified in myoepithelial or basal cells.<sup>4,15,22,25</sup> Finally, the HER2<sup>+</sup> subtype presents an elevated expression of HER2 and related genes.<sup>26</sup> Overall, ER<sup>+</sup> tumors are more common than ER<sup>-</sup> cancers whereas HER2<sup>+</sup> and basal-like subtypes exhibit clinically a poorer outcome than luminal and normal-like groups. Moreover, it has been observed that the prognosis is worse in a stage-independent manner for both HER2<sup>+</sup> and basal-like subtypes of ER<sup>-</sup>. HER2<sup>+</sup> and basal-like groups were also found to contain a larger percentage of stem cell-like cells, which contribute to their aggressive clinical behavior.<sup>2</sup>

Breast tumors that do not express either ER, PR or HER2 are called triple-negative breast cancers (TNBC) and fall into the basal-like subgroup, representing approximately 80% of the cases and 15% of the overall BC.<sup>4,15,22,25</sup> TNBC is a phenotype with very poor clinical outcome and occur more frequently in African-American or Hispanic women than in other racial or ethnic groups.<sup>15,21-23</sup>

Importantly, there is another form of BC, which is called inflammatory breast cancer. Its main characteristic is that it is presented as a tumor embolus in dermal lymphatic channels, with a generalized breast tenderness and is frequently diagnosed at an advanced stage. Almost half of the IBC have elevated levels of HER2, highly angiogenic nature and tend to metastasize.<sup>2</sup>

### 1.1.3. Treatments

#### 1.1.3.1. Conventional treatments

In clinical practice, three major subsets of BC can be readily recognized: hormone-receptor positive BC, HER2-overexpressing BC and the so-called TNBC, which lack ER, PR and HER2<sup>11,27,28</sup> (**Figure 3**).

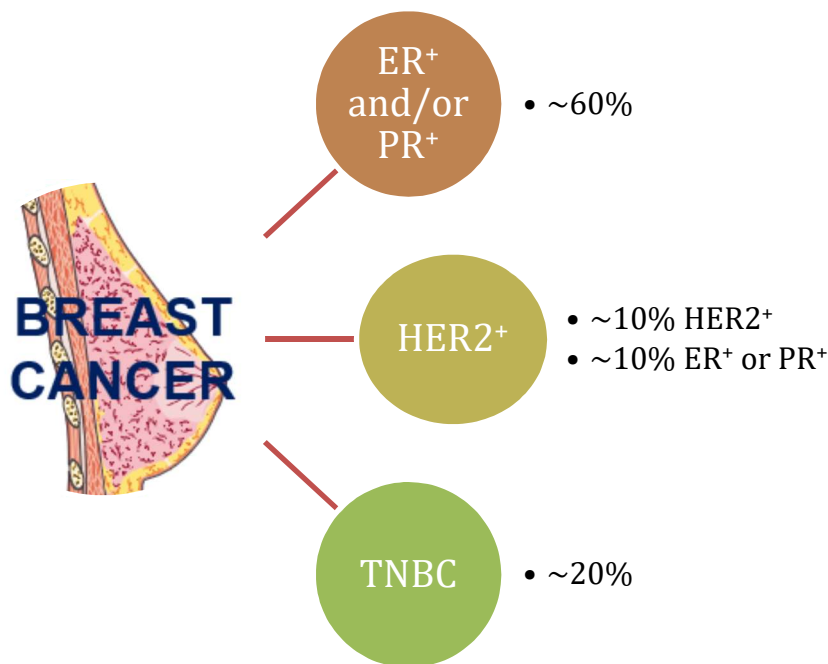


**Figure 3.** BC types according to clinical criteria

In general, in developed countries offering routine mammography programs, hormone receptor-positive BC constitute the large majority of all tumors and are very common in postmenopausal and older women. HER2<sup>+</sup> BC account for around 20% of all tumors and approximately half of them also express ER or PR, although in lower levels.<sup>29</sup> TNBC represent approximately 20% of all cases and, as the rest of basal-like BC, show a highly proliferative nature and serious invasive capacities.<sup>22,30</sup> Therefore, due to the lack of ER, PR and HER2 receptors,<sup>15</sup> the prognosis of TNBC remain poor and difficult to treat.<sup>10,14,22,25</sup> Both HER2<sup>+</sup> and TNBC subtypes are found more commonly in young women.<sup>3,4,10,14,15</sup>

Different treatment paradigms are emerging for each of the major clinical subsets of BC. For women having a hormone receptor-positive BC, endocrine therapy remains the mainstay alternative for early and advanced stages and frequently leads to good survival rates.<sup>4,31</sup> Additionally, these patients may also undergo chemotherapy on a selective basis in the adjuvant setting, or simply as treatment in case they become endocrine therapy-resistant. Those women with overexpressed HER2 receptor will typically be candidates for antiHER2 therapy with trastuzumab, the antiHER2-targeted mAb. However, this drug is commonly administered in combination with chemotherapy.

Finally, those patients with TNBC cannot benefit from targeted approaches, providing their lack of hormonal or HER2 receptors and therefore chemotherapy is currently their sole option.<sup>22,30,32</sup> The clinical outcome has shown a discouraging scenario for this BC subtype, since early relapse occurs very often and the chances of developing visceral and brain metastases are higher than for other BC subset.<sup>3,4</sup> In this case, chemotherapeutic agents include anthracyclines (i.e. doxorubicin and epirubicin) and microtubule pathway-inhibitors, such as taxanes (i.e. PTX and docetaxel) (**Figure 4**).<sup>4,14,33</sup>

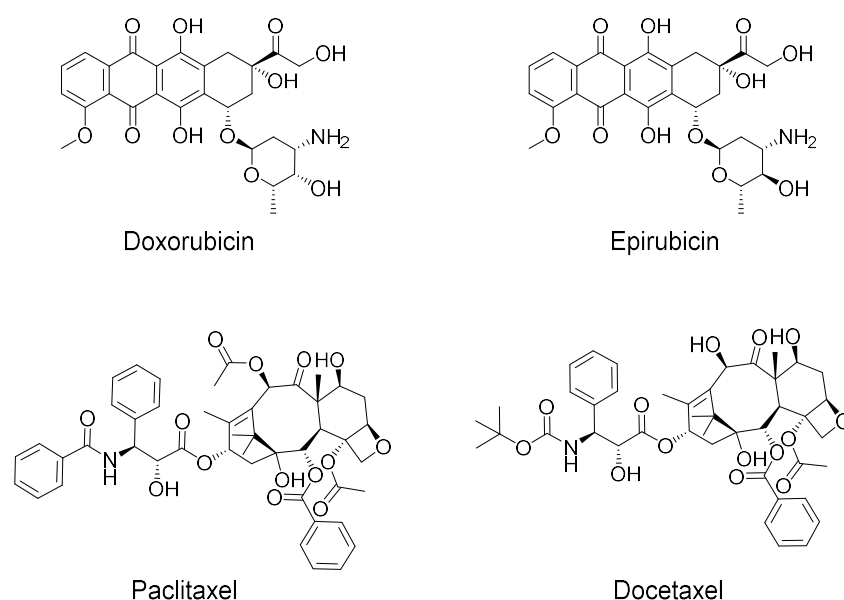


**Figure 4.** Chemical structure of some chemotherapeutic agents used to treat BC

Drug resistance to anthracyclines and taxanes, along with the fact that the time to progression is under 12 months, led to the development of more advanced chemotherapeutic agents. Among them, the most common ones are ixabepilone, eribulin mesylate, cyclophosphamide, methotrexate and fluorouracil (**Figure 5**).

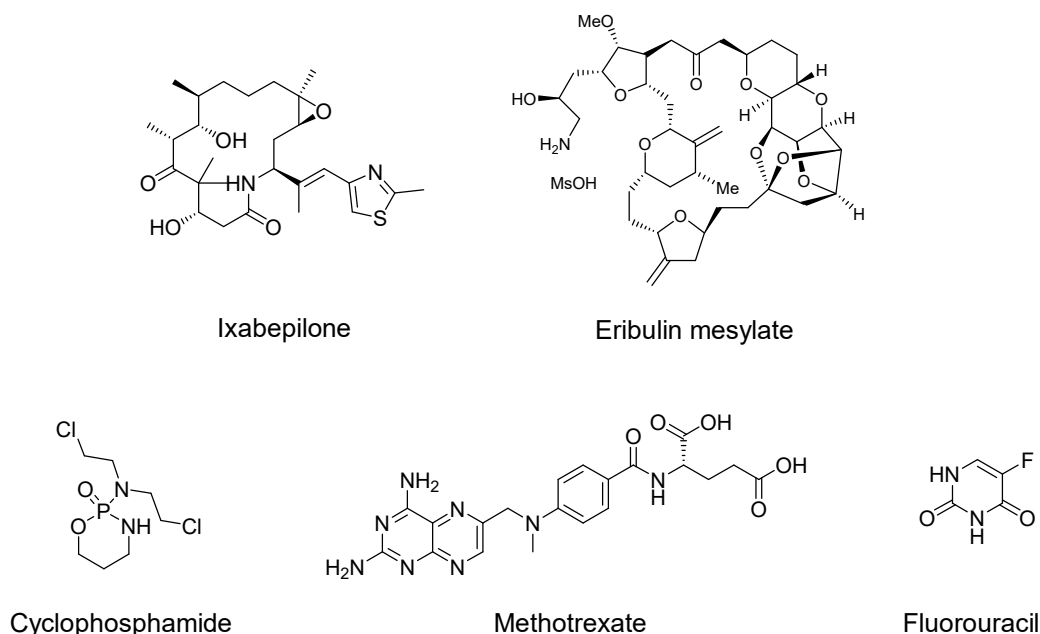


**Figure 5.** Chemical structure of some chemotherapeutic agents used to treat BC

The semi-synthetic epothilone B analog, ixabepilone, has shown similar cytotoxicity compared to taxanes and an increased aqueous solubility. Eribulin mesylate was developed for women with metastatic BC who had already received anthracycline and taxane-based chemotherapy. Its administration led to a response rate of 9% and a survival advantage compared to other treatment options. Finally, the combination of cyclophosphamide, methotrexate and fluorouracil is currently the option for patients with low to intermediate-risk of relapse or for those who cannot tolerate the aforementioned therapies. Oral administration of these drugs led to a 34% improvement in disease-free survival and overall survival.<sup>4,14,34</sup>

Finally, there are some types of BC in which the genes associated with the DNA repair are dysfunctional. In these cases, the use of Pt derivatives has been also proposed, since the efficacy of this kind of drugs is related to the cellular saturation to repair Pt adducts of DNA. In fact, it was demonstrated that the progression-free survival in TNBC patients receiving cisplatin- and carboplatin-based chemotherapies was significantly prolonged.<sup>4,14</sup>

### 1.1.3.2. Targeted therapies

- *Antiestrogen therapies*

Approximately 75% of invasive breast tumors are ER<sup>+</sup> or PR<sup>+</sup>. Therefore, the use of antiestrogen drugs has been a well-known paradigm for decades now. There are two main groups of antiestrogen therapies: selective ER modulators or ER downregulators and aromatase inhibitors.

On one hand, selective ER modulators' action is based on the competition to bind the ER with estrogen and the most frequent drugs are tamoxifen and toremifene, which were approved for metastatic and adjuvant BC treatments. Raloxifene is also administered but only to reduce the risk of invasive BC in high-risk postmenopausal women. On the other hand, ER downregulators reduce the levels of ER protein in cells, by potentiating its degradation. Fulvestrant has been proved to induce relatively good outcomes, with long periods of tumor control and no increased toxicity.

Finally, aromatase inhibitors base their mechanism of action on the inhibition of aromatase enzymes, which are crucial for the conversion of androgen to estrogen. The new generation of aromatase inhibitors have shown a significant disease-free survival benefit over tamoxifen and have replaced it as a standard of care for ER<sup>+</sup> BC in adjuvant and neoadjuvant settings. Among them, exemestane, anastrozole and letrozole are some of the common examples of aromatase inhibitors.

- *HER2-directed therapies*

Among HER2<sup>+</sup> BC treatment options, trastuzumab is the most common one. It is a humanized mAb directed against the extracellular domain of the HER2 protein. In randomized clinical trials, the addition of this antibody to standard chemotherapy regimens improved the response rate, time to progression and overall survival.<sup>26,35</sup> Trastuzumab is very well tolerated but can induce heart failure in those cases is administered with anthracyclines.

Lapatinib is another drug, approved by the FDA, for the treatment of HER2<sup>+</sup> BC with who previously received anthracyclines, taxanes and trastuzumab-based therapies. Clinical results have shown that adding lapatinib to a chemotherapeutic

agent named capecitabine improved response rates and time to progression. In line with these findings, lapatinib has led to small but better responses in those patients suffering from HER2-overexpressing tumors that have spread to brain and liver. Therefore, this drug, in combination with other agents, has opened new opportunities for larger and more successful trials of this challenging patient population.

Novel antibody therapies have emerged after realizing the potential of antibody-mediated therapies. In this regard, pertuzumab and trastuzumab-DM1, are two examples of next-generation mAb and has shown the capacity to potentiate the effects of trastuzumab in inhibiting the HER2<sup>+</sup> BC cells *in vivo*.<sup>36</sup>

- *Angiogenesis inhibitors*

The central hypothesis that underlies the development of this modality of therapy is that the formation of new blood vessels, angiogenesis, is a critical event in the maintenance and dissemination of clinically significant cancers. The most important mediators of angiogenesis include the epidermal growth factor receptor (EGFR) and the vascular endothelial growth factor receptor (VEGFR).<sup>31,36</sup>

EGFR is a membrane-bound tyrosine kinase receptor that is believed to play a central role in cancer growth and expression. Since this receptor has been observed in 60–70% of TNBC cases,<sup>15,22</sup> a great deal of investigations focused their efforts on exploiting such a promising research line. There are mainly two types of EGFR-targeted therapies: EGFR-directed antibodies, such as cetuximab, and inhibitors of receptor phosphorylation, like gefitinib and erlotinib. In a Phase II study, cetuximab was investigated in combination with irinotecan and carboplatin and the presence of the antibody led to a higher response rate, but with a higher incidence of grade 3 and 4 toxicities.<sup>15,28,37-39</sup>

Likewise, the vascular endothelial growth factor (VEGF) has been reported to show increased levels among women with TNBC. VEGF has been implicated in pathological angiogenesis associated with tumors, intraocular neovascular disorders and other conditions.<sup>40,41</sup> In this regard, bevacizumab has been prospectively investigated in combination with paclitaxel in women showing HER2-metastatic BC. The results indicated a significant improvement in progression-free

survival with the addition of the antibody, an effect that was also observed in women with TNBC.<sup>15</sup>

### 1.1.3.3. FDA-approved nanosystems applied to BC

In the last decades, the general tendency has evolved to small molecules or antibodies with the capacity to specifically target BC cells. In this scenario, a great deal of nanosystems have also been developed and tested in a variety of preclinical and clinical trials. However, despite of the intensive activity in the nanotechnology field, only some of them have reached the market or are being studied in very advanced phases.

Among them, the first one approved by the FDA was the liposomal doxorubicin Doxil (also known as Caelyx, Evacet and Lipodox), which was formulated to improve the balance between the efficacy and toxicity of the drug. Basically, Doxil is prepared from unilamellar liposomes of 80–90 nm of size, coated with PEG, and accumulates to the tumor passively due to the increased blood circulation times (**Figure 6**). This formulation generates lower heart-related side effects but high skin reactions, hypersensitivity and inflammation of the mucus lining. Moreover, despite of the expected targeting abilities of these systems, the increase in patients' survival has not been yet demonstrated.

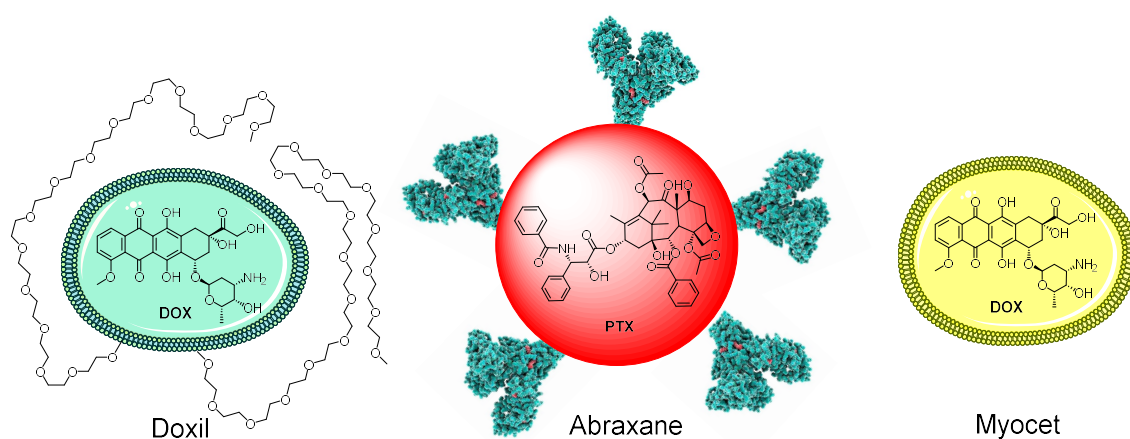


**Figure 6.** FDA-approved nanosystems to treat different modalities of BC

Abraxane, as described in Chapter 3, is based on albumin-bound PTX nanospheres of around 130 nm. Besides being applied for a specific type of LC, it was also approved for the treatment of metastatic BC.<sup>42,43</sup>

Finally, Myocet, approved in Europe and Canada, is another doxorubicin-loaded DDS, which is based on non-pegylated liposomes and is indicated for the first-line treatment of metastatic BC in combination with cyclophosphamide. It is currently being studied in combination with trastuzumab and paclitaxel for metastatic HER2<sup>+</sup> BC. In this case, the diameter of Myocet is around 180 nm and it has shown a significantly longer half-life compared to the free drug.<sup>42,43</sup> Moreover, in patients with metastatic BC, this product has proven to be as effective as free doxorubicin and less cardiotoxic, allowing longer treatment periods.<sup>44</sup>

## 2. Objectives

The particular goals for this Chapter are:

- **The preparation of amphoteric NCs loaded with a high concentration of PTX** by using the methodology presented in Chapter 2.
- **The study of the physicochemical properties** of highly concentrated amphoteric NCs and their *in vitro* cytotoxicity.
- **The synthesis of highly concentrated PTX-loaded NCs decorated with a peptide** targeting TNBC and luminal-A BC cells.
- **The study of the physicochemical properties** and the *in vitro* cell uptake of the NCs targeting TNBC and luminal-A BC cells.
- **The preparation of highly concentrated PTX-loaded NCs decorated with a peptide** targeting endothelial cells.
- **The study of the physicochemical properties** and the *in vitro* cell uptake of the NCs targeting endothelial cells.

### 3. Results and discussion

The results obtained in this Chapter are based on a collaboration project between Ecopol Tech, SL, Vall d'Hebron Research Institute (VHIR) and the Combinatorial Chemistry Unit from Parc Científic de Barcelona (UQC-PCB). Considering the objectives mentioned above, this section is divided into three main parts. The first one contains all the results regarding the synthesis and characterization of highly drug-concentrated amphoteric NCs. The second one presents the work carried out on the synthesis and characterization of NCs decorated with a specific peptide that targets luminal-A and TNBC cells. Finally, the last part is similar to the previous one, but with using another peptide to target endothelial cells.

A common feature that the three types of NCs share is that they contain PTX (**Figure 4**), since it is widely used as a chemotherapeutic agent against BC and it is an encapsulable drug, according to its hydrophobicity. However, for the *in vitro* studies, a fluorophore (DiO) was used instead of PTX. As part of the collaboration, the peptides were developed in the Combinatorial Chemistry Unit from Parc Científic de Barcelona (UQC-PCB) and the biological studies were performed in the Functional Validation and Preclinical Research laboratory (VHIR).

#### 3.1. Amphoteric NCs

##### 3.1.1. Preparation of the NCs

The NCs were synthesized following the typical nanoencapsulation process described in **Scheme 11** of Chapter 2, with the exception that a higher amount of drug was added in order to make the NCs highly concentrated. The target DL was around 17–18% wt, because that should guarantee the desired concentration of PTX in the aqueous solution.

As it was shown in the previous experiments, **Figure 7** displays the monitorization of the nanoencapsulation reaction by IR spectroscopy.

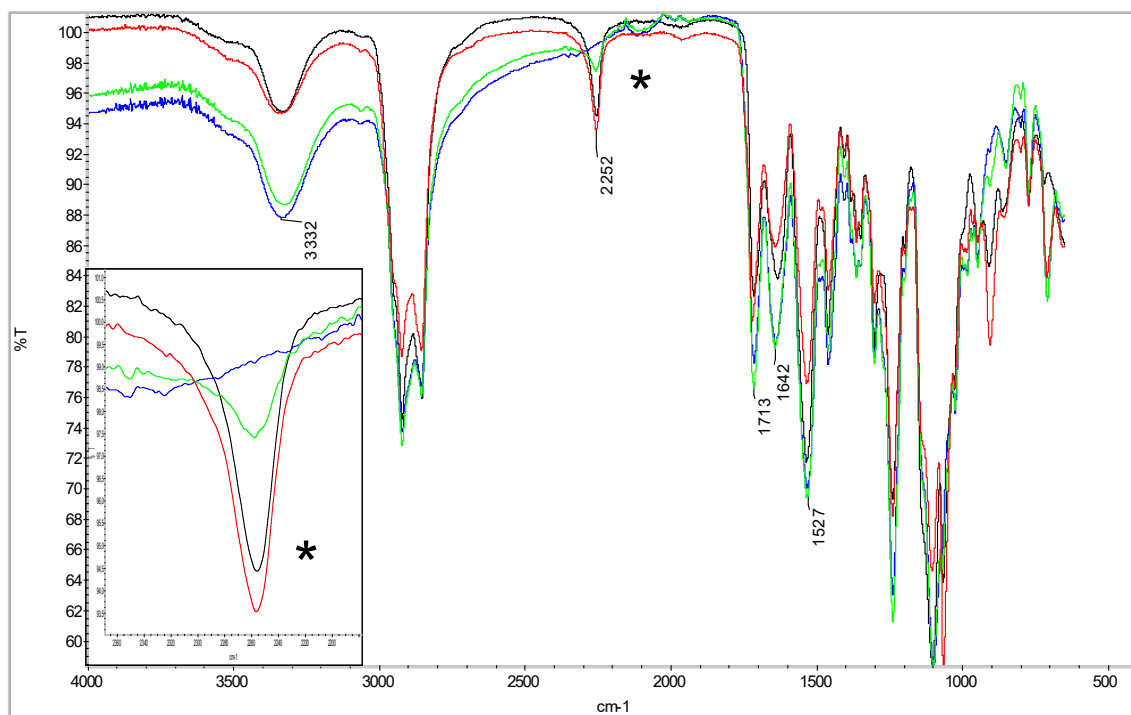


**Figure 7.** IR spectra showing the different steps of the nanoencapsulation process

The red line of the IR spectra corresponds to the sample when **P1**, along with PTX, was mixed with IPDI and the black line represents the sample after 30 min. In this step, the intensity of the NCO stretching band at  $2252\text{ cm}^{-1}$  decreased slightly, confirming the isocyanate consumption due to the reaction between the amines of **P1** and NCO groups of IPDI. In this step, an increase of the intensity of the bands at  $1642\text{ cm}^{-1}$  and  $1527\text{ cm}^{-1}$  was also observed, confirming the formation of new urea bonds. Afterwards, L-lysine sodium salt was added and reacted with the previously activated **P1** polymer. The sample was analyzed after 45 min (light green line) and another decrease of the NCO stretching band and an increase of the urea bands were noticed. Finally, DETA was added and the IR spectrum of the sample was recorded after 5 min (blue line). The NCO stretching band instantaneously disappeared because of the rapid reaction between remaining NCO groups and this polyamine.

The crosslinking reaction was also monitored measuring the pH of the nanoemulsion over time. The result is shown in **Figure 8**.

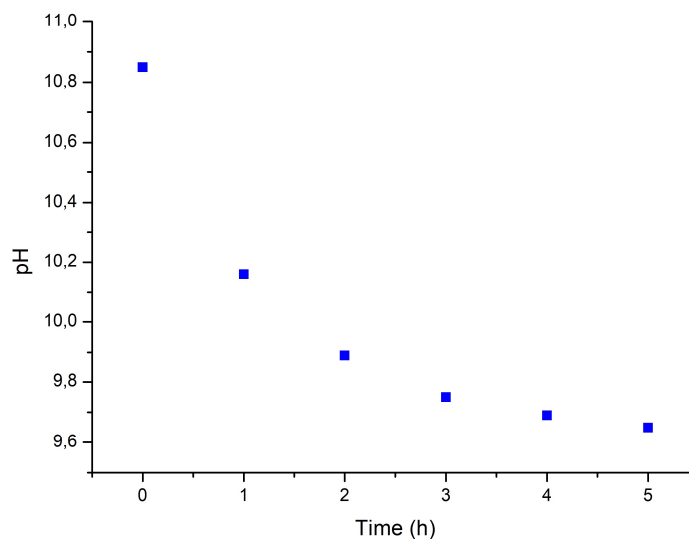


**Figure 8.** pH of the nanoemulsion after the addition of DETA

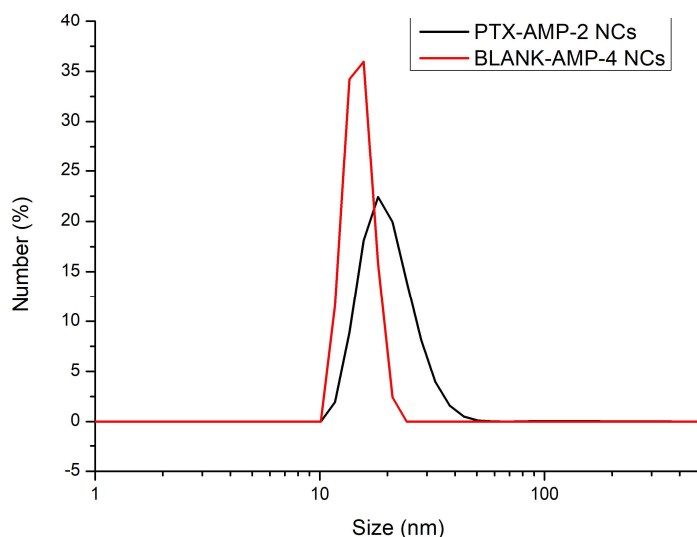
The pH of the medium became high ( $\sim$  pH = 11) when DETA was added, but it decreased over time, suggesting that the amine residues and the remaining NCO groups from the NCs reacted to form new urea bonds, therefore the pH of the emulsion decreased accordingly. After the crosslinking, the NCs were dialyzed prior to physicochemical characterization.

### 3.1.2. Characterization of the NCs

The **PTX-AMP-2 NCs** were characterized in terms of size, surface charge, EE and DL by the typical analytical methods used previously. However, the morphology of these NCs was not evaluated because it had been studied for analogous NCs loading a lower concentration of PTX (**PTX-AMP NCs**), as described in Chapter 2. Therefore, it was not considered necessary to repeat this study, since no significant morphological changes were expected.

### 3.1.2.1. Size

The particle size distribution of **PTX-AMP-2 NCs** was measured and compared to its corresponding blank, **BLANK-AMP-4 NCs**, to evaluate the effect of a high cargo concentration inside the NC (**Figure 9**).



Sample code	Mean $\bar{\phi}$ (nm)	SD (nm)	PDI
<b>PTX-AMP-2 NCs</b>	20.08	5.74	0.08
<b>BLANK-AMP-4 NCs</b>	14.26	1.835	0.02

**Figure 9.** Particle size distribution of the samples and statistical analysis

The average particle size of the sample was approximately 20 nm, while the blank particles were slightly smaller, with around 15 nm. This result is coherent with the fact that the higher the hydrophobic cargo, the larger the diameter. However, by comparing these results with the ones obtained for **PTX-AMP NCs**, described in Chapter 2 (**Figure 29** of Chapter 2), it can be concluded that an increase of the PTX cargo from around 13% wt to 17% wt did not have any significant effect on the NC size.

### 3.1.2.2. Surface properties

The surface charge was studied by  $\zeta$ -pot measurements at different pH values, ranging from 5.5 to 8.0 (**Figure 10**).

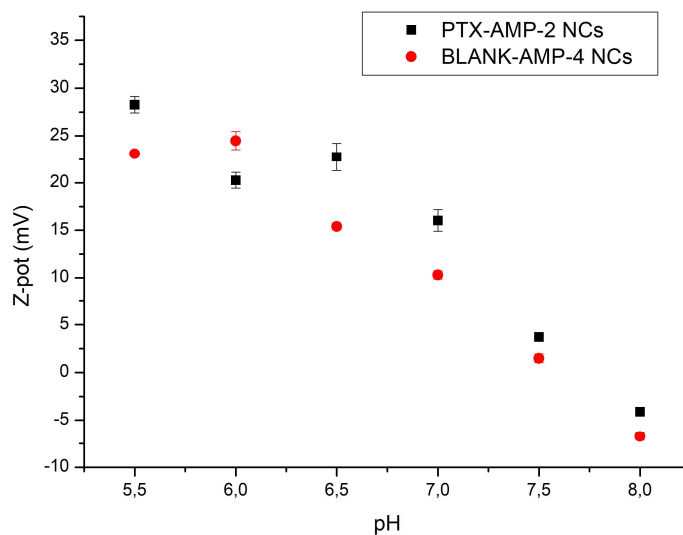


**Figure 10.**  $\zeta$ -Pot of PTX-AMP-2 NCs and BLANK-AMP-4 NCs

Both types of NCs showed a shell cationization that depended on the acidity of the medium, confirming the amphoteric properties of the NCs. The difference between the  $\zeta$ -pot of both samples analyzed was very low, suggesting that the presence of PTX inside the NC core did not have any effect in the surface properties of the system. These results are in line with the ones obtained for the previous sample loading PTX (PTX-AMP NCs), described in Chapter 2 (**Figure 31** of Chapter 2).

### 3.1.2.3. Encapsulation efficiency and drug loading

The EE and DL were also determined in order to evaluate the effect of a higher payload inside the NC. The results are shown in **Table 1**.

**Table 1.** EE and DL values for the PTX-AMP-2 NCs

Sample code	EE (% wt)	DL (% wt)
PTX-AMP-2 NCs	98.80 ± 0.67	17.35 ± 0.12

The EE value was almost 100%, which indicates that the PTX added in the nanoencapsulation process was successfully incorporated into the NC core. Therefore, the DL was also high and it nearly reached the theoretical value. Finally, these results are coherent with the conclusions of the work described in Chapter 3, which confirm that the more hydrophobic the drug, the greater the entrapment efficiency.

### 3.1.3. Cell viability

The cytotoxicity of the PTX-loaded NCs was evaluated *in vitro* in two well-established BC cell lines, MDA-MB-231 and MCF-7. The former belongs to the TNBC subtype, while the latter falls into the luminal-A subset. The cell viability was studied using the MTT assay by incubating the **PTX-AMP-2 NCs**, **BLANK-AMP-4 NCs** and free PTX for 72 h with each type of cells. The results are presented in **Figure 11**.

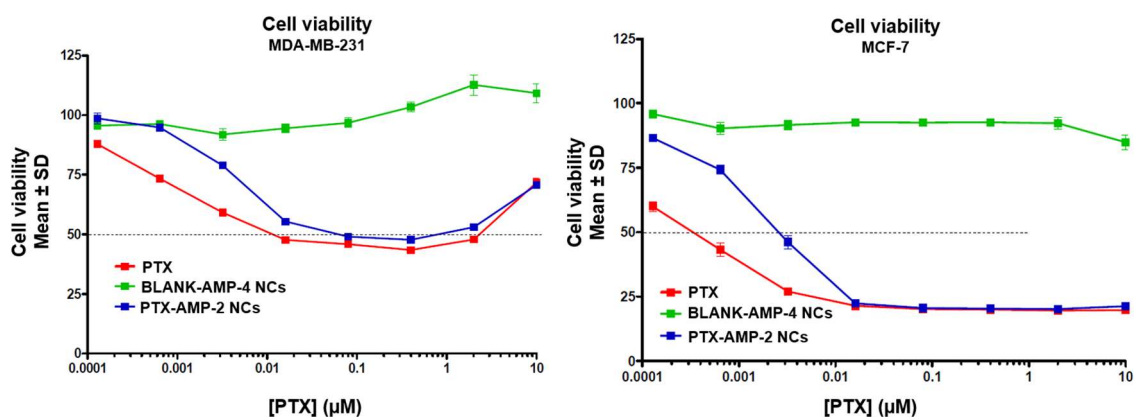


**Figure 11.** Cell viability curves in MDA-MB-231 cell line (left) and MCF-7 cell line (right)

On one hand, the cell viability of **BLANK-AMP-4 NCs** was almost 100% in the whole concentration range assayed for both cell lines, indicating that the unloaded NCs did not have any effect on the cell survival. On the other hand, the decrease on the cell viability in both cell lines caused by **PTX-AMP-2 NCs** followed a similar trend than free PTX, although there is a noticeable difference between their IC<sub>50</sub> values (intersection with the dotted line). Finally, the MCF-7 cells seemed more sensitive to PTX than the MDA-MB-231 cells, since the PTX concentration needed to induce 50% of cell death is lower. The exact values for the IC<sub>50</sub> are given in **Table 2**.

**Table 2.** IC<sub>50</sub> values obtained for MDA-MB-231 and MCF-7 after 72 h of treatment with the NCs

TYPE OF SUBSTANCE	MEAN ± SD (μM)	
	MDA-MB-231 (72 h)	MCF-7 (72 h)
PTX-AMP-2 NCs	0.0416 ± 0.01	0.1194 ± 0.04
BLANK-AMP-4 NCs	> 10	> 10
PTX	2.011·10 <sup>-4</sup> ± 1·10 <sup>-4</sup>	4.074·10 <sup>-3</sup> ± 1·10 <sup>-3</sup>

As observed previously in the cell viability curves, the **BLANK-AMP-4 NCs** did not induce cell death at the concentration range used, therefore, their exact IC<sub>50</sub> could not be calculated. On the other hand, **PTX-AMP-2 NCs** led to an IC<sub>50</sub> value that was one order of magnitude higher than the free PTX, suggesting that part of the drug remained entrapped in the shell and thus a larger concentration of NCs was needed to produce the same cytotoxic effect. Finally, according to the IC<sub>50</sub> values obtained, MCF-7 cells were more sensitive to PTX than MDA-MB-231 cells. This fact is explained by the difference in the nature of the cytoskeleton of both cell types, as reported in several publications.<sup>45-48</sup>

### 3.2. Use of peptides to target BC cells

Besides the studies performed with amphoteric NCs, this Chapter is also devoted to exploring the functionalization of the NCs with peptides that can target specific receptors in BC cells. In this regard, two different targets were considered. Firstly, the transmembrane glycoprotein CD44, which is a cell surface adhesion receptor that promotes migration and invasion processes involved in metastasis once it interacts with the appropriate extracellular matrix ligands.<sup>49-51</sup> Secondly, the transmembrane protein P-selectin, which is highly expressed in some types of

endothelial cells and plays an important role in metastatic processes, since they facilitate cancer cells to invade into the bloodstream.<sup>52-54</sup>

Considering these two membrane receptors, an array of peptides was developed and their targeting abilities were tested *in vitro*. The most promising ones were *N*-acetyl-A5 (from now on, A5) and IPEP, which developed to target CD44 and P-selectin, respectively (**Figure 12**).

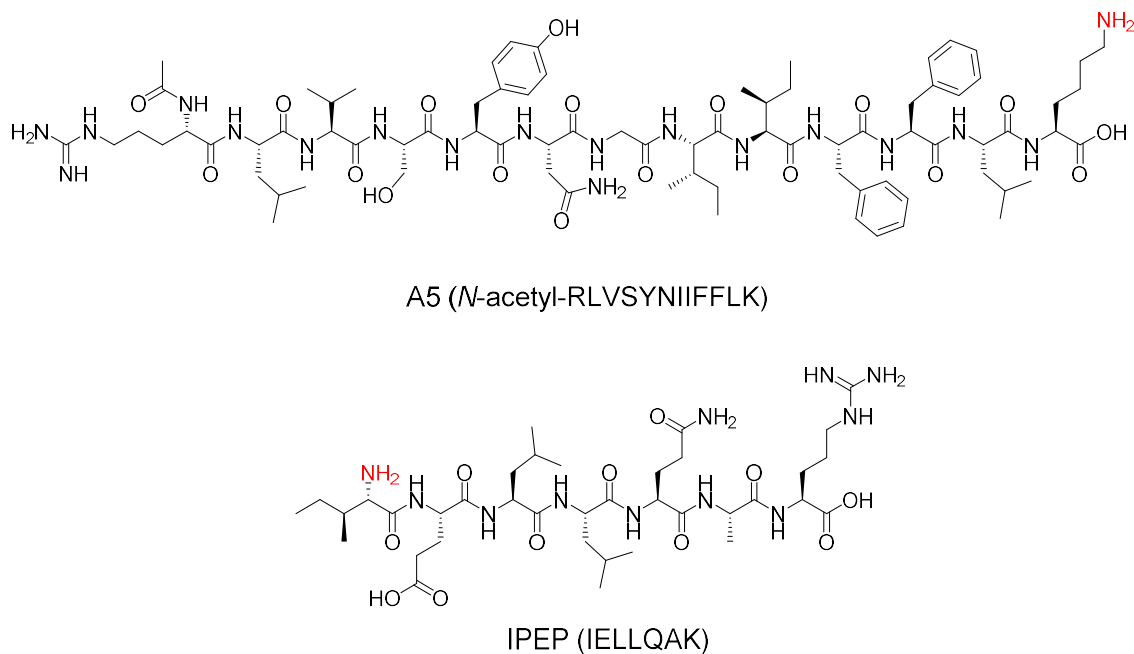


**Figure 12.** Chemical structures of the targeting peptides

A5 presented a good activity in MDA-MB-231 and MCF-7 BC cell lines (TNBC and luminal-A subtypes, respectively), while IPEP was a good candidate targeting HMEC-1 and Eahy-926 endothelial cells.

### 3.3. Functionalization considerations

Once these two targeting peptides were developed and tested *in vitro*, they were evaluated from the physicochemical point of view. In this regard, there were two important conditions that they had to fulfill. Firstly, they had to be relatively hydrophilic in order to ensure their correct exposition towards the aqueous phase and allow the receptor-peptide interaction. This concept is depicted in **Figure 13**.

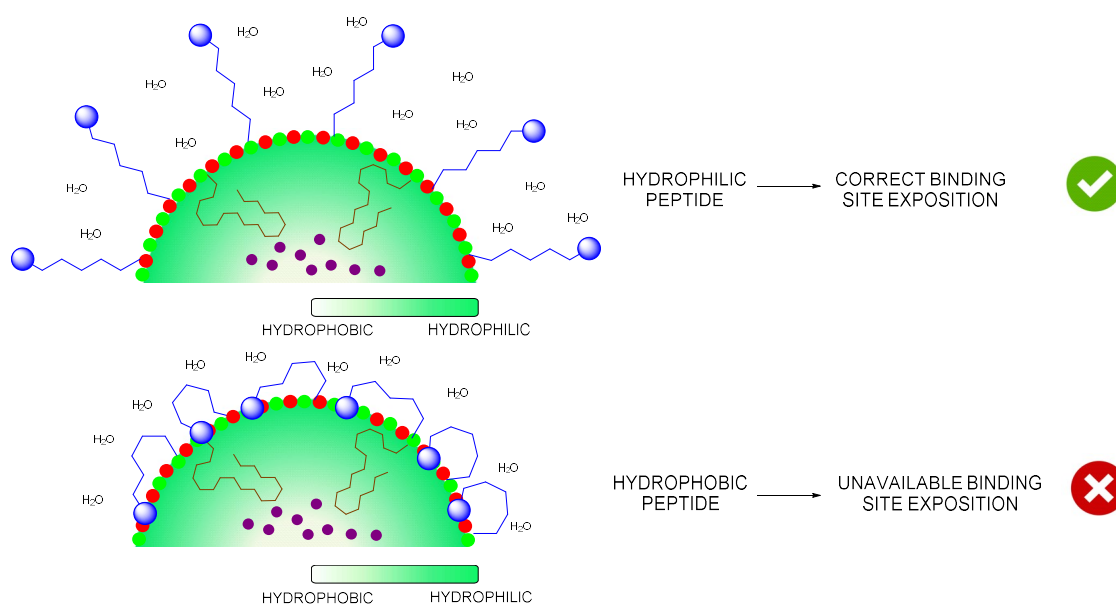


**Figure 13.** Peptide exposition depending on their nature

According to the image, the NCs are structured from a hydrophobic core to the hydrophilic surface. Therefore, if the targeting peptide is hydrophilic, it will have a tendency to establish interactions with water molecules and thus will be exposed outwards. On the contrary, hydrophobic peptides will present a different behavior, since they will have a certain tendency to become entrapped in order to avoid contact with water and gain thermodynamic stability. In this case, their targeting abilities will be reduced or completely lost.

The second requirement is based on the number of nucleophilic groups (primary or secondary amines and primary alcohols) found in the peptide. Ideally, the peptide should contain only one terminal nucleophilic group so that it can react with NCO groups present in the NC to allow functionalization. This is concept is depicted in **Figure 14**.

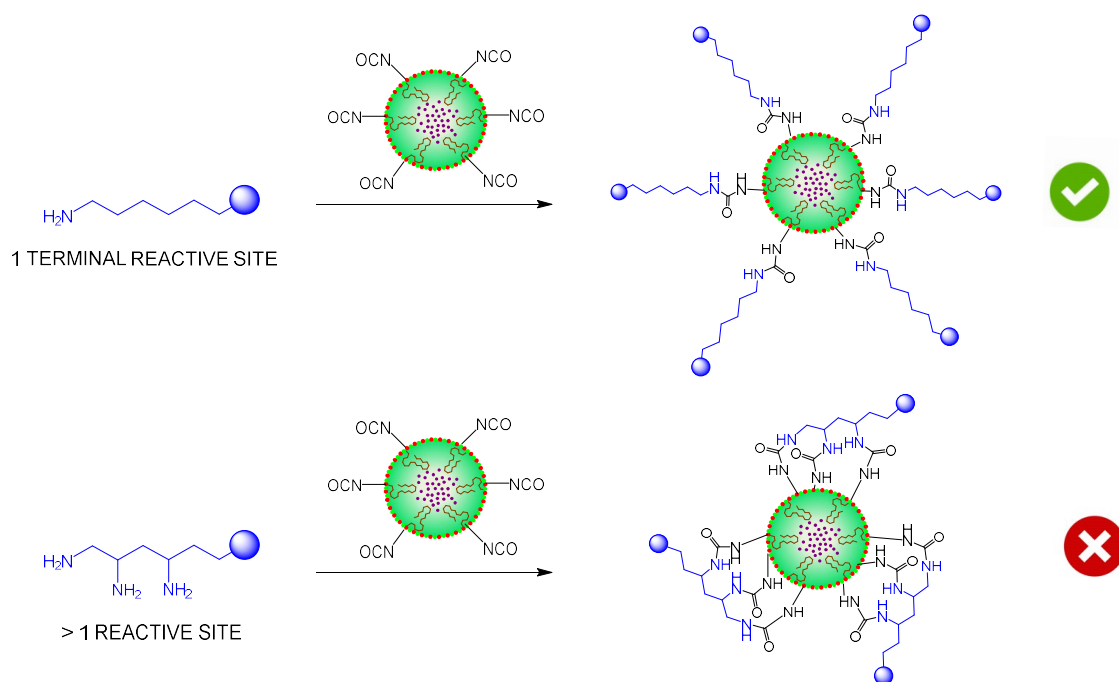


**Figure 14.** NC functionalization depending on the peptide reactivity

It can be seen in the figure that it is crucial that the targeting molecule presents only one terminal nucleophilic group for reaction with the isocyanate. On the contrary, multiple conjugation sites would lead to crosslinked structures along with a loss of biological activity.

The first requirement was assessed by calculating the partition coefficient value ( $\log P$ ) of each peptide. By definition, this physical parameter expresses the equilibrium concentration ratio of an organic compound partitioned between an organic liquid (*n*-octanol) and water. Therefore, positive  $\log P$  values will be associated to relatively hydrophobic molecules whereas negative ones will be related to hydrophilic compounds. The  $\log P$  was calculated for both peptides through three different calculation softwares<sup>55-57</sup>(**Table 3**).

**Table 3.**  $\log P$  values for A5 and IPEP peptides

Peptide	$\log P$ 1 <sup>55</sup>	$\log P$ 2 <sup>56</sup>	$\log P$ 3 <sup>57</sup>	Mean $\log P \pm$ SD
A5	-1.67	-0.23	-3.26	-1.72 $\pm$ 1.52
IPEP	-4.55	-1.72	-6.29	-4.19 $\pm$ 2.31

According to the calculations shown in the previous table, both peptides are hydrophilic, although IPEP is clearly more hydrophilic than A5.

The second condition, the presence of only one nucleophilic group, was also confirmed by observing their chemical structure. In fact, both A5 and IPEP have a terminal amino group available for NC conjugation, as highlighted in red in **Figure 12**. In the case of A5, the nucleophilic group available for conjugation to the NC was the amino group from a lysine side chain in the carboxy-terminal end. For IPEP, the nucleophilic group was the amino-terminal end itself.

Although both peptides fulfilled the two requirements, they were not bound directly to the NCs, but specific linkers were used. These linkers provided two important properties to the conjugates. First of all, they acted as physical spacers between the NC and the peptide in order to reduce the interference of the polymer shell during the peptide-receptor recognition and secondly, they provided hydrophilicity in order to guide the peptides to the external phase and avoid their entrapment in the shell.

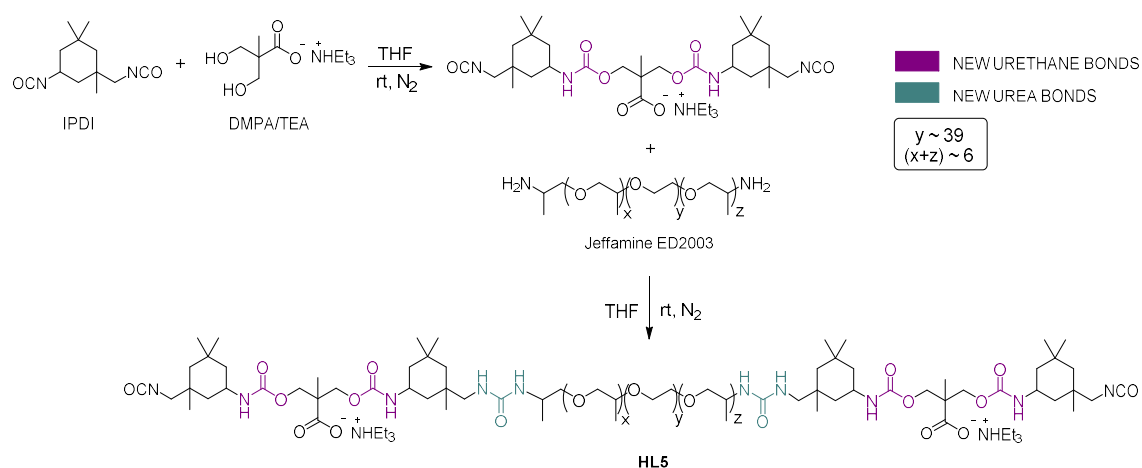
### **3.4. Functionalization with A5**

#### **3.4.1. Preparation of hydrophilic linkers and conjugates**

Different types of linkers were prepared for A5. All of them were hydrophilic and/or contained ionic moieties to enhance the hydrophilicity of the linker-A5 conjugate. The monomers considered to synthesize the linkers, including IPDI, are shown in **Figure 15**.



As seen in the figure, one side of the linker serves to bind to the NC and the other one is the conjugation site to the peptide. Among the linkers prepared in this Chapter, **HL1** is the simplest one because it is synthesized only from IPDI and Jeffamine ED2003. The rest are prepared from a combination of Jeffamine ED2003 and different ionomers with IPDI. For instance, **HL2** contain L-lysine as an ionomer and **HL3**, **HL4** and **HL5** contain diaminopimelic acid, Jeffcat DPA and DMPA, respectively. Therefore, the most hydrophilic linkers are **H2–H5**, since, besides Jeffamine ED2003, they also contain anionic or cationic fragments that provide more aqueous solubility. As an example, the preparation of **HL5** proceeded as **Scheme 1** shows.



**Scheme 1.** Preparation of **HL5**

The first reaction was carried out between DMPA and IPDI, yielding a NCO-reactive prepolymer with new urethane bonds. After the first step, Jeffamine ED2003 was added and new urea bonds were generated almost instantaneously, leading to a larger prepolymer. Thus, **HL5** is an NCO-reactive prepolymer composed of two DMPA molecules, one Jeffamine ED2003 and 4 linking IPDI molecules. The monitorization of these reactions was carried out by IR spectroscopy and the spectra are shown in **Figure 17**.

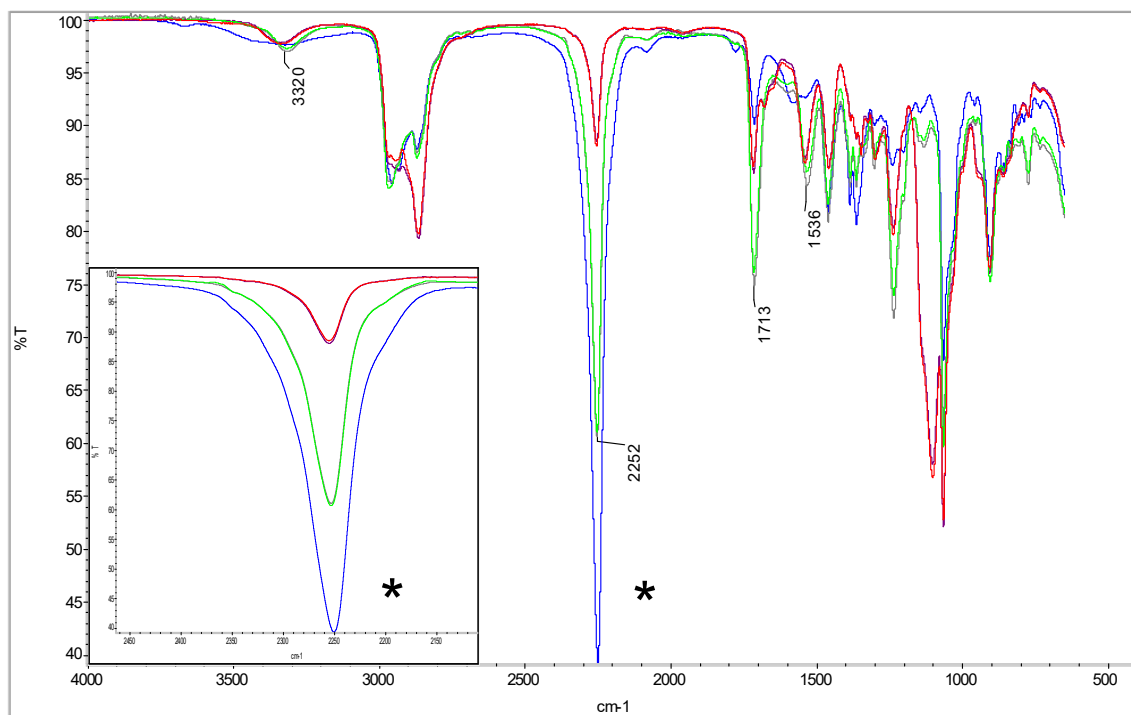
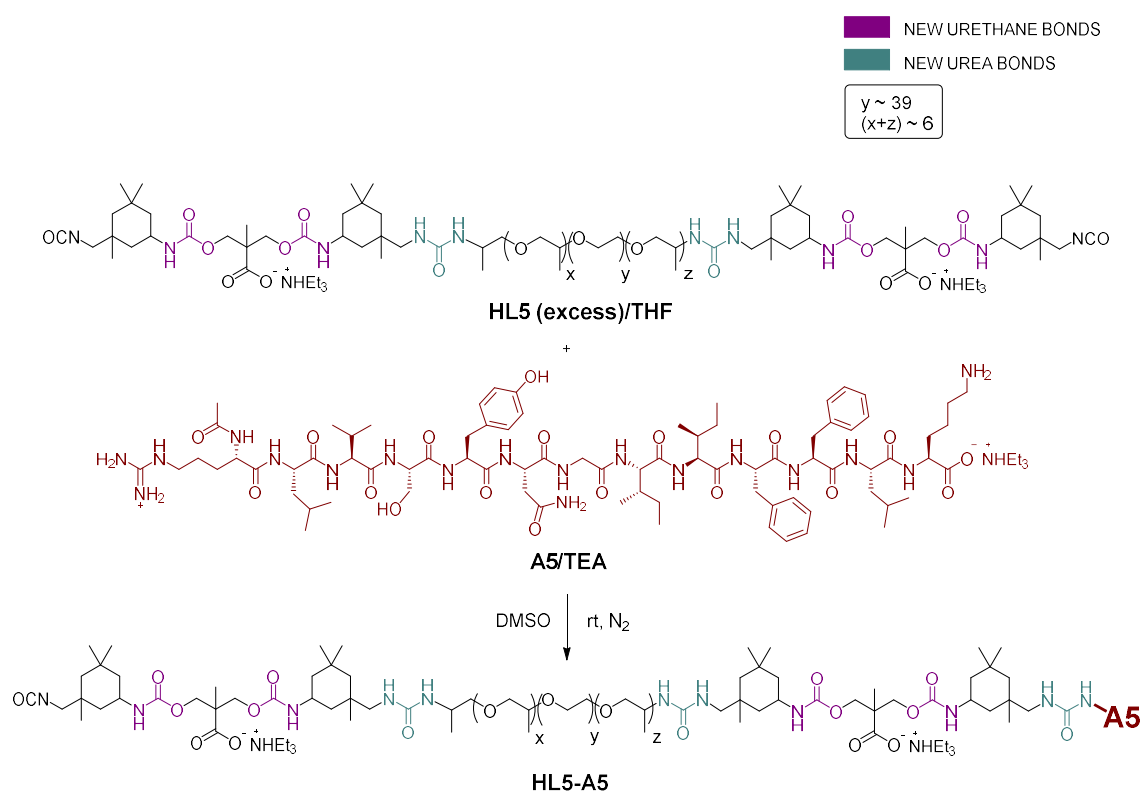


**Figure 17.** IR spectra of the preparation of **HL5**

The blue line corresponds to the first sample recorded, at the start of the reaction between IPDI and DMPA. At that time, the NCO asymmetric stretching band at  $2252\text{ cm}^{-1}$  was sharp and intense. After 1.5 h (grey line), the intensity of the NCO stretching band decreased significantly, while the CO stretching band at  $1713\text{ cm}^{-1}$  and the CN stretching band at  $1536\text{ cm}^{-1}$  increased.<sup>58-60</sup> After 3 h, the sample (light green line) was practically the same as the previous one, confirming that the first step was complete.

The second step started with the addition of Jeffamine ED2003. The first sample was analyzed after 30 min (purple line) and an important decrease of the intensity of the NCO asymmetric stretching band was noticed. The final sample was analyzed 1.5 h after the amine addition (red line) and the spectrum was found to be practically identical as the previous one, suggesting that the second step had finalized.

The conjugation reaction between **HL5** and A5 (**Scheme 2**) was also monitored by IR spectroscopy, but the changes in the intensity of the bands were undetectable, since a large excess of linker was used compared to the equivalents of A5.



**Scheme 2.** Conjugation reaction between **HL5** and **A5**

The conjugation reaction involved an excess of **HL5** and the TEA-preneutralized peptide. In this reaction, the decrease of the intensity of the NCO stretching band and the consequent increase of the urea-associated bands were insufficient to be detected by IR spectroscopy. Therefore, considering the high reactivity of amines and taking into account other experimental procedures dealing with peptides and NCO-reactive polymers,<sup>61-63</sup> the reaction time was set to 4 h in order to ensure the complete conjugation. The percentage of conjugation was determined by amino acid analysis once the NCs were synthesized (section 3.4.3.3).

### 3.4.2. Preparation of A5-functionalized NCs

The NCs prepared in this section are summarized in **Table 4**.

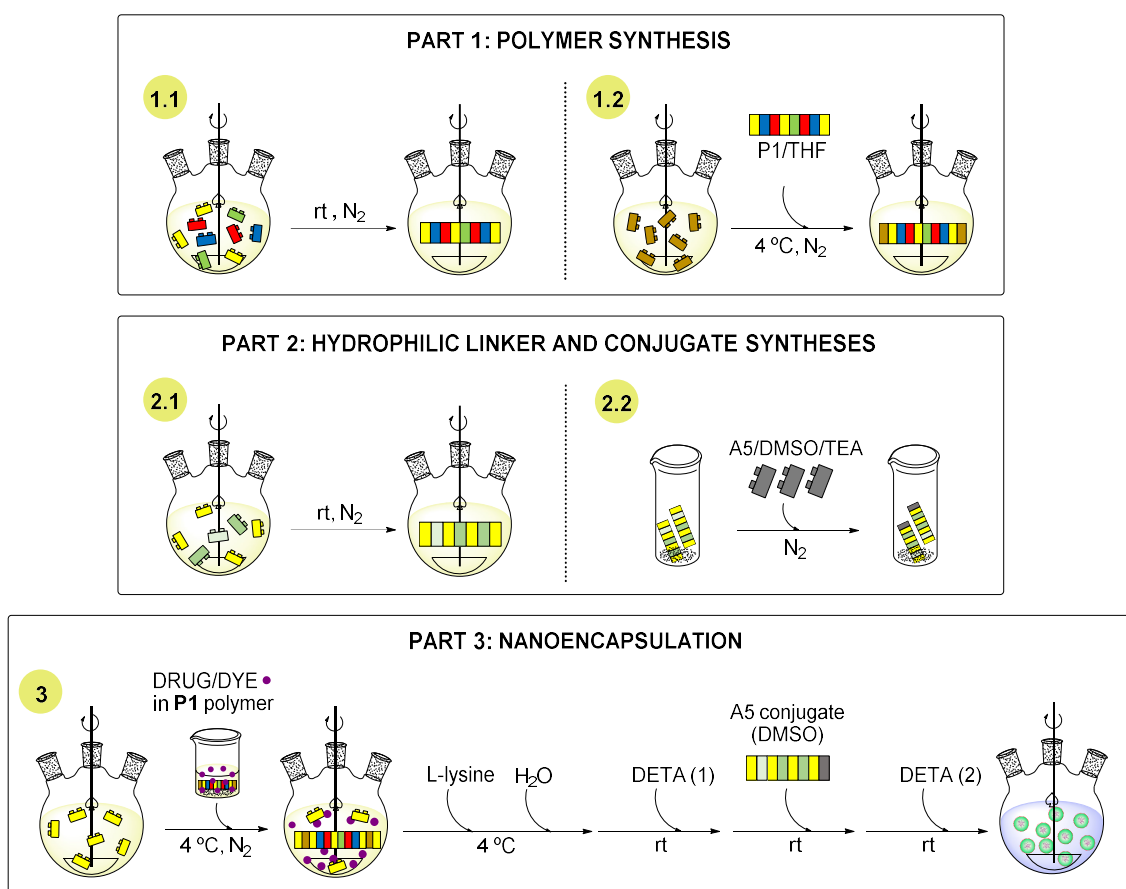
**Table 4.** Summary of the NCs synthesized in this section

Code	Core	Linker	A5 (%)
<b>PTX-HL1-A5 NCs</b>	PTX	HL1	~ 5
<b>PTX-HL2-A5 NCs</b>	PTX	HL2	~ 5
<b>PTX-HL3-A5 NCs</b>	PTX	HL3	~ 5
<b>PTX-HL4-A5 NCs</b>	PTX	HL4	~ 5
<b>PTX-HL5-A5 NCs</b>	PTX	HL5	~ 5
<b>DiO-HL5-A5-5 NCs</b>	DiO	HL5	~ 5
<b>DiO-HL5-A5-2 NCs</b>	DiO	HL5	~ 2
<b>DiO-AMP-3 NCs</b>	DiO	-	0

According to the table, the first versions of NCs were loaded with PTX (**PTX-HL1-A5 NCs** to **PTX-HL5-A5 NCs**) and were functionalized with A5 at a concentration of around 5% wt, since this peptide content was able to induce a biological effect *in vitro*. Once the NCs were optimized, new NCs were prepared with DiO instead of PTX (**DiO-HL5-A5-5 NCs**) to be able to monitor the NCs internalization *in vitro* and study their targeting abilities. As a comparison, another concentration of A5 was tested, yielding to NCs functionalized with around 2% wt of the peptide (**DiO-HL5-A5-2 NCs**). A control sample was used to determine the cell internalization of untargeted NCs (**DiO-AMP-3 NCs**). Once the NCs were obtained, they were dialyzed and characterized using the typical analytical techniques.

The nanoencapsulation reaction to prepare A5-functionalized NCs proceeded with some differences compared to the procedures described in Chapter 2. Firstly, the conjugates were synthesized and kept under N<sub>2</sub> atmosphere until utilization. Secondly, the crosslinker (DETA) was added in two different fractions, separated by the addition of the A5 conjugate. The whole process, from the synthesis of **P1** to the

final nanoencapsulation including the aforementioned changes, is described in **Scheme 3**.



**Scheme 3.** Synthetic process for the preparation of A5-functionalized NCs

As seen in the scheme, polymer **P1** was synthesized as previously described in Chapter 2, with no modifications (1.1 and 1.2 from the scheme). Then, the hydrophilic linker was prepared at  $\text{rt}$  and under  $\text{N}_2$  atmosphere (2.1). Once finished, an aliquot of this polymer was placed in a vial, also purged with  $\text{N}_2$ , and A5 peptide, premixed with DMSO and TEA, was added and was left to react with the linker (2.2). Finally, the nanoencapsulation reaction started with the dissolution of the lipophilic core molecule (drug/dye) in **P1**. Then, this mixture was transferred into a purged and precooled flask containing IPDI and L-lysine sodium salt was added after a certain time. Then, the organic phase was nanoemulsified with water and the first fraction of DETA was added to precrosslink the nanodroplets. Finally, the A5 conjugate was added, followed by the last fraction of DETA, which completed the shell crosslinking (3).

DETA was split into two different fractions because it was important to add A5 conjugate after the nanodroplets had been slightly crosslinked. This procedure was carried out this way to avoid a possible encapsulation of the peptide, since it was not water-soluble, despite the logP calculations (**Figure 18**).

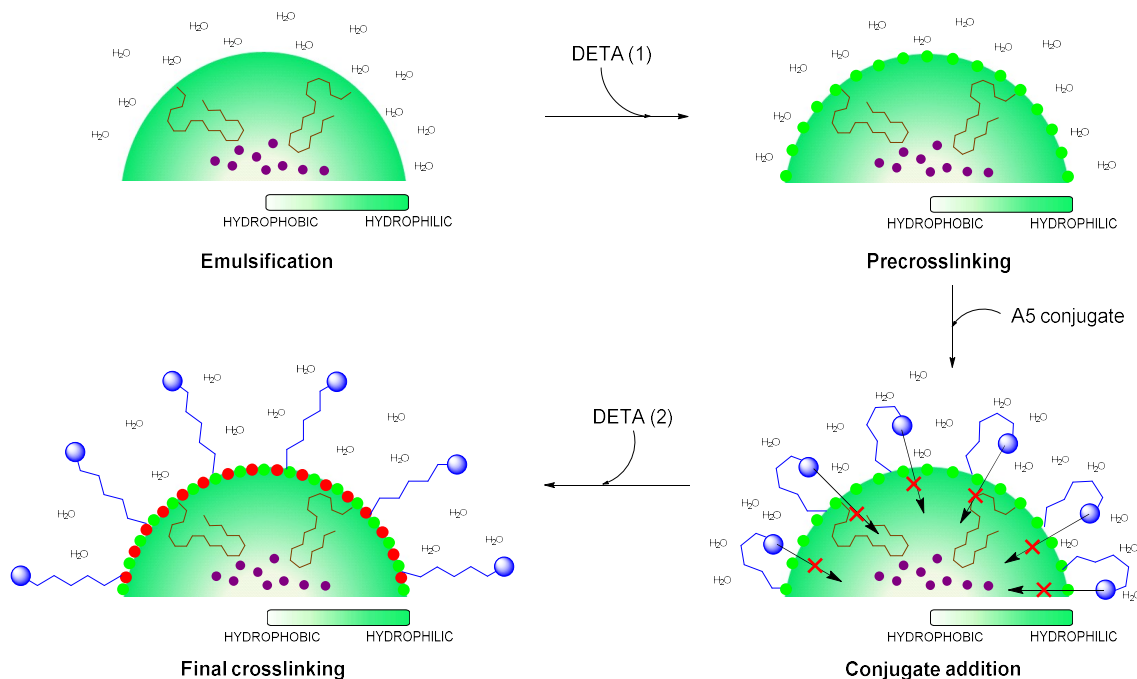


**Figure 18.** NC configuration during the last steps of the nanoencapsulation

According to the figure, the first addition of DETA led to a more hindered nanodroplet surface, hampering the entrapment of the conjugate. In the last step, the second fraction of DETA completed the crosslinking, making the NC robust and properly sealed.

The monitorization of the nanoencapsulation reaction was done by IR spectroscopy and by measuring the pH changes during the final crosslinking. The graphs are not shown, though, because they are very similar to those of **Figure 7**.

### 3.4.3. Characterization of the NCs

All the synthesized NCs were studied by DLS, but only four of them were found to be sufficiently stable to be further characterized by  $\zeta$ -pot: **PTX-HL5-A5 NCs**, **DiO-HL5-A5-2 NCs**, **DiO-HL5-A5-5 NCs** and **DiO-AMP-3 NCs**. Moreover, the last two were also analyzed by TEM.

### 3.4.3.1. Morphology and size

The TEM micrographs of samples **DiO-HL5-A5-5 NCs** and **DiO-AMP-3 NCs** are shown in **Figure 19**.

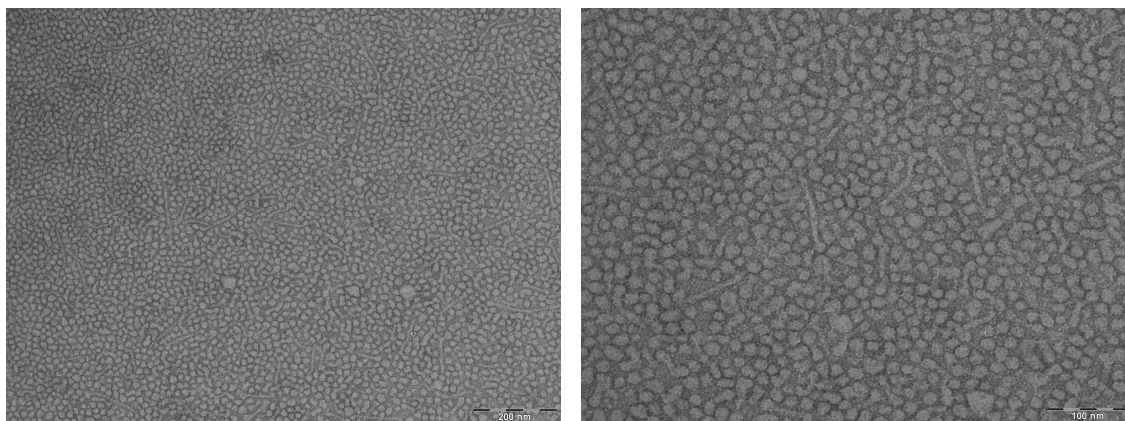
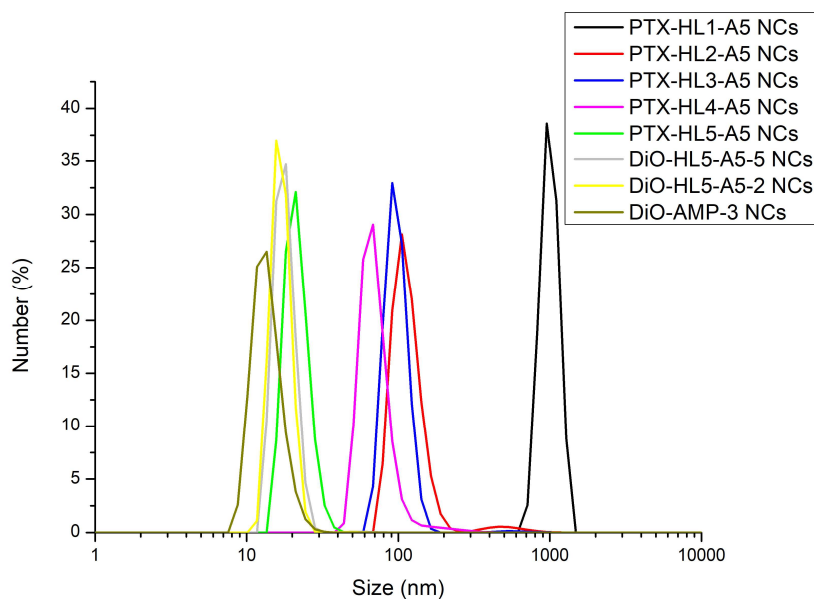


**Figure 19.** TEM micrographs of **DiO-HL5-A5-5 NCs**. Scale bars: left = 200 nm; right = 100 nm

The samples presented a quite homogeneous particle size distribution, but the morphology was unexpectedly different than the ones described in Chapters 2 and 3. In this case, roughly-round shaped NCs could be observed along with some long and narrow polymer segments. The NCs had the regular morphology, being very similar to the nanosystems loading PTX developed in Chapter 2 (**Figure 27**). However, the presence of worm-like entities had not been observed before. The formation of these structures could be driven by the hydrophobic domains of the NCs surface (basically A5 peptide), considering that A5 was not sufficiently hydrophilic despite the logP calculations. These hydrophobic segments tended to establish hydrophobic interactions between them, inducing aggregation and coalescence. The hydrophobic fractions of the NCs shell could lead to a certain physical approach in order to regain the thermodynamic stability that had been lost when A5 was forced to accommodate in the aqueous phase. Alternatively, this surprising morphology could be the result of the drying process during sample preparation. According to Rabani *et al.*,<sup>64</sup> there are basically four regimes of NP self-assembly mediated by the type of drying. Disk-like or ribbon-like domains form at early stages when solvent is evaporated homogeneously, but when these aggregates remain fluxional, they continue to evolve by diffusion and coalescence.

The particle size distributions of the eight samples were recorded and are shown, along with the statistical analyses in **Figure 20**. The first measurements correspond to the NCs loading a high concentration of PTX (nearly 18% wt) and A5 at 5% wt (**PTX-HL1-A5 NCs** to **PTX-HL5-A5 NCs**) and the last ones are associated to the samples containing DiO and A5 at 5, 2 and 0% wt (**DiO-HL5-A5-5 NCs**, **DiO-HL5-A5-2 NCs** and **DiO-AMP-3 NCs**).



Sample code	Mean $\bar{\phi}$ (nm)	SD (nm)	PDI
<b>PTX-HL1-A5 NCs</b>	962.28	220.9	0.568
<b>PTX-HL2-A5 NCs</b>	105.70	155.0	0.445
<b>PTX-HL3-A5 NCs</b>	91.28	127.7	0.568
<b>PTX-HL4-A5 NCs</b>	68.06	26.02	0.323
<b>PTX-HL5-A5 NCs</b>	21.04	4.05	0.253
<b>DiO-HL5-A5-5-NCs</b>	18.30	2.05	0.013
<b>DiO-HL5-A5-2-NCs</b>	15.69	2.98	0.033
<b>DiO-AMP-3 NCs</b>	12.70	2.88	0.055

**Figure 20.** Particle size distribution of the different samples and their statistical analysis

The particle sizes of the NCs were significantly different depending on the hydrophilic linker used for the peptide conjugation. **PTX-HL1-A5 NCs** were the largest ones, with an average diameter around a micron, along with a high SD and

PDI. In this case, the emulsion was white and numerous aggregates could be clearly observed at the bottom of the flask. This could indicate that **HL1** was not sufficiently hydrophilic to guarantee a global aqueous corona around the shell and therefore the effect of the hydrophobic peptide on the surface triggered aggregation and precipitation. However, the incorporation of ionomers along the linker caused a positive effect on the overall particle size, since this parameter decreased significantly to below 200 nm. When L-lysine was used in **HL2**, the corresponding NCs (**PTX-HL2-A5 NCs**) presented an average size around 100 nm and were associated to broad distributions and multiple particle populations. By using diaminopimelic acid in the preparation of the **HL3**, the resulting NCs (**PTX-HL3-A5 NCs**) were improved in terms of particle size, but they still had high SD. When Jeffcat DPA was introduced as an ionomer in the synthesis of **HL4**, the resulting NCs (**PTX-HL4-A5 NCs**) showed an acceptable average diameter around 70 nm, but the particle size distribution was broad, and the emulsion eventually precipitated. Finally, the best combination was achieved by using DMPA in the preparation of **HL5** linker, since the resulting nanosystems (**PTX-HL5-A5 NCs**) had the lowest particle size (approximately 20 nm) and the minimum SD value.

The same observation arose from **DiO-HL5-A5-5 NCs** and **DiO-HL5-A5-2 NCs**, which presented even lower diameters (due to a lower concentration of hydrophobic core) and also narrow particle size distributions. Finally, the amphoteric version of NCs, **DiO-AMP-3 NCs**, showed the typical size properties, with an average diameter below 20 nm and low SD. Therefore, **HL5** was the only hydrophilic linker that mediated the incorporation of a hydrophobic peptide on the NC surface without altering the desired size.

The main conclusion arising from this study was that the hydrophilic nature of Jeffamine ED2003, with almost 40 repeating units or PEG, was not sufficient to stabilize the peptide at the NC surface, but the introduction of ionomers was clearly needed. The use of L-lysine, diaminopimelic acid and Jeffcat DPA caused similar effects on the resulting NCs but the associated conjugates did not generate long enough stable emulsions. Finally, DMPA was the only ionomeric candidate that, when incorporated in form of conjugate, caused a clear decrease on the NCs size and an increase on the overall stabilization of the micelles.

### 3.4.3.2. Surface properties

As with the samples of the previous chapters, the surface charge of the stable NCs was evaluated in a pH range from 5.5 to 8.0. For the rest of the nanosystems, the precipitation observed hampered the preparation of the samples for  $\zeta$ -pot measurements. The results are presented in the same graph (**Figure 21**).

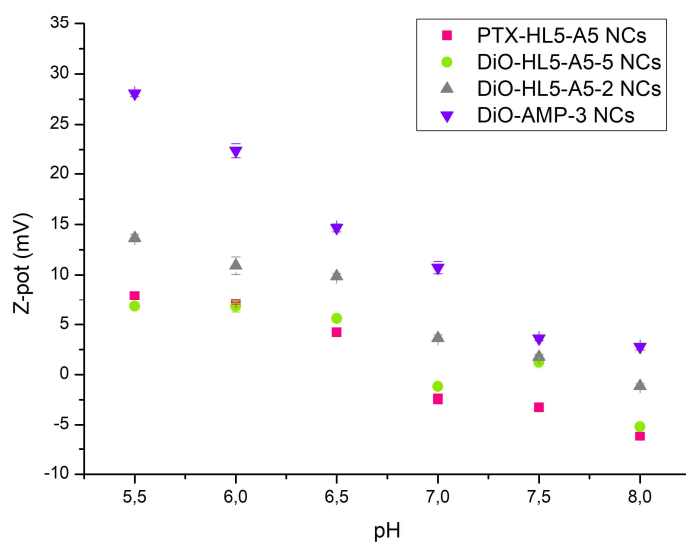


**Figure 21.**  $\zeta$ -Pot of some of some of the samples bearing A5 peptide

The amphoteric NCs, **DiO-AMP-3 NCs**, showed the typical surface charge profile that changed depending on pH, caused by the synchronized DPA/L-lysine effect. In this case,  $\zeta$ -pot shifted from nearly neutral values to clearly positive when the acidity of the medium increased, as expected. However, the patterns for the other samples were slightly different. Thus, **PTX-HL5-A5 NCs** and **DiO-HL5-A5-5 NCs** exhibited very similar variations, but they were not so accentuated compared to the amphoteric NCs. In these two cases, a slight increase of the surface charge was observed when the conditions became more acidic, but the profile was flatter. This result could be explained by the presence of the negatively charged DMPA monomer in **HL5 (Scheme 1)**, which produced a decrease on the overall surface charge. For **DiO-HL5-A5-2 NCs**, the  $\zeta$ -pot was slightly higher than the analogs bearing A5 at 5% wt, but it followed the same cationization pattern that depended on pH. This fact

could be related to the lower concentration of the **HL5-A5** conjugate on the NC surface.

### 3.4.3.3. *A5 conjugation efficiency*

The first attempt to determine the A5 conjugation efficiency was performed by analyzing the presence of peptide in the filtrates of precentrifuged NCs by HPLC. However, the characteristics of A5, especially its hydrophobicity and tendency to aggregate, did not allow a correct analysis by this technique. Therefore, other attempts were tried by measuring the content of arginine, but the experiments did not lead to coherent results. Finally, the characterization method that allowed the determination of the peptide conjugation efficiency was the amino acid analysis (AccQ·Tag pre-column derivatization method<sup>65,66</sup>) after hydrolyzing the samples in strong acidic conditions, high temperature and long hydrolysis time.

The chromatograms from **DiO-AMP-3 NCs**, **DiO-HL5-A5-5 NCs** and **DiO-HL5-A5-2 NCs** are shown, in this order, in section 6 of the Annexes. Regarding the first sample, there were only four identified peaks, corresponding to threonine, AABA, lysine and NLE. These results could be expected, because in **DiO-AMP-3 NCs** there is no functionalized peptide, and therefore AABA and NLE appear as IS, lysine as an ionomer introduced during encapsulation, and threonine may appear as an interference due to its low concentration.

The sample corresponding to the NCs bearing A5 at a concentration of around 5% (**DiO-HL5-A5-5 NCs**) led to significantly different results, since most of the expected amino acids were present in the chromatogram. For the quantification of the conjugation efficiency, three different amino acids were considered: Val, Ile and Leu. They were selected because they were not present into the control sample and thus their concentration would unequivocally belong to the peptide. Moreover, they are among those amino acids that do not undergo degradation during the hydrolysis step and therefore should be more reliable for quantification. To this aim, the amount per residue was firstly calculated, as shown in **Table 5**.

**Table 5.** Previous calculations for the peptide conjugation yield

<b>Amino acid</b>	<b>Number of residues</b>	<b>Amount</b>	<b>Amount/residue</b>
<b>Val</b>	1	0.020	0.020
<b>Ile</b>	2	0.044	0.022
<b>Leu</b>	2	0.048	0.024

Accordingly, the amount/residue was similar between the three amino acids considered. Therefore, the average value (0.022) was set as a reference to calculate the total amount A5 present in the sample of lyophilized NCs. The calculations took into account the volume injected to the HPLC, the total volume of derivatized sample, the aliquot that was used for the derivatization reaction, the volume of medium used to resuspend the hydrolyzed amino acids, the A5 molecular weight (1611.15 g/mol) and the amount of AABA added into the initial sample. After the necessary calculations, the average conjugation yield was:

$$\% \text{ conjugation yield} = \frac{\text{mg A5 (experimental)}}{\text{mg A5 (theoretical)}} * 100 = \mathbf{75.0 \%}$$

The A5 conjugation yield was fairly good, meaning that most of the peptide was successfully bound to the NC surface.

The same protocol was performed with **DiO-HL5-A5-2 NCs**, which were different from the previous ones regarding the concentration of peptide functionalized to the NC surface peptide (around 2% wt according to theoretical calculations). In this case, most of the expected amino acid residues were also detected in the chromatogram, and therefore the quantification of A5 on the NC surface was determined following the procedure mentioned above.

The same amino acids (Val, Ile and Leu) were considered for the calculations and the amount/residue obtained in this case is given in **Table 6**.

**Table 6.** Previous calculations for the peptide conjugation yield

Amino acid	Number of residues	Amount	Amount/residue
Val	1	0.044	0.044
Ile	2	0.090	0.045
Leu	2	0.097	0.049

After the necessary calculations, the average the conjugation yield was:

$$\% \text{ conjugation yield} = \frac{\text{mg A5 (experimental)}}{\text{mg A5 (theoretical)}} * 100 = \mathbf{62.5 \%}$$

In this case, the A5 conjugation yield was lower than those obtained for **DiO-HL5-A5-5 NCs**, but it was still acceptable.

#### 3.4.4. Cell uptake

Besides the physicochemical characterization, biological studies were also performed with the three fluorescent versions of NCs: **DiO-HL5-A5-5 NCs**, **DiO-HL5-A5-2 NCs** and **DiO-AMP-3 NCs**. In this regard, their cell internalization was tested *in vitro* in MDA-MB-231 BC cells and in MCF-7 cells. As mentioned previously, both cell lines overexpress the CD44 receptor, therefore the aim of this *in vitro* study was the assessment of the targeting abilities of the NCs functionalized with A5 and compare them with a control sample of amphoteric NCs.

To this aim, each cell line was treated with the NCs for different incubation times (30, 60 and 120 min) at a DiO concentration of 15  $\mu\text{M}$ . All the results are expressed in percentage of positive cells and in MFI. The first parameter indicates which percentage of the entire cell population has incorporated the NCs and thus has become fluorescent. On the other hand, MFI is related to the average fluorescence intensity emitted by the cells as a consequence of the NC uptake. Therefore, MFI can be understood as the concentration of NCs that have internalized the cells. The results are shown in **Figure 22**.

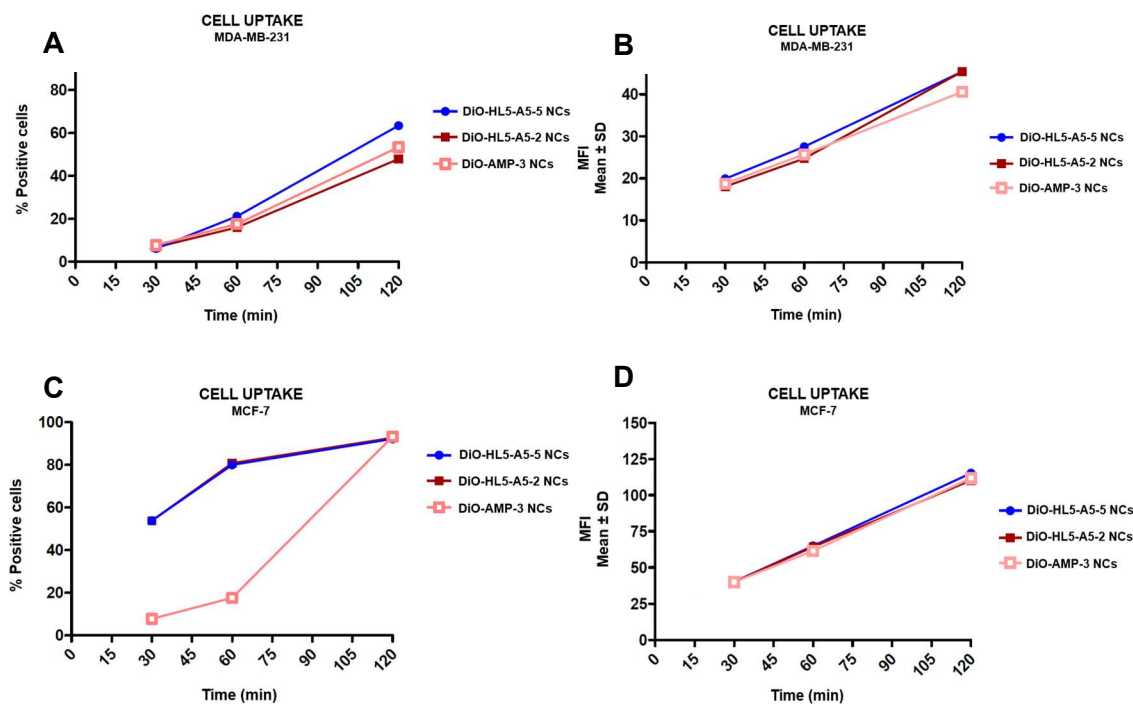


**Figure 22.** Cell internalization in MDA-MB-231 and MCF-7 cell lines. (A, C) Measurements in percentage of positive cells; (B, D) measurements in MFI

This experiment shows that, in general, the cell uptake increased over time in all the cases, indicating a clear time-effect relationship. More specifically, figure A indicates that **DiO-HL5-A5-5 NCs** were slightly more internalized by MDA-MB-231 cells than the rest of the samples at the longest incubation time, although the differences were not very significant. Analyzing these results in MFI (figure B) confirm that the cell uptake was very similar for the three cases and the NCs decorated with A5 had a slightly higher internalization only after 120 min of incubation.

The results obtained for MCF-7 cells expressed in percentage positive cells (figure C) show a clearly different trend, since the NCs functionalized with A5 were internalized more efficiently than the amphoteric NCs after 30 and 60 min of incubation. However, this observation was not valid for long treatments, since almost 100% of the cells were fluorescent-positive after 120 min of incubation, regardless the characteristics of the NCs. In contrast to these conclusions, cell uptake expressed in MFI (figure D) suggested that there was no significant difference between the fluorescence intensity measured in each case. This result suggests that even though the NCs bearing A5 were internalized more rapidly, only a low

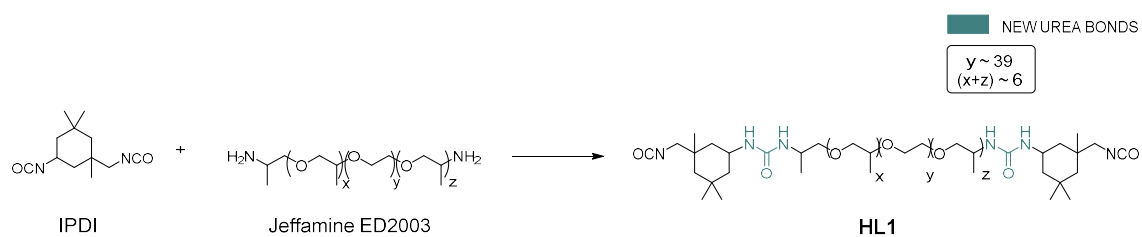
concentration could penetrate the cells. In contrast, although amphoteric NCs were uptaken less efficiently, a larger concentration of NCs could be internalized, leading to similar MFI values.

Overall, it can be concluded that the presence of A5 on the NC surface did not induce a clearly enhanced cell targeting effect, since amphoteric NCs achieved the same level of cell uptake after 120 min of incubation in both cell lines. This could be due to an inappropriate peptide exposition that hampered a correct interaction with the CD44 receptor. This could be the result of the peptide folding and aggregation, altering its binding site. Alternatively, it could also be explained by the loss of targeting abilities of the peptide after the conjugation to the NC.

### 3.5. Functionalization with IPEP

#### 3.5.1. Preparation of the hydrophilic linker and the conjugate

Given the higher hydrophilicity of IPEP, the linker used for conjugation was only intended to provide a physical spacing between the peptide and the NC surface, rather than more hydrophilicity. For this reason, the linker that was considered for IPEP conjugation was **HL1**, which was the least hydrophilic one and the easiest to prepare (**Scheme 4**).



**Scheme 4.** Synthesis of **HL1**

According to this scheme, **HL1** was prepared in only one step by mixing IPDI and Jeffamine ED2003. As usual, the reaction monitorization of the reaction was performed by IR spectroscopy (**Figure 23**).

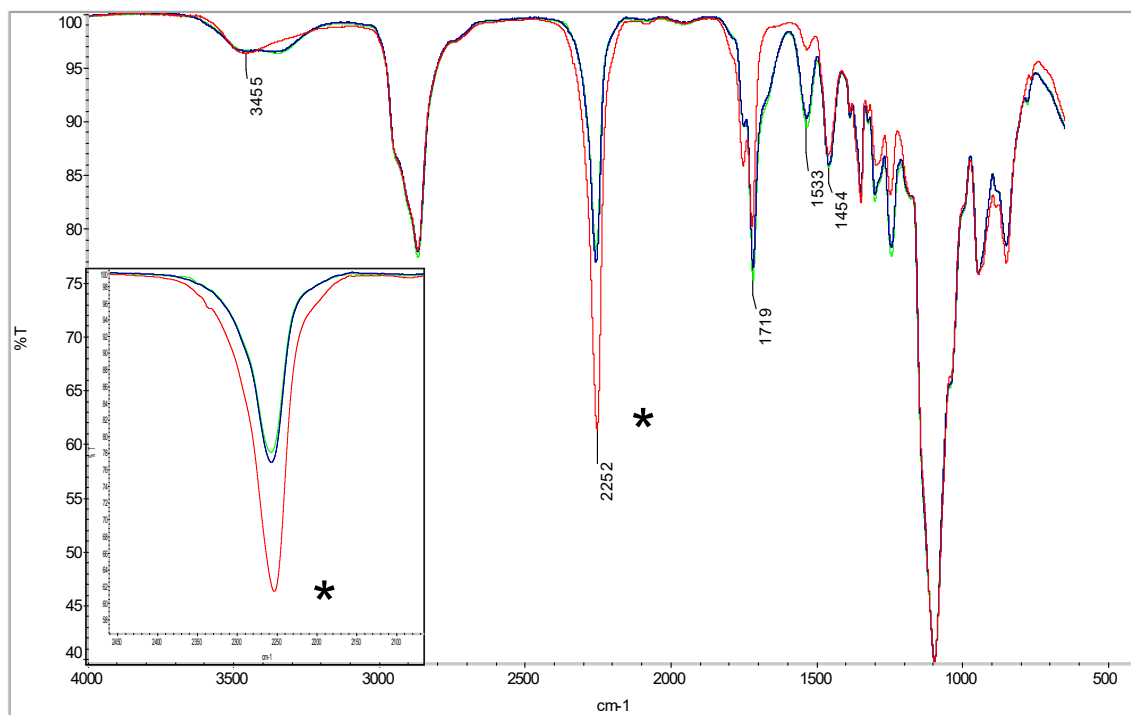
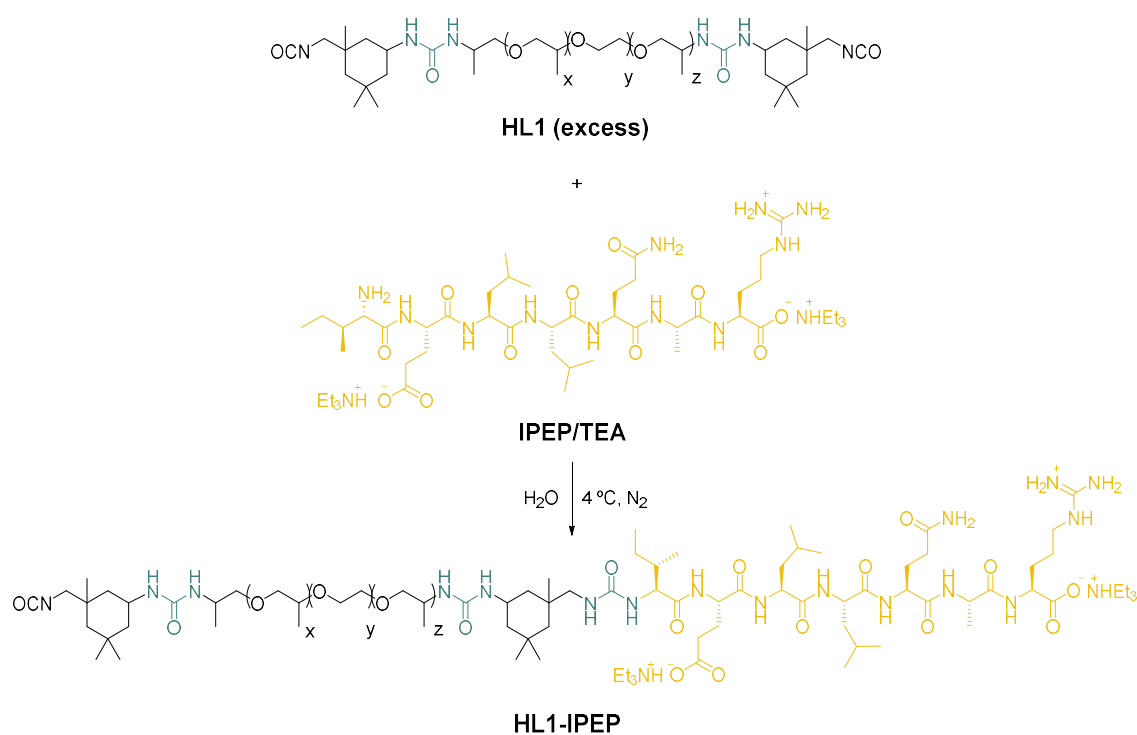


**Figure 23.** IR spectra of the **HL1** synthesis

The red line corresponds to the first sample, which was immediately recorded after the addition of jeffamine ED2003. In this case, the NCO asymmetric stretching band at 2252  $\text{cm}^{-1}$  was sharp and intense. After 30 min, another sample was analyzed (blue line) and a noticeable decrease on the intensity of the NCO asymmetric stretching band was observed, along with an increase of the urea-associated bands at 1719  $\text{cm}^{-1}$  and 1533  $\text{cm}^{-1}$ . The last sample (green line) was recorded after 1 h from the start of the reaction and was practically identical as the previous one, indicating the finalization of the reaction.

Once **HL1** was prepared, the synthesis of the conjugate with IPEP proceeded as **Scheme 5** shows.



**Scheme 5.** Preparation of **HL1-IPEP** conjugate

**HL1-IPEP** conjugate was obtained through a one-step reaction, involving an excess of the linker and the TEA-prenutralized IPEP. The monitorization of this reaction was done by HPLC (**Figure 24**), since the changes in the IR stretching bands were undetectable. The peak corresponding to IPEP is marked with an arrow.

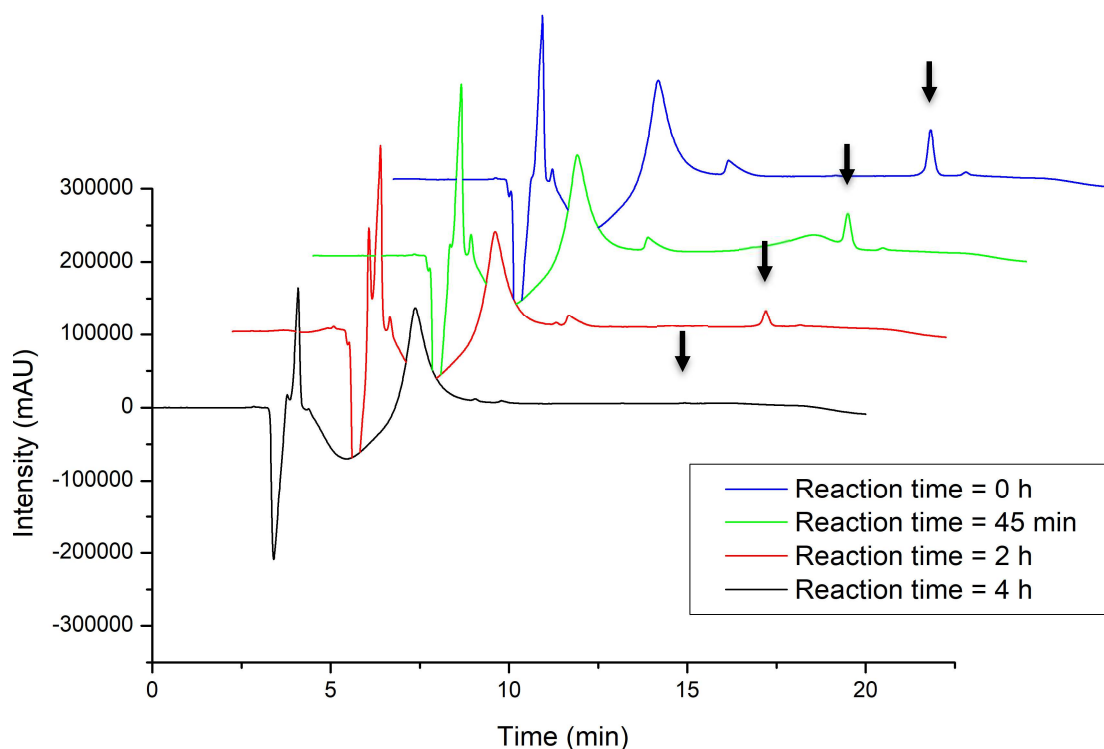


Figure 24. HL1-IPEP reaction monitorization by HPLC

Different samples of the mixture were taken and injected in the HPLC. Firstly, IPEP was dissolved in water and TEA was added in to deprotonate the free amine from lysine and make it more nucleophilic. At that time, an aliquot of the sample was taken and analyzed to establish a reference of IPEP in terms of retention time and intensity. Then, the desired amount of **HL1** was added and the reaction started. Samples were retrieved and injected to the HPLC after 45 min, 2 and 4 h from the start of the reaction. Accordingly, the reaction between the linker and the peptide was complete after 4 h and this time was set as a standard in the subsequent syntheses.

### 3.5.2. Preparation of IPEP-functionalized NCs

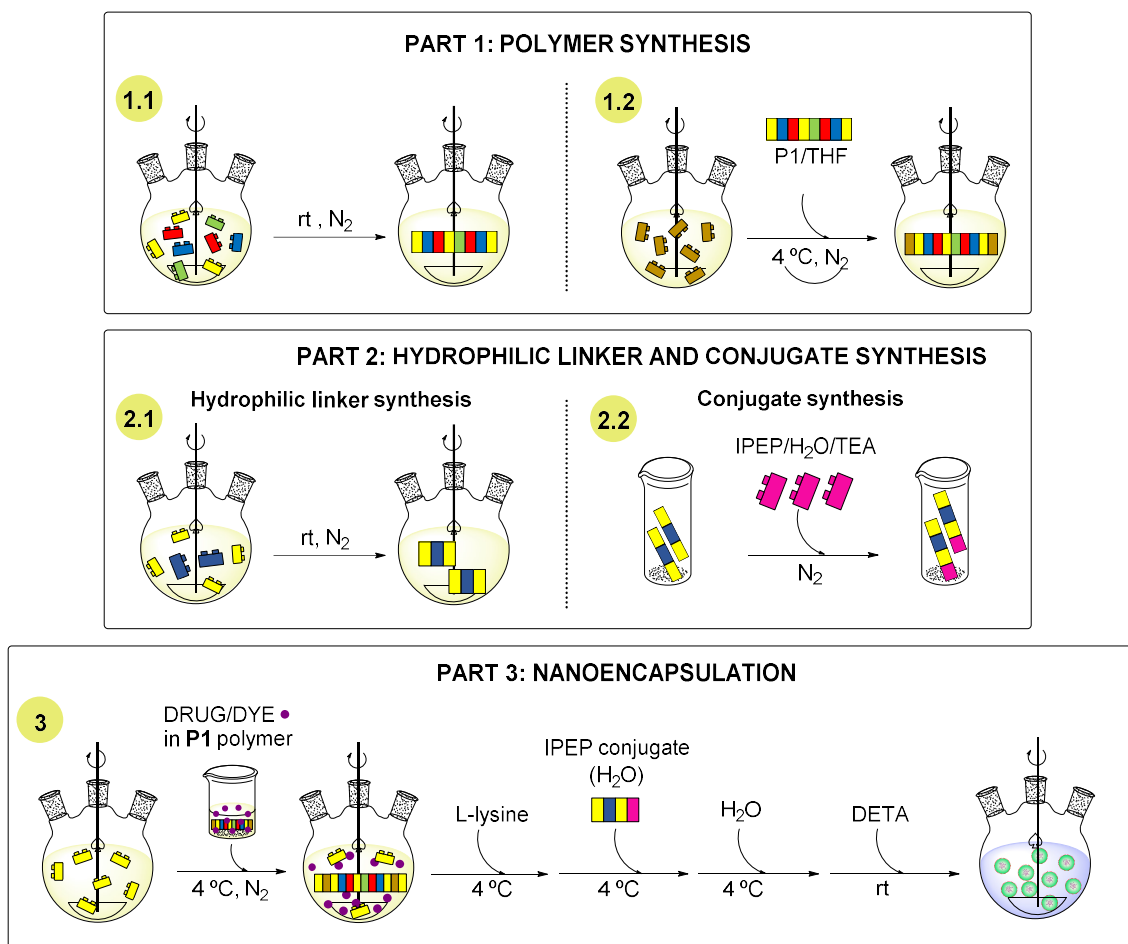
The NCs prepared in this section are listed in **Table 7**.

**Table 7.** Summary of the NCs synthesized in this section

Code	Core	Linker	A5 (%)
<b>PTX-HL1-IPEP NCs</b>	PTX	HL1	~ 5
<b>DiO-HL1-IPEP-5 NCs</b>	DiO	HL1	~ 5
<b>DiO-HL1-IPEP-2 NCs</b>	DiO	HL1	~ 2
<b>DiO-AMP-4 NCs</b>	DiO	-	0

As with the NCs functionalized with A5, the NCs bearing IPEP were decorated with the same concentration of peptide (5% wt) and loaded with PTX (**PTX-HL1-IPEP NCs**). In order to monitor their internalization *in vitro*, the core was replaced by DiO fluorophore (**DiO-HL1-IPEP-5 NCs**). Moreover, another concentration of peptide was included to compare the targeting abilities of the resulting NCs. Therefore, another analog was prepared with approximately 2% wt, leading to **DiO-HL1-IPEP-2 NCs**. A control sample of amphoteric NCs, **DiO-AMP-4 NCs**, was included in the assay. As in the previous cases, once the NCs were obtained, they were dialyzed and characterized using the typical analytical techniques.

The preparation of the NCs was similar to the one described for A5-functionalized NCs, with some differences in the conditions used for the conjugation reaction and in the nanoencapsulation process (**Scheme 6**).



**Scheme 6.** Synthetic process for the preparation of IPEP-functionalized NCs

According to the scheme, the first difference is that IPEP was dissolved in water instead of DMSO and that the IPEP conjugate was added after the reaction with L-lysine sodium salt and before the emulsification. No precrosslinking step took place in this case because of the hydrophilic nature of the peptide was sufficiently high to guarantee its correct exposition outwards.

The monitorization of the nanoencapsulation was done by IR spectroscopy and by measuring the pH changes during the crosslinking. The graphs are not shown, though, because they are very similar to those of **Figure 7**.

### 3.5.3. Characterization of the NCs

All the NCs were characterized by DLS and  $\zeta$ -pot but only **DiO-HL1-IPEP-5 NCs** and **DiO-AMP-4 NCs** were studied by TEM.

#### 3.5.3.1. Morphology and size

The TEM micrographs of **DiO-HL1-IPEP-5 NCs** and **DiO-AMP-4 NCs** are presented in **Figure 25**.

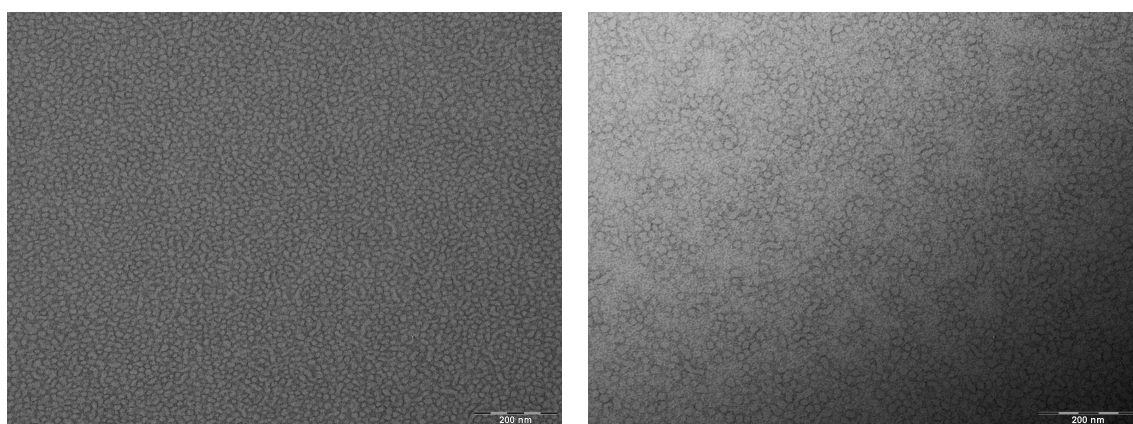
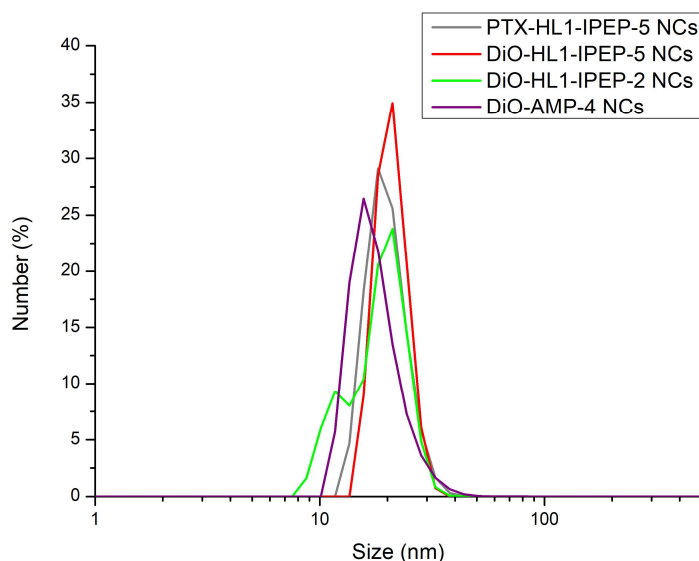


**Figure 25.** TEM micrographs of **DiO-HL1-IPEP-5 NCs**. Scale bars: left = 200 nm; right = 100 nm

The **DiO-HL1-IPEP-5 NCs** presented a considerably homogeneous particle size distribution and the shape of the nanosystems was roughly round. In some parts of the micrograph, however, worm-like structures could be noticed, but in a lower extent than for the NCs bearing A5 peptide. This could be explained by the fact that the **HL1-IPEP** conjugates were added before the emulsification step and therefore they took place in the o/w interface creation. Given that IPEP was not a totally hydrophilic peptide, but presented some hydrophobic moieties (one Ile and two Leu), the structuration of the interface from hydrophobic parts (interior) to hydrophilic sites (exterior) could not follow such an ordered gradient and therefore led to these unexpected morphologies.

The particle size distributions, along with the statistical analyses of the samples, are shown below in **Figure 26**.



Sample code	Mean $\bar{\phi}$ (nm)	SD (nm)	PDI
<b>PTX-HL1-IPEP-5 NCs</b>	18.83	3.96	0.044
<b>DiO-HL1-IPEP-5 NCs</b>	21.04	3.37	0.026
<b>DiO-HL1-IPEP-2 NCs</b>	17.25	3.58	0.043
<b>DiO-AMP-4 NCs</b>	21.04	4.09	0.037

**Figure 26.** Particle size distribution of the different samples and statistical analysis

The four samples prepared in this section had very similar mean particle sizes, which ranged between 17 and 21 nm, approximately, with low SD and PDI values. However, in the case of **DiO-AMP-4 NCs**, two different populations could be noticed, having different contributions in the sample. The large particles were more abundant than the small ones, of around 10 nm. This result is in accordance with the TEM micrographs shown above, where the sample was more heterogeneous and different types of particles could be distinguished.

By analyzing these results, it can be stated that the hydrophilic nature of the peptide plays a crucial role with the size of the obtained nanosystems. In section 3.4.3.1, the NCs prepared with the conjugates **HL1-A5** to **HL4-A5** had too large diameters and important SD values, indicating that the hydrophobicity of the

peptide hampered the generation of very small nanosystems. Therefore, the nature of the targeting molecule is highly relevant when designing the conjugates and the NCs.

### 3.5.3.2. Surface properties

The surface charge was studied through  $\zeta$ -pot measurements at different pH conditions, ranging from 5.5 to 8.0 (**Figure 27**).

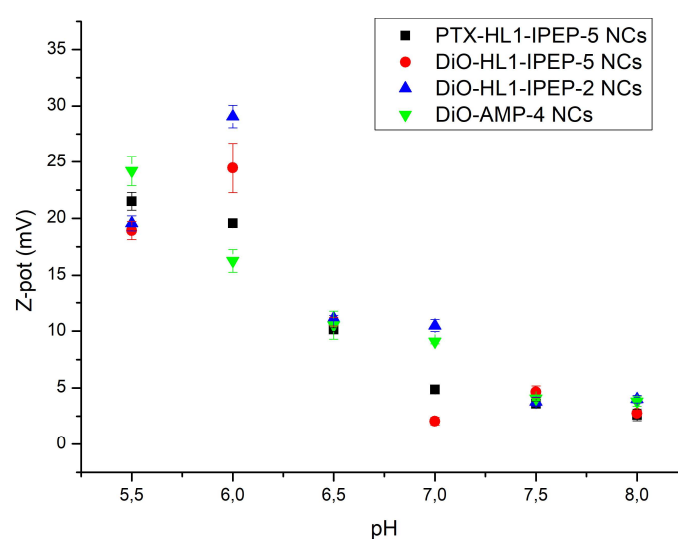
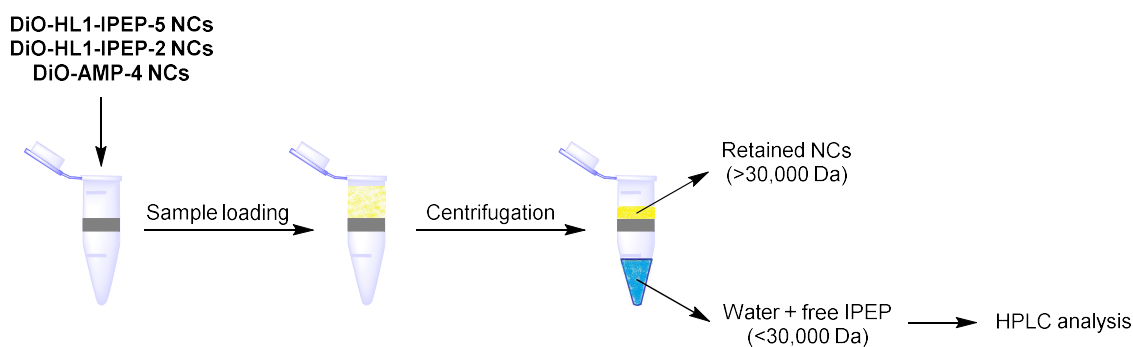


**Figure 27.**  $\zeta$ -pot of the NCs functionalized with IPEP and the amphoteric NCs

The surface charge of the samples followed the typical amphoteric profile, being clearly cationic at acidic environments and almost neutral at physiologic to alkaline conditions. In this case, the presence of **HL1-IPEP** conjugates did not induce to any significant charge shift because **HL1**, which was added in large excess, is neutral.

### 3.5.3.3. Peptide conjugation efficiency

In this case, the peptide conjugation efficiency was determined by centrifuging **DiO-HL1-IPEP-5 NCs**, **DiO-HL1-IPEP-2 NCs** and **DiO-AMP-4 NCs** and analyzing the resulting filtrates by HPLC (**Scheme 7**). This procedure was used because IPEP could be easily monitored by HPLC and the amino acid analysis was more time-consuming.



**Scheme 7.** Process performed before peptide quantification

Each sample was loaded into an Eppendorf containing a filter of 30,000 Da (MW of the peptide is 842.01 g/mol), to ensure that the NCs were retained while smaller molecules passed through the filter. Thus, the samples were placed in the centrifuge and the NCs were separated from the rest of the emulsion, which was filtered and was collected on the bottom. This fraction contained small molecules resulting from the nanoencapsulation reaction, such as non-reacted monomers, crosslinkers, salts and unconjugated IPEP. The recovered filtrates were then injected in the HPLC after a calibration curve was performed and the conjugation efficiency percentage was calculated as shown in section 2.5.1 of Chapter 5.

As it can be seen in the chromatograms shown in section 6 of the Annexes, there was no observable peak that could be attributed to IPEP. Therefore, it can be concluded that the fraction of free IPEP is negligible and therefore, the conjugation efficiency was nearly 100%.

### 3.5.4. Cell uptake

The targeting abilities of **DiO-HL1-IPEP-5 NCs**, **DiO-HL1-IPEP-2 NCs** and **DiO-AMP-4 NCs** were tested in HMEC-1 and EaHy-926 endothelial cell lines. In this case,

the DiO concentration was also set to 15  $\mu$ M and the incubation times assayed were 15, 30, 60 and 180 min. The results are shown in **Figure 28**.

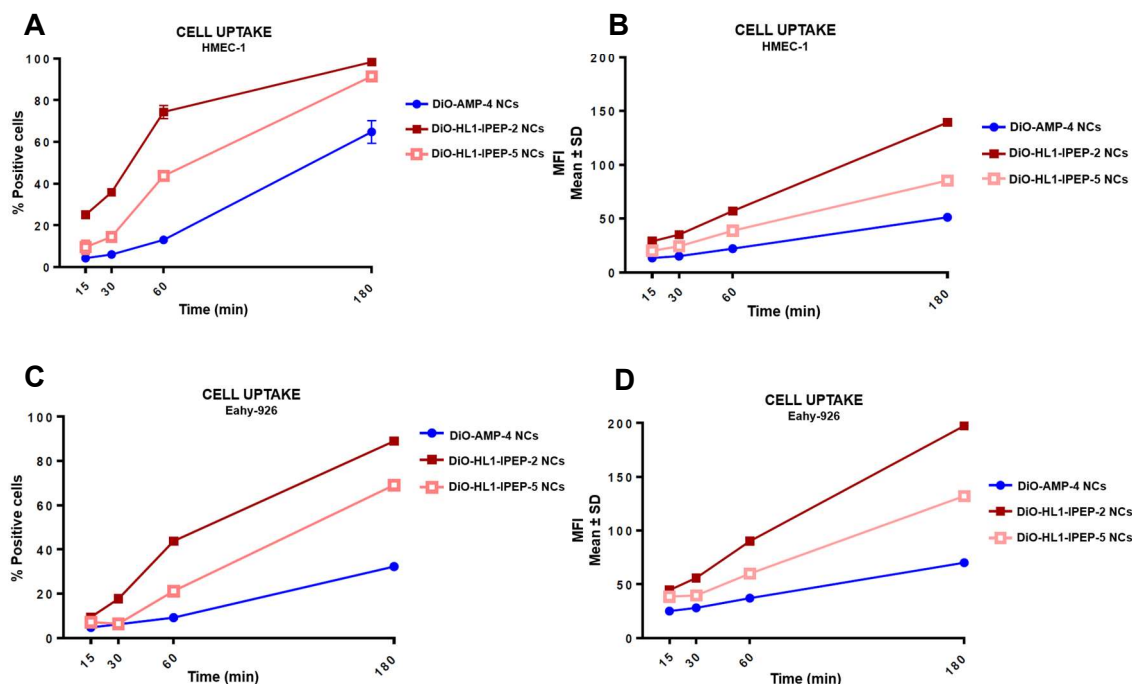


**Figure 28.** Cell internalization in HMEC-1 and Eahy-926 cell lines. (A, C) Measurements in percentage of positive cells; (B, D) measurements in MFI

As a general observation, the cell uptake increased over time in all the cases, indicating a clear time-effect relationship, as expected. In particular, the internalization of NCs in HMEC-1 cells, measured in percentage of positive cells (figure A), showed that **DiO-HL1-IPEP-2 NCs** and **DiO-HL1-IPEP-5 NCs** penetrated the cells more efficiently than the amphoteric NCs (**DiO-AMP-4 NCs**). However, there was not a significant difference between the NCs having 2% wt or 5% wt IPEP. By analyzing the results in MFI (figure B), **DiO-HL1-IPEP-2 NCs** presented the highest internalization rates in each incubation time assayed, followed by **DiO-HL1-IPEP-5** and **DiO-AMP-4 NCs**.

The internalization results for Eahy-926 cells, either expressed in percentage of positive cells or MFI (figures C, D), showed a similar trend to the previous cell line. The NCs functionalized with IPEP displayed a more efficient cell uptake than the amphoteric NCs, which confirmed the beneficial role of the peptide in the internalization process.

## 4. Conclusions

The amphoteric NCs (**PTX-AMP-2 NCs**) were prepared in a high drug loading, approximately 17% wt, and were properly characterized by the typical analytical methods. The results showed that the NCs preserved the desired size around 20 nm, selective shell cationization that responded to pH conditions and high EE and DL values. The *in vitro* cell viability of these NCs in MDA-MB-231 and MCF-7 BC cell lines showed that they were cytotoxic after 72 h of treatment, while the unloaded NCs (**BLANK-AMP-4 NCs**) were totally biocompatible at the concentration range assayed. Finally, the IC<sub>50</sub> values obtained for the NCs were higher than those measured from the free drug, suggesting that a fraction of PTX was not totally released. This finding could be potentially interesting to be used as a very slow-release DDS, therefore, *in vivo* efficacy studies should be performed to confirm this hypothesis.

Regarding the NCs functionalized with A5, an array of hydrophilic linkers was prepared to compensate the inherent hydrophobicity of the peptide. Among them, **HL5** was the most promising one, since it allowed the preparation of the NCs (**PTX-HL5-A5 NCs**) with a controlled size and amphoteric properties. The rest of the linkers led to large and unstable nanosystems that were not valid for characterization. The A5 conjugation efficiency was fairly good, with yields around 60–80%, according to the amino acid analyses. Finally, the cell uptake results of A5-functionalized NCs (**DiO-HL5-A5-5 NCs** and **DiO-HL5-A5-2 NCs**) did not lead to clear evidence of their targeting abilities, since the amphoteric NCs (**DiO-AMP-3 NCs**) were also very well internalized.

Finally, IPEP peptide was considered for NC functionalization and given its hydrophilic nature, it could be more easily incorporated to the NC surface. In this case, **HL1** was used for the decoration and the resulting NCs (**PTX-HL1-IPEP-5 NCs**) were characterized as usual. The results demonstrated a controlled particle size, shell cationization depending on the pH conditions and almost quantitative conjugation yields, assessed by HPLC. The cell uptake results showed a significant difference between the IPEP-functionalized NCs (**DiO-HL1-IPEP-5 NCs** and **DiO-HL1-IPEP-2 NCs**) and the amphoteric NCs (**DiO-AMP-4 NCs**), although the concentration of the peptide did not correlate with the targeting efficiency.

Considering the high conjugation yields obtained, this unexpected result has no explanation so far, therefore, more experiments should be performed.

## 5. Bibliography

- 1 F. Bray, P. McCarron and D. M. Parkin, *Breast Cancer Res.*, 2004, **6**, 229-239.
- 2 Z. Tao, A. Shi, C. Lu, T. Song, Z. Zhang and J. Zhao, *Cell Biochem. Biophys.*, 2015, **72**, 333-338.
- 3 E. A. Rakha and I. O. Ellis, *Pathology*, 2009, **41**, 40-47.
- 4 R. Bartsch, R. Ziebermayr, C. C. Zielinski and G. G. Steger, *Wien. Med. Wochenschr.*, 2010, **160**, 174-181.
- 5 C. DeSantis, J. Ma, L. Bryan and A. Jemal, *CA Cancer J. Clin.*, 2014, **64**, 52-62.
- 6 G. A. Colditz, K. Bohlke and C. S. Berkey, *Breast Cancer Res. Treat.*, 2014, **145**, 567-579.
- 7 C. Xuan, J. M. Shamonki, A. Chung, M. L. DiNome, M. Chung, P. A. Sieling and D. J. Lee, *PLOS ONE*, 2014, **9**, 1-7.
- 8 G. Dong, D. Wang, X. Liang, H. Gao, L. Wang, X. Yu and J. Liu, *Int J Clin Exp Med*, 2014, **7**, 3719-3724.
- 9 A. Pawar, Master Thesis, Indiana University, 2015.
- 10 J. S. Reis-Filho and A. N. J. Tutt, *Histopathology*, 2008, **52**, 108-118.
- 11 M. S. U. Hassan, J. Ansari, D. Spooner and S. A. Hussain, *Oncol. Rep.*, 2010, **24**, 1121-1131.
- 12 G. C. Barnett, M. Shah, K. Redman, D. F. Easton, B. A. J. Ponder and P. D. P. Pharoah, *J. Clin. Oncol.*, 2008, **26**, 3310-3316.
- 13 X. R. Yang, J. Chang-Claude, E. L. Goode, F. J. Couch, H. Nevanlinna, R. L. Milne, M. Gaudet, M. K. Schmidt, A. Broeks and A. Cox, *J. Natl. Cancer Inst.*, 2010, **103**, 250-263.
- 14 W. D. Foulkes, I. E. Smith and J. S. Reis-Filho, *N. Engl. J. Med.*, 2010, **363**, 1938-1948.
- 15 S. Dawood, *Drugs*, 2010, **70**, 2247-2258.
- 16 J. Russo, *The Pathobiology of Breast Cancer*, Springer, Berlin, 2016.
- 17 L. Dossus, M. C. Boutron-Ruault, R. Kaaks, I. T. Gram, A. Vilier, B. Fervers, J. Manjer, A. Tjonneland, A. Olsen, K. Overvad, J. Chang-Claude, H. Boeing, A.

- Steffen, A. Trichopoulou, P. Lagiou, M. Sarantopoulou, D. Palli, F. Berrino, R. Tumino, P. Vineis, A. Mattiello, H. B. Bueno-de-Mesquita, F. J. B. van Duijnhoven, M. F. Bakker, P. H. M. Peeters, E. Weiderpass, E. Bjerkaas, T. Braaten, V. Menéndez, A. Agudo, M. J. Sanchez, P. Amiano, M. J. Tormo, A. Barricarte, S. Butt, K. T. Khaw, N. Wareham, T. J. Key, R. C. Travis, S. Rinaldi, V. McCormack, I. Romieu, D. G. Cox, T. Norat, E. Riboli and F. Clavel-Chapelon, *Int. J. Cancer*, 2014, **134**, 1871-1888.
- 18 R. Qamar, M. A. Syed and J. Y. A. R. Carmichael, *Open Access Library Journal*, 2014, **1**, 1-10.
- 19 K. A. Ban and C. V. Godellas, *Surg. Oncol. Clin. N. Am.*, 2014, **23**, 409-422.
- 20 C. M. Perou, T. Sørlie, M. B. Eisen, M. van de Rijn, S. S. Jeffrey, C. A. Rees, J. R. Pollack, D. T. Ross, H. Johnsen and L. A. Akslen, *Nature*, 2000, **406**, 747-752.
- 21 R. Dent, M. Trudeau, K. I. Pritchard, W. M. Hanna, H. K. Kahn, C. A. Sawka, L. A. Lickley, E. Rawlinson, P. Sun and S. A. Narod, *Clin. Cancer Res.*, 2007, **13**, 4429-4434.
- 22 G. Stockmans, K. Deraedt, H. Wildiers, P. Moerman and R. Paridaens, *Curr. Opin. Oncol.*, 2008, **20**, 614-620.
- 23 W. J. Irvin and L. A. Carey, *Eur. J. Cancer*, 2008, **44**, 2799-2805.
- 24 B. Weigelt, F. C. Geyer and J. S. Reis-Filho, *Mol. Oncol.*, 2010, **4**, 192-208.
- 25 S. Cleator, W. Heller and R. C. Coombes, *Lancet Oncol.*, 2007, **8**, 235-244.
- 26 S. M. Swain, J. Baselga, S. B. Kim, J. Ro, V. Semiglazov, M. Campone, E. Ciruelos, J. M. Ferrero, A. Schneeweiss, S. Heeson, E. Clark, G. Ross, M. C. Benyunes and J. Cortés, *N. Engl. J. Med.*, 2015, **372**, 724-734.
- 27 E. Senkus, S. Kyriakides, F. Penault-Llorca, P. Poortmans, A. Thompson, S. Zackrisson and F. Cardoso, *Ann. Oncol*, 2013, **24**, vi7-vi23.
- 28 M. Kalimutho, K. Parsons, D. Mittal, J. A. López, S. Srihari and K. K. Khanna, *Trends Pharmacol. Sci.*, 2015, **36**, 822-846.
- 29 H. J. Burstein, *Targeted Therapies in Breast Cancer*, Oxford University Press, Oxford, New York, 2011.
- 30 C. Liedtke, C. Mazouni, K. R. Hess, F. André, A. Tordai, J. A. Mejia, W. F. Symmans, A. M. Gonzalez-Angulo, B. Hennesy, M. Green, M. Cristofanilli, G. N. Hortobagyi and L. Pusztai, *J. Clin. Oncol.*, 2008, **26**, 1275-1281.
- 31 M. J. Higgins and J. Baselga, *J Clin Invest*, 2011, **121**, 3797-3803.

- 32 C. Denkert, C. Liedtke, A. Tutt and G. von Minckwitz, *The Lancet*, 2017, **389**, 2430-2442.
- 33 L. A. Carey, E. C. Dees, L. Sawyer, L. Gatti, D. T. Moore, F. Collichio, D. W. Ollila, C. I. Sartor, M. L. Graham and C. M. Perou, *Clin. Cancer Res.*, 2007, **13**, 2329-2334.
- 34 P. Drullinsky, S. M. Sugarman, M. N. Fornier, G. D'Andrea, T. Gilewski, D. Lake, T. Traina, C. Wasserheit-Lieblich, N. Sklarin, D. Atieh-Graham, N. Mills, T. Troso-Sandoval, A. D. Seidman, J. Yuan, H. Patel, S. Patil, L. Norton and C. Hudis, *Clin. Breast Cancer*, 2010, **10**, 440-444.
- 35 G. Bianchini and L. Gianni, *Lancet Oncol.*, 2014, **15**, e58-e68.
- 36 A. Mohamed, K. Krajewski, B. Cakar and C. X. Ma, *Am. J. Pathol.*, 2013, **183**, 1096-1112.
- 37 M. L. Burness, T. A. Grushko and O. I. Olopade, *The Cancer Journal*, 2010, **16**, 23-32.
- 38 B. D. Lehmann, J. A. Bauer, X. Chen, M. E. Sanders, A. B. Chakravarthy, Y. Shyr and J. A. Pietenpol, *J Clin Invest*, 2011, **121**, 2750-2767.
- 39 F. Marmé and A. Schneeweiss, *Breast Care*, 2015, **10**, 159-166.
- 40 N. Ferrara, H. P. Gerber and J. LeCouter, *Nat Med*, 2003, **9**, 669-676.
- 41 O. Gluz, C. Liedtke, N. Gottschalk, L. Pusztai, U. Nitz and N. Harbeck, *Ann. Oncol*, 2009, **20**, 1913-1927.
- 42 G. Pillai, *SOJ Pharmacy & Pharmaceutical Sciences*, 2014, **2**, 1-13.
- 43 D. Bobo, K. J. Robinson, J. Islam, K. J. Thurecht and S. R. Corrie, *Pharm. Res.*, 2016, **33**, 2373-2387.
- 44 J. Lao, J. Madani, T. Puértolas, M. Álvarez, A. Hernández, R. Pazo-Cid, Á. Artal and A. Antón Torres, *J. Drug Delivery*, 2013, **2013**, 1-12.
- 45 N. M. Patel, S. Nozaki, N. H. Shortle, P. Bhat-Nakshatri, T. R. Newton, S. Rice, V. Gelfanov, S. H. Boswell, R. J. Goulet, G. W. Sledge and H. Nakshatri, *Oncogene*, 2000, **19**, 4159-4169.
- 46 R. Rouzier, R. Rajan, P. Wagner, K. R. Hess, D. L. Gold, J. Stec, M. Ayers, J. S. Ross, P. Zhang and T. A. Buchholz, *Proc. Natl. Acad. Sci. U. S. A.*, 2005, **102**, 8315-8320.

- 47 S. Tommasi, A. Mangia, R. Lacalamita, A. Bellizzi, V. Fedele, A. Chiriatti, C. Thomssen, N. Kendzierski, A. Latorre and V. Lorusso, *Int. J. Cancer*, 2007, **120**, 2078-2085.
- 48 A. L. Risinger, N. F. Dybdal-Hargreaves and S. L. Mooberry, *Anticancer Res.*, 2015, **35**, 5845-5850.
- 49 E. Marangoni, N. Lecomte, L. Durand, G. de Pinieux, D. Decaudin, C. Chomienne, F. Smadja-Joffe and M. F. Poupon, *Br. J. Cancer*, 2009, **100**, 918-922.
- 50 H. Wang, L. Wang, Y. Song, S. Wang, X. Huang, Q. Xuan, X. Kang and Q. Zhang, *Oncol. Lett.*, 2017, **14**, 5890-5898.
- 51 L. T. Senbanjo and M. A. Chellaiah, *Front Cell Dev Biol*, 2017, **5**, 1-6.
- 52 J. A. Koedam, E. M. Cramer, E. Briend, B. Furie, B. C. Furie and D. D. Wagner, *The Journal of Cell Biology*, 1992, **116**, 617-625.
- 53 N. Nishida, H. Yano, T. Nishida, T. Kamura and M. Kojiro, *Vasc. Health Risk Manage.*, 2006, **2**, 213-219.
- 54 M. Chen and J. G. Geng, *Arch. Immunol. Ther. Exp.*, 2006, **54**, 75-84.
- 55 Bratislava University, Molinspiration Cheminformatics, <http://www.molinspiration.com/cgi-bin/properties>, (accessed 4<sup>th</sup> March, 2015).
- 56 ChemAxon, <https://chemicalize.com/> (accessed 15<sup>th</sup> November, 2015).
- 57 ALOGPS 2.1, <http://146.107.217.178/web/alogps/>, (accessed 3<sup>rd</sup> March, 2015).
- 58 A. K. Mishra, D. K. Chattopadhyay, B. Sreedhar and K. V. S. N. Raju, *Prog. Org. Coat.*, 2006, **55**, 231-243.
- 59 K. K. Jena, D. K. Chattopadhyay and K. V. S. N. Raju, *Eur. Polym. J.*, 2007, **43**, 1825-1837.
- 60 E. Delebecq, J. P. Pascault, B. Boutevin and F. Ganachaud, *Chem. Rev.*, 2013, **113**, 80-118.
- 61 P. Rocas, Y. Fernandez, S. Schwartz, I. Abasolo, J. Rocas and F. Albericio, *J. Mater. Chem. B*, 2015, **3**, 8421-8421.
- 62 P. Rocas, M. Hoyos-Nogués, J. Rocas, J. M. Manero, J. Gil, F. Albericio and C. Mas-Moruno, *Adv. Healthcare Mater.*, 2015, **4**, 1956-1960.

- 63 P. Rocas, Y. Fernández, N. García-Aranda, L. Foradada, P. Calvo, P. Avilés, M. J. Guillén, S. Schwartz, Jr., J. Rocas, F. Albericio and I. Abasolo, *Nanomed. Nanotech. Biol. Med.*, 2017, **14**, 257-267.
- 64 E. Rabani, D. R. Reichman, P. L. Geissler and L. E. Brus, *Nature*, 2003, **426**, 271-274.
- 65 S. A. Cohen and D. P. Michaud, *Anal. Biochem.*, 1993, **211**, 279-287.
- 66 S. A. Cohen and K. M. De Antonis, *J. Chromatogr. A*, 1994, **661**, 25-34.



# **CHAPTER 5**

*Experimental Section*



## 1. Materials

### 1.1. *Building blocks and crosslinkers*

IPDI was purchased from Quimidroga (Barcelona, Spain), TMXDI was purchased from Cytec Solvay (Stamford, USA), YMER N-120 was supplied by Perstorp (Perstorp, Sweden) and Genamin TAP 100D was provided by Clariant (Barcelona, Spain). Jeffcat DPA, Jeffamine ED2003 and DMPA were purchased from Huntsman Corporation (Barcelona, Spain), 1,6-hexanediol was provided by MERCK (Barcelona, Spain), diaminopimelic acid was purchased from TCI Chemicals (Zwijndrecht, Belgium) and DEEDS, DETA and L-lysine hydrochloride were purchased from Sigma Aldrich (St Louis, USA).

### 1.2. *Targeting molecules*

A5 and IPEP peptides were kindly provided by Dr. Royo's group (UQC-PCB) and Anti-GD2 MAb (Dinutuximab) was purchased from Creative Biolabs (Shirley, USA).

265

### 1.3. *Encapsulated molecules*

PTX was purchased from Fujian South Pharmaceutical (Xuefeng, China), CU was obtained from TCI Chemicals (Zwijndrecht, Belgium), HP (originally named as HL3) and HQ (originally named as HL4) were kindly provided by Prof. Patrick Gamez (UB) and T17 and T18 were kindly provided by Dr. Quesada's group (UBU). Crodamol GTCC was provided by Croda (Barcelona, Spain), NALA and NAST were purchased from Sigma Aldrich (St Louis, USA), and tributyrin was purchased from TCI Chemicals (Zwijndrecht, Belgium). DiO, DiI and DiR were purchased from Thermo Fisher Scientific (Barcelona, Spain), CB was obtained from Risk Reactor (Santa Ana, USA).

#### **1.4. Solvents and auxiliary solutions**

THF, HNO<sub>3</sub> 65% by wt, dry toluene, HCl 1 M, absolute EtOH, absolute MeOH and *N,N*-dibutylamine were obtained by Panreac (Castellar del Vallès, Spain), Milli-Q water was obtained from a Merck Millipore purification system (Madrid, Spain), PBS was purchased from Merck (Madrid, Spain), HCl 37% by wt, NaOH in pellets, TEA, CDCl<sub>3</sub>, DMSO-*d*<sub>6</sub>, (CD<sub>3</sub>)<sub>2</sub>CO, L-phenylalanine, AABA acid, reduced GSH and uranyl acetate were purchased from Sigma-Aldrich (St Louis, USA) and DMSO was obtained from Alfa Aesar (Karlsruhe, Germany). Acetonitrile (HPLC grade) and TFA were purchased from Fischer (Madrid, Spain). AccQ·Fluor™ reagent was purchased from Waters (Cerdanyola del Vallès, Spain).

#### **1.5. Materials for biological studies**

##### **1.5.1. *In vitro* studies**

HSA, BSA, FBS and LysoTracker Red were obtained from Life Technologies (Madrid, Spain), DMEM, l-glutamine, penicillin, streptomycin, trypsin, RPMI medium, HAM-F-12, NEAA were purchased from Biological Industries (Cromwell, USA). MTT, DMSO, PFA, Mowiol 4-88 and DAPI were purchased from Sigma Aldrich (St Louis, USA). Neomycin, DMEM-F12, MCDB-131 and HAT were obtained from Invitrogen.

Human adenocarcinoma lung A549 cells, human small lung cancer DMS53 cells, human squamous lung carcinoma H520 cells, normal human lung fibroblasts, HFL-1 cells, human neuroblastoma CHLA-90 and SK-N-BE2 cells, human mammary gland adenocarcinoma MDA-MB-231 cells, human breast adenocarcinoma MCF-7 cells, human microvascular endothelial HMEC-1 cells and human vascular endothelial EA.hy926 cells were purchased from ATCC (Barcelona, Spain).

##### **1.5.2. *In vivo* studies**

Human CHLA-90 neuroblastoma cancer cells in exponential growth were purchased from ATCC (Barcelona, Spain), iodine solution was obtained from Meda Pharma (Madrid, Spain), Isoflurane was purchased from Abbott Laboratories (Barcelona, Spain), Matrigel was obtained from BD Biosciences (Madrid, Spain), PBS

1x in sterile water was purchased from Laboratorios Serra Pamies (Reus, Spain) and trypan blue 0.4 % was purchased from Invitrogen (Barcelona, Spain). Athymic Nude-Foxn1 mice (female, 5 weeks old) were purchased from ENVIGO (Santa Perpètua de la Mogoda, Spain) and were weighted at the beginning of the experimental phase.

## 2. Analytical techniques

The present work, including most of the characterization techniques, has been developed between Ecopol Tech's facilities and the Organic Chemistry section from the Inorganic and Organic Department of University of Barcelona. TEM, AFM, HPLC for the amino acid analysis and flow cytometers were used from Scientific and Technological Centers of University of Barcelona.

### 2.1. *Infrared spectroscopy (IR)*

IR spectra were performed in a Smart ATR (Nicolet iS10, Thermo Scientific, Raleigh, USA) using a transmittance mode (32 scans) and OMNIC software. For the monitoring of solvent-based samples, one drop was deposited onto the diamond crystal and the solvent was left to dry by evaporation. IR spectra were recorded from a dry film of the sample for the reaction control after emulsification.

### 2.2. *pH measurements*

The pH of the emulsion was determined right after the crosslinker was added and at different time intervals until the last polyaddition reaction was complete. All the determinations were carried out in a pH-meter HI 2211 pH/ORP-Meter (HANNA Instruments, Eibar, Spain) equipped with a pH electrode Crison 5029 (Crison Instruments, Barcelona, Spain) and a temperature probe.

### 2.3. *Automatic isocyanate titration*

Automatic isocyanate titrations were performed in a Titromatic (Crison, Instruments, Barcelona, Spain). Isocyanate-reactive polymers were dissolved in 20 mL cyclohexanone and reacted with 10 mL of a *N,N*-dibutylamine standard at 0.4 M (excess) in dry toluene. This mixture was stirred magnetically, methanol (20 mL) was added through a pump and the mixture was stirred upon homogenization. Residual *N,N*-dibutylamine was back-titrated with HCl 1 M to the endpoint. The isocyanate content in the polymer was calculated from the consumed volume and was expressed in percentage of NCO by weight.

### 2.4. *Nuclear magnetic resonance (NMR)*

<sup>1</sup>H NMR (400 MHz) and <sup>13</sup>C NMR (101 MHz) spectra were recorded in a Varian Mercury 400 (Varian, Yamton, UK), using CDCl<sub>3</sub>, DMSO-*d*<sub>6</sub> or (CD<sub>3</sub>)<sub>2</sub>CO as solvents and TMS as a reference.

### 2.5. *High Pressure Liquid Chromatography (HPLC)*

HPLC chromatograms were recorded in a SHIMADZU Instrument (Shimadzu, Riverwood Drive, USA) equipped with a LC-20AD quaternary pump, DGU-20A5 degasser, SIL-10ADVP auto injector and a 2PD-20A dual UV-Vis detector. The analyses were performed with a reverse phase column PROTONSIL 120-5-C18 (250 x 4.6 mm), AQ PLUS 5.0 μm (Bischoff Chromatography, Atlanta, USA) using Milli-Q water (0.045% v/v TFA) and acetonitrile (0.036% v/v TFA) as mobile phases A and B respectively. All samples were prefiltered through a 0.45 μm syringe filter.

#### 2.5.1. *IPEP determination*

For IPEP peptide characterization, L-phenylalanine (2.18 mg/mL) was used as an IS and the analyses were performed with a gradient of B from 15% to 20% in 17 min with UV detection at 220 nm.

In order to monitor the **HL1-IPEP** conjugation reaction, an initial sample was taken to check the presence of the peptide and to establish its relative absorbance. Then, **HL1** polymer was added and different samples were taken until all the IPEP

peptide was reacted. In all cases, 50  $\mu\text{L}$  of the reaction mixture were dissolved in a 2 mL-volumetric flask with Milli-Q water and a volume of 100  $\mu\text{L}$  of the resulting solution were injected.

For the calibration curve, IPEP peptide was prepared at different concentrations and a fixed volume of L-phenylalanine was added in each standard. Linearity: 0.0545 mg IPEP/mL - 0.872 mg IPEP/mL.

For conjugated IPEP peptide quantification, the samples (**DiO-HL1-IPEP-2**, **DiO-HL1-IPEP-5** and **DiO-AMP-4 NCs**) were firstly centrifuged in order to collect the filtrates that contained non-reacted (free) IPEP (see section 2.15). Then, the IS was added and the solution was brought to a final volume of 2 mL with Milli-Q water. Finally, 30  $\mu\text{L}$  of the sample were injected and the IPEP conjugation yield was indirectly calculated by withdrawing the amount of free peptide (analyzed by HPLC) from the known total amount of peptide.

$$\% \text{ conjugation yield} = \frac{\text{IPEP}(\text{total}) - \text{IPEP}(\text{free})}{\text{IPEP}(\text{total})} * 100$$

## 2.6. Amino acid analysis

Amino acids were analyzed by HPLC using the AccQ·Tag pre-column derivatization method. The reaction of the amino acids with 6-aminoquinolyl-*N*-hydroxysuccinimidyl carbamate yields specific derivatives that are detected at 254 nm.

The HPLC system consists of a Waters Delta 600 chromatographic system with a Waters 2487 Dual  $\lambda$  absorbance detector, a Water 717plus autosampler and a Waters TCM II module temperature controller. The column was a Waters Nova-Pak C18 4  $\mu\text{m}$ , 3.9 x 150 mm, the volume of injection was 20  $\mu\text{L}$  and the gradient conditions were those described in the Waters AccQ·Tag method protocol.

The identification of the amino acids was carried out according to the retention times of the corresponding standards and the quantification was calculated by the IS method. A known amount of AABA and norleucine (NLE) were added to the sample and the analyte amount was calculated using the areas of the analytes and the IS. Working amino acid standard solutions were prepared by dilution of commercial 2.5 mM standards (Thermo Scientific, Barcelona, Spain) and IS solutions

at 2.5 mM were prepared using AABA or NLE (Sigma-Aldrich, St Louis, USA). Data acquisition and treatment were performed using the Empower 2 software.

### 2.6.1. Hydrolysis

For conjugated A5 peptide quantification, 10–20 mg of lyophilized NCs (**DiO-HL6-A5-2**, **DiO-HL6-A5-5** and **DiO-AMP-3 NCs**) were dissolved in an Eppendorf with 120  $\mu\text{L}$  of HCl 12 M, 60  $\mu\text{L}$  of AABA and 60  $\mu\text{L}$  of NLE. The samples were vortexed and ultrasonicated until the solids were totally dissolved. Then, the solution was transferred to a hydrolysis tube and the Eppendorf was washed three times with 100  $\mu\text{L}$  of HCl 6 M containing 1% w/v of phenol. Then, the hydrolysis tube was flame-sealed.

Once sealed, the hydrolysis tube was left for 24 h at 110  $^{\circ}\text{C}$  in a sand bath. After that time, the tube was open and the hydrolyzed samples were brought to dryness under reduced pressure at 80  $^{\circ}\text{C}$  for 2 h. Then, they were resuspended in 400  $\mu\text{L}$  of Milli-Q water and ultrasonicated for 30 minutes. In those case the solutions were not clear, the sample was centrifugated at 6000 rpm for 10 min to separate the solid fraction from the supernatant amino acids. The supernatant fraction was filtered through a 0.22  $\mu\text{m}$  filter and was used for the derivatization step.

For conjugated antiGD2 antibody quantification in **DiR-antiGD2 NCs** and **DiR-AMP NCs**, the hydrolyzation procedure was followed as for the samples containing A5 peptide, with some modifications. Firstly, the sample weight was around 10 mg, the hydrolysis tube was left for 48 h at 110  $^{\circ}\text{C}$  instead of 24 h and the hydrolyzed samples were resuspended in 150  $\mu\text{L}$  of Milli-Q water (**DiR-AMP NCs**) and 250  $\mu\text{L}$  of Milli-Q water (**DiR-antiGD2 NCs**).

### 2.6.2. Derivatization

In a derivatization tube, 10  $\mu\text{L}$  of the hydrolyzed mixture were added to 70  $\mu\text{L}$  borate buffer and vortexed for 10–20 s. Then, 20  $\mu\text{L}$  of AccQ-Fluor reagent was added and the mixture was vortexed for additional 15–20 s. The tube was covered with Parafilm and after 1 min, it was placed in an aluminum block at 55  $^{\circ}\text{C}$  for 10 min. After that time, it was cooled down to rt and 100  $\mu\text{L}$  of acetate/phosphate buffer

(pH = 5.7) was added and vortexed for 15–20 s. The mixture was transferred to a microvial for posterior analysis.

### **2.7. Dynamic light scattering (DLS)**

The size distribution of the NCs was analyzed on a Zetasizer Nano-ZS90 (Malvern, Worcestershire, UK) in Milli-Q water at 25 °C at a concentration of 1 mg/mL.

### **2.8. Zeta potential ( $\zeta$ -pot)**

The  $\zeta$ -pot of the NCs was analyzed on a Zetasizer Nano-ZS90 (Malvern, Worcestershire, UK) in Milli-Q water at 25 °C at a concentration of 5 mg/mL, measured at different pH values.

### **2.9. Transmission electron microscopy (TEM)**

The morphology of NCs and the *in vitro* degradation in presence of reduced GSH were studied in a Jeol JEM 1010 (Jeol, Peabody, USA). A 200-mesh copper grid coated with 0.75% FORMVAR was deposited on 6  $\mu$ L of an aqueous NCs suspension at 10 mg/mL for 1 min. The excess of sample was removed by contact with a drop of Milli-Q water for 1 min and the grid was deposited on a drop of uranyl acetate 2% by wt in Milli-Q water for 1 min. The excess of uranyl acetate was removed and the grid was air-dried for at least 3 h prior to measurement.

For *in vitro* degradation experiments, 150  $\mu$ L of an aqueous NCs suspension at 20 mg/mL were filtered through a 0.22  $\mu$ m filter and added into a freshly prepared solution of reduced GSH in PBS (final GSH concentration of 10 mM). The mixture was incubated at 37 °C for 24, 48, 72 and 96 h.

### **2.10. Atomic force microscopy (AFM)**

AFM analyses were performed in a Multimode 8 Atomic Force Microscope in Quantitative nanoMechanical mode (QNM) and Nanoscope V electronics (Bruker, Billerica, USA). The measurements were performed using a rectangular-shaped silicon cantilever with a pyramidal tip curvature of 8 nm and a nominal spring

constant of 200 N/m, TAP 525, (Bruker, Billerica, USA). Mica discs were made of muscovite (Ted Pella, Redding, USA).

### 2.11. Ultraviolet/visible spectroscopy (UV/Vis)

The encapsulation efficiency (EE) and drug loading (DL) of the NCs were determined by UV-Vis measurements performed in a Cary 500 Scan UV-Vis-NIR spectrophotometer (Varian, Palo Alto, USA). Firstly, a calibration curve was developed by preparing a range of standard solutions containing the drug at different concentrations and analyzing their UV profile and maximum absorbance. Then, EE (%) and DL (%) were calculated from the following equations:

$$\% EE = \frac{\text{amount of drug incorporated in the nanocapsule}}{\text{total amount of drug added in the aqueous dispersion}} * 100$$

$$\% DL = \frac{\text{amount of drug incorporated in the nanocapsule}}{\text{total amount of lyophilized nanocapsules}} * 100$$

To determine the amount of drug incorporated in the NCs, a desired amount of lyophilized NCs was dissolved in an exact volume of solvent and the measurement was calculated from the calibration curve. Unloaded NCs were used as the reference. All measurements were recorded at the desired wavelength range depending on the drug under study and assayed in triplicates.

### 2.12. Fluorescence spectroscopy

Fluorescence experiments were performed in a Photon Technology International spectrofluorimeter (PTI, Birmingham, USA), equipped with a Brytebox, MD-5020 motor driver and LPS-220B lamp power supply.

#### 2.12.1. Förster Resonance Energy Transfer (FRET)

FRET experiments were carried out by exciting the donor (DiO) at 484 nm and recording the emission spectrum from 495 nm to 650 nm ( $\lambda_{em,DiO} = 506$  nm;  $\lambda_{exc,DiI} = 550$  nm,  $\lambda_{em,DiI} = 572$  nm). DiO and DiI stock solutions were prepared in PBS at 7.5

$\mu\text{g}$  fluorophore/mL (pH = 7.4) from predialyzed and prelyophilized samples (**DiO-AMP NCs** and **DiI-AMP NCs**). The experiments were carried out with a slitwidth of 0.55 mm and at a fixed temperature of 37 °C under constant magnetic stirring for 96 h.

To study the release kinetics of hydrophobic molecules in an aqueous buffer, a control assay with PBS was performed by diluting 16  $\mu\text{L}$  of each stock solution in 3 mL of PBS. In order to have a complete profile of the kinetics release of the system in this medium, the first measurements were performed every 30 min until 2 h. Afterwards, the delay between measurements was extended.

To assess the influence of HSA-rich and BSA-rich solutions, the previous experiment was repeated with a 40 mg/mL solution of HSA and BSA in PBS.

To evaluate the effect of reduced GSH, the experiment was carried out under the same conditions that those used in the control experiment for the first 2 h and then, the required amount of GSH was added to reach a concentration of 10 mM. In order to have a complete profile of the kinetics release of the system in this reductive medium, the first measurements were taken every 30 min for 2 h and then, the delay between measurements was extended.

To evaluate the effect of reduced GSH in non-labile NCs (**NL-DiO-AMP NCs** and **NL-DiI-AMP NCs**), the experiment was carried out following the same procedure that was used for the labile NCs under GSH medium.

### 2.12.2. *Fluorescence measurements to determine the content of arginine*

The A5 peptide content of the samples (**DiO-HL6-A5-2 NCs**, **DiO-HL6-A5-5** and **DiO-AMP-3 NCs**) was indirectly determined by measuring the arginine content of the filtrates. Firstly, the samples were centrifuged (see section 2.15) and the filtrates were collected and used for the assay. Then, the adequate volumes of the filtrates were introduced in a vial and mixed with 9,10-phenanthrenequinone reagent in EtOH (161  $\mu\text{M}$ ) and NaOH (2 N). The mixture was incubated for 3 h at 60 °C and HCl 1.2 N was added. Fluorescence of the reaction product was allowed to develop for 1 h in the dark at rt and the samples were excited at  $\lambda_{\text{exc}} = 312$  nm and recorded at 330–600 nm ( $\lambda_{\text{em}} = 395$  nm).

The calibration curve was built by running the same derivatization reaction with 2.5 mL of A5 peptide solution at 0.402 mg/mL, 12.58 mL of

9.10-phenanthrenequinone reagent in EtOH (161  $\mu$ M) and 6.75 mL of NaOH 2 N. The resulting product was aliquoted at different concentrations and completed with Milli-Q water. The linearity of the fluorescence signal was held in the range of 0–63.11  $\mu$ g of A5 and 0–6.82  $\mu$ g of arginine.

### **2.13. Lyophilization and reconstitution**

Lyophilization was carried out with purified aqueous samples in a Christ Alpha 2-4 LDplus freeze dryer (Martin Christ, Osterode am Harz, Germany). Previously dialyzed samples were lyophilized and redispersed in the desired solvent depending on the characterization method. For organic solvents, the dry samples were immediately dissolved without stirring; in the case of aqueous buffers or Milli-Q water, the dry samples were redispersed by vigorous magnetic stirring overnight and ultrasonication.

### **2.14. Solids concentration**

NCs concentration in the aqueous dispersion was determined by triplicate using an OHAUS MB25 moisture analyzer (Ohaus, Greifensee, Switzerland), with a temperature range from 23 °C to 160 °C in 5 °C increments.

### **2.15. Centrifugal separation**

The separation between the NCs and the rest of the dispersion, including non-reacted monomers, was performed in a Rotofix 32A (Hettich Zentrifugen, Tuttlingen, Germany). The samples were centrifuged using Vivaspin 2 Hydrosart 30,000 MWCO concentrators (Sartorius AG, Göttingen, Germany), which consist of a vertical membrane disposed as a thin channel filtration chamber attached to a conical tube. The membrane retains all the compounds with a molecular cut off equal or higher than 30,000 g/mol, while the tube collects the aqueous medium with lighter analytes.

The samples were centrifuged for 3 h in cycles of 60 min at 6,000 rpm (25 °C) to ensure that the NCs were well separated and that all the non-reacted monomers were collected.

## 2.16. *Dialysis purification*

The NCs were dialyzed against distilled water for 24 h for chemical characterization and against Milli-Q water for 72 h for biological assays using a Spectra/Por molecular porous membrane tubing with a 12–14 kDa molecular MWCO (Spectrum Laboratories, Rancho Dominguez, USA). For the *in vivo* experiments, the NCs (**DiR-antiGD2** and **DiR-AMP** NCs) were dialyzed against PBS 0.01 M (0.138 M NaCl; 0.0027 M KCl; pH 7.4 at 25 °C) using Spectra/Por molecular porous membrane tubing with a 300 kDa molecular MWCO.

## 3. *In vitro* assays

The biological characterization described in Chapter 3 was carried out in the Department of Pathology and Experimental Therapeutics of the Faculty of Medicine and Health Sciences of University of Barcelona. Biological assays reported in Chapter 4 as well as the *in vivo* biodistribution studies were performed in the Functional Validation and Preclinical Research lab, from Vall d'Hebron Research Institute.

275

### 3.1. *Lung cancer*

#### 3.1.1. *Cell culturing*

Human adenocarcinoma lung A549 cells were cultured in DMEM supplemented with 10% FBS, 1% of a stock solution of L-glutamine 200 mM, 1% of 1,000U/mL penicillin and 1% of 10 mg/mL streptomycin solution. The medium was renewed twice or three times a week and trypsinized to a dilution of 1:3 to 1:8. The cell concentration should be maintained between  $6 \cdot 10^3$  and  $6 \cdot 10^4$  cells/cm<sup>2</sup>. When cells were at 80–90% of confluence, they were trypsinized by adding 1 mL of trypsin for a p100 plate after washing it with PBS. Cells were incubated at 37 °C for 2–3 min until they were detached, which was confirmed by optical microscopy. Then, 9 mL of medium were added to inactivate trypsin and cells in suspension were collected. Finally, they were distributed to new plates according to the desired density.

Small lung cancer DMS53 cells were cultured in RPMI medium supplemented with 10% FBS, 1% of a stock solution of L-glutamine 200 mM, 1% of 1,000U/mL penicillin and 1% of 10 mg/mL streptomycin solution. The media was renewed twice or three times a week and trypsinized to a dilution of 1:2 to 1:3. When cells were at 80–90% of confluence, they were trypsinized by adding 1 mL of trypsin for a p100 plate after washing it with PBS. Cells were incubated at 37 °C during 8–10 min until they were detached, which was confirmed by optical microscopy. Then, 9 mL of medium were added to inactivate trypsin and cells in suspension were collected. Finally, they were distributed to new plates according to the desired density.

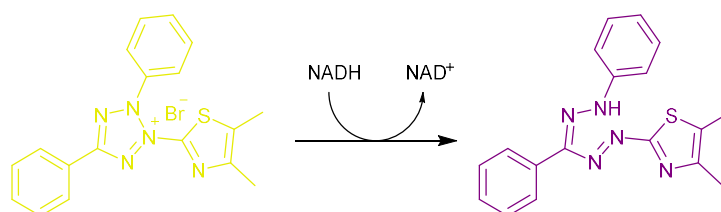
Lung squamous carcinoma H520 cells were cultured in RPMI medium supplemented with 10% FBS, 1% of a stock solution of L-glutamine 200 mM, 1% of 1,000U/mL penicillin, 10 mg/mL streptomycin and 1.5% of HEPES. The media was renewed twice or three times a week and trypsinized to a dilution of 1:3 to 1:6. Once cells were at 80–90% of confluence, they were trypsinized by adding 1 mL of trypsin for a p100 plate after washing it with PBS. Cells were incubated at 37 °C during 5–7 min until they were detached, which was confirmed by optical microscopy. Then, 9 mL of medium were added to inactivate trypsin and cells in suspension were collected. Finally, they were distributed to new plates according to the desired density.

Normal lung fibroblasts, HFL-1 cells, were cultured in HAM-F-12 medium supplemented with 10% FBS, 1% of a stock solution of L-glutamine 200 mM, 1% 1,000U/mL penicillin, 1% 10 mg/mL of streptomycin solution and 1% NEAA. The media was renewed twice or three times a week and trypsinized to a dilution of 1:4 to 1:6. When cells were at 80–90% of confluence, they were trypsinized by adding 1 mL of trypsin for a p100 plate after washing it with PBS. Cells were incubated at 37 °C during 20 s–1 min until they were detached, confirmed by optical microscopy. Then, 9 mL of medium were added to inactivate trypsin and cells in suspension were collected. Finally, they were distributed to new plates according to the desired density.

When cells were in p60 plate, they were trypsinized by adding 0.5 mL of trypsin whereas when they were in a p150 plate, they were trypsinized by adding 1.5 mL of trypsin.

### 3.1.2. Cell viability

Cell viability was measured by the MTT assay, which is a colorimetric method to assess cell metabolic activity. Viable cells with active metabolism are capable of converting MTT, a tetrazolium dye (yellow), into colored formazan (purple) with an absorbance maximum near 570 nm (**Scheme 1**). The reduction to formazan is not well understood, but it likely involves reaction with NADH or similar reducing molecules.



**Scheme 1.** MTT transformation to formazan

Therefore, when cells die due to the effect of the compound under study, they lose the ability for this transformation and thus the color serves as a clear marker of only viable cells.

The experiments were performed in 96-well plates with a density of  $20^4$  cells per well for H520 and DMS53 cell lines, whereas a density of  $10^4$  cells per well was used for A549 and HFL-1 cell lines. Firstly, cells were counted, seeded with the corresponding density and were incubated for 24 h. After that, cells were treated by adding the unloaded and loaded NCs at different drug concentrations.

After 48 or 72 h of treatment, a MTT solution was added to achieve a final concentration of 0.5 mg/mL. After 2 or 4 h of incubation, depending on the cell line, the solution was removed and 100  $\mu$ L of DMSO were added to dissolve formazan crystals. Finally, using a Thermo Multiskan microplate reader (Thermo Fisher Scientific, Barcelona, Spain), the absorbance was read at 570 nm and the percentage of cell viability in each well was calculated.

### 3.1.3. Cell uptake

#### 3.1.3.1. Physiological conditions

Cells were seeded in a 6-well plate with a cell density of  $10^5$  cells/mL per well and were allowed to grow for 24 h, confirming that the confluence was 50–60%. Afterwards, the medium was removed and cells were treated with DiO-loaded NCs (**DiO-AMP NCs**) and diluted with the appropriate volume of medium to reach a DiO concentration of 15  $\mu\text{g/mL}$ . The time course used was set to 1 h, 4 h, 8 h, 16 h, 24 h and 48 h for the samples and 8 h and 48 h for the controls (**BLANK AMP NCs**). After the corresponding treatment, cells were washed by adding 1 mL of PBS and then 200  $\mu\text{L}$  of trypsin were added and cells were incubated until complete detachment. After that, 1 mL of medium was added and the solution was transferred into a 50 mL Falcon tube. This solution was centrifuged at 800 rpm for 4 min at 20 °C. Afterwards, cells were washed with PBS and centrifuged using the same conditions as mentioned above. This procedure was repeated twice.

Cell fixation was done under the fume hood by filling another Falcon tube with 4 mL of PFA 4% in PBS and adding the cell solution into the former solution dropwise while vortexing. The addition of the cells was done slowly enough so that they did not aggregate into the PFA solution. After 20 min at rt, the solution was centrifuged and PFA was removed. Again, the solution was washed with PBS and centrifuged. Finally, 300  $\mu\text{L}$  of PBS were added and the Falcon tube was sealed with parafilm. The samples were kept in the fridge protected from light until they were analyzed in a FACS Canto cytometer (Beckman Coulter, Indianapolis, USA).

One-way ANOVA was carried out with the Statgraphics centurion statistical package and post hoc Tukey analyses were performed.

#### 3.1.3.2. Slightly acidic conditions

Different cell growing media were prepared by adding HEPES at a concentration of 15 mM and Bis-tris propane at 40 mM in the standard medium. Both buffers were separated into three different volumes and each of them was adjusted to pH 6.8, 7.1 and 7.4 by adding HCl 1 M (prefiltered with a 0.22  $\mu\text{m}$  syringe

filter, since they were not sterile). The growing media were kept in the fridge until they were used in the assays.

Cells were seeded in a 6-well plate using the standard medium with a cell density of  $10^5$  cells/ml per well and this medium was replaced by the new one having the desired pH after 24 hours of growing. Cells were allowed to adapt to the new conditions for 24 h and then were incubated with the DiO-loaded NCs (**DiO-AMP NCs**) at a DiO concentration of 15  $\mu\text{g}/\text{mL}$  and unloaded NCs (**BLANK-AMP NCs**) as a control. The time course selected for the assay with HEPES buffer was 1 h, 4 h, 8 h and 24 h. Regarding the assay containing Bis-tris propane, shorter time points were chosen (1 h, 4 h and 8 h). After each treatment, the medium at the end of the time point was measured in order to know the variation occurred during the incubation time.

The rest of the procedure, including cell washing, trypsinization, centrifugation and fixation was followed as in the previous section (3.1.3.1).

#### 3.1.4. Cell internalization

The coverslips were carefully placed inside the 12-well plate using alcohol-sterilized forceps. Afterwards, FBS was added on each well and was brought to dryness for cell attachment. Every well was seeded with a density of 100,000 cells/mL (total volume 500  $\mu\text{L}$ ). After 24 h, cells were treated with NCs at the desired concentration of DiO (15  $\mu\text{g}/\text{mL}$ ), confirming that cells were at 50–60% of confluence just before treatment. 1 h before finishing the treatment, the medium was removed and replaced by a new solution containing LysoTracker Red at a concentration of 0.25  $\mu\text{M}$  in order to tag the acidic organelles. After 1 h of incubation, cells were washed three times with 500  $\mu\text{L}$  of PBS for 2 min. Then, cells were fixed under the fume hood by adding a few drops of PFA at 4% by wt in PBS at rt. After 20 min, the coverslips were washed three times with 500  $\mu\text{L}$  of PBS for 1 min and were put upside down on a slide containing 15  $\mu\text{L}$  of Mowiol 4-88. The samples were kept in the cooling chamber and were let to warm up to rt 30 min before the visualization in a Leica TCS-SL filter-free spectral confocal microscope (Leica Microsystems, Barcelona, Spain).

## **3.2. Neuroblastoma**

### **3.2.1. Cell culturing**

Neuroblastoma CHLA-90 and SKNB-E-2 cells were cultured in DMEM supplemented with 20% FBS, 1% of a stock solution of L-glutamine 200 mM, 1% of 1,000U/mL penicillin, 10 mg/mL streptomycin and 5 µg/mL insulin, 5 µg/mL transferrin, 5 ng/mL selenous acid.

### **3.2.2. Cell viability**

*In vitro* activity of the NCs was tested using the MTT assay with both neuroblastoma cell lines following the same procedure as for the cell viability in lung cancer (see section 3.1.2).

## **3.3. Breast cancer**

### **3.3.1. Cell culturing**

Human mammary gland adenocarcinoma MDA-MB-231.Fluc. cells were cultured in DMEM-F12 medium with 500 µg/mL of neomycin. The medium was renewed twice or three times a week and once the cells were at 80–90 % of confluence, the p100 plate was washed with PBS and 1 mL of trypsin was added. They were incubated at 37 °C for 2–3 min until they were detached, confirmed by optical microscopy. Then, 9 mL of medium were added to inactivate trypsin and cells in suspension were collected. Finally, according to the desired density, they were distributed to new plates.

Human breast adenocarcinoma MCF-7 cells were cultured in DMEM-F-12 medium. The medium was renewed twice or three times a week and once the cells were at 80–90 % of confluence, the p100 plate was washed with PBS and 1 mL of trypsin was added. They were incubated at 37 °C for 2–3 min until they were detached, confirmed by optical microscopy. Then, 9 mL of medium were added to inactivate trypsin and cells in suspension were collected. Finally, according to the desired density, they were distributed to new plates.

Human microvascular endothelial HMEC-1 cells were cultured in MCDB-131 medium supplemented with 10 mM of L-glutamine. The medium was renewed twice or three times a week and once the cells were at 80–90 % of confluence, the p100 plate was washed with PBS and 1 mL of trypsin was added. They were incubated at 37 °C for 2–3 min until they were detached, confirmed it by optical microscopy. Then, 9 mL of medium were added to inactivate trypsin and cells in suspension were collected. Finally, according to the desired density, they were distributed to new plates.

Human endothelial hybrid EA.hy926 cells were cultured in DMEM supplemented with 1x HAT. The medium was renewed twice or three times a week and once the cells were at 80–90 % of confluence, the p100 plate was washed with PBS and 1 mL of trypsin was added. They were incubated at 37 °C for 2–3 min until they were detached, confirmed it by optical microscopy. Then, 9 mL of medium were added to inactivate trypsin and cells in suspension were collected. Finally, according to the desired density, they were distributed to new plates.

### 3.3.2. Cell viability

*In vitro* activity of the NCs (**PTX-AMP-2 NCs** and **BLANK-AMP-2 NCs**) was tested using the MTT assay in MCF-7 and MDA-MB-231. Cells were seeded in 96-well plates and were allowed to attach overnight. Then, they were treated with the NCs at different final doses for 72 h. At the end of the incubation period, a 5 mg/mL of MTT solution was added to the wells and 4 h later formazan crystals were dissolved and the resulting solution was spectrophotometrically measured at 590 nm with a Biotek ELx800 Absorbance Microplate Reader (Winooski, USA). Finally, the percentage of cell viability in each well was calculated.

### 3.3.3. Cell uptake

The time-dependent cell uptake of A5-targeted and non-targeted NCs (**DiO-HL6-A5-2 NCs**, **DiO-HL6-A5-5 NCs** and **DiO-AMP NCs**) was studied by flow cytometry (LRS Fortessa Becton Dickinson, Franklin Lakes, USA) in MDA-MB-231.Fluc. and MCF-7 cell lines. Firstly, exponentially grown cultures were detached using PBS-EDTA (5 mM), resuspended in Ca<sup>2+</sup>- and Mg<sup>2+</sup>-free PBS and incubated at 37 °C with the NCs at three different DiO concentrations (0.53 µg/mL,

1.32  $\mu\text{g}/\text{mL}$  and 52.90  $\mu\text{g}/\text{mL}$ ) for 60 min to assess the optimal DiO concentration. Secondly, the experiment was repeated with a fixed DiO dose of 1.32  $\mu\text{g}/\text{mL}$  and the cell uptake was tested after 15, 30, 60 and 120 min of incubation. After all incubation times, cells were washed twice with PBS, analyzed in the cytometer and processed with the Express 4 De Novo software (Los Angeles, USA).

The time-dependent cell uptake of IPEP-targeted and non-targeted NCs (**DiO-HL1-IPEP-2 NCs**, **DiO-HL1-IPEP-5 NCs** and **DiO-AMP NCs**) was studied following the same procedure, with the exception that the cell lines used, HMEC-1 and EA-hy926 instead of MDA-MB-231.Fluc. and MCF-7, and the most prolonged incubation time, which was 180 min instead of 120 min.

## 4. *In vivo* biodistribution

### 4.1. *Conditions*

*In vivo* biodistribution was studied using 5 weeks old athymic female mice Hsd: Athymic nude-Foxn1 nu/nu. Neuroblastoma CHLA-90 cell model was implanted subcutaneously with  $5 \cdot 10^6$  cells/animal.

### 4.2. *Test facilities*

Animals used in this study were housed, during the acclimatization period of 9 days, in the quarantine rooms. During the acclimatization period all observations were registered. All the animals were inspected by a veterinary to ensure their health. Once the acclimatization was carried out, the animals were moved to the corresponding animal rooms to perform the experimental phase.

### 4.3. *Housing*

The animals were randomly housed under specific pathogen free (SPF) conditions in autoventilated racks.

#### 4.3.1. *Habitat*

Animals were housed in groups of 6, in Innocage IVC mouse type II 523 cm<sup>2</sup> cages. Two enrichment elements were included, a cardboard tube and a square nestlet for nesting and thermoregulation. Each cage was identified by a card stating: the study code, the name of the TVPR responsible and the FVPR *in vivo* section technician, number of animals housed, species, sex, date of arrival, group, name, number of inoculated cells and the implantation route.

#### 4.3.2. *Cage litter*

Sterile corn cob bedding was used. The provider guaranteed that the litter was analyzed according to the regulations of the manufacturer for contaminants, such as microbiologic and physicochemical (heavy metals, aflatoxins, pesticides and organophosphorus) and the analytical results proved that the shaving was suitable for animal use.

#### 4.3.3. *Feed*

Maintenance 14% protein rodent irradiated diet, in cases of 10 kg vacuum packs *ad libitum*. The provider guaranteed that the feed was analyzed according to the regulations of the manufacturer for contaminants, microbiologic and physicochemical (heavy metals, aflatoxins, pesticides, estrogenic activity and organophosphorus). The analytical results proved that the feed was appropriate for animal consumption.

#### 4.3.4. *Drink*

Disposable water bottles decalcified and sterile *ad libitum*. The provider guaranteed that the water was regularly analyzed microbiologically, physicochemically and chemically. The analytical results proved that the limits set

by the Spanish regulations for human drinking water have been observed (drinking: *Real Decreto* 140/2003).

#### **4.3.5. Temperature and relative humidity**

Temperature and relative humidity was continuously recorded in the animal housing. The temperature ranged from 21.5 °C to 25.5 °C. Relative humidity ranged between 52% and 58%.

#### **4.3.6. Lighting**

Lighting was artificial, from an automatic controlled supply. The cycle gradually simulated twilight and sunset from 7.30 h to 8.00 h and from 19.30 h to 20.00 h, respectively, giving 12 h of light with an intensity of 300 Lux and 12 h of darkness for each 24 h period.

#### **4.3.7. Preparation and administration**

Both test items, **DiR-AMP NCs** and **DiR-antiGD2 NCs**, were prepared and maintained at 4 °C and protected from light until the administration day. Prior to administration, the test items were sonicated in an ultrasound bath for 4 min and vigorously vortexed. Additionally, **DiR-antiGD2 NCs** were filtered through a 0.7 µm filter. LD-antiGD2 test items was filter through a 0.7 µm filter. The NCs were administered at 0.8 mg DiR/kg in a single dose *per* intravenous route into the tail vein in a volume of 2.7 mL/kg and 4.1 mL/kg body weight for **DiR-AMP NCs** and **DiR-antiGD2 NCs**, respectively.

### **4.4. Experimental design**

Mice were divided into four experimental groups with

- 1 animal/group as an autofluorescence control
- 1 animal/group as a control with no tumor
- 3 animals/group with tumor and administered with **DiR-AMP NCs**
- 3 animals/group with tumor and administered with **DiR-antiGD2 NCs**

The organization of these experimental groups is better detailed in **Table 1**.

**Table 1.** Experimental design of *in vivo* biodistribution

Group	NCs	Mouse Model	Mice Number	End Point
<b>G0</b>	Autofluorescence control	Tumor-bearing mice	1	24 h
			1	48 h
<b>G1a</b>	<b>DiR-AMP NCs</b>	Non-tumor-bearing mice	1	24 h
		Tumor-bearing mice	3	
<b>G1b</b>		Non-tumor-bearing mice	1	48 h
		Tumor-bearing mice	3	
<b>G2a</b>	<b>DiR-antiGD2 NCs</b>	Non-tumor-bearing mice	1	24 h
		Tumor-bearing mice	3	
<b>G2b</b>		Non-tumor-bearing mice	1	48 h
		Tumor-bearing mice	3	

#### 4.5. Procedure

Mice received subcutaneous cell injection into the rear left flank. Body weight and tumor was measured twice a week by caliper measurements. The tumor volume was calculated according to the formula  $Dxd^2/2$ , where  $D$  and  $d$  are the longest and shortest diameters. Once the tumors reached a median volume of  $\sim 275 \text{ mm}^3$  (range  $90.54 \text{ mm}^3$  to  $409.46 \text{ mm}^3$ ), mice were randomized in the different groups according to their tumor volume. Randomized mice were treated with a unique dose of the test NCs at  $0.8 \text{ mg DiR/kg}$  by intravenous administration. For each group, a non-tumor-bearing mouse with the corresponding conjugate was included as a control for tumor accumulation, and a subcutaneous tumor-bearing mouse non-treated as a control to set the tissue autofluorescence. At 24 h and 48 h post administration, tumor-accumulation and whole-body biodistribution were measured non-invasively by DiR FLI monitoring from the dorsal and ventral mouse views. Moreover, at the same 24 h and 48 h post administration end time point, plasma, tumor, liver, spleen, kidneys and lung samples were collected, and the NC plasma and tissue accumulations were determined by *ex vivo* DiR FLI monitoring. Thereafter, all tissues were divided in two fragments and processed. One fragment

was snapped-frozen and stored at -80 °C, and the second one was fixed and further paraffin-embedded.

The animals were euthanized by cervical dislocation while still anaesthetized and following the euthanasia standard operating procedure (SOP).

#### **4.6. Evaluation and statistics**

FLI *in vivo* and *ex vivo* were performed with the IVIS Spectrum imaging system and images and measurements of fluorescence signals were acquired and analyzed using Living Image 4.5 software (PerkinElmer). The fluorescence signal was qualitatively quantified in *radiant efficiency* units (fluorescence emission radiance *per* incident excitation power). The mean FLI intensity and corresponding standard errors were determined. All the analyses and graphs were performed using GraphPad Prism 5 software.

## **5. Synthetic procedures of Chapter 2**

### **5.1. Amphiphilic cationic polymer (P1)**

DEDS (381.4 mg, 4.94 meq), YMER N-120 (4.54 g, 8.74 meq) and Jeffcat DPA (381.1 mg, 3.49 meq) were added into a three-necked round-bottom flask equipped with mechanical stirring at rt and purged with N<sub>2</sub>. When the mixture was homogeneous, IPDI (3.24 g, 29.15 meq) was added into the reaction vessel under gentle mechanical stirring. The polyaddition reaction was kept under these conditions until the NCO stretching band intensity did not change, monitored by IR and isocyanate titrations. At this point, dry THF (10 mL) was added into the reaction mixture in order to fluidify the polymer. In parallel, Genamin TAP 100D (2.54 g, 15.03 meq) was dissolved with dry THF (10 mL) into another 100 mL three-necked round-bottom flask, which had previously been purged with N<sub>2</sub> and precooled to 4 °C. The former reaction mixture was added dropwise onto the latter under smooth mechanical stirring. The reaction was monitored by IR until the NCO stretching band intensity had completely disappeared.

## 5.2. *Amphiphilic polymer (P2)*

The procedure was based on the amphiphilic cationic polymer (see section 5.1) with slight variations, detailed in **Table 2**.

**Table 2.** Amounts of reagents used to prepare **P2**

<b>Substance</b>	<b>Weight</b>	<b>Equivalentents</b>
<b>DEDS</b>	370.6 mg	4.81 meq
<b>YMER N-120</b>	4.42 g	8.51 meq
<b>Jeffcat DPA</b>	0 g	0 meq
<b>IPDI</b>	2.34 g	23.98 meq
<b>Genamin TAP 100D</b>	3.16 g	13.86 meq

## 5.3. *Non-labile amphiphilic cationic polymer (P3)*

The procedure was based on the amphiphilic cationic polymer (see section 5.1) with slight variations, detailed in **Table 3**.

**Table 3.** Amounts of reagents used to prepare **P3**

<b>Substance</b>	<b>Weight</b>	<b>Equivalentents</b>
<b>1,6-hexanediol</b>	302.9 mg	5.12 meq
<b>YMER N-120</b>	4.79 g	9.23 meq
<b>Jeffcat DPA</b>	394.5 mg	3.61 meq
<b>IPDI</b>	3.46 g	31.10 meq
<b>Genamin TAP 100D</b>	2.82 g	16.72 meq

#### 5.4. Paclitaxel-loaded amphoteric NCs (PTX-AMP NCs)

IPDI (30.9 mg, 0.28 meq) was added into a three-necked round-bottom flask equipped with mechanical stirring, precooled at 4 °C and purged with N<sub>2</sub>. In parallel, PTX (50.2 mg, 0.059 meq), the amphiphilic cationic polymer P1 (242.8 mg of P1, 0.069 meq) and dry THF (1 mL) were mixed in a vial, added into the flask and left to homogenize for 30 min at 150 rpm. At this point, an alkaline aqueous solution of L-lysine was prepared by dissolving 1.19 g in 9.33 g of Milli-Q water and adjusting pH to 11.0 with alkaline NaOH solutions at 3 M and 1 M (total L-lysine concentration 8.2% by wt). This solution (6.2 mg of L-lysine, 0.073 meq) was added and the polyaddition reaction was checked after 45 min by IR. Then, the organic phase was emulsified at 300 rpm with cold Milli-Q water (9.46 g) and finally an aqueous solution of DETA (4.2 mg of DETA, 0.12 meq) was added in order to generate crosslinked NCs from the nanodroplets present in the emulsion. The stirring was reduced to 100 rpm and the ice bath was removed to let the reaction reach rt. This polyaddition reaction was monitored by IR and pH measurements. Once the NCs were formed, THF was removed from the reactor at 40 °C under reduced pressure and the pH was adjusted to 7.0 using diluted aqueous HCl.

#### 5.5. Curcumin-loaded amphoteric NCs (CU-AMP NCs)

The procedure was based on the paclitaxel-loaded amphoteric NCs (see section 5.4) with slight variations, detailed in **Table 4**.

**Table 4.** Amounts of reagents used to prepare CU-AMP NCs

Substance	Amount	Equivalentents
IPDI	30.6 mg	0.28 meq
Drug (CU)	50.7 mg	0.15 meq
Polymer (P1)	256.8 mg	0.074 meq
Dry THF	1.2 mL	–
L-lysine	5.9 mg	0.070 meq
Milli-Q water	11.89 g	–
DETA	3.9 mg	0.11 meq

### 5.6. *HP-loaded amphoteric NCs (HP-AMP NCs)*

The procedure was based on the paclitaxel-loaded amphoteric NCs (see section 5.4) with slight variations, detailed in **Table 5**.

**Table 5.** Amounts of reagents used to prepare **HP-AMP NCs**

<b>Substance</b>	<b>Amount</b>	<b>Equivalentents</b>
<b>IPDI</b>	39.8 mg	0.36 meq
<b>Drug (HP)</b>	50.0 mg	0.13 meq
<b>Polymer (P1)</b>	396.0 mg	0.11 meq
<b>Dry THF</b>	1.4 mL	–
<b>L-lysine</b>	8.8 mg	0.10 meq
<b>Milli-Q water</b>	15.21 g	–
<b>DETA</b>	4.5 mg	0.13 meq

### 5.7. *HQ-loaded amphoteric NCs (HQ-AMP NCs)*

The procedure was based on the paclitaxel-loaded amphoteric NCs (see section 5.4) with slight variations, detailed in **Table 6**.

**Table 6.** Amounts of reagents used to prepare **HQ-AMP NCs**

<b>Substance</b>	<b>Amount</b>	<b>Equivalentents</b>
<b>IPDI</b>	30.9 mg	0.28 meq
<b>Drug (HQ)</b>	45.6 mg	0.093 meq
<b>Polymer (P1)</b>	242.6 mg	0.070 meq
<b>Dry THF</b>	1 mL	–
<b>L-lysine</b>	7.5 mg	0.089 meq
<b>Milli-Q water</b>	13.76 g	–
<b>DETA</b>	3.9 mg	0.11 meq

### 5.8. Unloaded amphoteric NCs (BLANK-AMP NCs)

The procedure was based on the paclitaxel-loaded amphoteric NCs (see section 5.4) with slight variations, detailed in **Table 7**.

**Table 7.** Amounts of reagents used to prepare **BLANK-AMP NCs**

Substance	Amount	Equivalentents
IPDI	46.4 mg	0.42 meq
Drug	0 mg	0 meq
Polymer (P1)	364.2 mg	0.10 meq
Dry THF	1 mL	–
L-lysine	11.3 mg	0.13 meq
Milli-Q water	14.13 g	–
DETA	5.4 mg	0.16 meq

### 5.9. DiO-loaded amphoteric NCs (DiO-AMP NCs)

The procedure was based on the paclitaxel-loaded amphoteric NCs (see section 5.4) with slight variations, detailed in **Table 8**. In this case, the three-necked round-bottom flask was protected from light.

**Table 8.** Amounts of reagents used to prepare **DiO-AMP NCs**

Substance	Amount	Equivalentents
IPDI	30.9 mg	0.28 meq
Fluorophore (DiO)	4.0 mg	4.5 $\mu$ eq
Polymer (P1)	242.4 mg	0.067 meq
Dry THF	1.5 mL	–
L-lysine	5.8 mg	0.070 meq
Milli-Q water	15.03 g	–
DETA	4.2 mg	0.12 meq

### 5.10. *DiI-loaded amphoteric NCs (DiI-AMP NCs)*

The procedure was based on the paclitaxel-loaded amphoteric NCs (see section 5.4) with slight variations, detailed in **Table 9**. In this case, the three-necked round-bottom flask was protected from light.

**Table 9.** Amounts of reagents used to prepare DiI-AMP NCs

Substance	Amount	Equivalentents
IPDI	29.9 mg	0.27 meq
Fluorophore (DiI)	4.0 mg	4.3 $\mu$ eq
Polymer (P1)	242.6 mg	0.067 meq
Dry THF	1.5 mL	–
L-lysine	5.8 mg	0.070 meq
Milli-Q water	15.04 g	–
DETA	4.1 mg	0.12 meq

### 5.11. *Paclitaxel-loaded cationic NCs (PTX-CAT NCs)*

The procedure was based on the paclitaxel-loaded amphoteric NCs (see section 5.4) with slight variations, detailed in **Table 10**.

**Table 10.** Amounts of reagents used to prepare PTX-CAT NCs

Substance	Amount	Equivalentents
IPDI	30.5 mg	0.27 meq
Drug (PTX)	44.0 mg	0.051 meq
Polymer (P1)	242.0 mg	0.072 meq
Dry THF	1 mL	–
L-lysine	0 mg	0 meq
Milli-Q water	12.16 g	–
DETA	5.8 mg	0.17 meq

### 5.12. Paclitaxel-loaded anionic NCs (PTX-AN NCs)

The procedure was based on the paclitaxel-loaded amphoteric NCs (see section 5.4) with slight variations, detailed in **Table 11**.

**Table 11.** Amounts of reagents used to prepare PTX-AN NCs

Substance	Amount	Equivalentents
IPDI	30.2 mg	0.27 meq
Drug (PTX)	45.2 mg	0.053 meq
Polymer (P2)	240.5 mg	0.072 meq
Dry THF	1.3 mL	–
L-lysine	7.6 mg	0.09 meq
Milli-Q water	14.90 g	–
DETA	3.4 mg	0.10 meq

### 5.13. Non-labile paclitaxel-loaded amphoteric NCs (NL-PTX-AMP NCs)

The procedure was based on the paclitaxel-loaded amphoteric NCs (see section 5.4) with slight variations, detailed in **Table 12**.

**Table 12.** Amounts of reagents used to prepare NL-PTX-AMP NCs

Substance	Amount	Equivalentents
IPDI	30.8 mg	0.28 meq
Drug (PTX)	44.0 mg	0.051 meq
Polymer (P3)	255.3 mg	0.069 meq
Dry THF	1.1 mL	–
L-lysine	5.8 mg	0.069 meq
Milli-Q water	13.88 g	–
DETA	4.0 mg	0.11 meq

### 5.14. *Non-labile DiO-loaded amphoteric NCs (NL-DiO-AMP NCs)*

The procedure was based on the paclitaxel-loaded amphoteric NCs (see section 5.4) with slight variations, detailed in **Table 13**. In this case, the three-necked round-bottom flask was protected from light.

**Table 13.** Amounts of reagents used to prepare NL-DiO-AMP NCs

Substance	Amount	Equivalents
IPDI	30.6 mg	0.28 meq
Fluorophore (DiO)	4.0 mg	4.5 $\mu$ eq
Polymer (P3)	251.6 mg	0.063 meq
Dry THF	1.5 mL	–
L-lysine	6.0 mg	0.070 meq
Milli-Q water	15.59 g	–
DETA	4.0 mg	0.12 meq

### 5.15. *Non-labile DiI-loaded amphoteric NCs (NL-DiI-AMP NCs)*

The procedure was based on the paclitaxel-loaded amphoteric NCs (see section 5.4) with slight variations, detailed in **Table 14**. In this case, the three-necked round-bottom flask was protected from light.

**Table 14.** Amounts of reagents used to prepare NL-DiI-AMP NCs

Substance	Amount	Equivalents
IPDI	30.7 mg	0.28 meq
Fluorophore (DiI)	4.0 mg	4.3 $\mu$ eq
Polymer (P3)	243.5 mg	0.064 meq
Dry THF	1.5 mL	–
L-lysine	6.0 mg	0.070 meq
Milli-Q water	15.54 g	–
DETA	4.0 mg	0.12 meq

## 6. Synthetic procedures of Chapter 3

### 6.1. *Tambjamine17-loaded amphoteric NCs at low concentration (T17-AMP-L NCs)*

IPDI (53.7 mg, 0.48 meq) was added into a three-necked round-bottom flask equipped with mechanical stirring, precooled at 4 °C, purged with N<sub>2</sub> and protected from light. In parallel, a mixture of T17 (25.2 mg, 0.066 meq), the amphiphilic cationic polymer P1 (314.5 mg of P1, 0.13 meq) and dry THF (1 mL) were dissolved in a vial and ultrasonicated for 15 min. Then, the organic mixture was added into the flask and left to homogenize for 30 min at 150 rpm. At this point, an alkaline aqueous solution of L-lysine prepared as in section 5.4 from this Chapter (8.3 mg of L-lysine, 0.098 meq) was added and the polyaddition reaction was checked after 45 min by IR. Then, the organic phase was emulsified at 300 rpm with cold Milli-Q water (9.99 g) and finally an aqueous solution of DETA (7.6 mg of DETA, 0.22 meq) was added in order to crosslink the nanodroplets of the nanoemulsion. The stirring was reduced to 100 rpm and the ice bath was removed to let the reaction reach rt. This polyaddition reaction was monitored by IR and pH measurements. Once the NCs were formed, THF was removed from the reactor at 40 °C under reduced pressure and the pH was adjusted to 7.0 using diluted aqueous HCl.

### 6.2. *Tambjamine18-loaded amphoteric NCs at low concentration (T18-AMP-L NCs)*

The procedure was based on the tambjamine17-loaded amphoteric NCs at low concentration (see section 6.1) with slight variations, listed in **Table 15**.

**Table 15.** Amounts of reagents used to prepare T18-AMP-L NCs

<b>Substance</b>	<b>Amount</b>	<b>Equivalents</b>
<b>IPDI</b>	53.7 mg	0.48 meq
<b>Drug (T18)</b>	25.1 mg	0.070 meq
<b>Polymer (P1)</b>	311.4 mg	0.13 meq
<b>Dry THF</b>	1.4 mL	-
<b>L-lysine</b>	8.3 mg	0.098 meq
<b>Milli-Q water</b>	10.44 g	-
<b>DETA</b>	7.2 mg	0.21 meq

### **6.3. Tambjamine17-loaded amphoteric NCs at medium concentration (T17-AMP-M NCs)**

The procedure was based on the tambjamine17-loaded amphoteric NCs at low concentration (see section 6.1) with slight variations, detailed in **Table 16**.

**Table 16.** Amounts of reagents used to prepare T17-AMP-M NCs

<b>Substance</b>	<b>Amount</b>	<b>Equivalents</b>
<b>IPDI</b>	59.3 mg	0.53 meq
<b>Drug (T17)</b>	40.6 mg	0.11 meq
<b>Polymer (P1)</b>	350.7 mg	0.12 meq
<b>Dry THF</b>	1.2 mL	-
<b>L-lysine</b>	9.7 mg	0.12 meq
<b>Milli-Q water</b>	9.13 g	-
<b>DETA</b>	8.4 mg	0.25 meq

#### 6.4. *Tambjamine18-loaded amphoteric NCs at medium concentration (T18-AMP-M NCs)*

The procedure was based on the tambjamine17-loaded amphoteric NCs at low concentration (see section 6.1) with slight variations, included in **Table 17**.

**Table 17.** Amounts of reagents used to prepare T18-AMP-M NCs

Substance	Amount	Equivalentents
IPDI	22.0 mg	0.20 meq
Drug (T21)	17.2 mg	0.045 meq
Polymer (P1)	172.4 mg	0.048 meq
Dry THF	1.3 mL	–
L-lysine	4.4 mg	0.053 meq
Milli-Q water	10.06 g	–
DETA	3.0 mg	0.087 meq

#### 6.5. *Tambjamine17-loaded amphoteric NCs at high concentration (T17-AMP-H NCs)*

The procedure was based on the tambjamine17-loaded amphoteric NCs at low concentration (see section 6.1) with slight variations, shown in **Table 18**.

**Table 18.** Amounts of reagents used to prepare T17-AMP-H NCs

Substance	Amount	Equivalentents
IPDI	17.6 mg	0.16 meq
Drug (T17)	31.9 mg	0.084 meq
Polymer (P1)	172.7 mg	0.047 meq
Dry THF	1.2 mL	–
L-lysine	4.2 mg	0.050 meq
Milli-Q water	9.99 g	–
DETA	1.8 mg	0.052 meq

### 6.6. *Tambjamine18-loaded amphoteric NCs at high concentration (T18-AMP-H NCs)*

The procedure was based on the tambjamine17-loaded amphoteric NCs at low concentration (see section 6.1) with slight variations, included in **Table 19**.

**Table 19.** Amounts of reagents used to prepare T18-AMP-H NCs

Substance	Amount	Equivalentents
IPDI	17.9 mg	0.16 meq
Drug (T18)	14.9 mg	0.041 meq
Polymer (P1)	130.0 mg	0.025 meq
Dry THF	1.2 mL	–
L-lysine	2.2 mg	0.026 meq
Milli-Q water	6.10 g	–
DETA	3.6 mg	0.104 meq

### 6.7. *Unloaded amphoteric NCs-2 (BLANK-AMP-2 NCs)*

The procedure was based on the tambjamine17-loaded amphoteric NCs at low concentration (see section 6.1) with slight variations, included in **Table 20**.

**Table 20.** Amounts of reagents used to prepare BLANK-AMP-2 NCs

Substance	Amount	Equivalentents
IPDI	17.7 mg	0.16 meq
Drug (T18)	0 mg	0 meq
Polymer (P1)	129.4 mg	0.025 meq
Dry THF	1.1 mL	–
L-lysine	2.2 mg	0.026 meq
Milli-Q water	6.08 g	–
DETA	3.6 mg	0.104 meq

### 6.8. *Tambjamine18-loaded amphoteric TMXDI NCs (T18-TMXDI-AMP NCs)*

The procedure was based on the tambjamine17-loaded amphoteric NCs at low concentration (see section 6.1) with slight variations, detailed in **Table 21**. In this case, IPDI was replaced by TMXDI.

**Table 21.** Amounts of reagents used to prepare T18-TMXDI-AMP NCs

Substance	Amount	Equivalentents
TMXDI	6.0 mg	0.049 meq
Drug (T18)	7.0 mg	0.019 meq
Polymer (P1)	49.0 mg	0.013 meq
Dry THF	1.4 mL	–
L-lysine	1.7 mg	0.020 meq
Milli-Q water	9.36 g	–
DETA	0.7 mg	0.019 meq

### 6.9. *Tambjamine18-loaded amphoteric GTCC NCs (T18-GTCC-AMP NCs)*

The procedure was based on the tambjamine17-loaded amphoteric NCs at low concentration (see section 6.1) with slight variations, detailed in **Table 22**. In this case, Crodamol GTCC was added in the organic phase as a hydrophobizing agent.

**Table 22.** Amounts of reagents used to prepare T18-GTCC-AMP NCs

Substance	Amount	Equivalentents
IPDI	5.9 mg	0.052 meq
Drug (T18)	7.3 mg	0.020 meq
Crodamol GTCC	0.7 mg	1.23 $\mu$ eq
Polymer (P1)	51.5 mg	0.014 meq
Dry THF	1.4 mL	–

<b>L-lysine</b>	1.7 mg	0.020 meq
<b>Milli-Q water</b>	10.05 g	–
<b>DETA</b>	0.5 mg	0.015 meq

### 6.10. *Tambjamine18-loaded amphoteric TMXDI GTCC NCs (T18-TMXDI-GTCC-AMP NCs)*

The procedure was based on the tambjamine17-loaded amphoteric NCs at low concentration (see section 6.1) with slight variations, listed in **Table 23**. In this case, Crodamol GTCC was added in the organic phase as a hydrophobizing agent and IPDI isocyanate was replaced by TMXDI.

**Table 23.** Amounts of reagents used to prepare **T18-TMXDI-GTCC-AMP NCs**

<b>Substance</b>	<b>Amount</b>	<b>Equivalentents</b>
<b>TMXDI</b>	6.1 mg	0.050 meq
<b>Drug (T18)</b>	7.2 mg	0.020 meq
<b>Crodamol GTCC</b>	0.7 mg	1.23 $\mu$ eq
<b>Polymer (P1)</b>	51.5 mg	0.014 meq
<b>Dry THF</b>	1.4 mL	–
<b>L-lysine</b>	1.5 mg	0.017 meq
<b>Milli-Q water</b>	9.12 g	–
<b>DETA</b>	0.5 mg	0.015 meq

### 6.11. Unloaded amphoteric TMXDI GTCC NCs (BLANK TMXDI-GTCC NCs)

The procedure was based on the tambjamine17-loaded amphoteric NCs at low concentration (see section 6.1) with slight variations, detailed in **Table 24**.

**Table 24.** Amounts of reagents used to prepare BLANK-TMXDI-GTCC NCs

Substance	Amount	Equivalents
TMXDI	6.2 mg	0.050 meq
Drug (T18)	0 mg	0 meq
Crodamol GTCC	0.7 mg	1.23 $\mu$ eq
Polymer (P1)	50.8 mg	0.014 meq
Dry THF	1.2 mL	–
L-lysine	1.5 mg	0.017 meq
Milli-Q water	9.12 g	–
DETA	0.5 mg	0.015 meq

### 6.12. Tambjamine18-loaded amphoteric NAST NCs (T18-NAST-AMP NCs)

The procedure was based on the tambjamine17-loaded amphoteric NCs at low concentration (see section 6.1) with slight variations, detailed in **Table 25**. In this case, sodium stearate was added with the organic phase.

**Table 25.** Amounts of reagents used to prepare T18-NAST-AMP NCs

Substance	Amount	Equivalents
IPDI	15.8 mg	0.14 meq
Drug (T18)	17.5 mg	0.049 meq
Sodium stearate	14.8 mg	0.048 meq
Polymer (P1)	123.6 mg	0.033 meq
Dry THF	1.4 mL	–

<b>L-lysine</b>	4.5 mg	0.053 meq
<b>Milli-Q water</b>	7.09 g	–
<b>DETA</b>	1.6 mg	0.046 meq

### 6.13. *Tambjamine17-loaded amphoteric NAST NCs (T17-NAST-AMP NCs)*

The procedure was based on the tambjamine17-loaded amphoteric NCs at low concentration (see section 6.1) with slight variations, detailed in **Table 26**. In this case, sodium stearate was added with the organic phase.

**Table 26.** Amounts of reagents used to prepare T17-NAST-AMP NCs

<b>Substance</b>	<b>Amount</b>	<b>Equivalents</b>
<b>IPDI</b>	15.6 mg	0.14 meq
<b>Drug (T17)</b>	18.0 mg	0.047 meq
<b>Sodium stearate</b>	14.8 mg	0.048 meq
<b>Polymer (P1)</b>	123.6 mg	0.033 meq
<b>Dry THF</b>	1.4 mL	–
<b>L-lysine</b>	4.5 mg	0.053 meq
<b>Milli-Q water</b>	7.10 g	–
<b>DETA</b>	1.5 mg	0.044 meq

### 6.14. *Unloaded amphoteric NAST NCs (BLANK-NAST NCs)*

The procedure was based on the tambjamine17-loaded amphoteric NCs at low concentration (see section 6.1) with slight variations, detailed in **Table 27**.

**Table 27.** Amounts of reagents used to prepare **BLANK-NAST NCs**

<b>Substance</b>	<b>Amount</b>	<b>Equivalents</b>
<b>IPDI</b>	47.4 mg	0.33 meq
<b>Drug (T17)</b>	0 mg	0 meq
<b>Sodium stearate</b>	44.4 mg	0.14 meq
<b>Polymer (P1)</b>	370.9 mg	0.1 meq
<b>Dry THF</b>	1.4 mL	–
<b>L-lysine</b>	13.4 mg	0.16 meq
<b>Milli-Q water</b>	10 g	–
<b>DETA</b>	4.7 mg	0.14 meq

### 6.15. *Tambjamine18-loaded amphoteric NALA NCs (T18-NALA-AMP NCs)*

The procedure was based on the tambjamine17-loaded amphoteric NCs at low concentration (see section 6.1) with slight variations, detailed in **Table 28**. In this case, sodium stearate was replaced by a shorter fatty acid salt, sodium laurate.

**Table 28.** Amounts of reagents used to prepare **T18-NALA-AMP NCs**

<b>Substance</b>	<b>Amount</b>	<b>Equivalents</b>
<b>IPDI</b>	12.5 mg	0.11 meq
<b>Drug (T18)</b>	12.2 mg	0.034 meq
<b>Sodium laurate</b>	7.3 mg	0.033 meq
<b>Polymer (P1)</b>	84.8 mg	0.026 meq
<b>Dry THF</b>	1.2 mL	–
<b>L-lysine</b>	2.7 mg	0.032 meq
<b>Milli-Q water</b>	3.96 g	–
<b>DETA</b>	1.4 mg	0.041 meq

### 6.16. DiO-loaded amphoteric NCs-2 (DiO-AMP-2 NCs)

The procedure was based on the paclitaxel-loaded amphoteric NCs (see section 5.4) with slight variations, detailed in **Table 29**. In this case, the three-necked round-bottom flask was protected from light.

**Table 29.** Amounts of reagents used to prepare DiO-AMP-2 NCs

Substance	Amount	Equivalentents
IPDI	32.1 mg	0.29 meq
Fluorophore (DiO)	4.0 mg	5.5 $\mu$ eq
Polymer (P1)	259.7 mg	0.079 meq
Dry THF	1.5 mL	–
L-lysine	5.7 mg	0.067 meq
Milli-Q water	8.63 g	–
DETA	2.8 mg	0.081 meq

### 6.17. Unloaded amphoteric NCs-3 (BLANK-AMP-3 NCs)

The procedure was based on the paclitaxel-loaded amphoteric NCs (see section 5.4) with slight variations, detailed in **Table 30**. In this case, the three-necked round-bottom flask was protected from light.

**Table 30.** Amounts of reagents used to prepare BLANK-AMP-3 NCs

Substance	Amount	Equivalentents
IPDI	32.0 mg	0.29 meq
Fluorophore (DiO)	0 mg	0 $\mu$ eq
Polymer (P1)	261.4 mg	0.08 meq
Dry THF	1.1 mL	–
L-lysine	5.8 mg	0.068 meq
Milli-Q water	10.09 g	–
DETA	2.8 mg	0.081 meq

### 6.18. DiR-loaded amphoteric NCs (DiR-AMP NCs)

The procedure was based on the paclitaxel-loaded amphoteric NCs (see section 5.4) with slight variations, detailed in **Table 31**. In this case, the three-necked round-bottom flask was protected from light.

**Table 31.** Amounts of reagents used to prepare DiR-AMP NCs

Substance	Amount	Equivalents
IPDI	39.3 mg	0.35 meq
Fluorophore (DiR)	3.8 mg	3.7 $\mu$ eq
Tributyrin	38.8 mg	0.13 meq
Polymer (P1)	328.4 mg	0.063 meq
Dry THF	1.2 mL	–
L-lysine	11.55 mg	0.14 meq
Milli-Q water	10.01 g	–
DETA	4.2 mg	0.12 meq

### 6.19. DiR-loaded NCs functionalized with antiGD2 (DiR-antiGD2 NCs)

IPDI (42.4 mg, 0.38 meq) was added into a purged three-necked round-bottom flask equipped with a mechanical stirrer, precooled at 4 °C and protected from light. In parallel, DiR (3.8 mg, 3.7  $\mu$ eq), tributyrin (40.0 mg, 0.13 meq), the amphiphilic cationic polymer P1 (331.9 mg of P1, 0.064 meq) and dry THF (1 mL) were mixed in a vial, added into the flask and left to homogenize for 30 min at 150 rpm. At this point, an alkaline aqueous solution of L-lysine (11.5 mg of L-lysine, 0.14 meq) was added and the polyaddition reaction was checked after 45 min by IR. The organic phase was emulsified at 300 rpm with cold Milli-Q water (10.02 g) and when the nanoemulsion was formed, part of the solution (6.70 mL) was rapidly transferred into another three-necked round-bottom flask. The rest of the volume was used for the antibody conjugation. To this end, an extra IR spectrum was recorded in order to confirm the presence of NCO in the sample and then an aqueous solution of DETA (1.1 mg of DETA, 0.035 meq) was added to precrosslink the NCs. At this point, the

stirring was reduced to 200 rpm and an aqueous solution of antiGD2 antibody (6.4 mg at 1 mg/mL in PBS pH 7.4) was added dropwise. The ice bath was removed to let the reaction reach rt and the conjugation reaction was monitored by pH measurements. The reaction was left overnight at rt and 40 rpm. The next day, THF was removed from the reactor at rt under reduced pressure and the pH was adjusted to 7.4 with diluted aqueous HCl. Finally, the excess of water was evaporated with a continuous N<sub>2</sub> flow at 37 °C.

## 7. Synthetic procedures of Chapter 4

### 7.1. Paclitaxel-loaded amphoteric NCs (PTX-AMP-2 NCs)

The procedure was based on the paclitaxel-loaded amphoteric NCs (see section 5.4) with slight variations, shown in **Table 32**.

**Table 32.** Amounts of reagents used to prepare PTX-AMP-2 NCs

Substance	Amount	Equivalents
IPDI	30.1 mg	0.27 meq
Drug (PTX)	71.3 mg	0.083 meq
Polymer (P1)	293.0 mg	0.07 meq
Dry THF	1 mL	–
L-lysine	7.9 mg	0.094 meq
Milli-Q water	8.25 g	–
DETA	3.6 mg	0.11 meq

### 7.2. Unloaded amphoteric NCs-4 (BLANK-AMP-4 NCs)

The procedure was based on the paclitaxel-loaded amphoteric NCs (see section 5.4) with slight variations, detailed in **Table 33**.

**Table 33.** Amounts of reagents used to prepare **BLANK-AMP-4 NCs**

<b>Substance</b>	<b>Amount</b>	<b>Equivalents</b>
<b>IPDI</b>	30.6 mg	0.27 meq
<b>Drug</b>	0 mg	0 meq
<b>Polymer (P1)</b>	293.0 mg	0.072 meq
<b>Dry THF</b>	1 mL	-
<b>L-lysine</b>	7.6 mg	0.091 meq
<b>Milli-Q water</b>	8.05 g	-
<b>DETA</b>	3.7 mg	0.11 meq

### **7.3. Hydrophilic linker 1 (HL1)**

Jeffamine ED2003 was dried under vacuum at 100 °C for 30 min. Meanwhile, IPDI (707.1 mg, 6.36 meq) and dry DMSO (6 mL) were added into a three-necked round-bottom flask equipped with mechanical stirring and purged with N<sub>2</sub>. Then, dry Jeffamine ED2003 (3.91 g, 3.71 meq) was added dropwise into the flask at 200 rpm and the reaction was monitored by IR until NCO stretching band intensity did not change.

### **7.4. Hydrophilic linker 2 (HL2)**

Jeffamine ED2003 was dried under vacuum at 100 °C for 30 min. Meanwhile, IPDI (1.75 g, 15.8 meq) was added into a purged three-necked round-bottom flask equipped with mechanical stirring. Then, a suspension of L-lysine preneutralized with NaOH 3 M (665.2 mg, 7.92 meq) in dry DMSO (3.5 mL) was slowly added and the reaction was monitored by IR until NCO stretching band intensity did not change. Finally, dry Jeffamine ED2003 (4.14 g, 3.90 meq) in dry DMSO (4 mL) was added dropwise at 200 rpm and the reaction was monitored by IR until the NCO stretching band intensity did not change.

### 7.5. *Hydrophilic linker 3 (HL3)*

This procedure was based on the synthesis of hydrophilic linker 2 (see section 7.4) with some variations, detailed in **Table 34**.

**Table 34.** Amounts of reagents used to prepare **HL3**

Substance	Amount	Equivalents
IPDI	369.3 mg	3.32 meq
Diaminopimelic acid/NaOH 3M	157.9 mg	1.66 meq
Dry DMSO	1.2 mL	–
Jeffamine ED2003	873.3 mg	0.83 meq
Dry DMSO	1 mL	–

### 7.6. *Hydrophilic linker 4 (HL4)*

This procedure was based on the synthesis of hydrophilic linker 2 (see section 7.4) with some variations, given in **Table 35**.

**Table 35.** Amounts of reagents used to prepare **HL4**

Substance	Amount	Equivalents
IPDI	710.2 mg	6.39 meq
Jeffcat DPA	351.1 mg	3.22 meq
Dry DMSO	1 mL	–
Dry DMSO	2 mL	–
Jeffamine ED2003	1.65 g	1.57 meq

### 7.7. Hydrophilic linker 5 (HL5)

This procedure was based on the synthesis of hydrophilic linker 2 (see section 7.4) with some variations, shown in **Table 36**.

**Table 36.** Amounts of reagents used to prepare HL5

Substance	Amount	Equivalents
IPDI	1.28 g	11.53 meq
Dry THF	1 mL	–
DMPA	382.3 mg	5.70 meq
TEA	500 $\mu$ L	3.58 meq
Dry THF	2 mL	–
Jeffamine ED2003	2.97 g	2.82 meq

### 7.8. HL1-A5 to HL5-A5 conjugates

A stirring bar and the hydrophilic linker were placed in a vial. After purging the system with N<sub>2</sub>, dry DMSO (250  $\mu$ L) was added and left to homogenize for 5 min. At this point, the peptide, pre-mixed with TEA and dry DMSO (250  $\mu$ L), was added into the vial in several fractions in order to prevent aggregation. The mixture was left to react for 4 h at rt.

This procedure was followed for the synthesis of all A5 conjugates using the required amounts of reagents, as shown in **Table 37**.

**Table 37.** Amounts of reagents used to prepare from HL1-A5 to HL5-A5

Code	Linker type	Linker amount	NCO eq.	A5 amount	A5 eq.	TEA amount
HL1-A5	HL1	211.4 mg	0.050 meq	20.1 mg	12 $\mu$ eq	5 $\mu$ l
HL2-A5	HL2	92.1 mg	0.025 meq	10.0 mg	6.2 $\mu$ eq	3 $\mu$ l
HL3-A5	HL4	137.9 mg	0.028 meq	11.4 mg	7.0 $\mu$ eq	3 $\mu$ l
HL4-A5	HL5	129.1 mg	0.032 meq	13.0 mg	8.1 $\mu$ eq	3 $\mu$ l
HL5-A5	HL6	229.8 mg	0.043 meq	17.5 mg	0.01 meq	4 $\mu$ l

<b>HL5-A5-2</b>	HL6	44.3 mg	0.015 meq	6.1 mg	3.8 $\mu$ eq	2 $\mu$ l
<b>HL5-A5-5</b>	HL6	119.4 mg	0.041 meq	16.5 mg	10 $\mu$ eq	4 $\mu$ l

### 7.9. *HL1-IPEP conjugate (HL1-IPEP)*

**HL1** linker (255.6 mg, 0.079 meq) was placed in a vial, purged with N<sub>2</sub> and precooled at 4 °C. Separately, IPEP peptide (16.0 mg, 0.019 meq) was dissolved in cold Milli-Q water (500  $\mu$ L) and TEA (8  $\mu$ L, 0.057 meq) was added. The peptide solution was slowly added into the vial and the reaction was left stirring for 4 h.

### 7.10. *HL1-IPEP-2 and HL1-IPEP-5 conjugates*

This procedure was based on the synthesis of **HL1-IPEP** conjugate (see section 7.9) with slight variations, detailed in **Table 38**.

**Table 38.** Amounts of reagents used to prepare **HL1-IPEP** to **HL1-IPEP-5**

Code	Linker type	Linker amount	NCO eq.	IPEP amount	IPEP eq.	TEA amount
<b>HL1-IPEP-2</b>	HL1	73.0 mg	0.032 meq	6.2 mg	7.4 $\mu$ eq	4 $\mu$ l
<b>HL1-IPEP-5</b>	HL1	194.9 mg	0.086 meq	16.0 mg	19 $\mu$ eq	10 $\mu$ l

### 7.11. *Paclitaxel-loaded NCs functionalized with HL1-A5 (PTX-HL1-A5 NCs)*

The procedure was based on the paclitaxel-loaded amphoteric NCs (see section 5.4), with the modification that the order of addition was altered. In this case, after the emulsification, a first fraction of DETA was added at rt and an IR spectrum was recorded. Then, the **HL1-A5** conjugate was added and the reaction finished with the addition of the second fraction of DETA. The amounts used are shown in **Table 39**.

**Table 39.** Amounts of reagents used to prepare **PTX-HL1-A5 NCs**

Substance	Amount	Equivalents
IPDI	14.0 mg	0.13 meq
Drug (PTX)	34.9 mg	0.041 meq
Polymer (P1)	127.7 mg	0.037 meq
Dry THF	1 mL	–
L-lysine	2.7 mg	0.033 meq
Milli-Q water	20.01 g	–
DETA	0.7 mg	0,019 meq
DETA	1.3 mg	0.039 meq

### 7.12. Paclitaxel-loaded NCs functionalized with HL2-A5 (PTX-HL2-A5 NCs)

The procedure was based on the paclitaxel-loaded amphoteric NCs (see section 5.4), with the modification that the order of addition was altered. In this case, after the emulsification, a first fraction of DETA was added at rt and an IR spectrum was recorded. Then, the **HL2-A5** conjugate was added and the reaction finished with the addition of the second fraction of DETA. The amounts used are shown **Table 40**.

**Table 40.** Amounts of reagents used to prepare **PTX-HL2-A5 NCs**

Substance	Amount	Equivalents
IPDI	14.4 mg	0.13 meq
Drug (PTX)	36.1 mg	0.042 meq
Polymer (P1)	130.3 mg	0.037 meq
Dry THF	1.1 mL	–
L-lysine	3.1 mg	0.036 meq
Milli-Q water	11.08 g	–
DETA 1	0.8 mg	0.024 meq
DETA 2	1.6 mg	0.048 meq

### 7.13. Paclitaxel-loaded NCs functionalized with HL3-A5 (PTX-HL3-A5 NCs)

The procedure was based on the paclitaxel-loaded amphoteric NCs (see section 5.4), with the modification that the order of addition was altered. In this case, after the emulsification, a first fraction of DETA was added at rt and an IR spectrum was recorded. Then, the **HL3-A5** conjugate was added and the reaction finished with the addition of the second fraction of DETA. The amounts used are shown in **Table 41**.

**Table 41.** Amounts of reagents used to prepare PTX-HL3-A5 NCs

Substance	Amount	Equivalents
IPDI	14.5 mg	0.13 meq
Drug (PTX)	39.1 mg	0.046 meq
Polymer (P1)	164.7 mg	0.047 meq
Dry THF	1.2 mL	–
L-lysine	3.0 mg	0.033 meq
Milli-Q water	9.51 g	–
DETA 1	0.8 mg	0.022 meq
DETA 2	1.5 mg	0.045 meq

### 7.14. Paclitaxel-loaded NCs functionalized with HL4-A5 (PTX-HL4-A5 NCs)

The procedure was based on the paclitaxel-loaded amphoteric NCs (see section 5.4), with the modification that the order of addition was altered. In this case, after the emulsification, a first fraction of DETA was added at rt and an IR spectrum was recorded. Then, the **HL4-A5** conjugate was added and the reaction finished with the addition of the second fraction of DETA. The amounts used are shown in **Table 42**.

**Table 42.** Amounts of reagents used to prepare **PTX-HL4-A5 NCs**

Substance	Amount	Equivalents
IPDI	15.5 mg	0.14 meq
Drug (PTX)	37.8 mg	0.044 meq
Polymer (P1)	180.9 mg	0.049 meq
Dry THF	1 mL	–
L-lysine	3.2 mg	0.035 meq
Milli-Q water	9.75 g	–
DETA 1	0.7 mg	0.021 meq
DETA 2	1.5 mg	0.043 meq

### 7.15. Paclitaxel-loaded NCs functionalized with HL5-A5 (PTX-HL5-A5 NCs)

The procedure was based on the paclitaxel-loaded amphoteric NCs (see section 5.4), with the modification that the order of addition was altered. In this case, after the emulsification, a first fraction of DETA was added at rt and an IR spectrum was recorded. Then, the **HL5-A5** conjugate was added and the reaction finished with the addition of the second fraction of DETA. The amounts used are shown in **Table 43**.

**Table 43.** Amounts of reagents used to prepare **PTX-HL5-A5 NCs**

Substance	Amount	Equivalents
IPDI	15.0 mg	0.14 meq
Drug (PTX)	51.1 mg	0.044 meq
Polymer (P1)	280.3 mg	0.06 meq
Dry THF	1.1 mL	–
L-lysine	3.7 mg	0.04 meq
Milli-Q water	9.79 g	–
DETA 1	0.7 mg	0.019 meq
DETA 2	1.5 mg	0.043 meq

### 7.16. *DiO-loaded NCs functionalized with HL5-A5-2 (DiO-HL5-A5-5 NCs)*

The procedure was based on the paclitaxel-loaded NCs functionalized with **HL5-A5** (see section 7.15), with the modification that the **HL5-A5-2** conjugate was used instead, and that the reactor was protected from light. The amounts used are shown in **Table 44**.

**Table 44.** Amounts of reagents used to prepare **DiO-HL5-A5-2 NCs**

Substance	Amount	Equivalents
IPDI	17.3 mg	0.16 meq
Fluorophore (DiO)	7.8 mg	8.8 $\mu$ eq
Polymer (P1)	200.8 mg	0.054 meq
Dry THF	1.3 mL	–
L-lysine	4.0 mg	0.048 meq
Milli-Q water	7.13 g	–
DETA 1	0.9 mg	0.027 meq
DETA 2	1.2 mg	0.034 meq

### 7.17. *DiO-loaded NCs functionalized with HL5-A5-5 (DiO-HL5-A5-5 NCs)*

The procedure was based on the paclitaxel-loaded NCs functionalized with **HL5-A5** (see section 7.15), with the modification that the **HL5-A5-5** conjugate was used instead, and that the reactor was protected from light. The amounts used are shown in **Table 45**.

**Table 45.** Amounts of reagents used to prepare **DiO-HL5-A5-5 NCs**

<b>Substance</b>	<b>Amount</b>	<b>Equivalents</b>
<b>IPDI</b>	16.5 mg	0.15 meq
<b>Fluorophore (DiO)</b>	7.8 mg	8.8 $\mu$ eq
<b>Polymer (P1)</b>	201.9 mg	0.055 meq
<b>Dry THF</b>	1.3 mL	–
<b>L-lysine</b>	3.7 mg	0.044 meq
<b>Milli-Q water</b>	7.10 g	–
<b>DETA 1</b>	0.85 mg	0.025 meq
<b>DETA 2</b>	1.85 mg	0.053 meq

### 7.18. *DiO-loaded amphoteric NCs-3 (DiO-AMP-3 NCs)*

The procedure was based on the paclitaxel-loaded amphoteric NCs (see section 5.4) with slight variations, listed in **Table 46**. In this case, the three-necked round-bottom flask was protected from light.

**Table 46.** Amounts of reagents used to prepare **DiO-AMP-3 NCs**

<b>Substance</b>	<b>Amount</b>	<b>Equivalents</b>
<b>IPDI</b>	18.2 mg	0.16 meq
<b>Fluorophore (DiO)</b>	7.7 mg	8.7 $\mu$ eq
<b>Polymer (P1)</b>	202.1 mg	0.055 meq
<b>Dry THF</b>	1.4 mL	–
<b>L-lysine</b>	4.5 mg	0.053 meq
<b>Milli-Q water</b>	7.70 g	–
<b>DETA</b>	1.6 mg	0.046 meq

### 7.19. Paclitaxel-loaded NCs functionalized with HL1-IPEP (PTX-HL1-IPEP NCs)

The procedure was based on the paclitaxel-loaded amphoteric NCs (see section 5.4), with the modification that the **HL1-IPEP** conjugate was added right before the emulsification step and that was left to homogenize for 5 min. The amounts used are shown in **Table 47**.

**Table 47.** Amounts of reagents used to prepare **PTX-HL1-IPEP NCs**

Substance	Amount	Equivalents
IPDI	19.2 mg	0.17 meq
Drug (PTX)	59.1 mg	0.069 meq
Polymer (P1)	182.0 mg	0.055 meq
Dry THF	1.2 mL	–
L-lysine	4.6 mg	0.055 meq
Milli-Q water	6.51 g	–
DETA	4.1 mg	0.12 meq

### 7.20. DiO-loaded NCs functionalized with HL1-IPEP-2 (DiO-HL1-IPEP-2 NCs)

The procedure was based on the paclitaxel-loaded amphoteric NCs (see section 5.4), with the modification that the reactor was protected from light and that the **HL1-IPEP-2** conjugate was added right before the emulsification step and that was left to homogenize for 5 min. The amounts used are shown in **Table 48**.

**Table 48.** Amounts of reagents used to prepare **DiO-HL1-IPEP-2 NCs**

Substance	Amount	Equivalents
IPDI	18.2 mg	0.16 meq
Fluorophore (DiO)	2.9 mg	3.3 $\mu$ eq
Polymer (P1)	180.8 mg	0.043 meq

<b>Dry THF</b>	1.2 mL	–
<b>L-lysine</b>	4.5 mg	0.053 meq
<b>Milli-Q water</b>	6.59 g	–
<b>DETA</b>	2.8 mg	0.081 meq

### 7.21. *DiO-loaded NCs functionalized with HL1-IPEP-5 (DiO-HL1-IPEP-5 NCs)*

The procedure was based on the paclitaxel-loaded amphoteric NCs (see section 5.4), with the modification that the reactor was protected from light and that the **HL1-IPEP-5** conjugate was added right before the emulsification step and that was left to homogenize for 5 min. The amounts employed are given in **Table 49**.

**Table 49.** Amounts of reagents used to prepare **DiO-HL1-IPEP-5 NCs**

<b>Substance</b>	<b>Amount</b>	<b>Equivalentents</b>
<b>IPDI</b>	18.2 mg	0.16 meq
<b>Fluorophore (DiO)</b>	2.9 mg	3.3 $\mu$ eq
<b>Polymer (P1)</b>	180.5 mg	0.043 meq
<b>Dry THF</b>	1.1 mL	–
<b>L-lysine</b>	4.5 mg	0.053 meq
<b>Milli-Q water</b>	6.55 g	–
<b>DETA</b>	4.2 mg	0.12 meq

### 7.22. *DiO-loaded amphoteric NCs-4 (DiO-AMP-4 NCs)*

The procedure was based on the paclitaxel-loaded amphoteric NCs (see section 5.4) with slight variations, shown in **Table 50**. In this case, the three-necked round-bottom flask was protected from light.

**Table 50.** Amounts of reagents used to prepare **DiO-AMP-4 NCs**

<b>Substance</b>	<b>Amount</b>	<b>Equivalentents</b>
<b>IPDI</b>	18.1 mg	0.16 meq
<b>Fluorophore (DiO)</b>	2.9 mg	3.3 $\mu$ eq
<b>Polymer (P1)</b>	180.0 mg	0.043 meq
<b>Dry THF</b>	1.2 mL	-
<b>L-lysine</b>	4.5 mg	0.053 meq
<b>Milli-Q water</b>	7.01 g	-
<b>DETA</b>	2.2 mg	0.063 meq



***General Conclusions  
and Future Prospects***



## **General conclusions**

The general conclusions derived from this Thesis are organized in three different parts: the methodology developed, the properties of the NCs and the results obtained from the biological studies.

### **1. Methodology**

- The NCs were prepared in almost a one-pot process under mild temperatures (only high temperatures were used to dry some of the starting monomers) and using very small volumes of organic solvents.
- The methodology yielded water-based NCs and avoided the use of external surfactants.
- The process was reproducible for different types of drugs, hydrophobic and amphiphilic, although some modifications had to be applied in the latter.
- The polymers prepared were functionalized in a few steps with different kinds of chemical groups and targeting moieties. In this regard, hydrophilic and hydrophobic side chains were inserted (YMER N-120 and Genamin TAP100D, respectively), as well as charged groups (L-lysine and Jeffcat DPA) and redox-cleavable bonds (DEDS).
- Targeting peptides (A5 and IPEP) were conjugated with moderate to good efficiency to the NCs surface through hydrophilic linkers that were prepared for this purpose.
- A specific mAb (antiGD2) was successfully functionalized to the NCs surface via direct coupling.

### **2. Properties of the NCs**

- The NCs loading hydrophobic molecules (PTX, CU, HP, HQ, DiO, DiI, DiR) were monodisperse and presented particle sizes around 20 nm on average. The same properties were observed for the NCs functionalized with antiGD2, IPEP and A5.
- The stability studies revealed that the NCs were only degraded under reductive conditions (presence of GSH), while they were stable in physiological medium and in protein-rich solutions.

- The NCs loading amphiphilic molecules (T17 and T18) were monodisperse with diameters around 20 nm after adding fatty-acid derived salts (NAST and NALA) in the process. By using these agents, the surface charge of the NCs and the entrapment efficiencies were also improved. However, the NCs were not improved when hydrophobizing agents (GTCC) and/or an aliphatic diisocyanate bearing an aromatic ring (TMXDI) was added.
- The study of the surface charge revealed a shell cationization effect that depended on the pH conditions: the NCs were neutral/anionic at physiological pH and cationic at slightly acidic conditions. This behavior was observed for NCs loading hydrophobic molecules, T17 and T18 once the process was optimized.

### **3. *Biological studies***

- The unloaded NCs were totally biocompatible with the cell lines studied.
- In the case of LC and NB cell lines, the drug-loaded NCs showed a cytotoxic effect that was maximum after 72 h of incubation, although the cells were slightly less sensitive to the encapsulated drug than to the free drug. These differences were more accentuated in NB cell lines than in LC cell lines. In addition, the drug-loaded NCs were more cytotoxic to LC cell lines than to normal cell fibroblasts (healthy cells), suggesting a slight selectivity to cancer cells.
- The NCs were internalized by endocytosis, were transported within the cells as endosomes and late endosomes and finally colocalized into the lysosomes.
- The cell uptake study revealed that the NCs were already internalized after 1 h of incubation and no saturation was observed after long treatments (48 h), confirming a sustained uptake. No differences were observed by performing the assays in slightly acidic pH values because of a technical limitation regarding the cell metabolism and the incubation conditions.
- The NCs conjugated to A5 did not lead to an enhanced internalization efficiency compared to the amphoteric NCs. In contrast, IPEP-functionalized NCs were more rapidly internalized after short incubation periods than their untargeted counterparts. However, the concentration of the peptide did not correlate with the targeting efficiency

- *In vivo* biodistribution studies showed that antiGD2-functionalized NCs were more accumulated in detoxification organs (liver and spleen) than the amphoteric NCs did, although this trend was reversed in the lungs. The tumor targeting abilities of amphoteric NCs were almost twice than those observed for antiGD2-functionalized NCs. The kidneys presented low uptake of both types of NCs and plasma analyses did not show any significant presence of them.

### ***Future prospects***

The results obtained from this Thesis have led to future prospects that aim the extension of the developed methodology to other applications. In this regard, the future studies involve:

- The performance of a biodistribution study with amphoteric NCs in well-established mice models developing tumors with a reasonable size and weight. In this regard, lower doses and more prolonged treatments could be tested according to the sustained accumulation and release of the NC. Besides carrying out the study with the cancer cell lines used in the Thesis (LC, BC and NB), other types of cancers could be also considered, and especially those of difficult access (pancreatic cancer, liver cancer).
- The study of an *in vivo* efficacy study to determine the capacity of the NCs to reduce the tumor volumes, compared to the free drug. This experiment could also be performed in different mice models, as long as the tumors have been well developed.
- The synthesis of polymers with other isocyanates containing aromatic rings in order to increase the barrier between the encapsulated molecule and the external environment. These studies could involve volatile compounds or highly sensitive molecules that are easily degraded by light, oxygen or humidity.
- The exploration of other hydrophilic targeting moieties, such as carbohydrates or gene sequences, to target specific cells or organelles.

- The preparation of polymers with another hydrophilic/lipophilic composition so as to explore the encapsulation of hydrophilic drugs such as peptides, proteins or DNA/RNA sequences.
- The synthesis of polymers containing other building blocks that provide responsiveness to other types of stimuli, such as temperature or light, to evaluate the NCs for theranostic purposes.

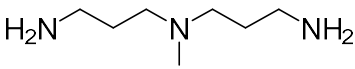
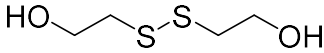
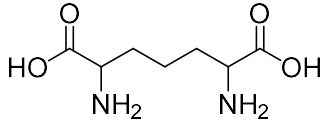
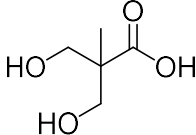
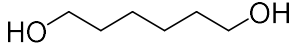
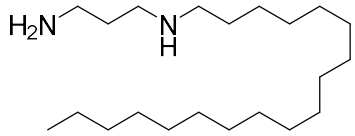
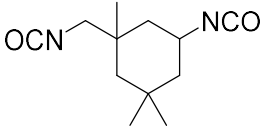
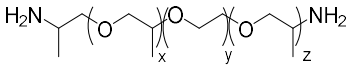
# **ANNEXES**

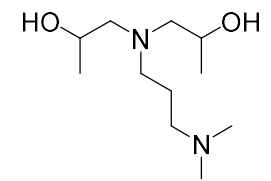
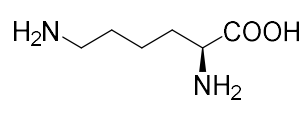
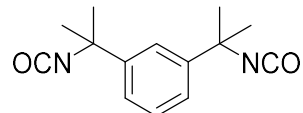
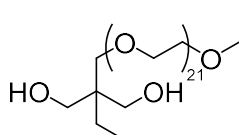
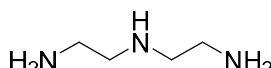


## 1. Reactive molecules

Polyisocyanates, polyols and polyamines used to synthesize the polymers and prepare the NCs.

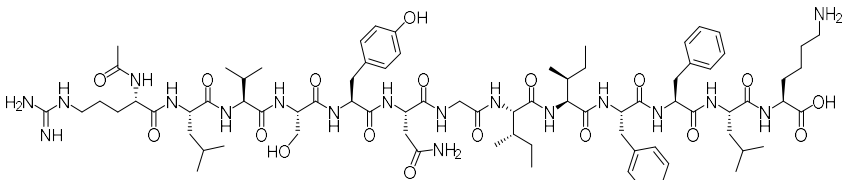
### 1.1. Building blocks and crosslinkers

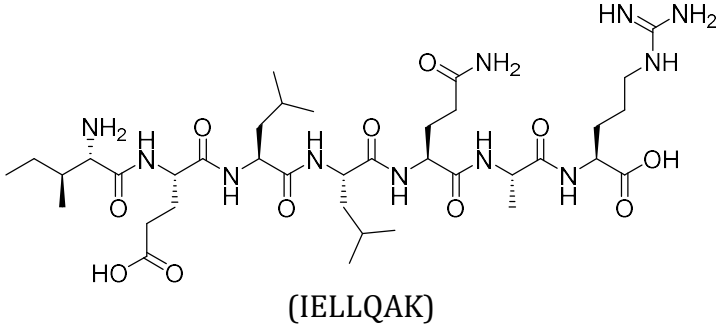
Abbreviated name	Nomenclature	Chemical structure
<b>BAPMA</b>	<i>N,N</i> -bis(3-aminopropyl)- <i>N</i> -methylamine	
<b>DEDS</b>	2,2'-Dihydroxyethyl disulfide	
<b>Diaminopimelic acid</b>	2,6-Diaminoheptanedioic acid	
<b>DMPA</b>	2,2-Dihydroxymethylpropanoic acid	
<b>1,6-Hexanediol</b>	1,6-Dihydroxyhexane	
<b>Genamin TAP100D</b>	1,3-Diamino- <i>N</i> -octadecylpropane	
<b>IPDI</b>	1,3,3-Trimethyl-1-(isocyanatomethyl)-5-isocyanatocyclohexane	
<b>Jeffamine ED2003</b>	-	 (x+z) ~ 6; y ~ 39

<b>Jeffcat DPA</b>	<i>N</i> -(3-Dimethylaminopropyl)- <i>N,N</i> -diisopropanolamine	
<b>L-Lysine·HCl</b>	L-lysine hydrochloride	
<b>TMXDI</b>	Tetramethyl-1,3-xylylene diisocyanate	
<b>YMER N-120</b>	-	
<b>DETA</b>	2,2'-Diaminodiethylamine	

## 1.2. Targeting molecules

Targeting molecules used to functionalize the NC shell.

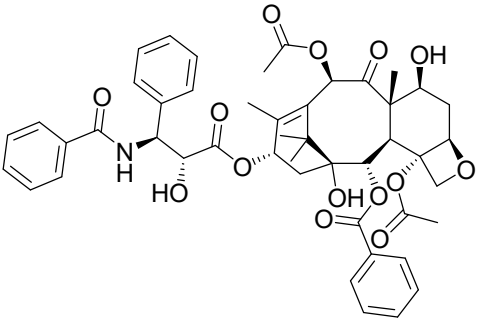
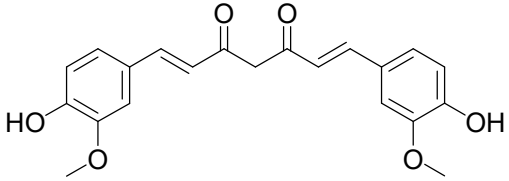
Abbreviated name	Chemical structure and amino acid sequence
<b><i>N</i>-acetyl A5 (A5)</b>	 <p>(<i>N</i>-acetyl-RLVSYNIIFFLK)</p>

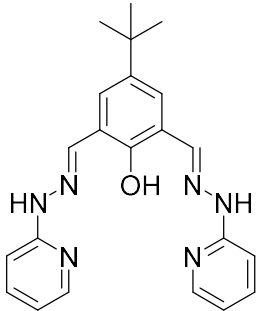
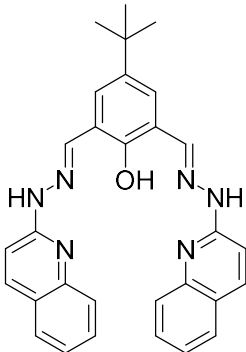
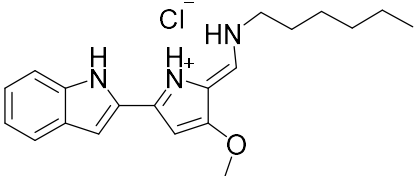
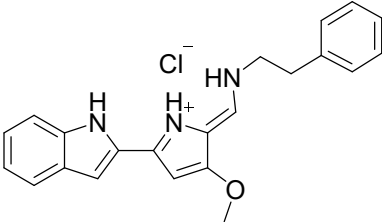
<b>IPEP</b>	 <p style="text-align: center;">(IPELLQAK)</p>
<b>AntiGD2 antibody</b>	Amino acid sequence shown in Chapter 3

## 2. Encapsulated molecules

### 2.1. Drugs

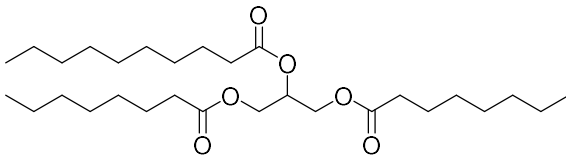
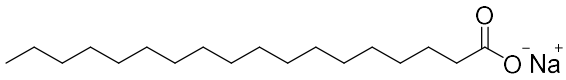
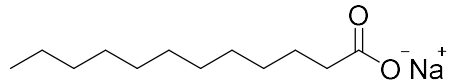
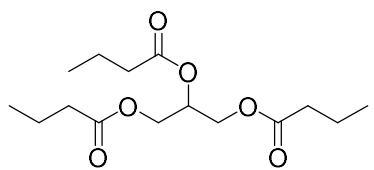
Bioactive molecules which have been introduced inside the nanocapsules.

Abbreviated name	Chemical structure
<b>PTX</b>	
<b>CU</b>	

<b>HP</b>	
<b>HQ</b>	
<b>T17</b>	
<b>T18</b>	

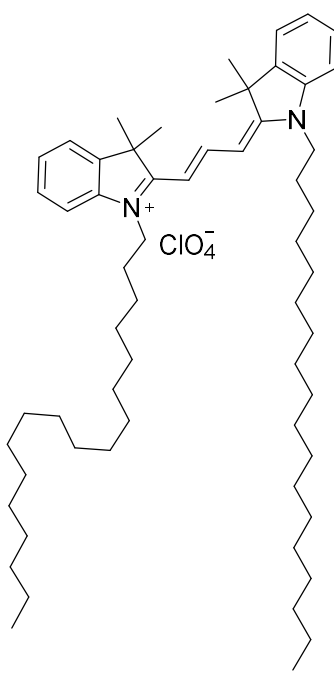
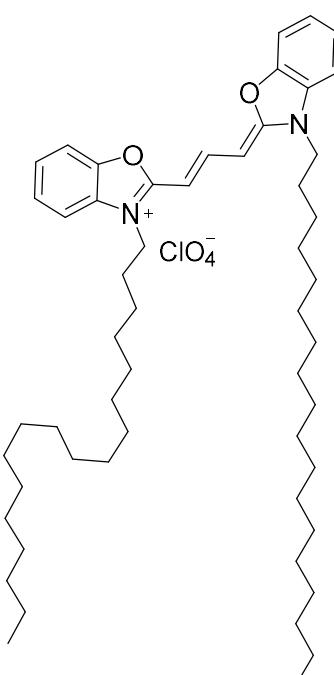
## 2.2. Superhydrophobic agents

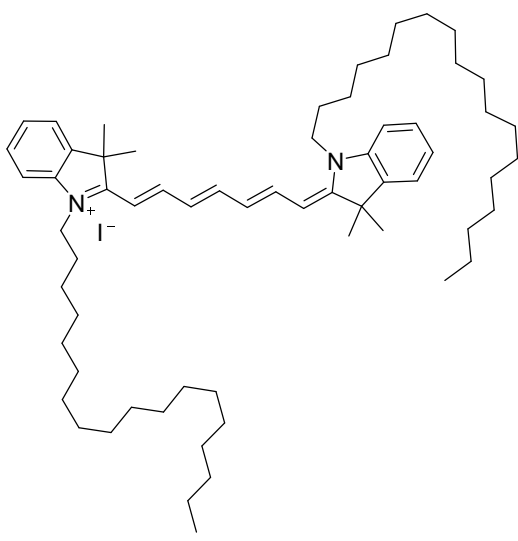
Oils or derivatives used to define better the o/w interface

Abbreviated name	IUPAC nomenclature	Chemical structure
<b>GTCC</b>	C <sub>8</sub> -C <sub>10</sub> glycerides	
<b>NAST</b>	Octadecanoic sodium salt	
<b>NALA</b>	Dodecanoic sodium salt	
<b>Tributyryn</b>	Glycerol tributanoate	

### 2.3. Fluorophores

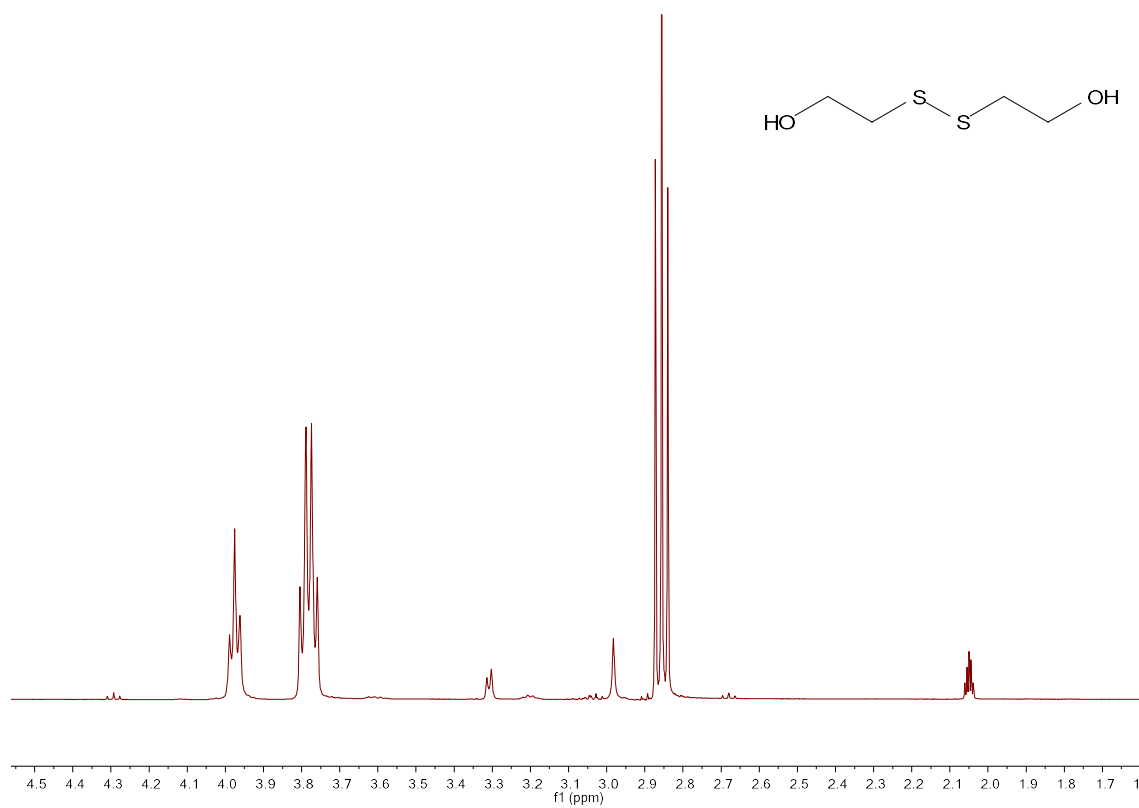
Fluorescent molecules used to load the NCs.

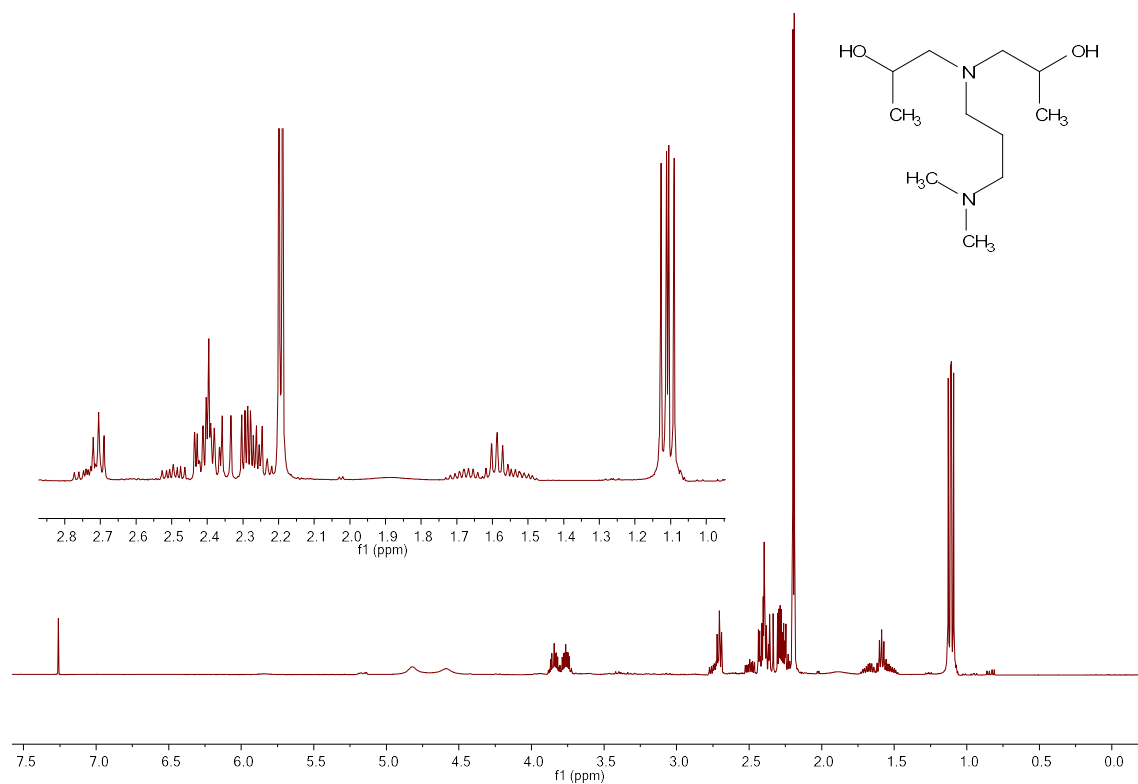
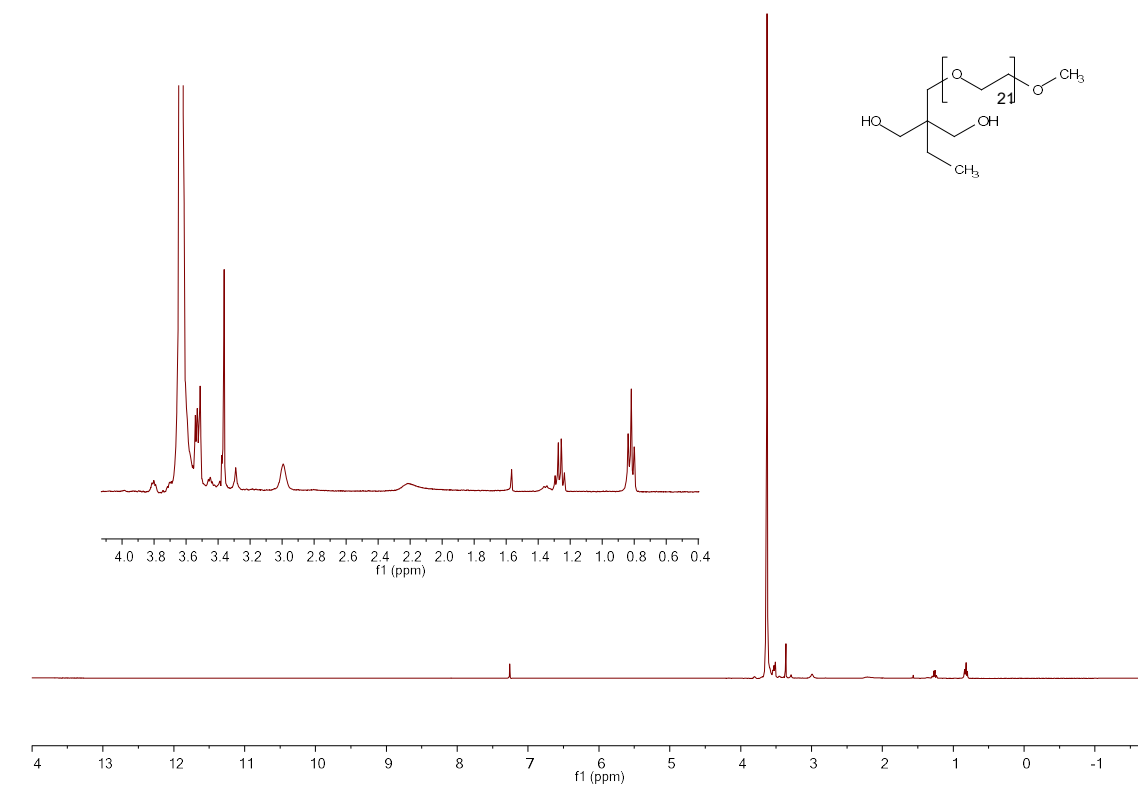
Abbreviated name	Nomenclature	Chemical structure
<b>DiI</b>	1,1'-Dioctadecyl-3,3,3',3'-tetramethylindocarbocyanine perchlorate	
<b>DiO</b>	3,3'-Dioctadecyloxacarbocyanine perchlorate	

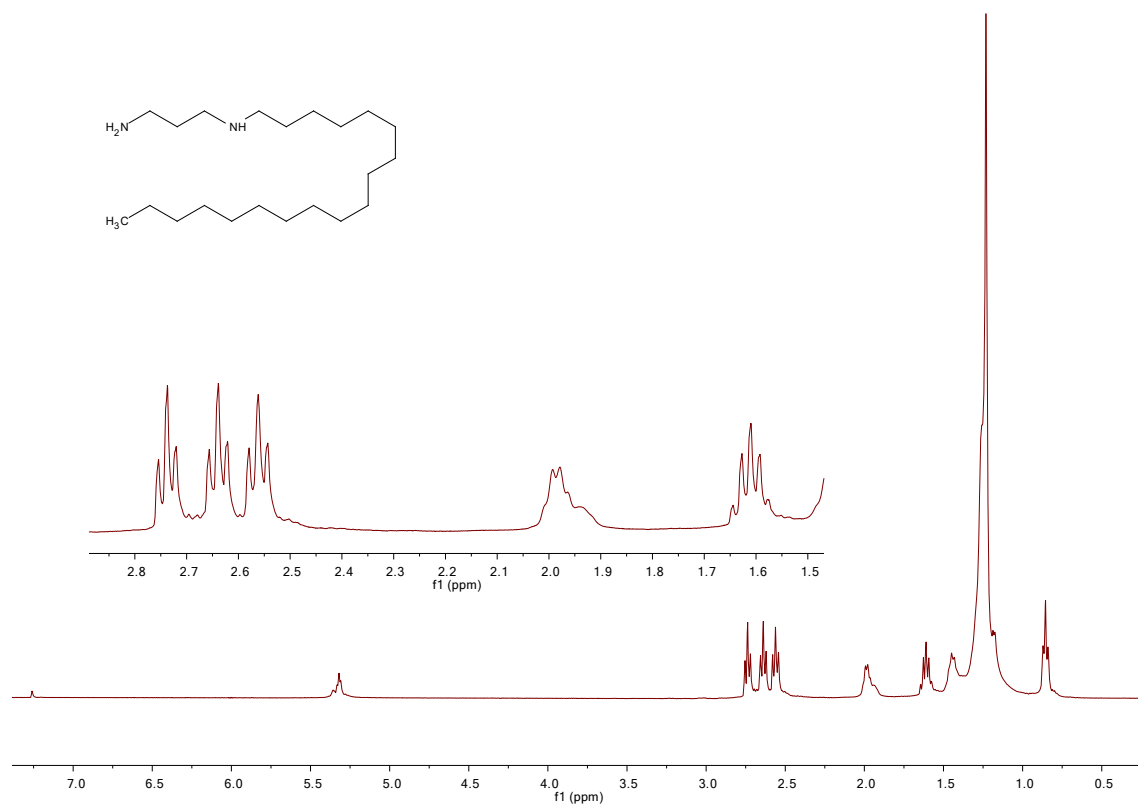
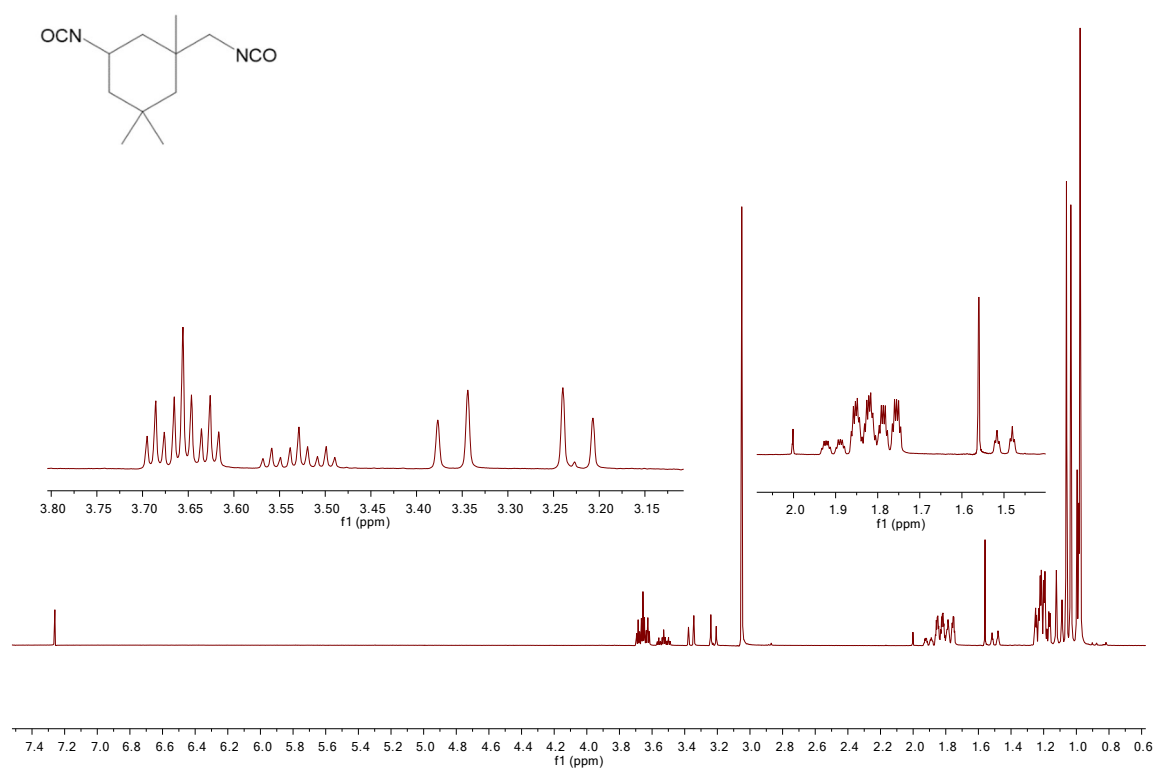
<b>DiR</b>	1,1'-Dioctadecyl-3,3,3',3'-tetramethylindotricarbocyanine iodide	
------------	--	--

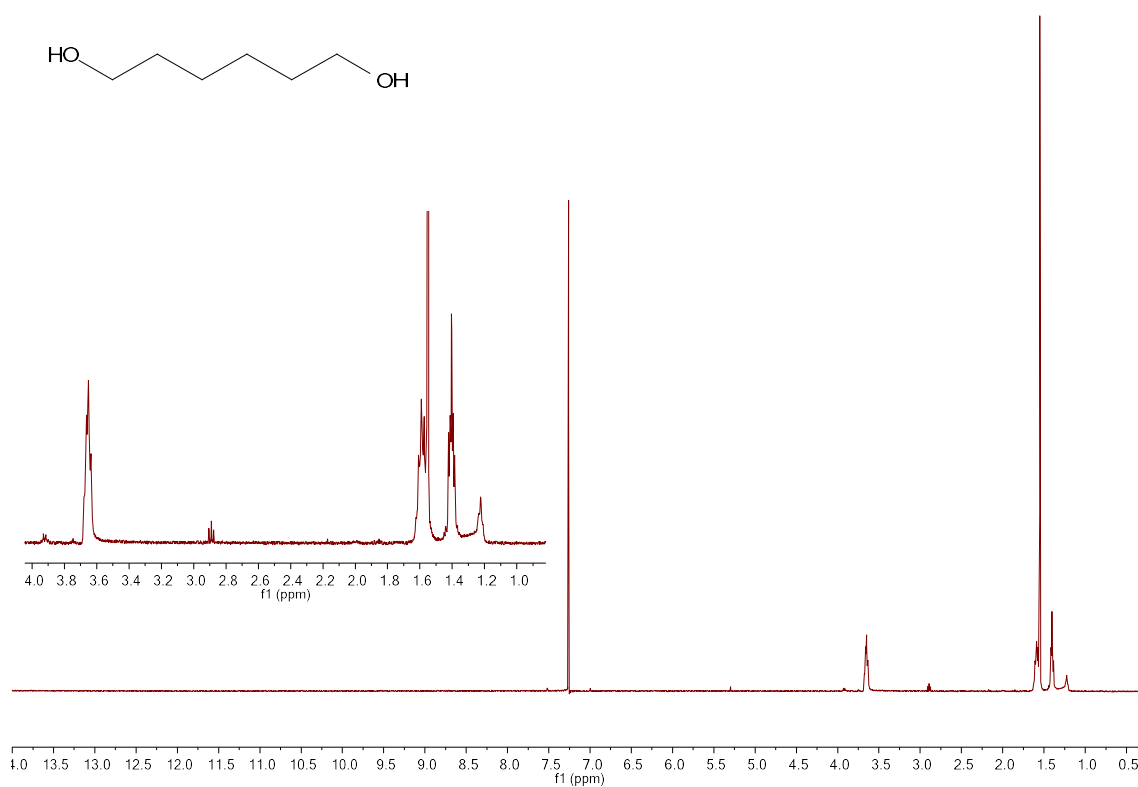
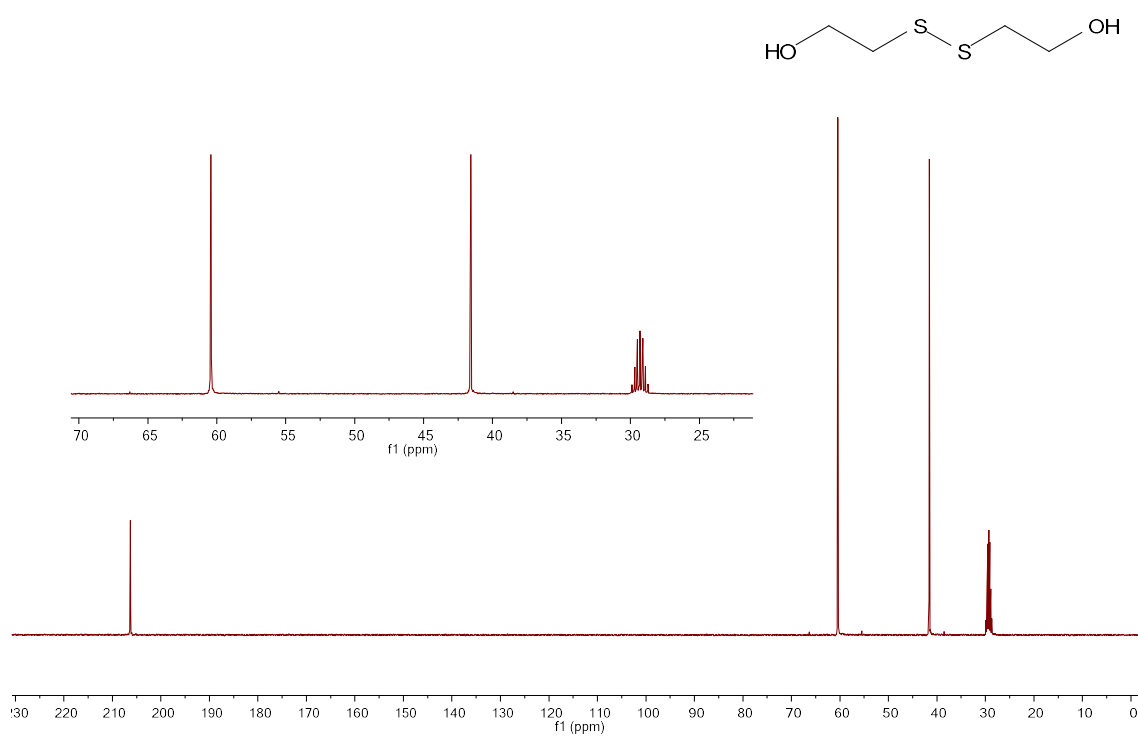
### 3. NMR spectra of the monomers

#### <sup>1</sup>H NMR DEDS

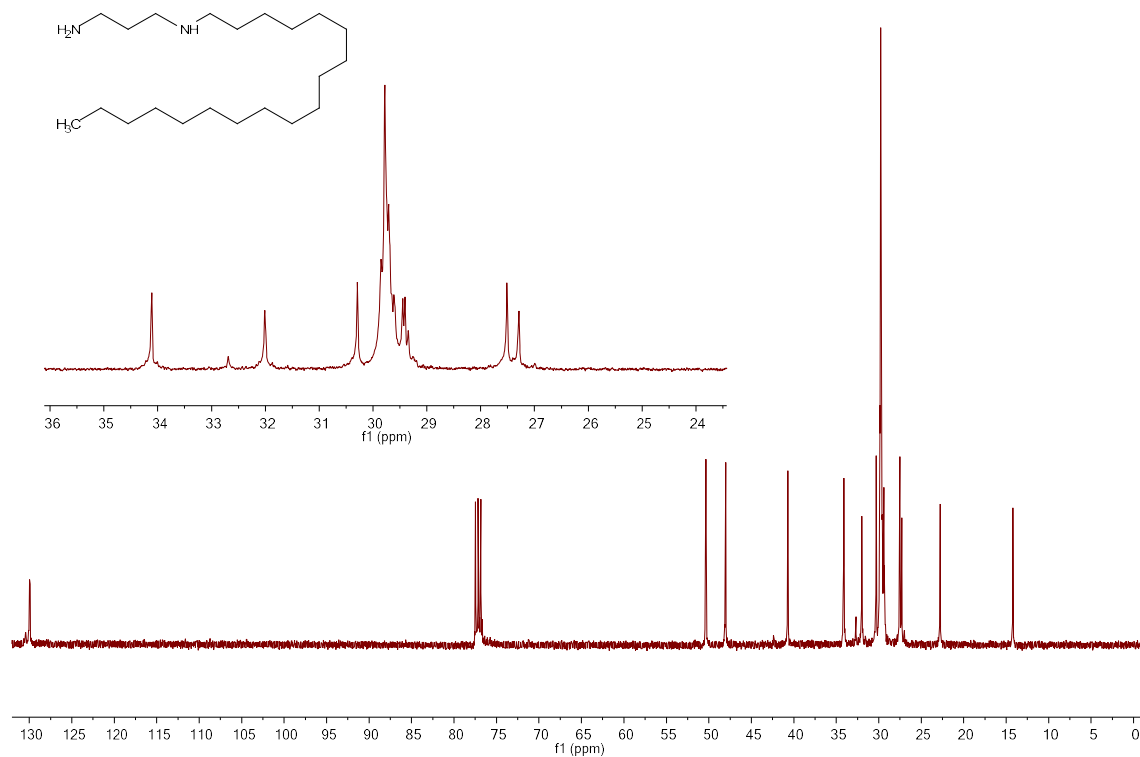
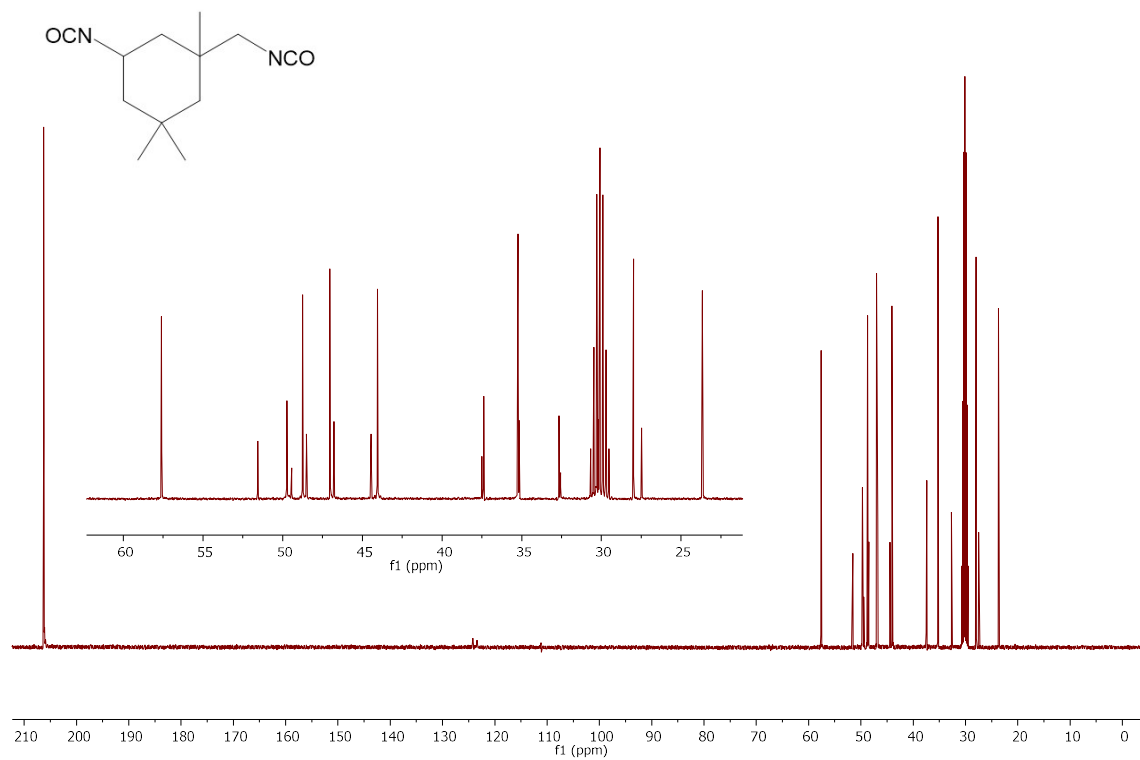


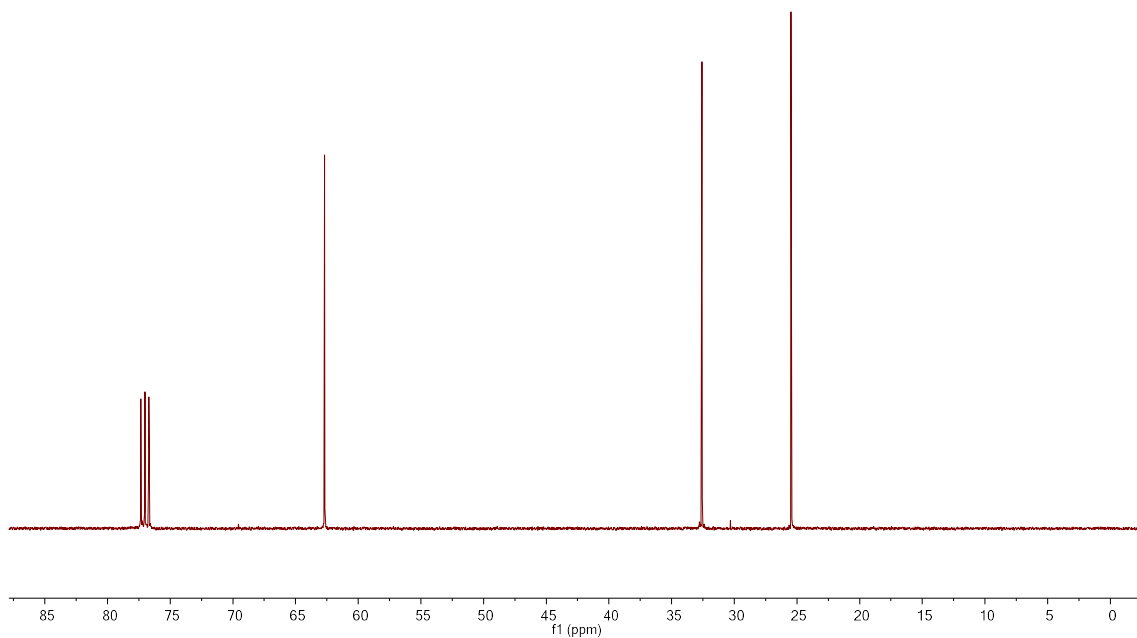
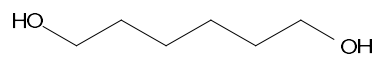
**<sup>1</sup>H NMR Jeffcat DPA****<sup>1</sup>H NMR YMER N-120**

**<sup>1</sup>H NMR Genamin TAP100D****<sup>1</sup>H NMR IPDI**

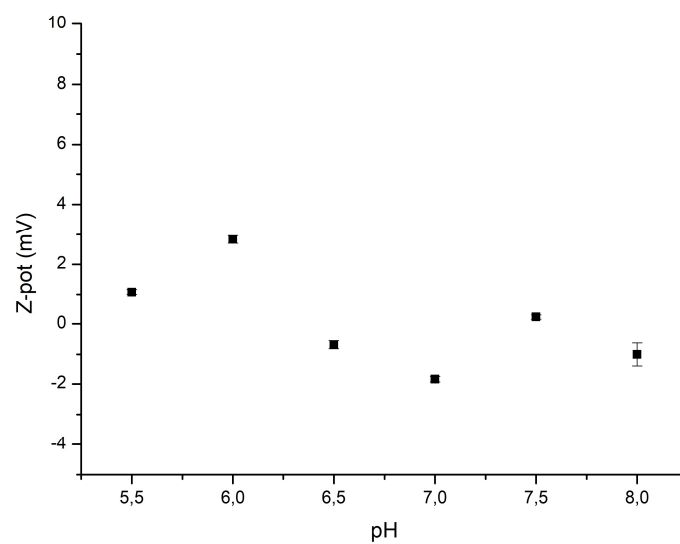
**$^1\text{H}$  NMR 1,6-hexanediol** **$^{13}\text{C}\{^1\text{H}\}$  NMR DEDS**



**$^{13}\text{C}\{^1\text{H}\}$  NMR Genamin TAP100D** **$^{13}\text{C}\{^1\text{H}\}$  NMR IPDI**

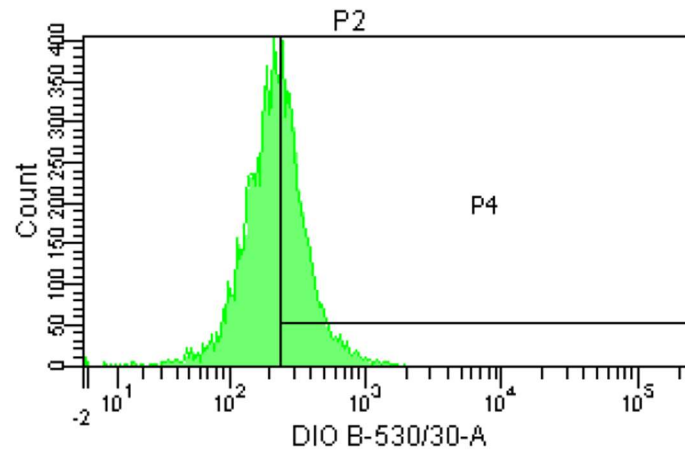
**$^{13}\text{C}\{^1\text{H}\}$  NMR 1,6-hexanediol****4. Z-potential measurements**

339

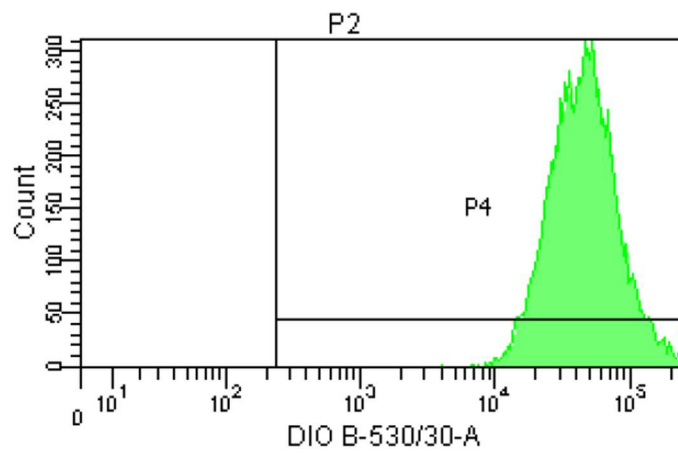
**Sample prepared from BAPMA**

## 5. Cytometry raw data

DiO-AMP-2 NCs incubated for 1 h

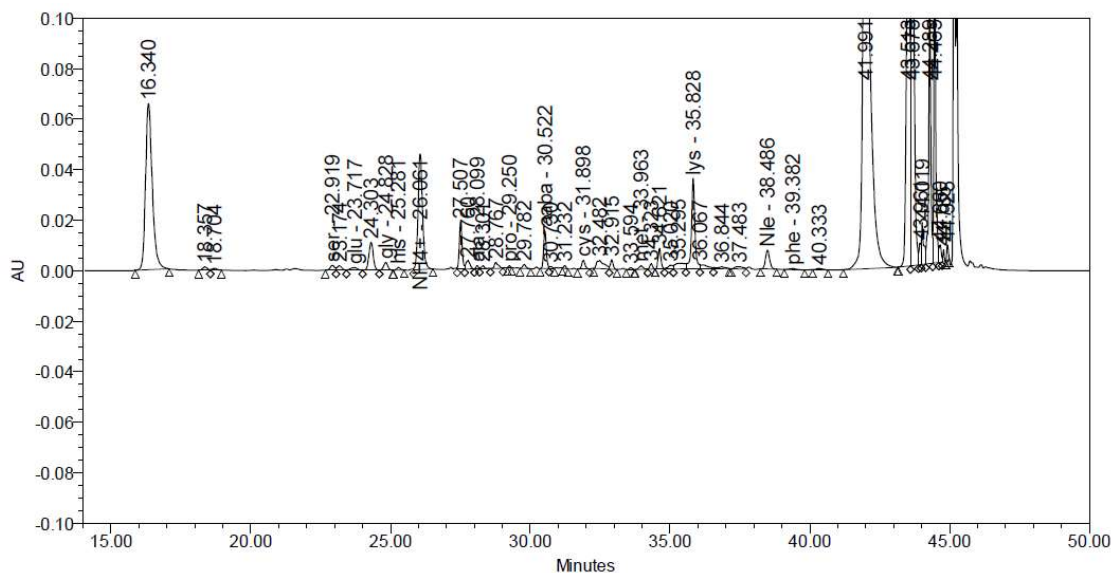


DiO-AMP-2 NCs incubated for 48 h



## 6. Chromatograms

### DiR-AMP NCs (CHAPTER 3)

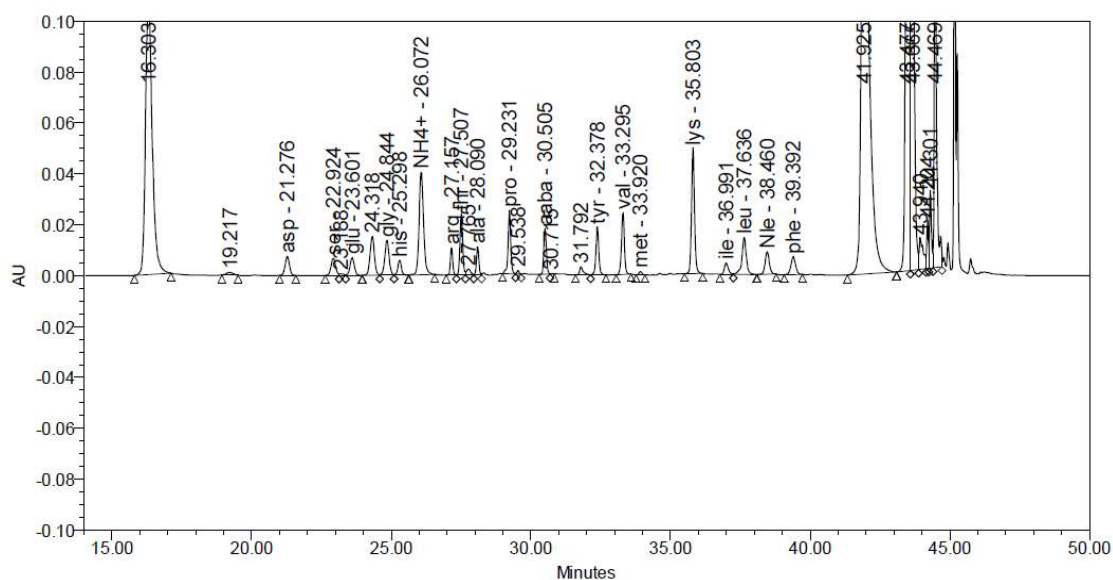


	Peak Name	RT	Area	% Area	Height	Amount
1	-	16.340	1103372	10.82	65925	-
2	-	18.357	15150	0.15	1282	-
3	-	18.704	9428	0.09	754	-
4	Asp	21.277	-	-	-	-
5	Ser	22.919	22096	0.22	1984	0.011
6	-	23.174	20733	0.20	1735	-
7	Glu	23.717	18675	0.18	1062	0.010
8	-	24.303	120380	1.18	11066	-
9	Gly	24.828	32653	0.32	3065	0.018
10	His	25.281	9280	0.09	1086	0.005
11	NH <sub>4</sub> <sup>+</sup>	26.061	505986	4.96	45843	-
12	Thr	26.061	-	-	-	-
13	-	27.507	130518	1.28	18725	-
14	Arg	27.760	-	-	-	-
15	-	27.760	34106	0.33	3199	-
16	Ala	28.099	6891	0.07	1255	0.004

17	-	28.301	9132	0.09	1087	-
18	-	28.767	23002	0.23	2344	-
19	Pro	29.250	3266	0.03	675	0.002
20	-	29.782	12398	0.12	1570	-
21	AABA	30.522	96834	0.95	14945	0.052
22	-	30.730	4867	0.05	677	-
23	-	31.232	6287	0.06	1123	-
24	Cys	31.898	29658	0.29	3410	0.018
25	-	32.482	62023	0.61	3213	-
26	Tyr	32.482	-	-	-	-
27	-	32.915	26571	0.26	3754	-
28	-	33.594	5142	0.05	683	-
29	Val	33.594	-	-	-	-
30	Met	33.594	14675	0.14	1373	0.007
31	-	33.963	14073	0.14	2089	-
32	-	34.323	58695	0.58	8238	-
33	-	34.621	18554	0.18	1502	-
34	-	35.020	54930	0.54	2227	-
35	Lys	35.295	311535	3.05	35882	0.108
36	-	35.828	29578	0.29	1555	-
37	Ile	36.067	12867	-	-	-
38	-	36.844	-	0.13	670	-
39	-	37.483	18153	0.18	895	-
40	Leu	37.483	-	-	-	-
41	NLE	38.486	74730	0.73	7344	0.041
42	Phe	39.382	9255	0.09	530	0.005
43	-	40.333	8113	0.08	535	-
44	-	41.991	3180997	31.19	169595	-
45	Trp	41.991	-	-	-	-
46	-	43.513	1163946	11.41	132538	-

47	-	43.678	1415711	13.88	204660	-
48	-	43.961	43455	0.43	8529	-
49	-	44.019	95690	0.94	15840	-
50	-	44.289	534451	5.24	105670	-
51	-	44.465	755534	7.41	183425	-
52	-	44.660	35744	0.35	6889	-
53	-	44.785	17601	0.17	4533	-
54	-	44.925	22763	0.22	5970	-

### DiR-antiGD2 NCs (CHAPTER 3)



343

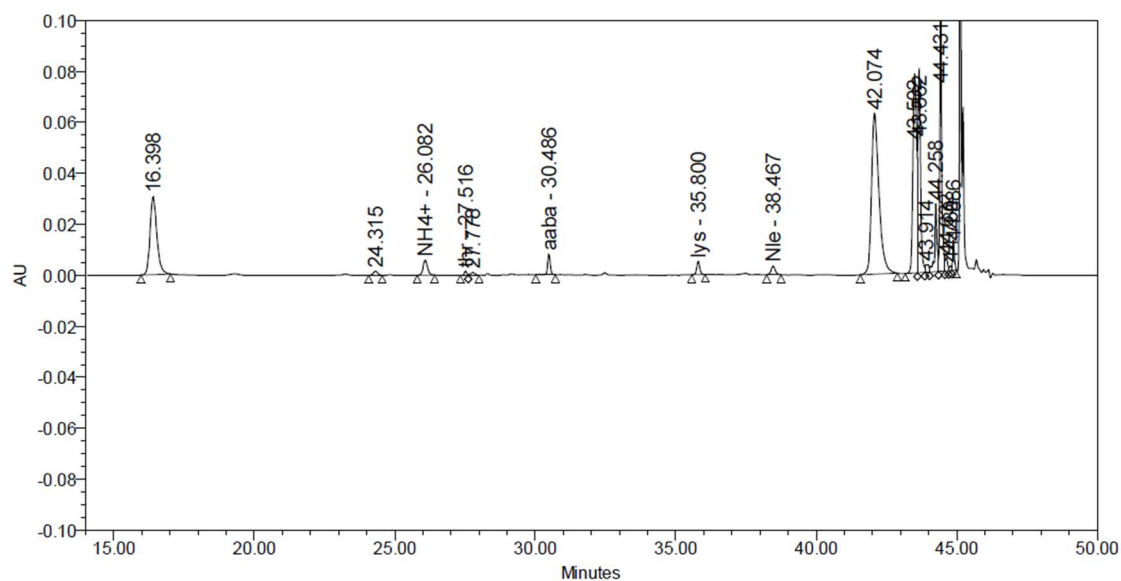
	Peak Name	RT	Area	% Area	Height	Amount
1	-	16.303	1821688	13.49	109304	-
2	-	19.217	18536	0.14	1060	-
3	Asp	21.276	80305	0.59	7535	0.045
4	Ser	22.924	76199	0.56	6703	0.039
5	-	23.188	6427	0.05	596	-
6	Glu	23.601	74470	0.55	6815	0.042
7	-	24.318	166338	1.23	15143	-
8	Gly	24.844	149685	1.11	13694	0.084
9	His	25.298	52617	0.39	5842	0.028

---

<b>10</b>	NH <sub>4</sub> <sup>+</sup>	26.072	448705	3.32	40337	-
<b>11</b>	Arg	27.157	60663	0.45	10723	0.031
<b>12</b>	Thr	27.507	170246	1.26	24080	0.091
<b>13</b>	-	27.765	25248	0.19	2378	-
<b>14</b>	Ala	28.090	66237	0.49	11111	0.036
<b>15</b>	Pro	29.231	162869	1.21	24858	0.082
<b>16</b>	-	29.538	7629	0.06	1319	-
<b>17</b>	AABA	30.505	114344	0.85	17940	0.061
<b>18</b>	-	30.715	1188	0.01	234	-
<b>19</b>	-	31.792	28906	0.21	3197	-
<b>20</b>	Cys	31.792	-	-	-	-
<b>21</b>	Tyr	32.378	131230	0.97	18819	0.066
<b>22</b>	Val	33.295	177746	1.32	24228	0.093
<b>23</b>	Met	33.920	9042	0.07	1328	0.005
<b>24</b>	Lys	35.803	372840	2.76	49308	0.129
<b>25</b>	Ile	36.991	43414	0.32	4466	0.022
<b>26</b>	Leu	37.636	160584	1.19	14501	0.084
<b>27</b>	NLE	38.46	93105	0.69	8836	0.051
<b>28</b>	Phe	39.392	83018	0.61	6988	0.043
<b>29</b>	-	41.925	3765188	27.89	203040	-
<b>30</b>	Trp	41.925	-	-	-	-
<b>31</b>	-	43.477	1837706	13.61	188936	-
<b>32</b>	-	43.665	1664215	12.33	224592	-
<b>33</b>	-	43.940	125576	0.93	12309	-
<b>34</b>	-	44.204	73245	0.54	18279	-
<b>35</b>	-	44.301	145594	1.08	29480	-
<b>36</b>	-	44.469	1286485	9.53	303921	-

---

## DiO-AMP-3 NCs (CHAPTER 4)

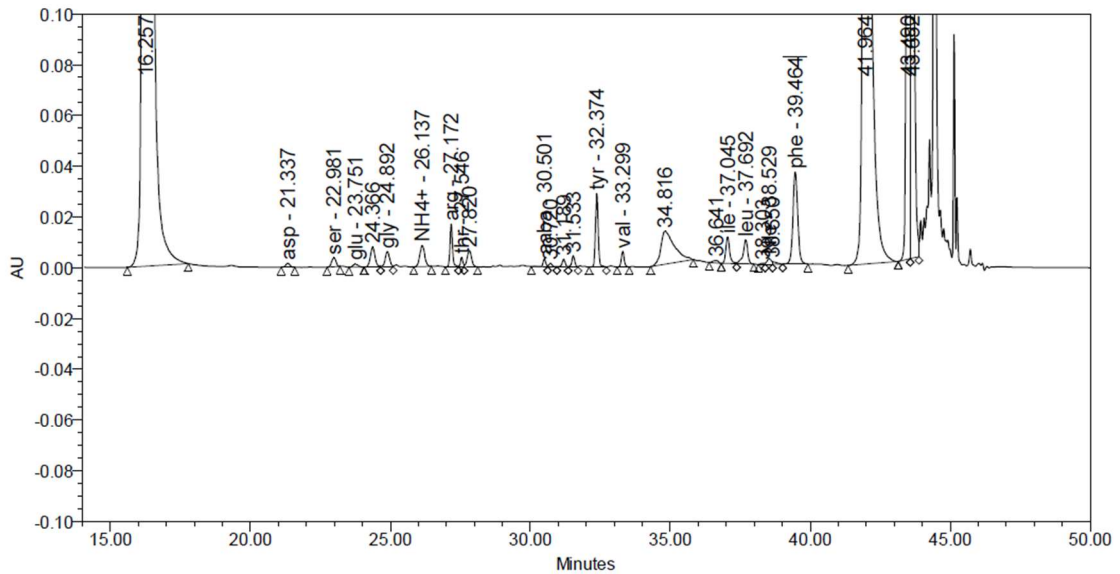


	Peak Name	RT	Area	% Area	Height	Amount
1	-	16.398	516782	13.31	30500	-
2	Asp	21.269	-	-	-	-
3	Ser	22.912	-	-	-	-
4	Glu	23.578	-	-	-	-
5	-	24.315	17452	0.45	1608	-
6	Gly	24.817	-	-	-	-
7	His	25.276	-	-	-	-
8	NH <sub>4</sub> <sup>+</sup>	26.082	64320	1.66	5865	-
9	Arg	27.138	-	-	-	-
10	Thr	27.516	10048	0.26	1687	0.005
11	-	27.778	11105	0.29	1025	-
12	Ala	28.067	-	-	-	-
13	Pro	29.213	-	-	-	-
14	AABA	30.486	52271	1.35	8079	0.025
15	Cys	31.871	-	-	-	-
16	Tyr	32.354	-	-	-	-
17	Val	33.281	-	-	-	-
18	Met	33.903	-	-	-	-

19	Lys	35.800	40280	1.04	5281	0.012
20	Ile	37.005	-	-	-	-
21	Leu	37.655	-	-	-	-
22	NLE	38.467	34333	0.88	3322	0.017
23	Phe	39.412	-	-	-	-
24	Trp	41.868	-	-	-	-
25	-	42.074	1167405	30.07	63248	-
26	-	43.502	695528	17.91	78129	-
27	-	43.662	514065	13.24	79885	-
28	-	43.914	26240	0.68	3094	-
29	-	44.258	153930	3.96	26378	-
30	-	44.431	496076	12.78	113476	-
31	-	44.632	28947	0.75	5076	-
32	-	44.780	10773	0.28	2001	-
33	-	44.886	43135	1.11	10174	-

346

## DiO-HL5-A5-5 NCs (CHAPTER 4)

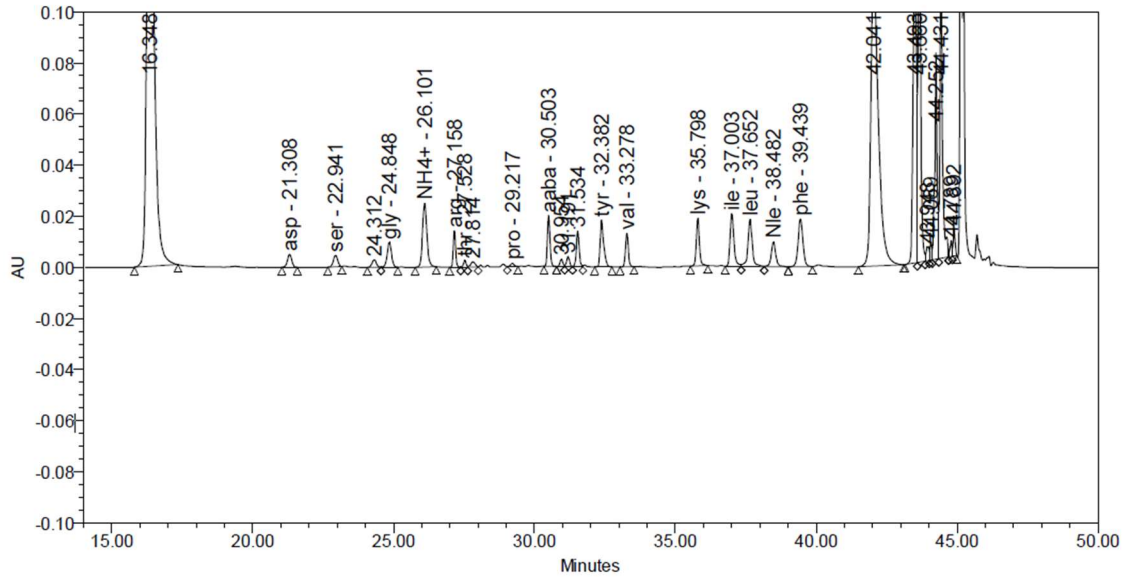


	Peak Name	RT	Area	% Area	Height	Amount
1	-	16.257	14677236	53.81	833610	-
2	Asp	21.337	16845	0.06	1600	0.008

3	Ser	22.981	38327	0.14	3600	0.017
4	Glu	23.751	15549	0.06	1190	0.007
5	-	24.366	92229	0.34	7987	-
6	Gly	24.892	66206	0.24	6044	0.032
7	His	25.314	-	-	-	-
8	NH <sub>4</sub> <sup>+</sup>	26.137	101932	0.37	8289	-
9	Arg	27.172	102416	0.38	16869	0.046
10	Thr	27.546	22761	0.08	3765	0.011
11	-	27.820	70285	0.26	6431	-
12	Ala	28.097	-	-	-	-
13	Pro	29.243	-	-	-	-
14	AABA	30.501	21838	0.08	3117	0.010
15	-	30.720	10935	0.04	1417	-
16	-	31.189	23138	0.08	3038	-
17	-	31.533	32701	0.12	4397	-
18	Cys	31.533	-	-	-	-
19	Tyr	32.374	192947	0.71	29044	0.086
20	Val	33.299	43555	0.16	6140	0.020
21	-	34.816	436974	1.60	12971	-
22	Met	34.816	-	-	-	-
23	-	36.641	12998	0.05	944	-
24	Lys	36.641	-	-	-	-
25	Ile	37.045	100033	0.37	10519	0.044
26	Leu	37.692	105937	0.39	9526	0.048
27	-	38.303	4080	0.01	430	-
28	NLE	38.529	23792	0.09	2269	0.011
29	-	38.650	10748	0.04	1010	-
30	Phe	39.464	434497	1.59	36341	0.199
31	-	41.964	5884651	21.57	312084	-
32	Trp	41.964	-	-	-	-

<b>33</b>	-	43.490	1860398	6.82	231140	-
<b>34</b>	-	43.652	2873078	10.53	418581	-

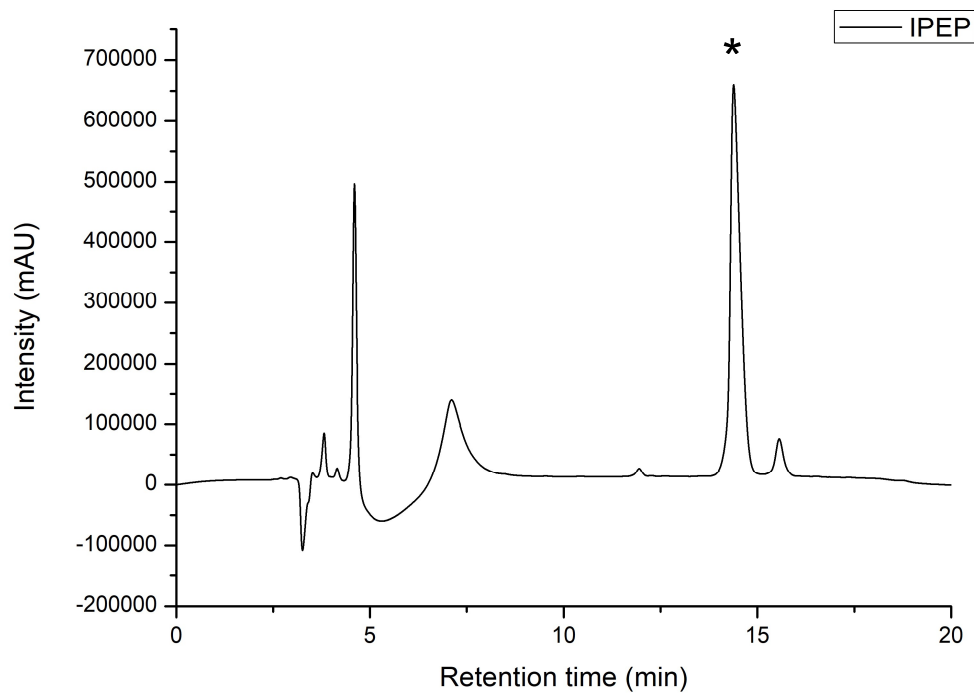
#### DiO-HL5-A5-2 NCs (CHAPTER 4)



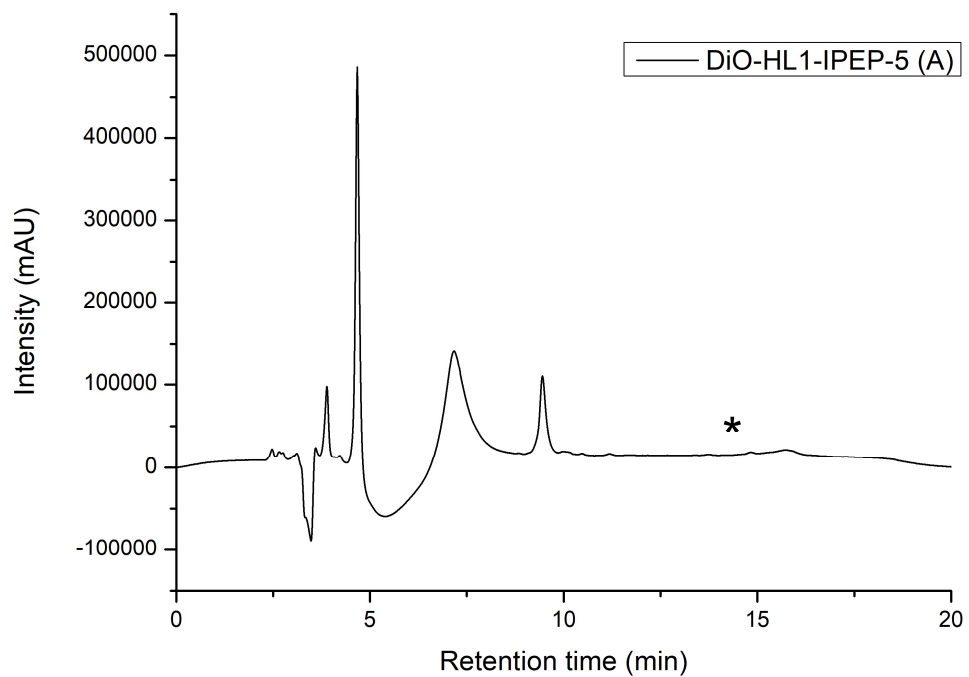
	Peak Name	RT	Area	% Area	Height	Amount
<b>1</b>	-	16.348	3574552	32.19	833610	-
<b>2</b>	Asp	21.308	53810	0.48	1600	0.028
<b>3</b>	Ser	22.941	48239	0.43	3600	0.023
<b>4</b>	Glu	23.578	-	-	1190	-
<b>5</b>	-	24.312	31765	0.29	7987	-
<b>6</b>	Gly	24.848	105088	0.95	6044	0.054
<b>7</b>	His	25.276	-	-	-	-
<b>8</b>	NH <sub>4</sub> <sup>+</sup>	26.101	270344	2.43	8289	-
<b>9</b>	Arg	27.158	80559	0.73	16869	0.038
<b>10</b>	Thr	27.528	17574	0.16	3765	0.009
<b>11</b>	-	27.814	23315	0.21	6431	-
<b>12</b>	Ala	28.067	-	-	-	-
<b>13</b>	Pro	29.217	10324	0.09	-	0.005
<b>14</b>	AABA	30.503	124588	1.12	3117	0.06
<b>15</b>	-	30.954	18836	0.17	1417	-

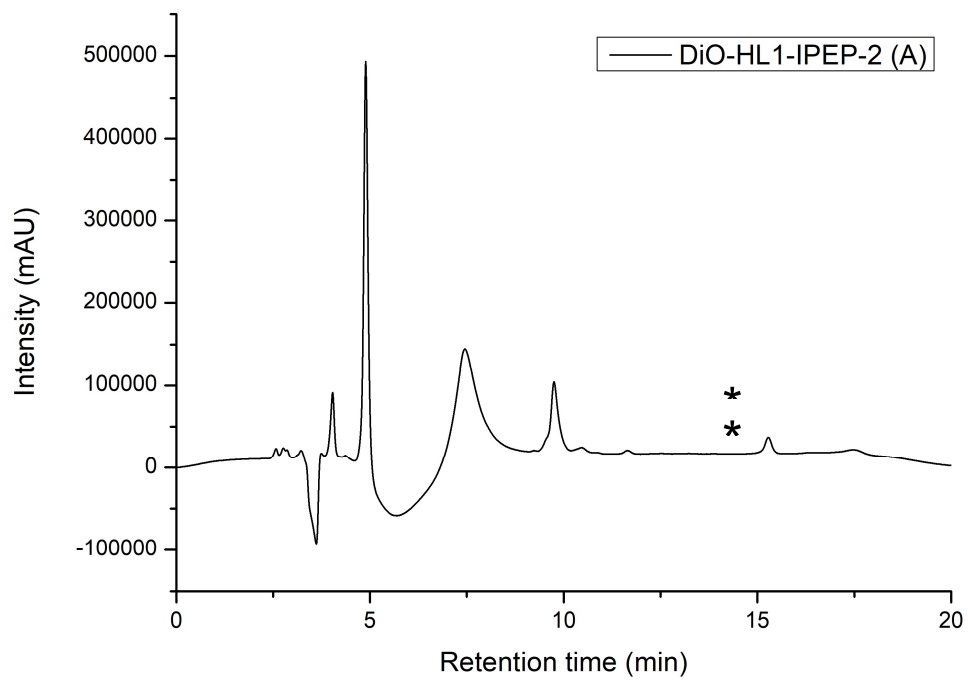
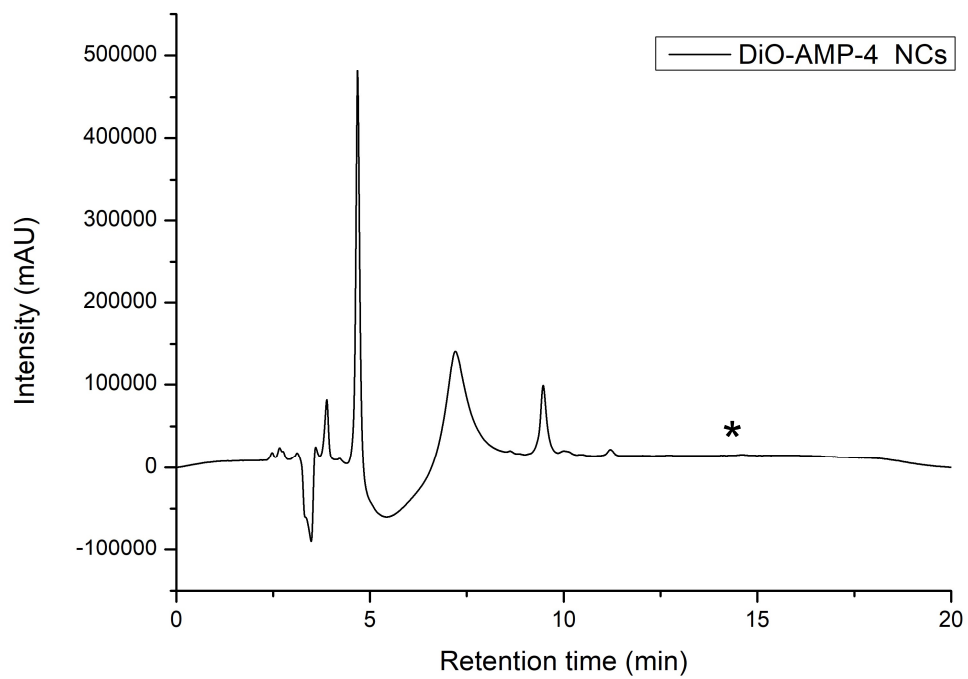
<b>16</b>	-	31.191	28263	0.25	3038	-
<b>17</b>	-	31.534	98211	0.88	4397	-
<b>18</b>	Cys	31.534	-	-	-	-
<b>19</b>	Tyr	32.382	157698	1.42	29044	0.074
<b>20</b>	Val	33.278	92175	0.83	6140	0.044
<b>21</b>	Met	34.903	-	-	12971	-
<b>22</b>	Lys	35.789	143307	1.29	-	0.044
<b>23</b>	Ile	37.003	195881	1.76	944	0.090
<b>24</b>	Leu	37.652	200469	1.81	-	0.097
<b>25</b>	NLE	38.482	110877	1.00	10519	0.056
<b>26</b>	Phe	39.439	224322	2.02	9526	0.108
<b>27</b>	-	42.041	2154877	19.41	430	-
<b>28</b>	Trp	42.041	-	-	2269	-
<b>29</b>	-	43.493	982998	8.85	1010	-
<b>30</b>	-	43.660	960393	8.65	36341	-
<b>31</b>	-	43.948	38934	0.35	312084	-
<b>32</b>	-	44.069	32582	0.29	-	-
<b>33</b>	-	44.252	471942	4.25	231140	-
<b>34</b>	-	44.431	773019	6.96		-
<b>35</b>	-	44.789	29429	0.27		-
<b>36</b>	-	44.892	49749	0.45	418581	-

**IPEP**



**DiO-HL1-IPEP-5 NCs**



**DiO-HL1-IPEP-2 NCs****DiO-AMP-4 NCs**

7. *In vivo* data (organs weight)

	Non-treated		DIR-AMP NCS						
	w/tumor	w/o tumor	w/tumor						
			G0-1 -2	G1-1 -5	G1-2 -6	G1-3 -7	G1-4 -8	G1-2R	G1-3R
Tumor	24 h	0,2123			0,2550	0,0877	0,1085	0,1110	0,0812
	48 h	0,1920			0,1598	0,0379	0,0548		
Spleen	24 h	0,1520	0,1495	0,1340	0,0982	0,1149	0,1340		
	48 h	0,1623	0,1135	0,1099	0,1361	0,1275	0,1099		
Liver	24 h	1,4137	1,3780	1,1721	1,4056	1,2556	1,1721		
	48 h	1,2912	1,4362	1,3859	1,1647	1,3659	1,3859		
Kidney	24 h	0,2909	0,3272	0,3384	0,3415	0,3582	0,3384		
	48 h	0,3538	0,3386	0,3486	0,3778	0,2878	0,3486		
Lung	24 h	0,1260	0,2035	0,1659	0,1749	0,1655	0,1659		
	48 h	0,2089	0,1696	0,1646	0,1632	0,1794	0,1646		
Plasma	24 h	0,0450	0,0509	0,0522	0,0511	0,0492	0,0522		
	48 h	0,0457	0,0529	0,0526	0,0488	0,0513	0,0526		

	Non-treated		DIR-antiGD2 NCS						
	w/tumor	w/o tumor	w/tumor						
			G0-3 -4	G2-1 -5	G2-2 -6	G2-3 -7	G2-4 -8	G2-2R	G2-8R
Tumor	24 h	0,0913			0,1301	0,0827	0,1183	0,4287	
	48 h	0,1478			0,0980	0,0258	0,1254		0,0477
Spleen	24 h	0,1652	0,1339	0,1352	0,1013	0,1677	0,1352		
	48 h	0,1855	0,1436	0,1987	0,1162	0,1406	0,1987		
Liver	24 h	1,1513	1,2274	1,3445	1,3924	1,4859	1,3445		
	48 h	1,4574	1,4166	1,3369	1,1676	1,1190	1,3369		
Kidney	24 h	0,3502	0,2731	0,3598	0,3420	0,3787	0,3598		
	48 h	0,3692	0,4053	0,3612	0,3372	0,3061	0,3612		
Lung	24 h	0,1252	0,1791	0,1933	0,1555	0,1836	0,1933		
	48 h	0,1935	0,1608	0,1732	0,1755	0,1510	0,1732		
Plasma	24 h	0,0496	0,0482	0,0473	0,0466	0,0561	0,0473		
	48 h	0,0569	0,0506	0,0479	0,0472	0,0545	0,0479		



